Development of a Novel Electrochemical Pyroprocessing Methodology for Spent Nuclear Fuels

By

Anthony John Stevenson

MSc, BSc (Hons)

Thesis submitted to the University of Nottingham

for the degree of Doctor of Philosophy

Department of Chemical and Environmental Engineering

The University of Nottingham

August 2016

Abstract

Nuclear power remains the most dense and reliable primary form of energy supply worldwide. Electricity generation via fission is also inherently carbon free, with environmental footprints rivalling modern renewable options. However issues arise from the production of highly irradiated spent fuels, with current management options limited to geological repository storage or, more desirably, closing of the fuel cycle by partitioning to recover fissionable species.

Extensive research has been pursued over the past half century in an effort to address an accumulating oxide spent fuel inventory and to circumvent shortcomings of raw uranium supplies. Pyrochemical reprocessing or 'pyroprocessing' using molten salt electrolysis for the recovery of desirable spent fuel components is an increasingly sought after solution to the above issues. First developed in the late 1990's, the FFC Cambridge Process has shown to be a cornerstone in the electrochemical reduction of metal oxides and potentially offers a new iteration of pyroprocessing by introducing a direct conversion of spent oxide fuels to metals. These metals are easier to reprocess and specifically recovered elements can be used directly in advanced civilian nuclear reactors and metallic fuel cycles.

This thesis considers the role that an FFC based process could play in establishing a more sustainable, efficient and safer method for the select recovery of key metals from mixed oxide composites. Using an array of surrogate materials, the appropriation of an effective procedure was investigated in both $CaCl_2$ and $LiCl-CaCl_2$ Eutectic (LCE) molten salts at $810^{\circ}C$ and $600^{\circ}C$ respectively. At all stages of the process, feeds and electrolysis products have been examined by an assortment of ex-situ analytical tools, primarily SEM, EDS and XRD.

Abstract

A process engineering approach was taken to designing suitable reactors and cells with the aim of improving operational characteristics, greater electrochemical reduction efficiency and high yields of pure products.

Preparation of electrolyte and feed oxide electrodes (surrogate or spent fuel) was investigated, including unique electrochemical treatment for the two molten salts and precedent for the creation of the oxide electrode via cold pressing or slip casting to kinetically aid optimal reduction. A series of investigations considering the thermodynamic performance of $CaCl_2$ from a standpoint of electronic conduction were carried out, and considerable improvements found via the implementation of a simple cathodic sheath.

Selective partitioning was shown possible by the intended mechanism of partial direct reduction and anodic dissolution in the $2NiO\text{-}CeO_2$ binary. Partitioning of Zr from $ZrO_2\text{-}CeO_2$, and Ti from $TiO_2\text{-}CeO_2$ was also achieved, however in both cases it was via the gradual chemical dissolution of partially reduced Ce(III) into the molten salt or phase separation between liquid Ce and solid Zr. Extensive CV experiments were performed to enhance understanding of redox chemistry for each species investigated. CeOCl was found to be the only semi-stable phase of Ce present at potentials between -1.0 V vs. Ag/AgCl and its final reduction potential at approximately -1.95 V in $CaCl_2$ at $810^{\circ}C$.

Active CV experiments using PuO_2 and a MOX fuel sample containing 5% PuO_2 were initiated, revealing remarkably similar electrochemical behaviour of PuO_2 and the CeO_2 surrogate. Both PuO_2 and the bulk UO_2 content MOX could be reduced in $CaCl_2$ and in the lower temperature LCE whilst avoiding any decomposition of the electrolyte. Consequently a route for the direct electrochemical reduction of spent oxides fuels was shown plausible and offers a promising alternative to current pyroprocessing technology, with beneficial implications to the wider materials processing field.

Acknowledgements

"For a successful technology, reality must take precedence over public relations, for nature cannot be fooled."

— Richard Feynman

"All seats provide equal viewing of the universe."

— Museum Guide, Hayden Planetarium

Table of Contents

CHAPTER 5 ENHANCING ELECTROLYTE IONICITY

List of Figures

List of Tables

List of Abbreviations

3PI	3-Phase-Interline
AC	Alternating Current
ADU	Ammonium Diurinate
AGR	Advanced Gas Reactor
ANL	Argonne National Laboratory
AUC	Ammonium Uranyl Carbonate
BNFL	British Nuclear Fuels Ltd.
BTP	Bis-trianzinyl Pyridine
CANDU	Canadian Deuterium Uranium *[reactor]*
CEA	Commissariat à l'énergie atomique et aux énergies alternatives, "French Alternative Energies and Atomic Energy Commission"
CER	Chlorine Evolution Reaction
COEX	Co-extraction Process
CRIEPI	Central Research Institute of Electric Power Industry
CV	Cyclic Voltammetry
DFT	Density Function Theory
DMSO	Dimethyl Sulfoxide
DPA	Displacements Per Atom
EBR	Experimental Breeder Reactor
EDS	Energy Dispersive X-ray Spectroscopy
EDXD	Energy Dispersive X-ray Diffraction
EIS	Electrochemical Impedance Spectroscopy
ELR	Extremely Low Resistance
EPOR	End Point of Reduction
ExAm	Amine Extraction Process
FBR	Fast Breeder Reactors
FFC	Fray-Farthing-Chen
FP	Fission Product
FR	Fast Reactor
GANEX	Group Actinide Extraction Process
GBZ	Glass Bonded Zeolites
GC	Gas Chromatography
GPES	General Purpose Electrochemistry Software
HLW	High Level Waste

ICP-OES	Inductively Coupled Plasma Optical Emission Spectroscopy
IDR	Integrated Dry Route
IEA	International Atomic Agency
IFR	Integral Fast Reactor
INL	Idaho National Laboratories
IO	Intermediate Oxide
IPCC	Intergovernmental Panel on Climate Change
KAERI	Korean Atomic Energy Institute
LCE	Lithium Chloride - Calcium Chloride Eutectic
LKE	Lithium Chloride - Potassium Chloride Eutectic
LSV	Linear Sweep Voltammetry
LWR	Light Water Reactor
MA	Minor Actinides
MCE	Metallic Cavity Electrode
MDR	Metal Dissolution Reaction
MOFR	Metal Oxide Formation Reaction
MOX	Mixed Oxide Fuel
MP	Melting Point
MSR	Molten Salt Reactor
OAT	Oxidation Activation Temperature
OCP	Open Circuit Potential
OER	Oxygen Evolution Reaction
OK	Odourless Kerosene
OOT	Onset Oxidation Temperature
OS	Ono-Suzuki
P&T	Partitioning and Transmutation
PBR	Pilling-Bedworth Ratio
PHWR	Pressurised Heavy Water Reactor
PWR	Pressurised Water Reactor
RIAR	Research Institute of Atomic Reactors
RMBK	*Reaktor Bolshoy Moshchnosti Kanalnyy*, "High Power Channel-type Reactor"
SANEX	Selective Actinide Extraction Process
SE-SEM	Secondary Emission - Scanning Electron Microscopy
SFR	Sodium-Cooled Fast Reactor
SIA	Self-Interstitial Atom
SILEX	Separation of Isotopes by Laser Extraction
SS	Stainless Steel

SSA	Specific Surface Area
TBP	Tributyl Phosphate
TGA-DSC	Thermal Gravimetric Analysis with Differential Scanning Calorimetry
tHM	Tonnes Heavy Metal
THORP	Thermal Oxide Reprocessing
TRU	Trans-Uranics
TTC	Twice Through Cycle
UN	United Nations
UREX	Uranium Extraction Process
VVER	Water-Water Energetic Reactor
XPS	X-ray Photon Spectroscopy
XRD	X-ray Diffraction
YSZ	Yttrium Stabilised Zirconia
YSZME	Yttrium Stabilised Zirconia Membrane Electrode

Chapter 1

Introduction

1.1   Research Motivation

Considerable increases in global energy consumption are envisioned in both the near and medium term caused by continued growth in world population and economic prosperity. Recent projections made by the United Nations (UN) anticipate a population in the range of 9.7 billion by 2050, rising to approximately 11.2 billion by 2100; before stabilising[1]. Economic development is directly related to energy consumption, driven by those in emerging countries that seek to advance and leading to significant increases in total energy usage. Currently, nearly 80% of generated primary energy demand is delivered from fossil fuel sources and this dependency is predicted to perpetuate until at least 2035 according to the most recent report by the International Energy Agency (IEA)[2]. Direct utilisation of these sources by combustion is understood to contribute to both anthropogenic warming of the atmosphere via green house gas release and the associated detrimental impacts to the environment, health and society. Accompanying concerns regarding the energy security of nations reliant on rapidly depleting fossil fuel reserves also highlights the implicit necessity to seek substitute forms of energy[3]. In the most recent Intergovernmental Panel on Climate Change (IPCC) Report, claims of unprecedented CO_2 emissions from fossil fuel use are exemplified and that the mitigation of CO_2 release in particular requires a greater than tripling of zero- and low-carbon energy supply[4]. As a carbon free option during operation, nuclear power has the capacity to address these issues. Furthermore, uranium for nuclear reactors remains the most energy dense

form of fuel available (8.3 x 10^6 kWh kg^{-1}), making approximately 780 g (40.7 cm^3) enough to supply a developed nation citizen with enough energy for 80 years[5]. Of course renewable technologies should comprise an integral role in any future energy paradigm; however these alone cannot at present meet an essential baseline supply or the demands of our ceaselessly expanding consumption. Additionally, renewable options possess considerable drawbacks in terms of spatial requirements, intermittency and geopolitical issues. According to globally aggregated results, a renewables only scenario would convert an additional 7.6 % of global land coverage to meet predicted energy demands for 2060 (vs. 0.4 % for a maximum nuclear scenario) and involve a 50 % increase in cumulative capital investment to $73.7 trillion[6]. In **Figure 1.1** the environmental footprint for nuclear power in France with a 'twice through cycle' (TTC, where the spent fuel is recycled once) is shown to be relatively low compared to traditional alternatives and on the same order as renewables[7]. Contributions to acidification, NO_x and SO_2 are nearly entirely from UO_2 mining, with the electricity generation itself contributing little.

For these reasons, nuclear fission provides strong candidacy as an essential component in civilian energy programmes. However risks associated with the use of nuclear power, including waste management and weapons proliferation, need to be adequately addressed in order to ease the economic burden and social stigmatism of the technology. Reprocessing to recover fertile and fissile components of spent nuclear fuel coupled with the implementation of advanced reactor systems can alleviate total quantities and absolute toxicity of waste produced whilst simultaneously desensitising the system to proliferation. Developing novel and optimal methods for the efficient extraction of desirable components in spent fuel therefore remains a substantial barrier to a more absolute acceptance of nuclear power.
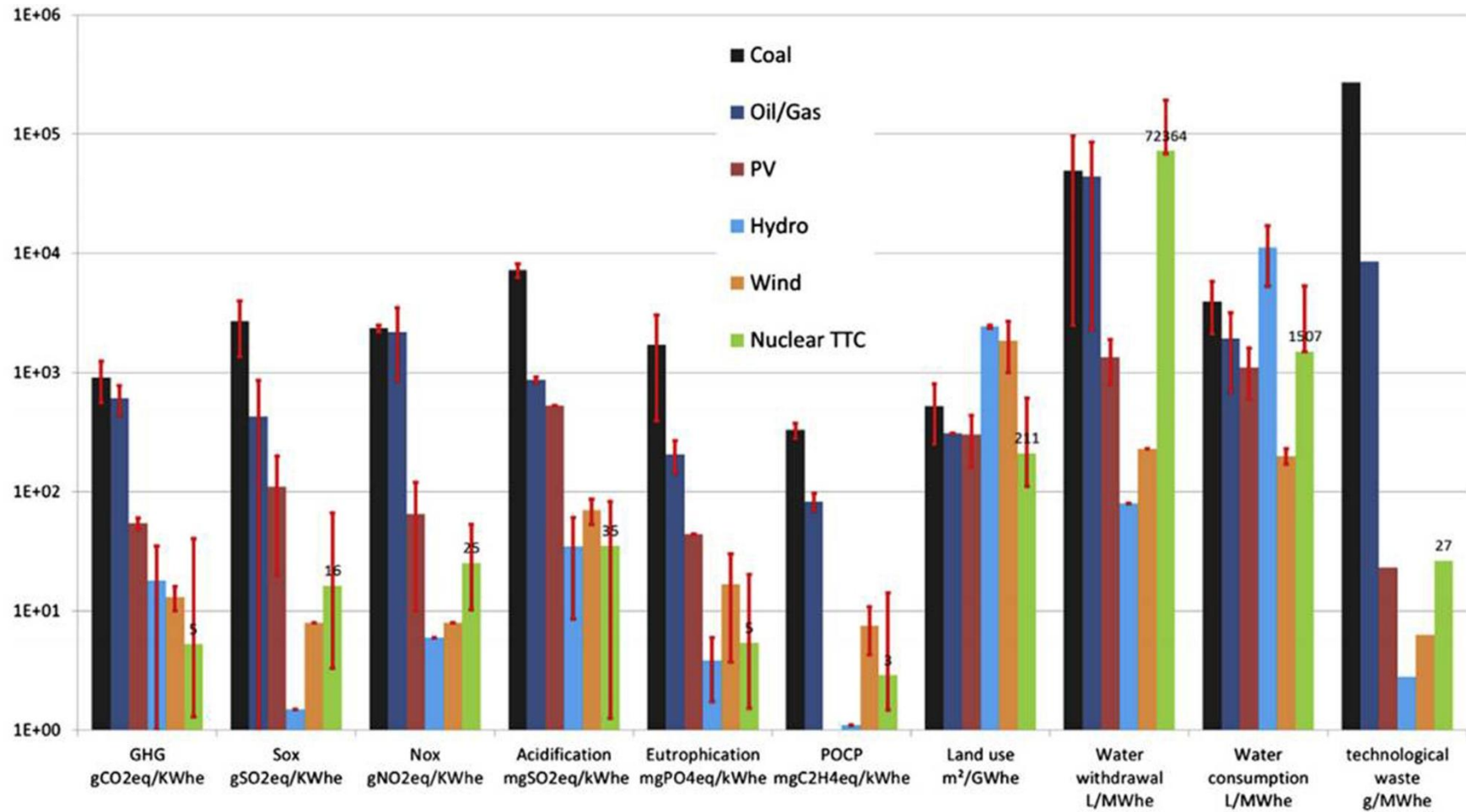
Figure 1.1 – Comparison of various environmental indicators for the different available forms of primary energy generation[7].

1.2 The Nuclear Fuel Cycle

1.2.1 Uranium Extraction, Processing and Enrichment

Fuel for civilian fission reactors is principally based around uranium, which essentially is the heaviest naturally occurring element on earth. In rare cases and under extraordinary conditions, plutonium has been found from natural fission sites created billions of years ago[8,9], albeit in such minor quantities to be impractical for extraction and use in nuclear reactors. Uranium however is considered relatively abundant with an estimated crustal concentration of between 1.5 to 2.8 ppm[10] but with distribution confined to twenty countries of which approximately 54 % of all present output comes from just ten mines[11]. As with all energy supplies, the political stability of the nations with access to the natural resource is paramount and this precedent is exacerbated with uranium sources owing to the capacity for nuclear armament. Fortunately, besides the stringent international regulation in its trade, nearly 41 % of known uranium reserves and current supply have origins in Canada, Australia and the USA.

Extraction of uranium is almost exclusively from open pit or shallow (<600 m) mines, where a combination of traditional excavation techniques and leaching using sulphuric acid are used to produce uranyl sulphate solutions, $UO_2(SO_4)_3{}^{4-}$. In ores which contain a considerable amount of basic minerals, such as calcite, leaching can be performed using sodium carbonate solutions to form the uranyl carbonate complex ion, $UO_2(CO_3)_3{}^{4-}$. Several stages of either polymer ion exchange or solvent extraction then follow, dictated by the species formed during leaching and conditions of the extraction process but with the purpose of removing impurities such as hydrated oxides and other absorbed ions. Precipitation is achieved by the addition of gaseous ammonia or by sodium hydroxide (again depending on

the complex ion being treated) to neutralise the solution as shown by **Equation 1.1** for the sulphate example:

$$6NH_4OH + 2UO_2SO_{4(aq)} \rightleftharpoons 2(NH_4)_2U_2O_7 + 2(NH_4)_2SO_{4(aq)} + 3H_2O \qquad \textbf{1.1}$$
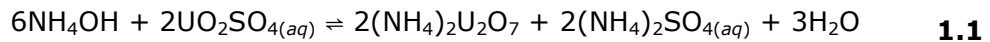
The concluding step is a drying process of the diurinate to yield U_3O_8, commonly referred to as 'yellow cake' uranium which is marketed and exported to destination facilities for enrichment.

Several natural isotopes of uranium exist ($^{235-239}$U) of which all undergo radioactive decay at various half-lives, though most are predominantly alpha particle emitters. Quantitatively ^{238}U is by far the most abundant and stable of these (99.27 %) however in itself cannot sustain a fission chain reaction in nearly all current reactor designs, but rather absorbs an incident neutron to produce ^{239}Pu, a fertile transuranic (TRU) product in spent fuel. At 0.7 % natural presence, ^{235}U is the second most prolific uranium isotope and crucially can initiate fission from neutrons in the thermal energy spectrum (0.025 eV). For nearly all current civilian reactors (with the exclusion of CANDU designs) the raw yellowcake uranium requires enrichment to approximately 2-5 % ^{235}U by mass. This enrichment is usually performed via well established gaseous diffusion or centrifugation technologies, however modern alternatives are actively investigated and research into laser induced separation (SILEX) as well as electromagnetic, chemical or plasma based isolation techniques are being investigated[12].

Increasingly the diffusion driven separation process is viewed as obsolete in terms of energy requirements, total efficiency and capital costs and so most facilities operate under a centrifugation program. In both practices, the uranium oxide is fluorinated, first to tetra- then hexafluoride (UF_6) which sublimes at approximately 56°C. The UF_6 in the diffusion technique is then passed repeatedly through a series of semi-permeable membranes

under high pressures[13] to selectively isolate the ^{235}U isotope. In centrifugation the gas is passed through a parallel cascade of cylinders under constant centrifugal motion to induce a strong centripetal force. The lighter fissile ^{235}U (0.852 % lighter than ^{238}U) is more likely to remain closer to the core of the cylinder which then is selectively pumped to the next unit; hence through each pass the UF_6 becomes gradually more enriched until the desired level is reached. Gas centrifugation is more commonly employed due to considerable reductions in energy use over the diffusion method, however still requires a significant capital expenditure in both establishing capability and in operation.

Figure 1.2 highlights both the total cost analysis for nuclear sourced electricity supply in France and also the head end fuel costs for a typical US Light Water Reactor (LWR) to produce 1 kg of enriched uranium fuel for use in the reactor core[14,15]. Enrichment clearly represents a large proportion of the total expense. Uranium destined for military use requires a more substantial enrichment level of around 70 %, and for weapons grade use, enrichment to 90 % ^{235}U is necessitated. Also noteworthy with the complete French fuel cycle costs, is that reprocessing via a once through route contributes a marginal 2.9% to total expense.

The fabrication procedure following enrichment is mostly dependant on the destination reactor configuration. Over half of all civilian plants are LWRs, which use regular water as a moderator (a medium to curb the energy of incident neutrons and to control the rate of fission during criticality). Other plant designs, including the Soviet Union developed Graphite Moderated Light Water Cooled Reactors (RBMKs) and British Advanced Gas Cooled Reactors (AGRs), also require enriched forms of uranium and, together with LWRs, constitute nearly 90 % of globally installed nuclear power plants[16].

Relative Contributions to the Final Cost of Electricity by Nuclear Power in France

Front-End Costs – 14.94%

Investment – 61%

Operations – 21%

Repository* – 0.14%

Extraction – 7.2%

Recycling – 2.88%

Conversion – 0.54%

Fabrication – 1.98%

Enrichment – 5.22%

Fabrication – **$300** (16%)

Extraction – **$892** (46%)

Breakdown of 1kg Enriched UO_2 Fuel Costs for a Typical US LWR

At a 45 GWd/t burn up, this yields 3.6 MWh/kg UO_2 or 0.52¢/kWh

*short-term surface wet or dry storage.

Enrichment – **$599** (32%)

Conversion – **$120** (6%)

Figure 1.2 – A systematic cost analysis of French nuclear power generation and the head-end processes associated with the use of enriched nuclear fuel for a typical US Light Water Reactor (data as of July 2015)[14,15].

With all of these reactors the fuel of choice is small pelletized uranium oxide in the form of UO_2 which are typically stacked and clad in zirconium alloys with relatively high neutron transparencies to form the fuel rods. Collectively several of these fuel rods are specifically arranged to produce the fuel assemblies ready for insertion into the reactor core, as illustrated by **Figure 1.3**.
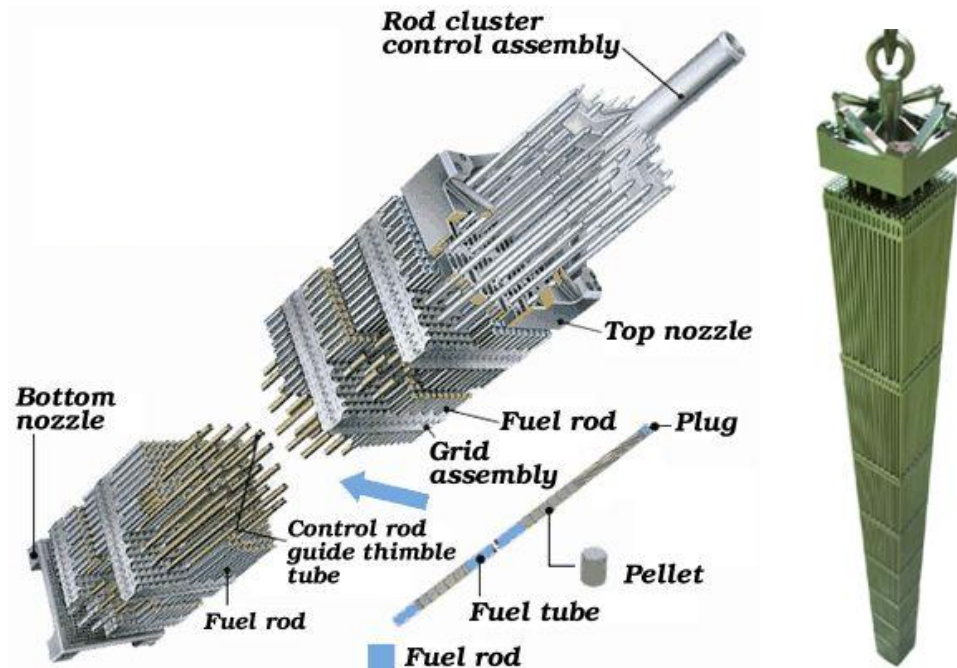
Figure 1.3 – Schematic illustration of a Pressurised Water Reactor (PWR) fuel assembly and a photograph of the completed assembly [17].

Reconversion of the UF_6 to UO_2 can be achieved via several routes, but in essence is similar to the reversed UF_6 fabrication method. There are two possible wet processes, termed the ammonium diurinate (ADU) or ammonium uranyl carbonate (AUC) method and a dry method developed by the British Nuclear Fuel Limited (BNFL, now Sellafield, Ltd.) known as the integrated dry route powder process (IDR), all of which are described in **Figure 1.4**[18–20]. Particular characteristics of the final pellet form are required in order to accurately predict and control the rate of fission during reactor burn up. Various stages to improve preform quality and unity are implemented for this reason, including blending with small quantities of U_3O_8 to increase the mechanical strength of green pellets and the use of pore forming agents and lubricants to assist mechanical pressing and gain a desirable porosity.

ADU Reconversion

UF$_6$ Vapour
(Enriched/Depleted)

Add Steam
(200°C)

UO$_2$F$_2$ + HF

Add Ammonia and
Dilute Nitric Acid (60°C)

ADU
Precipitate

Filter, Wash
and Dry

UO$_3$

H$_2$ reduction
(700-800°C)

UO$_2$
(Enriched/Depleted)

AUC Reconversion

UF$_6$ Vapour
(Enriched/Depleted)

Add Water, Ammonia
and CO$_2$ (50°C)

AUC Precipitate
Slurry

Filter, Wash
and Dry

AUC Cake

Add Steam, H$_2$ and N$_2$
(500°C) in a Fluidised Bed

UO$_2$
(Enriched/Depleted)

IDR Reconversion

UF$_6$ Vapour
(Enriched/Depleted)

Add Steam

UO$_2$F$_2$ Powder

Rotating
Kiln

Add Steam
and H$_2$

UO$_2$ Powder
(Enriched/Depleted)

Wet Processes   Dry Process

Figure 1.4 – Flow sheets for the proven commercially available anhydrous and aqueous methods for the conversion of UF$_6$ to UO$_2$.

A final crucial step is sintering on the pressed green pellets to introduce densification and is followed by grinding, cleaning and drying to yield the necessary geometrical requirements for fuel rod fabrication[21]. The completed fuel rods are loaded into the nuclear reactor and fission initiated.

Natural uranium metal can also be used as a fuel under certain reactor conditions and designs, as with the PHWR or generation I MAGNOX reactor (a precursor to the AGR) which was purposed originally for the production of plutonium for the UK nuclear weapons program. However the burn up for these variants of nuclear reactor for electricity generation is extremely poor at approximately 4 gigawatt-days per metric ton of heavy metal (4 GWD/tHM) for a typical MAGNOX facility, compared to around 60 GWD/tHM for an efficient PWR. **Table 1.1** shows the basic characteristics and

quantity of the most common types of nuclear reactors as of December 31st, 2014[16] and highlights the large divergence in operational conditions.

Table 1.1 – Characteristics of currently operating nuclear reactors, those under construction and their fuel types[16].

Reactor Type	LWR		PHWR	RBMK	AGR	Fast Reactor (FR)
	PWR/ VVER	BWR				
Neutron Spectrum	Thermal	Thermal	Thermal	Thermal	Thermal	Fast
Moderator	H_2O	H_2O	D_2O	Graphite	Graphite	-
Fuel Type	UO_2 or MOX	UO2 or MOX	UO_2	UO_2	UO_2	UO_2
Enrichment Level	up to 5% ^{235}U	up to 5% ^{235}U	Natural U	up to 3% ^{235}U	2.5-3.8% ^{235}U	17-26% ^{235}U
Coolant Type	Pres. H_2O	Boiling H_2O	Pres. D_2O	Boiling H_2O	CO_2	Na/ Molten Salts
Pressure (bar)	155	70	110	70	40	5
Temperature Outlet (°C)	320	286	310	284	630	550 - 1000
Cladding Material	Zr Alloy	Zr Alloy	Zr Alloy	Zr Alloy	SS	SS
Burn up (GWD/tHM)	up to 60	up to 55	7	up to 25	up to 30	up to 100
Number of Operating Reactors	277	80	49	15	15	2
Total Power (GWe)	257.23	75.46	24.6	10.22	8.12	0.58
Reactors Under Construction	59	4	4	0	0	2

In place of an enriched ^{235}U presence in processed UO_2, naturally fissile ^{239}Pu obtained from reprocessing of spent fuels can be mixed with ^{238}U to create the fissionable Mixed Oxide (MOX) fuel. MOX fuels have become attractive in nations which have a reprocessing strategy as the inclusion of stores of weapons grade Pu both reduces the amount of uranium ores needed to be purchased and reduces risks of proliferation and radioactive hazards of a pure Pu store.

1.2.2   Fission

As atoms consist of mostly 'empty space', uncharged particles such as neutrons can travel distances of hundreds of meters before a contact event with a nucleus, unlike alpha and beta particles which readily interact with matter. **Table 1.2** summarises the basic properties of neutrons and other sources of ionising radiation that are produced by nuclear processes and which have the capacity to cause harm to humans and other life.

Table 1.2 – Different types of ionising radiation and their properties.

Radiation	Mass (amu)	Charge	Range in Air	Range in Tissue
Alpha	4	+2	<7.5cm	0.05mm
Beta	0.00055	-1	4-5m	Several mm
Gamma/X-ray	0	0	100s of m	Through body
Neutron	1	0	100s of m	Through body

There are four potential outcomes after an incident neutron interacts and is absorbed into a target nucleus to create a nuclear isomer. The most common means of releasing the excess energy is by the nucleus ejecting the neutron i.e. a scattering event, thereby potentially influencing the inherent energy of the neutron but leaving the nucleus effectively unchanged. Alternatively the energised nucleus can undergo beta (β^-) decay where the absorbed neutron transforms into a proton, releasing an electron and antineutrino and consequently inducing transmutation of the target element, as shown by **Equation 1.2** for the method of Pu production in nuclear reactors after two beta decays.

$$^{238}_{92}\text{U} \xrightarrow{\ n\ } {}^{239}_{92}\text{U} \xrightarrow{\ \beta^-\ } {}^{239}_{93}\text{Np} \xrightarrow{\ \beta^-\ } {}^{239}_{94}\text{Pu} \qquad \textbf{1.2}$$
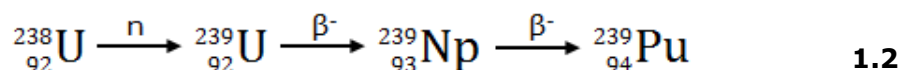
The neutron absorption event may also be stabilised by isomeric transition, either by fluorescence and the resultant emission of gamma radiation or an electromagnetic internal conversion of energy from the nucleus to an

orbital electron, causing the electron to eject. This creates a heavier isotope of the target element, for instance ^{239}U, which is returned to a ground state awaiting radioactive decay to a more stable element. Finally, under specific conditions nuclear fission may occur. Fission is the process whereby an eligible atomic nucleus absorbs an incident neutron with sufficient energy to overcome the strong nuclear force binding the protons and neutrons together. The resultant phenomenon is a destabilisation and cleaving of the nucleons within the atomic nucleus, leading to formation of two (or in rare cases three) lighter daughter isotopes, which are termed fission products (FP), and two or three released neutrons, as presented in **Figure 1.5**.
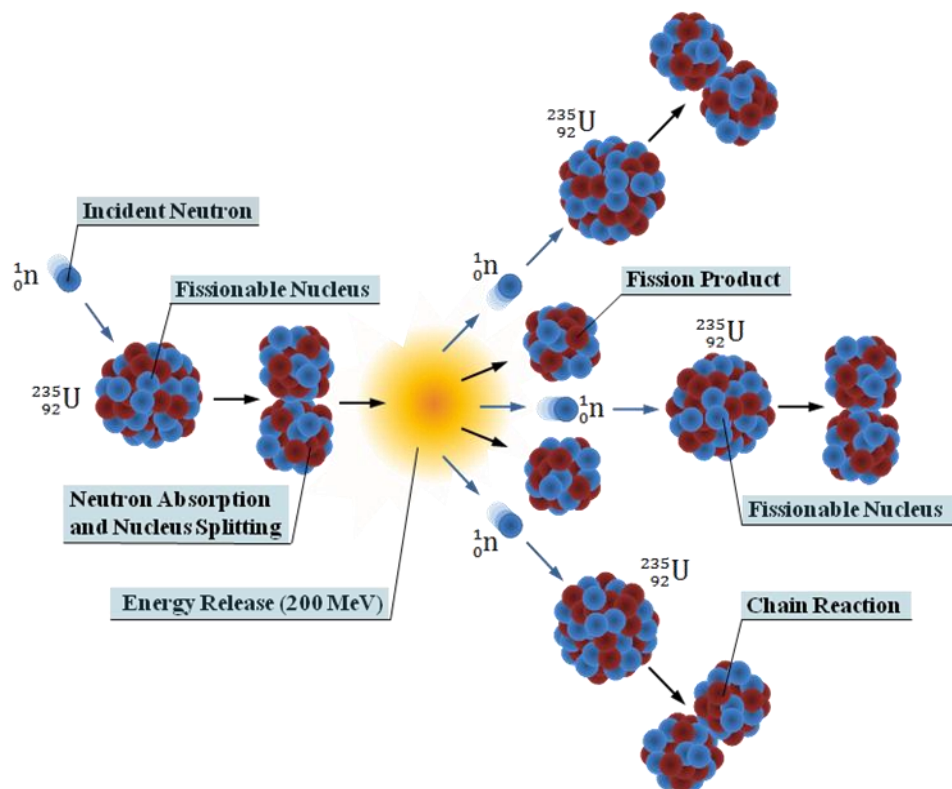
Figure 1.5 – Illustration of neutron absorption and supercritical fission of ^{235}U within a nuclear reactor core.

The eligibility of an atom to undergo fission is related to two intrinsic and coupled parameters of the process. Firstly, as the size and nucleonic arrangement of the target nucleus directly influences the nuclear forces,

the number of protons and neutrons within a nucleus determines the capacity to achieve fission and produce daughter isotopes after absorbing a neutron. Whilst every atom heavier than iron can release energy during a fission incident, the relative ease of initiating that reaction generally increases with atomic number, related to the binding energy of those atoms i.e. the destabilisation influence of having a large number of nuclides. Similarly the total yield of energy released during fission approximates the nucleus size and in order to achieve a critical chain reaction very few isotopes remain eligible as nuclear fuel candidates. The second condition is the kinetic energy and hence velocity of the incident neutrons. Neutrons released from the fission of ^{235}U are in the 'fast' spectrum (classed as possessing energies between 1-20 MeV), which is beneficial in increasing the number of prospective elements and isotopes able to undergo fission via the increased energy transfer to overcome nucleon binding forces. However the rate of interaction between neutron and nucleus at these high incident energies, i.e. the neutron cross-section of atoms, decreases substantially and so reduces the probability of a fission event occurring. For this reason in particular, all current civilian reactors (besides the handful of operational Fast Neutron Reactors FNRs) use a moderator to impede the energy of released neutrons to the thermal range of 0.025eV which permits a relatively low enrichment level to be used (higher chance of neutron-nucleus interaction).

Precise design of the fuel rod assemblies, including control of the UO_2 pellet weight, density and geometry, is imperative to predict and maintain the fission process. The reactor is operated in such a way to be slightly supercritical, meaning that per neutron absorbed, on average more than one neutron goes on to be involved in the fission of another fissile element, hence a chain reaction propagates[22]. Control rods are used to restrain the

rate of criticality by absorbing excess neutrons produced from each fission reaction. The internal reactor temperature can therefore be manipulated based on the insertion or removal of these control rods into fuel assemblies. During each process of a single ^{235}U atomic fission the energy released is on the magnitude of 200 MeV[23]. This large output is a consequence of the combined mass of produced daughter nuclei (FPs) and neutrons being approximately 0.1 % less than the initial ^{235}U mass, with the loss in mass and subsequent impressive energy release governed by Einstein's equation, $E = mc^2$. Primarily it is the kinetic momentum of the FP, prompt and delayed beta decays and the emission of gamma ray photons which contribute towards the thermal conditions within the nuclear reactor allowing for eventual electricity generation through steam turbines.

1.2.3   Spent Fuel Legacy

Following a four year operational life span, typical uranium fuel rods from a thermal neutron reactor will contain 96 % uranium (reduced to a slightly above natural enrichment level), 3 % FP and 1 % plutonium and Minor Actinides (MAs). As shown by **Equation 1.2**, plutonium presence accumulates due to the absorption of a neutron by the non-enriched ^{238}U isotope which precedes a series of beta decays into ^{239}Pu. The amalgamation of elements within the fuel rod at the end of this lifespan is called spent nuclear fuel. Because of the accrual of long lived radioactive nucleotides during transmutation and fission, coupled with the associated difficulties of how best to safely handle and dispose of them, spent fuel remains the primary basis for the considerable amount of stigmatism nuclear power receives.

Regardless of the fate of the spent fuel, the immediate back-end operation following power generation is to seal used rod assemblies in Stainless Steel (SS) containers lined in neutron absorbing boron plates and then to store

in robust concrete cooling ponds for a period of several years. During this time the FPs and TRUs in spent fuel generate significant amounts heat and radiation from the decay of produced shorter half-life isotopes. These effects are partially mitigated by the thick concrete walls and the presence of water within the pond providing radiation protection and acting as a heat transfer medium for the spent fuel as it continues to generate thermal output. Many FPs approach relatively stable nuclear conditions after several years, however there are seven long lived isotopes with half-lives greater than two hundred thousand years and indeed most of the actinides produced via transmutation have half lives in the range of one hundred to two hundred thousand years.
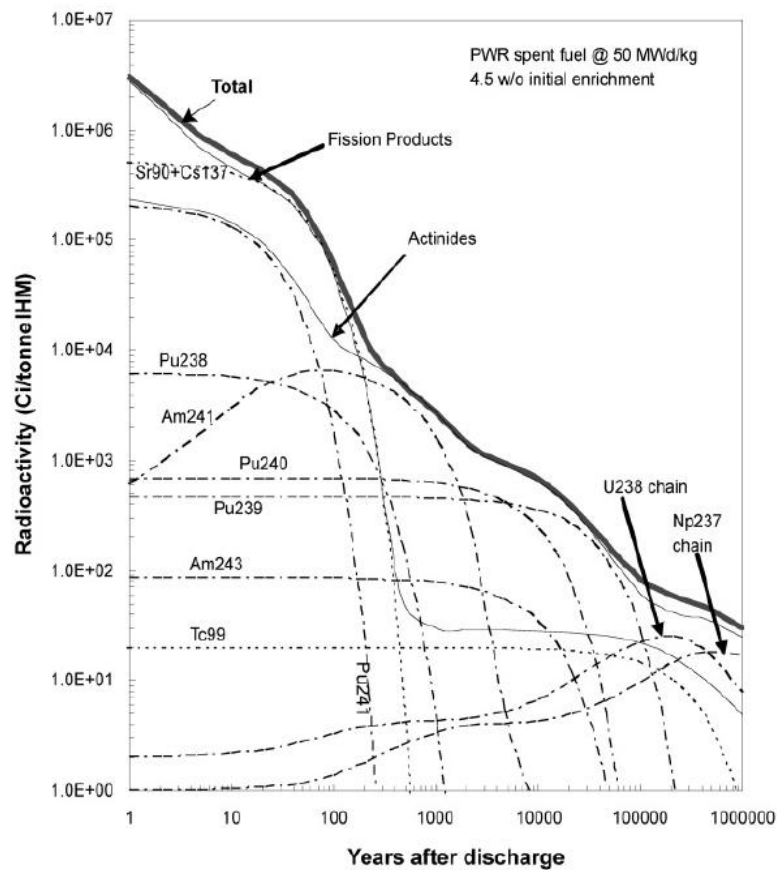
Figure 1.6 – Radioactivity of various spent fuel species from a PWR at 50MWd/kg burn up[24].

Figure 1.6 shows the radioactivity (in curies per tonne of initial heavy metal) of various species in spent fuel recovered from a PWR at 4.5 %

enrichment and burn up of 50 MWd/kg, from one to one-million years after discharge, calculated via core analysis using the CASMO-4, TABLES-3, and SIMULATE-3 code packages[24]. Despite the seven longer lived fission products, actinides dominate the radioactive productivity at extended durations whilst FPs, particularly ^{90}Sr and ^{137}Cs are heavy emitters in the immediate years following end of fission. The prolonged decay series creates issues regarding the design and implementation of storage options needed to house the radioactive waste for periods of thousands of years and more. Additionally owing to the more immediate generated heat there is a considerable safety case for limiting the total quantity of spent fuel stored in the interim cooling pond facilities.

For a typical LWR of 1 GWe capacity there will be around 27 tonnes of used fuel removed from the reactor per year[25], or 20 tHM/GWe generating capacity[26]. Whilst Geological disposal is an inevitable consequence of a nuclear energy program, a process that can selectively separate uranium from plutonium, FPs and other TRUs would permit recovery of huge quantities of usable fuel and simultaneously dramatically reduce the absolute volume and radioactivity of material required for geological storage.

1.3 Thesis Scope

The aim of this thesis is to use surrogates to investigate and develop the prospect of novel molten salt based reprocessing technologies for spent fuel from LWRs with eventual use in advanced FR fuel cycles. The use of benign materials, besides the obvious safety case, facilitates a relatively unrestricted operation and permits more flexibility during research. Yet as long as the carefully chosen surrogate materials are electrochemically similar enough to the live materials, the processes explored herein should be transferable to nuclear fuel cycle stewardship.

Chapter 1 has discussed the involvement of nuclear power in current and future global energy programs, covering the fundamental aspects of the nuclear fuel cycle. Reprocessing can be defined into two broad subcategories; namely pyroprocessing and aqueous reprocessing. Pyroprocessing methods produce less specific waste compared to their aqueous counterparts and the radioactive decay of remaining non-utilised nuclides is far shorter. All pyrochemical systems rely on the electrochemical separation of phases during electrorefining in molten salts, with the onset conditions being achieved by either manipulation of chemical equilibriums or by electrolytically derived metallothermic reduction. It is however the yield of metallic product streams, produced via electrochemical methods that arguably has the greatest prospective utility with regards to future advanced fuel cycles and fast reactors. Following head end treatment, research performed here is dedicated to examining the potential for an electrochemically mediated, single-step process for metallic fuel production, combining the stages of reduction and electrorefining (speciation).

Chapter 2 begins by defining these reprocessing approaches and then exploring and critically evaluating literature on the recent advances in pyroprocessing of spent nuclear fuels with emphasis applied towards advanced fuel cycle application. An introduction the Fray-Farthing-Chen (FFC) Cambridge Process as a method for electro-deoxidation of metal oxides is given and examples of the previous usage of the FFC Cambridge Process to the nuclear industry are highlighted. Manipulation of this unique electrochemical process for the combined partitioning method of partial direct reduction and selective anodic dissolution is also explored and is the principle research objective of this thesis.

The various equipment and chemicals used to perform experimental aspects of this work are discussed in Chapter 3, including the design and operation of the molten salt reactor and bespoke equipment fabricated for specific tasks. In-situ electroanalytical techniques and the physical and optical analytical ex-situ analysis methods employed during research are also discussed. Fundamental background knowledge of each analysis tool used is also given in order to better understand experimental results.

Kinetic factors play an integral role in the behaviour of the oxide materials during reduction. Chapter 4 will therefore describe the molten salt treatment method employed in this work, the characterisation of single and binary oxide systems investigated and examine two different pellet preparation techniques.

Chapter 5 continues with the characterisation of molten salt electronic behaviour, exploring the simple but unique optimisation methods designed to improve qualitative and quantitative responses during electroreduction. Constant cell voltage electrolysis of Cr_2O_3 and ZrO_2 is used to shown how manipulation of electronic field lines can influence the products of reduction and how this understanding can be applied to improve pyroprocessing efficiency.

The initial feasibility investigation of a partial direct reduction and selective anodic dissolution technology is considered in Chapter 6, using the binary oxide of $2NiO\text{-}CeO_2$. Reduction is achieved by the FFC Cambridge Process and the significance of precise potential control to achieve partitioning is exemplified.

Chapter 7 continues to explore more analogous surrogates to spent nuclear fuel and their ability to undergo the novel partitioning method being studies here. Both $ZrO_2\text{-}CeO_2$ and $TiO_2\text{-}CeO_2$ binaries were tested in $CaCl_2$

and LiCl-CaCl$_2$ eutectic (LCE) respectively. Results of direct Cyclic Voltammogram (CV) investigations into PuO$_2$ and the UO$_2$-PuO$_2$ binary are also presented and compared to those achieved using surrogate materials. The comparative will reveal how well various electrochemical surrogates emulate the active spent fuel components and whether the concept of a single step pyrochemical partitioning method could be applied to spent nuclear fuel.

Finally conclusions are drawn from work performed as part of this thesis and further work is suggested in Chapter 8.

Chapter 2

Literature Review

2.1 Reprocessing Technology

2.1.1 Reprocessing Fundamentals

The advent of reprocessing was first implemented solely for the purpose of extracting usable quantities of weapons grade plutonium from spent fuel of the first fission reactors. As nuclear power became more prevalent as a source of civilian energy supply, the desire to limit the capacity for proliferation increased. Nuclear states that have foregone the economic burden of engaging in a reprocessing program instead pursue a solution involving storage in a long term geological repository, not only for non-fissile fission products, but for all facets of radioactive spent fuel. A comprehensive, efficient and cost effective reprocessing technology could however provide strong political force in pacifying negative public dogma in nuclear power. This sway in opinion could then further remove barriers to investments in the nuclear industry, aiding the global progression into a more carbon neutral and environmentally friendly energy model. **Figure 2.1** illustrates both an open nuclear fuel cycle void of actinide recovery and how reprocessing is integrated to close the loop[27]. There are two options with regards in how to reprocess spent fuel; by either aqueous based solvent extraction or high temperature pyrochemical speciation. The foundation for developing safeguards for nuclear materials began with aqueous techniques for current and past reactor wastes. However in the envisioned advanced reactor systems such as liquid sodium or molten salt cooled reactors with their respective fuel cycles, it is intended that new variations of aqueous and particularly pyrochemical reprocessing methods

will take a more centric and further reaching role in nuclear nations and is aimed at increasing proliferation resistance.
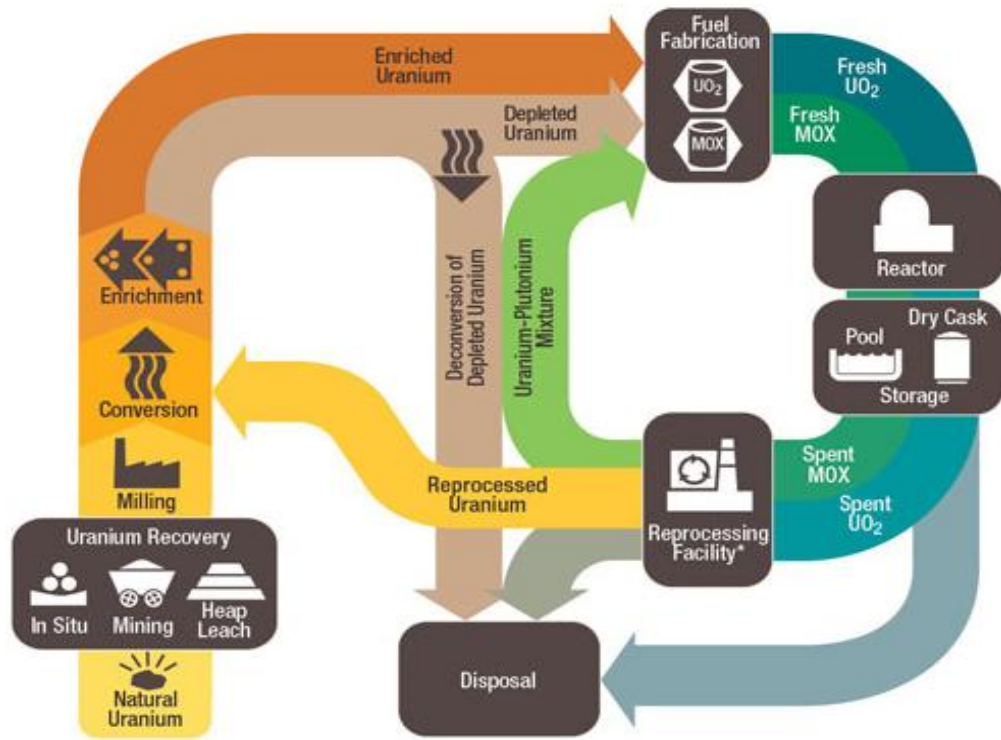
Figure 2.1 – An example of how open and closed nuclear fuel cycles operate[27].

2.1.2 Aqueous Reprocessing

2.1.2.1 Fundamentals and Current Operation

By far the most significant and currently the only commercial reprocessing method is the aqueous based Plutonium-URanium EXtraction (PUREX) process. Since the original patent was filed in 1947 at the University of Chicago, only a handful of facilities worldwide have been commissioned despite a near exclusive operational distribution. One such facility is the Thermal Oxide Reprocessing Plant (THORP) at Sellafield, Cumbria; of which a schematic of the process is outlined in **Figure 2.2**.

From **Figure 2.2** it can be seen that after initial receipt and remotely operated mechanical shearing of the spent fuel it is dissolved in nitric acid with chemical separation achieved by solvent extraction. The aqueous stream with dissolved U, Pu and FPs is reacted with a solution of tributyl

phosphate (TBP) in a paraffinic diluent (odourless kerosene; OK), which facilitates extraction of UO_2^{2+} and Pu^{3+} from the nitric layer into the organic phase[28]. Nearly all of the fission products are removed from this first solvent extraction stage and are sent for vitrification and eventual storage.
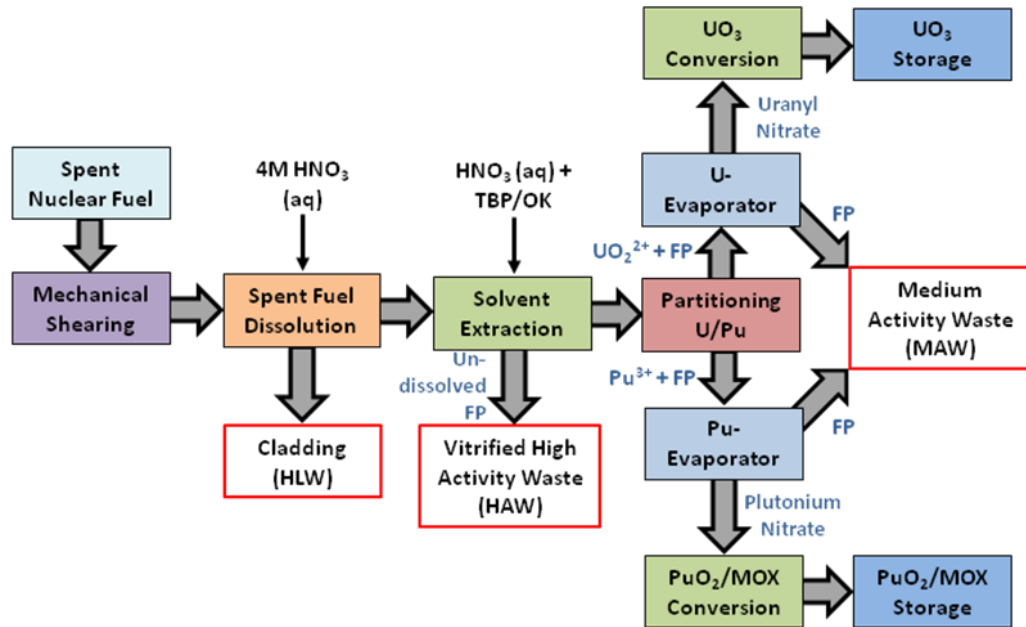
Figure 2.2 - Simplified representation of the PUREX process performed at the THORP facility In Sellafield.

Uranium and plutonium are separated from the organic phase individually by initial chemical reduction of plutonium in the 4^+ valency to the 3^+ valent oxidation state using a reducing agent and then placing the TBP/OK in contact with a fresh aqueous stream[29]. Final purification to remove the remaining dissolved FP and minor actinides (MAs, e.g Np) is achieved by careful control of the contaminant chemistry and oxidation states. The final purified uranyl nitrate and plutonium nitrate solutions are converted to their oxide states by oxalate precipitation and thermal denitration respectively, ready for storage or reintroduction into the fuel cycle.

Clearly a substantial drawback of the PUREX process is the large volumes of solvent waste produced, which then requires secondary processing stages in order to recover valuable feed materials. Additionally the

manufacturing costs and spatial requirements for aqueous facilities are quite considerable, and facilities are often built away from the nuclear reactor producing the spent fuel which creates security risks in the transportation of hazardous material between sites. Without scrupulous observation and control of the entire PUREX process there are several areas of safety concern, including the potential criticality risk of precipitating too much plutonium too quickly, for instance if the concentration of nitric acid isn't precisely monitored. Perhaps the largest concern however is that the process yields a pure, separate stream of weapons grade plutonium, which constitutes an obvious proliferation risk and is the reason why in the 1970's the USA ceased commercial PUREX reprocessing[30],[31].

2.1.2.2 Advanced Aqueous Reprocessing

Advanced aqueous methods in development aim to address several of the above issues, primarily in designing novel ligands with selectivity towards particular actinides; for example the bis-trianzinyl pyridine (BTP) family[32,33]. Gaining additional resistance to radiolysis and hydrolysis is also of paramount importance during the advancement of these unique molecules. One of the first working iterations of PUREX has been developed in France by AREVA and the French Alternative Energies and Atomic Energy Commission (CEA) called the COEX (or co-extraction) process. As the name suggests the flow sheet aims to avoid pure plutonium extraction by a co-precipitation of both uranium and plutonium oxides, which are suitable for direct MOX fuel fabrication. A large collective of other variations to the wet extraction paradigm are currently being considered, including but by no means limit to: UREX (uranium extraction), GANEX (group actinide extraction, to include neptunium), SANEX (selective actinide extraction, with regular r-, innovative i-, and once through 1c- variants) and DIAMEX

(diamine extraction). Difficulty during separation arises however due to the similar chemical behaviour between the elements, although recent demonstrations by the French ExAm process have shown a 99% selective recovery of americium is possible. As with all aqueous processes however, a complete understanding and careful supervision of the process parameters (chemical equilibria and pH levels, for example) are a must if the technology is to be both safe and productive.

2.1.3 Pyrochemical Reprocessing

Conventional aqueous reprocessing in its current iteration is not appropriate for the treatment of metallic fuels or for those destined for use in most future fast reactors. Pyrochemical operations for actinide recycling however are able to recover usable nuclear materials applicable to both current LWRs and next generation Fast Breeder Reactors (FBRs). They are often simple, compact units with superior environmental and safety attributes compared to aqueous systems and crucially are inherently proliferation resistant[34,35]. Additionally the chemicals used are tolerant of high radiation doses and heat loads, which allows for treatment of used fuels without having to wait for extended periods of time for materials to decay into lower activity levels. Unlike PUREX, which is the benchmark for aqueous reprocessing technology, there are several different pyroprocessing concepts actively under development[36]. Many more R&D programs exist in countries such as Japan, India and South Korea, although by scale of operation and investment there are currently two primary unique methods of pyroprocessing; namely the Argonne National Laboratory (ANL, USA) and the Research Institute of Atomic Reactors (RIAR, Russia) processes, discussed below.

Most nuclear states are now pursuing the attractive prospect of Partitioning and Transmutation (P & T), with the potential to reduce the radiotoxicity

risk of nuclear waste destined for disposal from 3×10^5 years to as little as 3×10^2 [37]. Generally, pyroprocessing of spent nuclear fuels as part of a P & T programme can accomplish the following feats[38,39]:

- High active actinides and some FPs can be incorporated into the fuel cycle for fission and/or transmutation

- The number of operations required to achieve a holistic fuel reprocessing and fabrication system is reduced

- Vastly reduce the amount of waste required for geological storage.

- As the waste sent for disposal is comprised of shorter half life FP, the radiotoxicity threshold (to return to a level of natural uranium) is 3 orders of magnitude shorter in duration.

- 97-98% (99%+ for FBRs) of the original uranium quantity is recovered, reducing demand for raw sources and extending power generating capacities of nuclear fission by thousands of years.

- Economic superiority, safer operation and proliferation resistance are intrinsic properties factored in to the designs of pyroprocessing facilities.

2.1.3.1   ANL Process

After the USA discontinued aqueous treatment of its spent fuel inventory in the 1970's, the ANL process was instead developed to coincide with an Integral Fast Reactor (IFR) program. In advance fuel cycles the recovered TRU nuclides will be mixed with U-Pu-Zr to create fresh fuel ready for the FBR, meaning only minor quantities of TRU will need to be disposed of geologically[40]. In this process the spent oxide fuel from thermal reactors is introduced to a molten LiCl-KCl bath at $650^{\circ}C$[41] and undergoes chemical reduction by Li metal within the molten salt, as shown by **Equation 2.1**, where 'An' denotes the collective actinide matrix.

$$AnO_x + x2Li(LiCl) = An \text{ (metal)} + xLi_2O(LiCl)$$

2.1
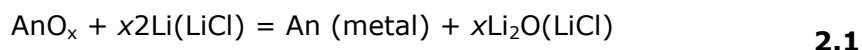
The produced Li_2O has a solubility in LiCl of 12 % at 650^oC[42] but is generally maintained at much lower concentrations to prevent solubility of various rare earth oxychlorides species formed during reduction[42]. Li_2O is recovered by flushing the cell with fresh LiCl which helps limit the concentration. The flushed salt rich in Li_2O then undergoes electrolysis to recover Li metal for reuse as a reductant for the further actinide oxides, as shown by the half cell reactions in **Equations 2.2** and **2.3**, with **Equation 2.3** being known at the oxygen evolution reaction (OER).

$$\text{Cathode: } Li^+ + e^- = Li$$

2.2

$$\text{Anode: } 2O^{2-} = O_2 + 4e^-$$

2.3

The produced metallic lithium has a low solubility compared to its oxide counterpart so remains in a liquid phase at the cathode for recovery and reuse. Produced metallic phases are then purified by an electrorefining stage at 500^oC[43,44] in a different molten salt media using both a solid iron/steel cathode for uranium recovery and a liquid cadmium or bismuth cathode for other minor actinides and trace uranium. Noble fission products such as the metal cladding, Mo, Pa and Rh do not dissolve and so remain on the anode due to the difference in redox potentials between the different elements[45]. The actinides can be purified in metallic ingot form and the salt recovered by adsorption using zeolites which permits salt reuse back into the electrorefining cell. The more radioactive fission products (Cs, St and rare earths) accumulate in the molten salt via dissolution. Hence both irradiated anode materials and electrolyte salt stabilised in the form of Glass Bonded Zeolites (GBZ) are removed for geological storage. The purified metallic U can be mixed with the other

metal actinides from the liquid cathode after purification to form fuel pins for FBRs. An example of the whole process can be seen in **Figure 2.3**.
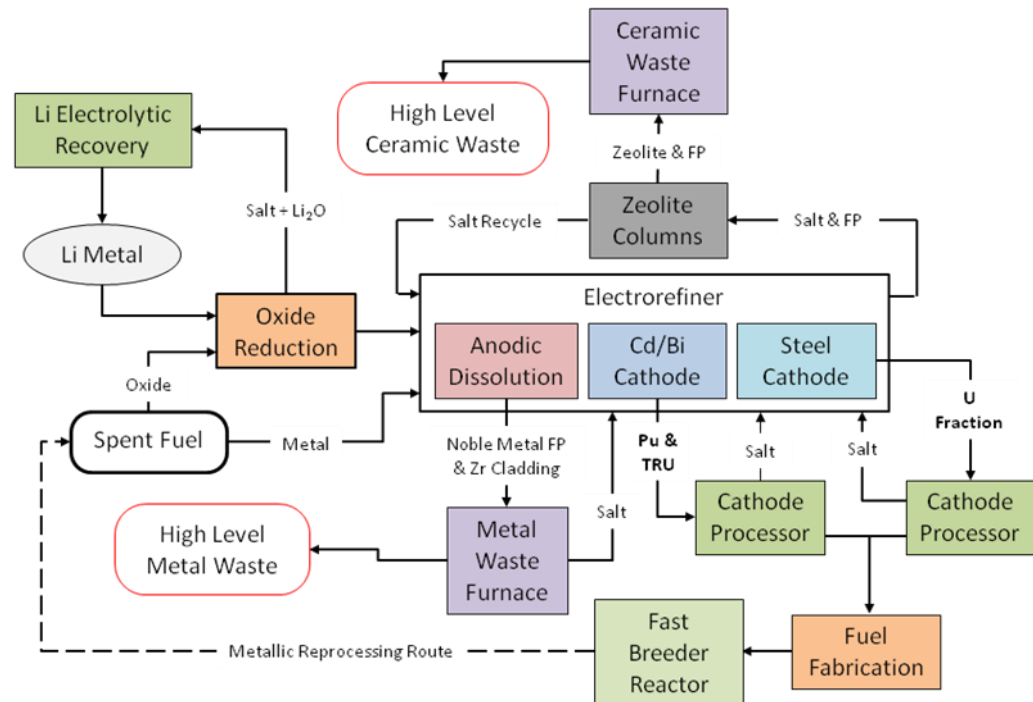
Figure 2.3 – Flow sheet for the ANL pyro-metallurgical reprocessing technology currently under development at Idaho National Laboratory, USA.

2.1.3.2   RIAR Process

Electrochemically, the oxides of uranium and plutonium behave similarly to metals in that they can form complex ionic forms during salt dissolution, e.g. MO_2^{n+} which are reduced at the cathode to oxides. In the RIAR process under development in Russia, a NaCl/CsCl molten salt (in a 1:2 ratio) is used as an electrolytic medium for MOX fuel production from spent nuclear wastes. Spent fuel, in either oxide or metallic form is first introduced into the molten salt via oxidative dissolution. Precise mixtures of O_2 and Cl_2 are sparged into the melt in order to create PuO_2^{2+} and UO_2^{2+} concentrations which can then be reduced at a more positive potential than the FP present[46]. Therefore selective purification of PuO_2 and UO_2 occurs during co-electrodeposition onto a cathode, usually a graphite electrode, leaving the highly active FP behind. It is possible using the RIAR process to selectively electrodeposit PuO_2 as under oxidising conditions UO_2 remains

27

in the melt and plutonium is preferentially removed, a process called precipitative crystallisation. The molten salt and FP comprise the waste stream which are treated and sent for geological storage. The RIAR process, like the ANL process, is an example of proliferation resistant reprocessing technology where weapons grade plutonium is not partitioned separately, but rather in a collective of UO_2 (U + MAs in the ANL process), making application to weapons manufacture difficult. Although it could be argued that the RIAR process is much simpler in regards to the number of stages compared to the ANL process, there is difficulty in maintaining a constant and accurate molten salt oxidation state for the desired actinide ions to form. More indicatively, the fuels produced are in the oxide phase, making them applicable to MOX fabrication for LWRs but directly unsuitable for advanced fuel cycles without additional treatments[47].

2.1.3.3   Advanced Reactor Concepts

Several advanced reactor designs exclusively operate with metallic fuels and are unmoderated, meaning fission is initiated by higher energy fast neutrons. As the rate of neutron interaction generally decreases at higher energies a high initial content of fissile material is necessitated, for example a ^{235}U enrichment of 20 % must be used for the proposed GENIV Molten Salt Reactor (MSR). Alternatively to avoid the costs of producing higher enriched uranium and to simultaneously deplete hazardous spent fuel inventories, fissile ^{239}Pu from LWR spent fuel reprocessing can be introduced to the fuel matrix for fast reactors along with natural ^{238}U. Fast neutrons are extremely useful in that they are much more efficient at breeding fissile materials from fertile precursors than thermal reactor designs, meaning the conversion of fissile ^{239}Pu from ^{238}U after neutron absorption and beta decay is much more probable and the addition of neutron emitting species ensures the chain reaction continues. So fast

reactors can both 'burn' fuels (including TRUs and some FPs not currently possible in thermal reactors) and 'breed' natural uranium into fissile materials at a rate faster than that of fuel consumption. **Table 2.1** presents some basic information regarding the array of fast neutron, GEN IV reactors[16].

Table 2.1 – Generation IV fast neutron reactor technologies

	Neutron Spectrum	Temperature (^{o}C)	Coolant	Pressure	Fuel
Gas-cooled fast reactors	Fast	850	He	High	^{238}U + ^{235}U-$^{239}Pu*$
Lead-Cooled Fast Reactors	Fast	480-800	Pb/Pb-Bi	Low	^{238}U + ^{235}U-$^{239}Pu*$
Molten Salt Fast Reactors	Fast	700-800	Fluoride Salts	Low	UF in salt
Sodium Cooled Fast Reactors	Fast	550	Na	Low	^{238}U and MOX
Supercritical Water cooled Reactors	Fast or Thermal	510-625	H_2O	V. High	UO_2

* ^{235}U-^{239}Pu can be acquired through the pyroprocessing of LWR spent fuels.

Perhaps the most promising of the proposed advanced fast reactor concepts is the Sodium Cooled Fast Reactor (SFR) which uses sodium as coolant and a solid fuel of ^{238}U mixed with MOX at near atmospheric pressures. The advantage of a liquid metal coolant is a relatively high thermal conductivity which permits a higher thermodynamic efficiency than the use of water. Sodium does not corrode steel reactor parts and can also be manoeuvred around the reactor and heat exchanger by electromagnetic pumps. In one of the proposed intermediate sized variations of this reactor (150-600 MWe), TRUs are incorporated into metallic U-Pu-Zr as a fuel source and supported by a closed cycle pyroprocessing in unit operation integrated with the reactor. Although the use of FRs does not make the need for international proliferation security redundant, they do limit the exposure of plutonium as it is consumed via fission within the reactor. Combining advanced reactor systems with onsite pyroprocessing is a

logical solution to optimise resource utilisation, improve economics and to enhance safety.

2.2 Current State of Pyroprocessing

This section details the current advances in molten salt technology and pyroprocessing, focussing on the requirements for effective metal oxide reduction. Issues of optimal materials selection (for cells, electrolytes and electrodes), pre-treatment strategies, metal extraction processes, waste treatment and foresight of disposal options are all of primary concern and are being addressed by researchers in the field. From an economic and viability perspective as a competitive technology to aqueous methods, the yield of useful materials extractable during reprocessing is of paramount concern. Sections below are dedicated to exploring progress made by individual groups into the development and advancement in these fields.

2.2.1 Materials selection

2.2.1.1 Reactor and Cell Considerations

The local molten salt environment in pyroprocessing cells poses significant challenges in the design and materials selection[48]. The structural components must be able to survive the following conditions: (a) An extremely corrosive environment, (b) extended exposure to high temperatures and (c) High neutron and irradiation doses. Consequently advanced reprocessing systems will require new high-performance structural materials able to provide extended service under harsh conditions[49],[50]. **Figure 2.4** gives the results from a relatively brief 100 h exposure of various alloys to molten NaCl at $840^{o}C$ in air. Interestingly the results reveal that Inconel® 600, which is known for its high temperature corrosion resistance, performed the poorest in terms of material loss. Conversely several more common and more economic SS types, such as 304 and 316 exhibit less than half the corrosion rates over the same period

and have relative cost factors at approximately 1.7, 2.1 and 3.9 for 304, 316 and Inconel® 600 respectively[51]. The specific reason for this observation was not given but it may be the various redox activity of alloy components in the inconel®600 are more active within the molten NaCl. Refractory ceramics provide a viable alternative due to thermodynamic stability and far superior corrosion resistance, reportedly less than 0.1mm/year for Al_2O_3[52]. Although concerns of thermal shock by differential material expansion must be factored with ceramic materials, for example the rate of thermal expansion coefficient of Al_2O_3 ($\sim 8 \times 10^{-6}$/K) is less than 5 times that of LiCl (4.3×10^{-5}/K)[53].
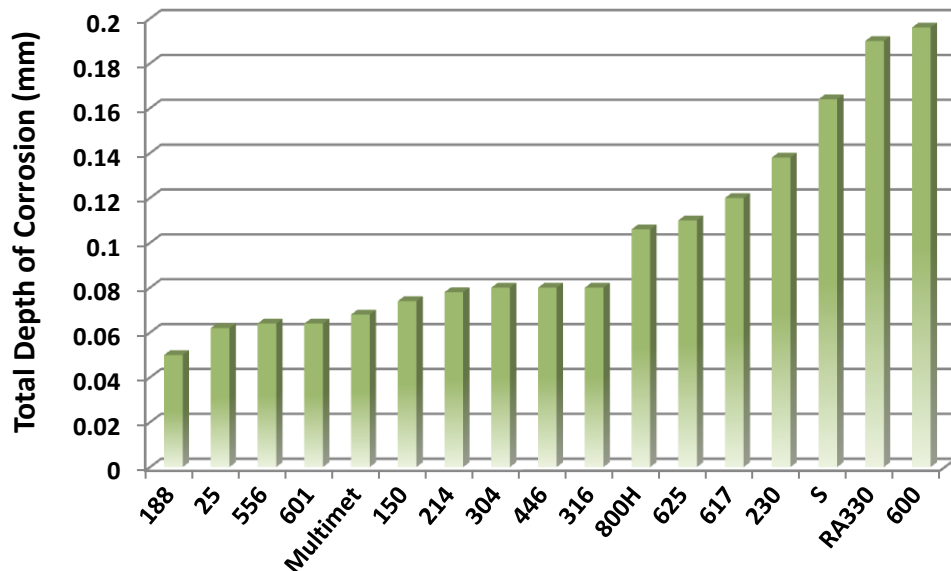
Figure 2.4 – Corrosion of various alloys from 100 h exposure to molten NaCl in air at 840°C (plotted with data from[54]).

During spent fuel reprocessing emphasis has to be placed on the effect of high energy radiation can have on reactor and cell structural materials. Research has shown that atoms in irradiated materials, for instance in time-varying fission reactor service conditions, can change lattice positions up to 200 times[55] which creates vacancy and Self-Interstitial Atom (SIA) defects; typically characterised by the displacements per atom (DPA) unit. These displacements cause complex microstructural and microchemical

changes in the cell/reactor materials leading to void propagation and a multitude of other undesirable attributes. Nuclear transmutation events also alter the elemental alloy composition, in the process forming incorporated radioactive nuclides with an array of decay times. The specific effect on material performance is severe and can include hardening or softening, embrittlement, near complete loss of ductility, enhanced rates of creep and void swellings[56–58].

Limiting the concentration of Ni (due to Ni transmutation by neutrons generating He) and providing highly stable dislocation densities and large interface areas (smaller grain sizes) has been forwarded as a means to control defect accumulation. Recent data has suggested however that larger quantities of nano-sized He bubbles can actually prevent void swellings by acting as defect sinks[59,60]. Other findings have demonstrated the ability to engineer ultra-fine grained (UFG) 304L stainless steel with an average grain size of 100 nm using equal channel angular pressing (ECAP)[61] that reduced the rate of void swellings by a factor of five. Further reductions in energetically founded DPAs, and hence defect production, has been achieved by increasing metal/alloy complexity (to form high entropy alloys), from pure Ni to NiCo, NiFe and NiCoFeCr[62]. This suggest that defect production and recombination is highly dependent on alloy complexity, believed to aid energy dissipation with the effects of solid solutions modifying the transport of energy under irradiation[62–64].

The case for ceramic materials is broadly similar to the metallic examples discussed above, whereby increasing irradiation exposure incurs a crystalline-to-amorphous transformation from the accumulation of point defects[65]. Several attempts have been made to understand the exact nature of ion bombardment (e.g.[66,67]) and electron irradiation effects[68] in alumina. This is both useful and relevant to this work as the pyroprocessing

technology investigated here utilises an alumina crucible for experimental electrochemistry, owing the superb chemical inertness of alumina to chloride and fluoride molten salt corrosion and it being relatively inexpensive. However, for industrial pyroprocessing and fast reactor applications generally metallic structural materials, such as ferric/martensitic (F-M) steels, Ni base alloys, austentic SS, refractory alloys or even graphite are favoured owing to better dimensional stability, mechanical properties, workability and radiation resistance[48].

2.2.1.2 Electrolytes

In the proposed GENIV liquid MSRs, molten fluorides are the choice medium for operation because of their high boiling temperature (1400°C) and chemical stability. Fertile, fissile and fission products (including all actinides from spent fuel) can also be dissolved into the melt for fast neutron fission reactions and the generated heat distributed throughout the salt medium and onwards for electrical power generation via heat exchangers. Hence the molten salt serves as both fuel source and cooling medium and is capable of burning actinides to reduce the long term radiotoxicity of waste from nuclear electricity generation[69].

For pyroprocessing of spent fuel, molten salts are also the medium of choice to host oxide reduction[70]. Nearly exclusively, all pyroprocessing research currently undertaken is in high temperature, alkali or alkali earth chlorides owing to their stability, ability to act as a solvent for an array of metallic species and being relatively abundant and inexpensive. A schematic for the electrorefining from a typical pyroprocessing setup is given in **Figure 2.5**[71]. The spent fuel rods are placed in an anode basket and dissolved into the melt in order of oxidation potential to be electro-deposited onto a solid cathode (for U and small quantities of Pu), and a liquid cathode for bulk Pu and MAs. Lanthanides and fission products

remain the melt for purification and disposal. For the direct electroreduction of oxides to metals whereby produced O^{2-} ions dissolve into the melt to be discharged on either a sacrificial (graphite) or inert anode, $CaCl_2$ is frequently employed as the molten salts of choice due to its high solubility of oxide ions in the form of CaO and favourable thermodynamics from an operational temperature in the range of 800°C-950°C[72].
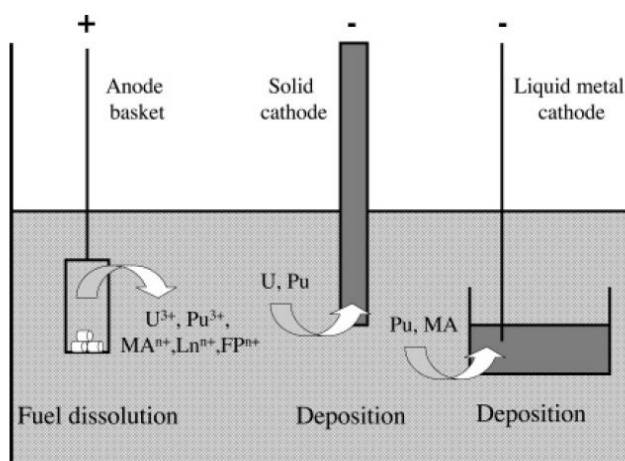
Figure 2.5 – Schematic representation of electrorefining of spent fuel waste[71].

Despite $CaCl_2$ being an attractive medium for electroreduction, it remains difficult to apply to pyroprocessing owing to its high operational temperature and the low melting point of Pu metal making electroreduction and electroplating to a solid cathode difficult. Often low melting single chloride systems are used (i.e. LiCl for the ANL process at 650°C), or a eutectic mixture of two or more salts that yields a system with a lower melting point than either constituent alone. The LiCl-KCl Eutectic (LKE) is a popular example of this type of binary salt, and has been implemented previously for pyroprocessing research[73–76].

In the explicit application to electro-reduction of metal oxides, a shift to a lower temperature melt reduces the diffusivity of oxide ions in the solidus and hence negatively influences the required electrolysis time and could

inhibit a full electroreduction. This effect has obvious negative connotations to industrial application. A reasoned and balanced approach must be taken in this respect, although the electrolysis time, energy input and indeed current efficiency may be poorer in the lower temperature molten salt eutectic, the requirements of safe reprocessing necessitates such a system. However the fundamental pyroprocessing feasibility must be established and this is best achieved in an amenable environment. Consequently, in addition to $CaCl_2$ used in this work at approximately 810^oC a $LiCl$-$CaCl_2$ Eutectic (LCE) was also implemented in an attempt to replicate the partitioning process in a lower temperature and more viable system. The experimentally derived phase diagram for this eutectic system is presented in **Figure 2.6** as assessed by Differential Scanning Calorimetry (DSC) and shows the eutectic point at a LiCl concentration as 65 mol %[77].

As a result of the difficulty in predicting the behaviour of multicomponant systems there are appreciable variations in the eutectic point of the $LiCl$-$CaCl_2$ molten salt from various research groups, with a derived concentration of 60 mol %[78], 62 mol %[79] and 65 mol %[77] LiCl. However in practical terms the variation expressed in the literature isn't problematic as the absolute ceiling temperature of the melt in accordance to pyroprocessing is the melting point of Pu at 639.4^oC at which the melt will still be liquid between the ranges of LiCl concentrations given for all examples above.
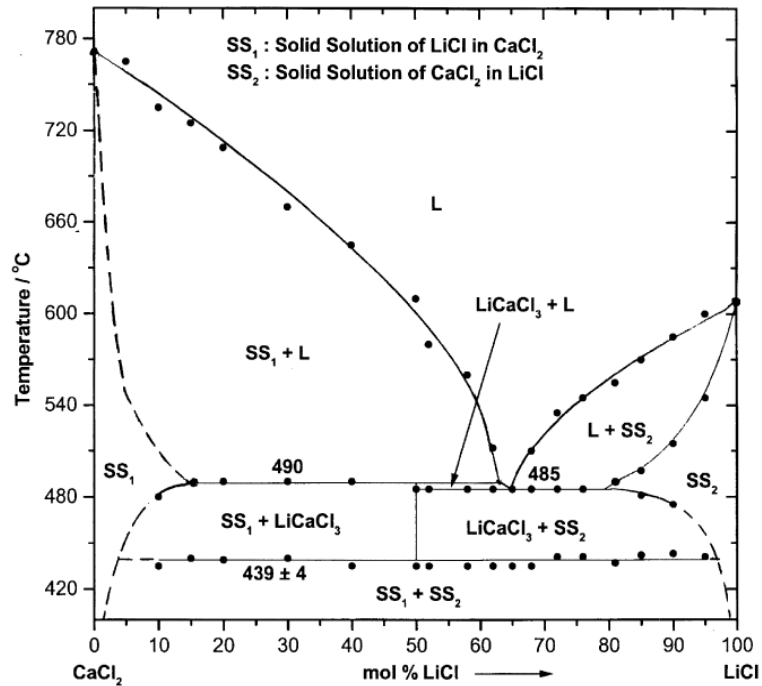
Figure 2.6 – Phase diagram of the LiCl-CaCl$_2$ system as derived from DSC analysis[77].

2.2.1.3 Electrodes

In traditional pyroprocessing the choice of electrode material is paramount as the selectivity of electrorefining is determined by the ability to partition produced metallic phases to a solid and liquid cathode. Similarly during electroreduction the anode selected must exhibit good conductivity, be electrochemically stable and ideally be inert to the oxide ions which are oxidised at the material interface. More generally the electrodes must exhibit longevity within the melt, being corrosion resistant, conductive and relatively stable. Both the cathode and anode in established pyroprocessing technology are replaced interchangeably with the working electrode and counter electrode in a three electrode cell, depending on the polarisation energies applied at a given time. The cell is completed by a reference electrode which is discussed in detail within Chapter 3. For the purpose of the discussion given in this chapter the cathode is synonymous with the

working electrode and anode with counter electrode unless stated otherwise, as the dominant reactions discussed are for electroreduction.

2.2.1.3.1 Cathode

Concerning electro-deoxidation, spent fuel obtained from the nuclear reactor after head-end treatment forms the basis of the cathode arrangement, typically using refractory or high grade SS baskets to hold the oxide spent fuel pellets. Refractory metals such as Mo, Ta, W and Ti are also viable candidates as current collectors in either basket form or simple wires with or without the use of meshes. Regardless of material, basket arrangements are fabricated either by use of a perforated sheet or a mesh of a variable gauge which permits the full inclusion and saturation of molten salt around the oxide cathode. This is necessary to achieve a complete removal of oxide ions and also in the case of the ANL process to provide a source of Li ions and solvent for Li_2O accumulation. Several examples of cathode assemblies from various research teams around the world are shown in **Figure 2.7**, and demonstrate the requirements of both adequate contact between pellets and current collector and sufficient void space for electrolyte penetration. Ample space for the electrolyte to surround the oxide part of the cathode is crucial requirement throughout reduction, as encasing the cathode can lead to O^{2-} (or CaO in $CaCl_2$) accumulation, known to perturb the ability to continue oxygen removal.

Oxide fuels from nuclear reactors can be classified into three types: rod-cut, porous or powder forms; depending on the head-end processing methods employed. Research to assess how UO_2 density and particle size of each of the three spent fuel types influences the electroreduction rate was performed in molten 1 mol % Li_2O-LiCl[80]. Here, the densities of each fuel type were varied from 40 % to 95 % and select results from the experimentation are given in **Figure 2.8**.
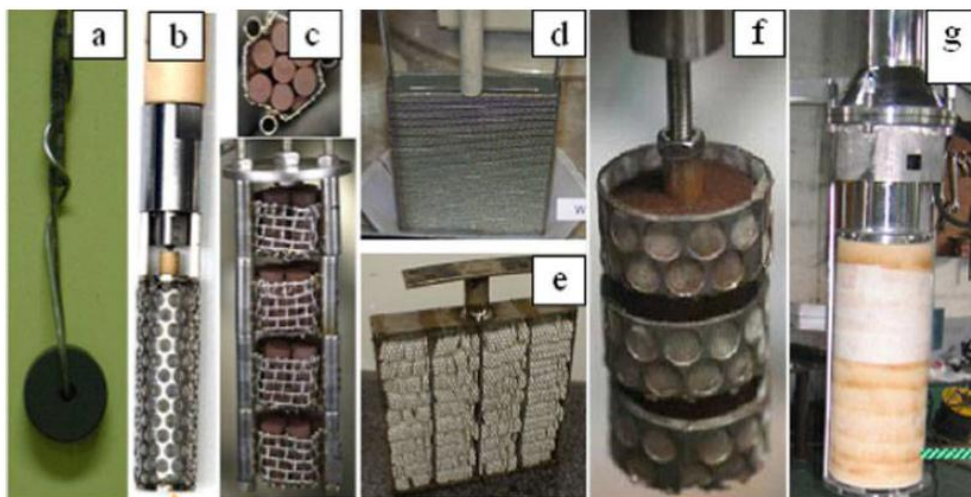
Figure 2.7 – Photographs of cathode assemblies for reduction of a variety of metal oxides collected and combined from various research groups and commercial sources[72]: (a)[81 82 83], (b)[84], (c)[85], (d)[86], (e)[87], (f)[85], (g)[88,89].

In the study a cylindrical SS basket cathode (20 mm diameter) surrounded in a 325 mesh (45 μm sieve) was used to house UO_2 during bulk reductions. The conclusions drawn suggest that the lower density and particularly the smaller particle size UO_2 samples led to a much faster and more complete reduction (as in **Figure 2.8e-g**).
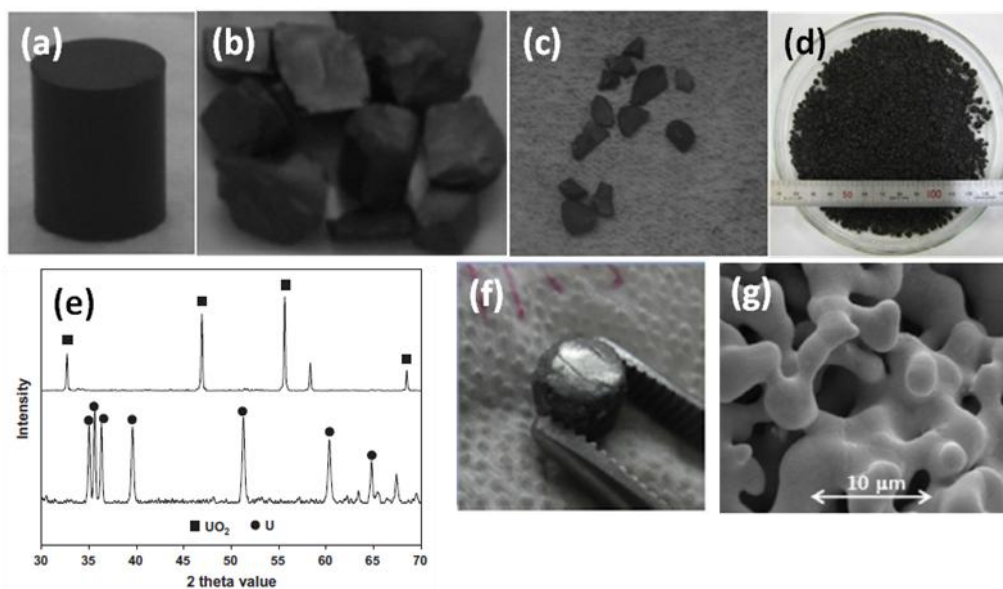
Figure 2.8 – Images of different UO_2 forms (a) cylindrical pellet, (b) crushed lumps at 95 % density, (c) crushed particles at 95 % density and (d) granules. (e) XRD results before (top) and after (bottom) of a 55 % dense UO_2. (f) Sample obtained after electrolysis from (e), and (g) SEM image of the microstructure of a typical UO_2 pellet at 40 % density[80].

The Korea Atomic Energy Institute (KAERI) is developing an integrated pyroprocessing technology for spent LWR fuels involving sequential electroreduction, electrorefining and electrowinning treatments. In recent published results investigating the ability to fully reduce UO_2 in a Li_2O-LiCl bath, researchers at KAERI attempted to navigate issues regarding the use of a Li reductant; primarily the potential loss of Li_2O from Li deposition on the cathode (by possible contamination or alloying) and the associated detrimental influence on post processing. Their advocated solution during the electrolytically derived metallothermic reduction of UO_2 pellets was to implement a two circuit, three electrode cell, using a SS-316 basket cathode (**Figure 2.9a**) and two anodes; namely a Pt rod for oxygen discharge and a SS-316 rod for the secondary regeneration of Li reductant (system configuration in **Figure 2.9b**).
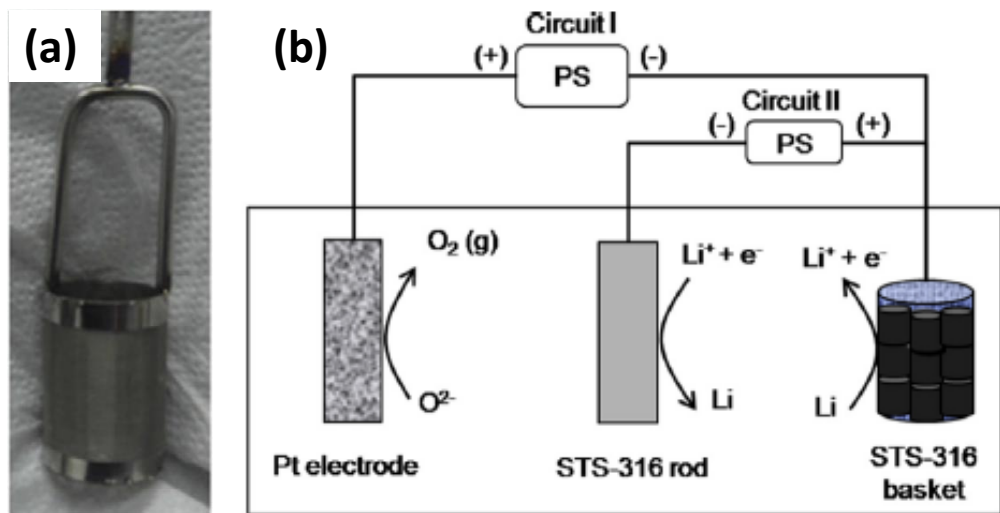
Figure 2.9 – (a) SS-316 basket cathode used for UO_2 during electrolysis and (b) the two circuit system employed as a method of recovering excess Li reductant[90].

The experiments attempted were successful in both reduction UO_2 with an impressive yield of 99.6 % and also recovering the recycled Li metal at a cell voltage of 0.3 V. Whilst this system offers an innovative solution to the issue of Li accumulation in cathode products, core concerns of using a

metal reductant in pyroprocessing, such as poorer current efficiency and the necessity of relatively high reduction voltages, cannot be avoided.

At Idaho National Laboratories, research is ongoing into the development of broad functioning electrochemical cells for the treatment of conventional and fast Experimental Breeder Reactor (EBR-II) fuels, supported by data collection from modelling efforts[91]. The EBR-II fuels (high enriched uranium-zirconium) have an impressive typical burn up of 80 MWd per tHM, with some advanced uranium-plutonium-zirconium experimental fuels reaching 180 MWd per tHM. The result of these high burn ups is typically a unique spent fuel composition, e.g. the EBR-II fuels having noble metal concentrations of 2.36 % Mo, 1.96 % Ru, 0.28 % Rh and 0.19 % Pd. Besides fast fuels, the developed cell has been configured on a laboratory scale to either act as the electrolytic reduction vessel of spent LWR fuels or as an electrorefiner of small (50 g) metallic samples in cathode baskets. The benefits of such an arrangement are far greater in the simplicity of fabrication, consistent online monitoring, and the ability to aggregate operational knowledge. Being able to adapt multiple uses from cells and materials greatly benefits this axiom of simplification and is the focus of much of the process design of pyroprocessing.

2.1.1.1.2 Anode

Compared to geometry concerns of cathodes, anode designs are often very simple, taking the form of dense rods or plates. The choice of material however is a subject of considerable interest as a chemically inert anode is highly desirable to increase the working electrochemical window and hence provide improved stability. In electroreduction of metal oxides the anode acts as the destination for O^{2-} ions produced at the cathode, with implications regarding the thermodynamic interactions between anode and O^{2-} ions. By far the most popular anode of choice for the electrodeoxidation

of metal oxides by the FFC Cambridge Process in molten salts (see section 2.3) is graphite, owing to its high affinity for oxygen and inertness to chlorine at high temperatures. During electrolysis O^{2-} ions are released at the cathode and transported through the molten salt electrolyte via diffusion and convection to be discharged primarily in the form of CO_2, although both CO and O_2 have been detected by Gas Chromatography (GC) when investigated[92,93]. Example full cell reactions for the reduction of TiO_2 and Ta_2O_5 in the presence of a graphite anode are given below (**Equations 2.4** and **2.5**).

$$TiO_2 + C = Ti + CO_2 \qquad (\Delta E^o_{850°C} = 0.894 \text{ V}) \qquad \textbf{2.4}$$

$$2Ta_2O_5 + 5C = 4Ta + 5CO_2 \qquad (\Delta E^o_{850°C} = 0.585 \text{ V}) \qquad \textbf{2.5}$$
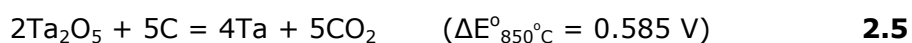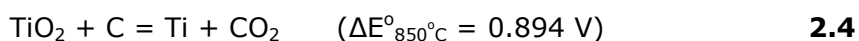
Where ΔE^o is the standard cell voltage derived from the Gibbs free energy (ΔG^o). From the calculations in the presence of graphite, the apparent cell voltage required is for the production of metallic species from their respective oxides is very low. However in practice often much higher voltages are required (frequently >3.0 V) to ensure a complete reduction of the oxide precursors[94,95]. One main reason for this divergence between thermodynamically predicted and experimentally observed data is the nature of cathodic reactions during electroreduction being often more complex than those portrayed in **Equations 2.4** and **2.5**, for instance the formation of cation intercalated species or suboxide intermediates. Another source of deviation is derived from the contributions of cell resistance, but as the influence of cell resistance is limited when the electrolysis current decays with time its cumulative effect cannot account for such large discrepancies. Experimental work has been undertaken to investigate this divergence using graphite anodes with varying surface areas[96]. **Figure 2.10** displays a CV curve taken using a graphite anode in molten $CaCl_2$ at

850°C along with the recorded relationship between graphite anode surface area and both cell voltage and anode potential.

The electrochemical analysis by CV revealed a two-step mechanism of O^{2-} oxidation to CO_2 (peaks A4 and A3) through an initial adsorption of O^{2-} to form C_xO. Also implied was a direct oxidation route to CO or O_2 on the graphite anode. These reactions proceed at a wide range of potentials, reaching very high current densities when O^{2-} ions are present in sufficient concentrations.
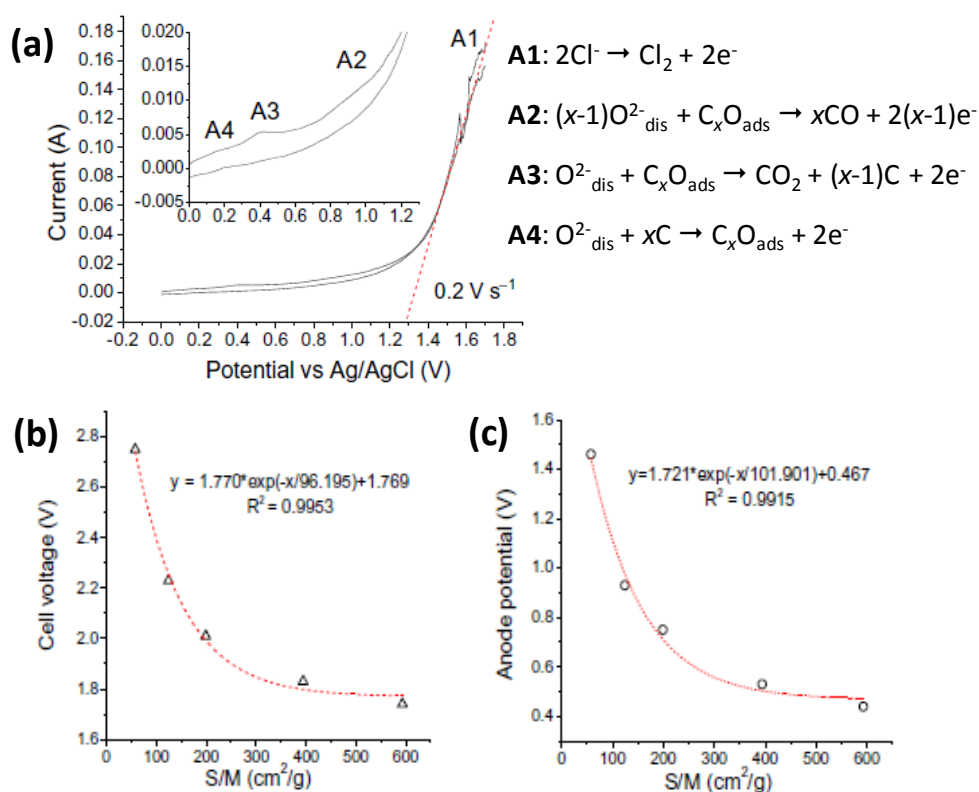
Figure 2.10 – (a) CV of graphite rod electrode (0.63 cm^2) recorded in $CaCl_2$ under argon at 850°C (anodic peak descriptions given to the right). (b) and (c) plots the relationship between the 'anode area/cathode mass' (S/M) ratio versus cell voltage and anode potential respectively[96].

The authors continued that by increasing the anode surface area to achieve a strategy of low current density, and hence limit energy consumption, could reduce the both the cell voltage and the anode potential by a maximum of approximately 1 V (**Figure 2.10b** and **c**). The near identical

relationships displayed by cell voltage and anodic polarisation indicate that the cell voltage is largely determined by the anodic polarisation rather than mass transport of O^{2-} ions in the electrolyte (although the O^{2-} concentration remains a significant parameter during electrolysis), emphasising the importance of using a suitable anode with favourable properties.

Beyond the many positive characteristics carbon possesses as an anode material in molten salt electrolysis, there are issues, chief among which is the degradation over time of the carbon through the evolution of carbon oxides. Furthermore different groups have reported very low current efficiencies using a graphite anode for metal oxide electro-deoxidation, attributed to secondary reactions from the formation of CO_3^{2-} [72,81,97–100]. The ideal anode reaction between O^{2-} ions and graphite is given in **Equation 2.6**, to yield CO_2 which is then immediately discharged from the anode surface. However CO_2 gas also has solubility in molten $CaCl_2$ containing CaO and can react with dissociated Ca^{2+} to form $CaCO_3$ (**Equation 2.7**).

$$O^{2-} + C = CO_2(g) + 2e^- \qquad \textbf{2.6}$$

$$O^{2-} \text{ (in the melt)} + CO_2 + Ca^{2+} \rightarrow CaCO_3 \text{ (in the melt)} \qquad \textbf{2.7}$$
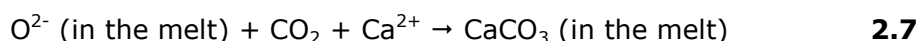
Subsequently the CO_3^{2-} can diffuse within the electrolyte to the cathode surface and undergo electrolysis as given in **Equation 2.8**.

$$CO_3^{2-} + 4e^- \rightarrow C + 3O^{2-} \qquad \textbf{2.8}$$

The presence of **Equation 2.8** allows the regeneration of O^{2-} back into the melt, facilitating further carbon consumption by **Equation 2.6**. Carbonate reduction by **Equation 2.8** is also parasitic to the primary electrolysis of the oxide cathode, consuming electrons and driving down the overall current efficiency of the process. **Figure 2.11** visualises the constant feedback mechanisms involved with using a graphite anode, using an example of a Nb_2O_5 cathode[101].

Additionally, due to the cyclic nature of the above reactions, carbon particles can gradually accumulate in the cell, tending to float atop the salt. Researchers have frequently observed the reaction between carbon and the nascent metals produced at the cathode during ex-situ crystallographic analysis to yield metal carbides, or at best carbon contaminated products.
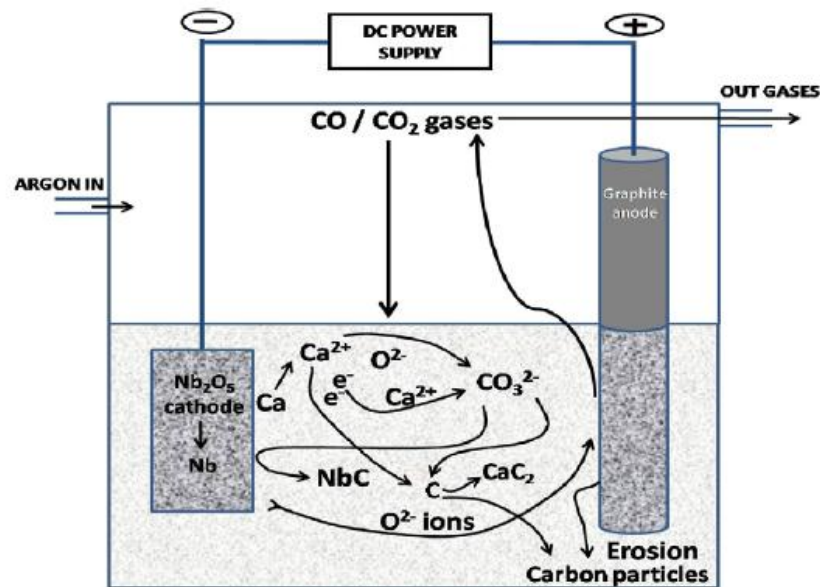
Figure 2.11 – Schematic of carbon generation and distribution routes in an electro-deoxidation cell using Nb_2O_5 as a cathode and graphite as anode in $CaCl_2$ at 900°C[101].

Should the layer of floating carbon become sufficiently concentrated then a route of direct electronic conduction via a bridge between cathode and anode can form, effectively short circuiting the cell and halting any further deoxidation of the cathode. During extended durations of electroreduction this phenomenon can be overtly problematic and from an industrial position would require a physical mechanism of removal to permit larger scale cathode reductions using graphite. Furthermore it is possible that Ca or Li metal procedurally generated during high voltage electrolysis can directly reduce carbon oxides and $CaCO_3$ to give further free carbon powders. At the graphite anode interface where O^{2-} ions may not be homogenously distributed during adsorption, pitting frequently occurs, providing shelter for further accumulation of CO_2 and preventing its

discharge. The development of turbulent flow near to the molten salt meniscus by these pitting features can help to physically dislodge further carbon particles close to the melt-gas interface.

Reduction of UO_2 has been successful using graphite as an anode in Li_2O-LiCl at 650°C at ~180 mV positive of the lithium deposition potential but as the amount of Li_2O added to the melt increased above 1 wt%, the reduction was adversely affected due to in-situ generated carbonate ions[102]. Further discussion into alleviating some of the issues described with the use of a graphite anode is given in Chapter 4.

Addressing many of these concerns, the move towards more inert anode materials is receiving a great deal of attention within the wider electrochemistry field. Platinum is a common metal employed for the anode as it promotes the discharge of molecular oxygen (O_2, **Equation 2.3**)[103,104]. The nobility of Pt ideally helps avoid the formation of PtO_x surface species during electroreduction or during the anodic sweep in a three electrode cell where Pt is used as the counter electrode[105]. Pt rods or plates used in electrochemical cells can be surrounded by a ceramic sheath, often non-porous MgO, which acts as a guide for the discharge path and outgassing of produced oxygen, preventing significant re-dissolution (and subsequent unfavourable shifts in molten salt oxygen activity) from occurring. The issue in implementing a non-porous sheath is that the path of O^{2-} ions is significantly limited to the portion of the Pt rod not directly covered by the sheath, reducing current density and increasing the required duration for a full reduction of a given oxide cathode (**Figure 2.12a**). Some researchers are investigating the possibility of using a porous sheath for Pt electrodes, enabling O^{2-} ions to penetrate but still providing a low energetic path for oxygen discharge and so increasing the achievable current density.
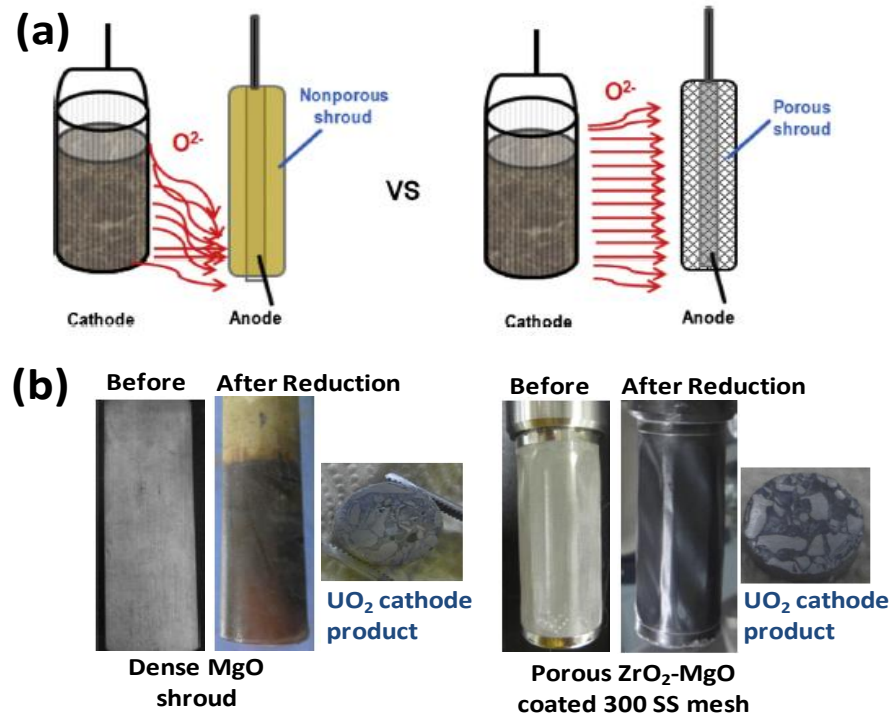
Figure 2.12 – (a) Schematic diagram of a non-porous and porous type sheaths used for a Pt anode in the electrochemical reduction process. (b) Picture of the two sheaths from (a) before and after reduction and showing the cathodic U product after reduction[106].

By introducing a ZrO_2-MgO coated SS mesh around a Pt anode, the rate of reduction of UO_2 in a basket cathode was sped up significantly (**Figure 2.12b**), with the current density increasing from 0.34 A cm^{-2} to 0.76 A cm^{-2}, and taking less than half the time to reach a charge supplied of 150 % for a theoretic full reduction (1.5 h vs. 3.5 h)[106]. Despite the inertness of Pt to oxidation, the Pt anode can still suffer damage in conditions typical of a molten salt bath, but mostly due to anodic dissolution and the known formation of multi-component oxides under certain conditions (e.g. Li_2PtO_3 in a LiCl electrolyte)[105]. **Figure 2.13a-d** shows some observations made when using a Pt anode in both pure LiCl molten salt and LiCl with an addition of 0.5 % Li_2O (Li_2O addition being necessitated by ANL pyroprocessing).
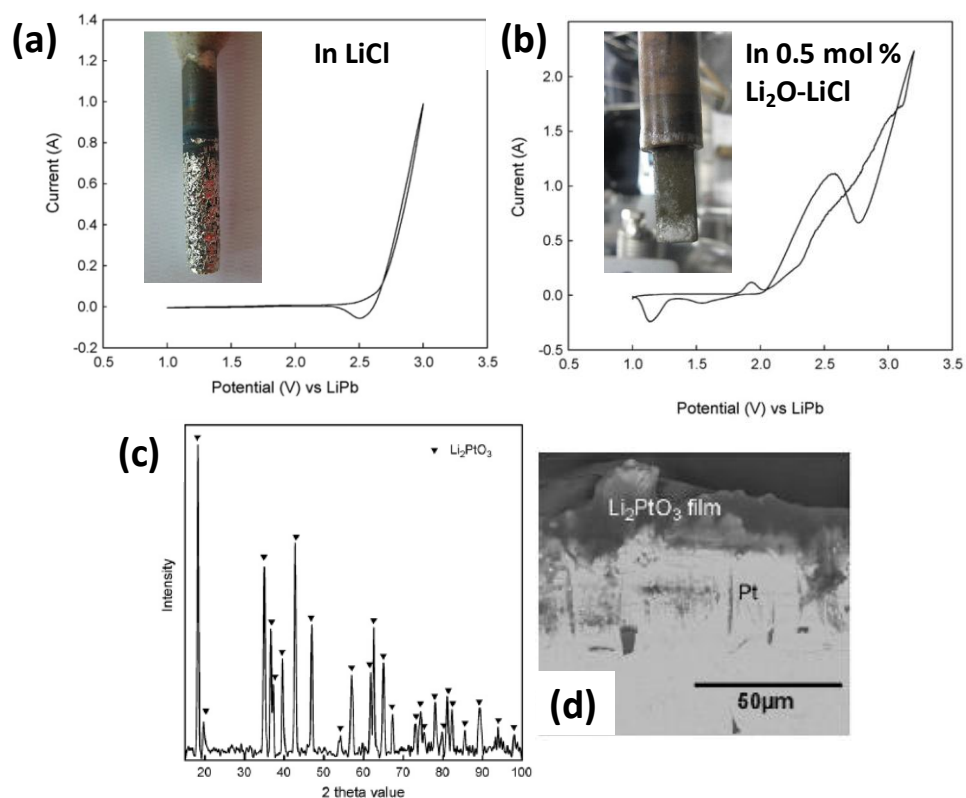
Figure 2.13 – Anodic sections of CV curves of a Pt wire (a) in pure LiCl (inset electrode electrolysis in LiCl) and (b) in 0.5 wt% Li_2O-LiCl (inset electrode after electrolysis in 1 wt% Li_2O-LiCl). (c) XRD spectra of a Pt anode after electrolysis in 1 wt% Li_2O-LiCl and (d) SEM results of anode from (c)[105].

When the concentration of Li_2O was as low as 0.5 wt%, Li_2PtO_3 scales still formed on the surface of the Pt electrode (**Figure 2.13c and d**) and a clear electrochemical discrepancy on the anodic tail of CV scans observed (**Figure 2.13a and b**) attributed to Li_2PtO_3 formation by **Equation 2.9**,

$$2Li^+ + Pt + 3O^{2-} \rightleftharpoons Li_2PtO_3 + 4e^-$$ **2.9**
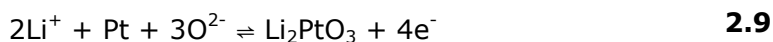
Clearly the presence of Li_2O, which is used in the capacity of metallothermic reduction, has the potential to cause significant damage to the Pt anode, which in turn cascades to influencing the rate and quality of reduction. It should be noted that even when a pure LiCl melt was used to test the Pt anode, spallation was observed after short electrolysis durations, leading to the author's conclusion of intergranular corrosion of Pt in the molten salt and so the notion that Pt can be considered truly inert in

molten salts is facile. At potentials more positive than the OER using a metal anode, further reactions can be observed, but ones which should be actively avoided in order to maintain a stable electrochemical window (**Equations 2.10** and **2.11**). Some metals also provide candidacy for oxidation in the presence of O^{2-} ions at variable potentials (**Equation 2.12**), an outcome that should equally be avoided as metal oxides can both electrochemically and chemically dissolve into the melt.

$$2Cl^- \rightleftharpoons Cl_2 + 2e^-$$

2.10

Chlorine evolution reaction (CER)

$$M \rightleftharpoons M^{n+} + ne^- \text{ (M refers to metal)}$$

2.11
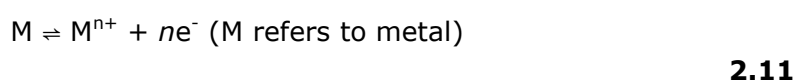
Metal dissolution reaction (MDR)

$$M + xO^{2-} = MO_x + 2xe^-$$

2.12

Metal oxide formation reaction (MOFR)

These reactions become vital when considering the high cost of raw Pt, and consequently have driven the large international effort in developing cost effective, conductive and chemically inert anodes for electrochemistry. In a CaO containing $CaCl_2$ electrolyte, a wide range of metals were examined in their suitability as comparatively more inexpensive anode materials for electro-deoxidation of various test oxides[107]. Of all those investigated, the thermodynamic stability of metals in the molten salt under anodic polarisation went in the following ascending order: Fe, Cu, Ag, Co, Ni, Mo, Pt; and that none of the non-noble metals tested were stable in the region between OER and CER.

Novel approaches to overcome the shortfall in apparent holistic suitability for an anode in such aggressive environments have also been considered. The possibility of using a liquid Sb anode was suggested[108], as the ordinary difficulties of mechanical integrity of solid anodes become redundant,

eliminating the possibilities of thermal stress related delaminating and mechanical damage. Whilst theoretically a favourable alternative, the authors note that the Sb was not inert, acting as a sacrificial anode from the electroplating of Sb which also inhibited the complete reduction of UO_2. Another approach is to develop conductive oxide anodes, such as ceramics and cermets[109], as these are notoriously more corrosion resistant in oxoacidic conditions and may even offer better current efficiencies than graphite. SnO_2 has been used for this purpose previously[97,110], with varying success. At standard conditions SnO_2 is an excellent electrical insulator, however at elevated temperatures, particularly those required for the electroreduction of oxides in molten $CaCl_2$, the oxide phase becomes far more conductive. Interestingly it was found that during the use of a SnO_2 anode for the electroreduction of Ta_2O_5, some intermetallic Ta_3Sn_2 compounds were observed in the final reduction product[110]. Visually the tin oxide rod after use displayed a change in colour to off-white, indicating (according to the researchers) the formation of calcium stannate ($CaSnO_3$) and reduced tin oxide compounds (SnO and Sn_3O_4). The authors suggested the dissociation of CaO, leading to Ca intercalation and freeing of Sn on the anode that is then anodically dissolved and is free to migrate to the cathode to form the observed alloy (**Equations 2.13** and **2.14**). The formation of the partially reduced tin oxide phases could be caused by a similar process at the anode, as given by **Equations 2.15** and **2.16**.

Although the authors continue to promote SnO_2 as a favourable alternative to the traditionally used graphite anode in terms of current efficiency, there are quite clearly some issues regarding the absolute stability of SnO_2 in $CaCl_2$ and the loss of conduction from $CaSnO_3$ formation. In addition to the impurity bias introduced to the produced cathodic product, the reactivity of SnO_2 causes mass loss in the anode.

$$\text{In the } CaCl_2 \text{ melt: } CaO = Ca + O \qquad \textbf{2.13}$$

$$\text{At the anode: } 2SnO_3 + 2Ca = 2CaSnO_3 + Sn \qquad \textbf{2.14}$$

$$2SnO_2 + Ca = CaSnO_3 + SnO \qquad \textbf{2.15}$$

$$5SnO_2 + 2Ca = 2CaSnO_3 + Sn_3O_4 \qquad \textbf{2.16}$$
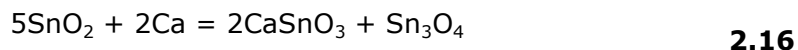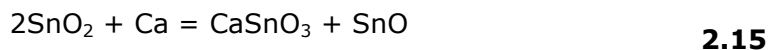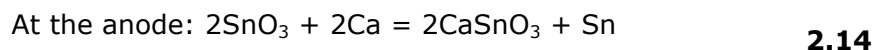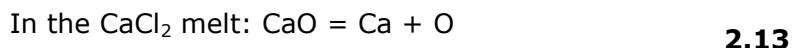
More recently effort has been made to the development of mixed, non-stoichiometric oxide anodes in various molten salts. Initial work was built on the observations that the molten salt cation almost always was introduced into the structure of the pure oxide anode (e.g. $CaSnO_3$ above) and that these new forms were relatively stable although lacked satisfactory conductivity. Attempts of doping calcium titanate have been made, but with poor success; the highest performing dopant measured was Fe^{3+} which substituted Ti^{4+} in the structure to give $CaTi_{(1-x)}Fe_xO_{(3/2x+1)}$ with a new conductivity of just 0.1 ohm^{-1} cm^{-1} at 1000°C[111]. Further work was pursued in search of compounds with a similar structure to calcium titanate but that were highly electronically conductive. $CaRuO_3$ was chosen in one example having a measured conductivity of 400 ohm^{-1} cm^{-1} at 20°C and vitally the calculated standard free energy change for the formation of $RuCl_3$ is unfavourable, even in the presence of pure chlorine. Additionally the decomposition to RuO_2 is unlikely in standard conditions within the cell[112] and the corrosion rate, as calculated from the change of weight over time by immersing a pelletised $CaRuO_3$ anode in $CaCl_2$ for 150 h, was shown to be an order of magnitude less than SnO_2 in cryolite (Na_3AlF_6). The material cost of ruthenium oxide however is prohibitively high for large scale mass production. Further inclusions of dopants to reduce the quantity of ruthenium (e.g. Ti^{4+}) have yielded some success, transitioning from a conductor to an insulator at room temperature but being an excellent conductor at the operational temperature range in molten $CaCl_2$.

An assessment of an alternative conducting oxide was made in LiCl melts for the reduction of UO_2. The development of such an anode in LiCl is more difficult as the temperature gradient for operation is much narrower and much lower than in $CaCl_2$, hence the beneficial influence of thermally assisted conductivity diminished. $La_{0.33}Sr_{0.67}MnO_3$ was chosen based on these criteria and investigated in the Li_2O-LiCl electrolyte at 650°C using a voltage of 3.25 V between the UO_2 contained cathode basket and anode. Basic features of its electrochemical and physical performance are given in **Figure 2.14**.
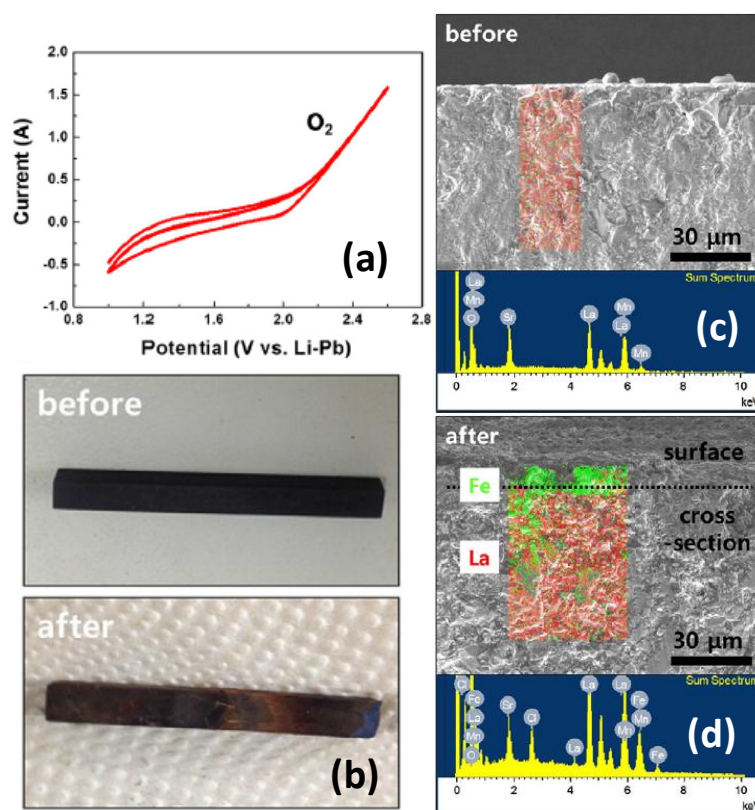
Figure 2.14 – (a) CV curve of the $La_{0.33}Sr_{0.67}MnO_3$ electrode in LiCl showing oxygen evolution at the anodic tail. (b) Images of the $La_{0.33}Sr_{0.67}MnO_3$ anode before and after extended electrolysis of UO_2, with (c) and (d) showing SEM micrographs and EDS elemental analysis of the before and after anode [113].

Unlike the $CaRuO_3$ material tested in $CaCl_2$, staining was observed on the $La_{0.33}Sr_{0.67}MnO_3$ anode in Li_2O-LiCl (**Figure 2.14b**). The authors claim this was only a superficial consequence of the electrolysis and that phase stability was maintained as judged by crystallographic analysis. The major

contribution to the discolouration was found to be Fe (as in **Figure 2.14d**) and was believed to manifest from the corrosion of the anode lead or electrolyte container which were both made of stainless steel. The absolute cost of this particular anode was not defined but the constituent oxides are more freely available and so should be less expensive than RuO_2.

2.3   The FFC Cambridge Process

2.3.1   Introduction

An early applied example of an electrochemical purification process came in 1961 during an attempt to remove non-metallic impurities from a molten copper cathode[114]. However, the first reported attempt of applying this concept to the ionisation of an insulating cathode was in 1996 whilst trying to reduce the oxygen content of oxygen-rich titanium alpha phases in a molten $CaCl_2$ electrolyte. The reaction was predicted to occur via a cathodic formation of O^{2-} ions within the titanium-oxygen solid solution leading to deoxygenation, as shown by **Equation 2.17**:

$$O_{(Ti)} + 2e^- \rightarrow O^{2-} \hspace{3cm} \textbf{2.17}$$

Instead, what was observed in the Pre-electrolysed molten $CaCl_2$ bath at $850^{\circ}C$ was not only the leaching out of absorbed oxygen, but also the reduction of the native TiO_2 layer which had previously existed, noted by the metallic lustre gained following electrolysis and subsequent elemental analysis. The work was extended to include pure TiO_2 pelletised preforms, of which the results were published[115] and the Fray-Farthing-Chen (FFC) Cambridge Process patented[116–119]. A schematic representation of the cell used to reduce the TiO_2 cathode using a graphite anode in $CaCl_2$ is shown in **Figure 2.15**, along with a 'before and after' SEM micrograph of the feed and metallic product. The net outcome of the direct electrolytic reduction of solid oxides in molten $CaCl_2$ is that bound oxygen is ionised, leaving behind

the (pure) metal at the cathode/working electrode. For this process to occur the minimum energy required is understood to be the theoretical ionisation potential of the solid oxide to be reduced, which is nearly always less than the decomposition potential of the $CaCl_2$ electrolyte, e.g. $E^o_{CaCl_2}$ = 3.2 V at 900^oC[120].
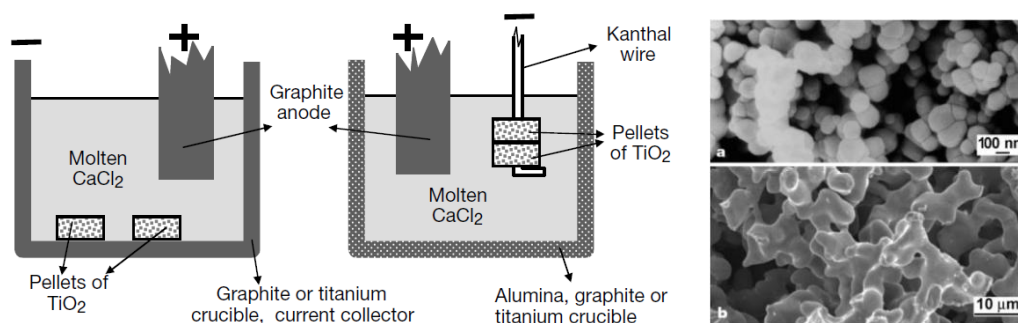
Figure 2.15 – Example FFC Cambridge cell configurations for electrochemical deoxygenation of TiO_2 (left) and SEM images of the TiO_2 feed (right, a) and metallic product (right, b).

Consequently, what distinguishes the FFC Cambridge Process as a unique electrochemical method for the production of metallic states compared to, for example, the practices applied in the ANL process, is the ability de-oxidise insulating materials without the degradation of the electrolyte from sufficiently negative applied potentials. Essentially the process remains predominantly one of electro-deoxidation rather than indirect metallothermic reduction, as excess production of the metallic cation (Ca, Li etc...) can be avoided, hence leading to the cathodic and anodic reactions **(Equations 2.18** and **2.19)** respectively (for the case of TiO_2 reduction).

$$TiO_{2(s)} + 4e^- \rightarrow Ti_{(s)} + 2O^{2-} \qquad \textbf{2.18}$$

$$2O^{2-} + 4e^- \rightarrow O_{2(g)} \text{ (or CO/CO}_2 \text{ with C anode)} \qquad \textbf{2.19}$$
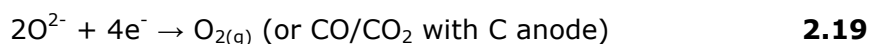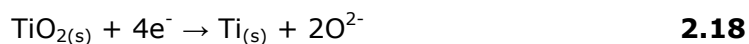
The benefits of developing such a method for the production of metals from ores or general oxide precursors was recognised early, with the formation

of a commercial spin-off Metalysis Ltd., and the significant continued research for application within the electrochemical, metallurgical and materials fields. An illustration of the condensed ore to product FFC Cambridge Process based on the electrochemical reduction of a solid oxide in a molten salt electrolyte is shown in **Figure 2.16**.
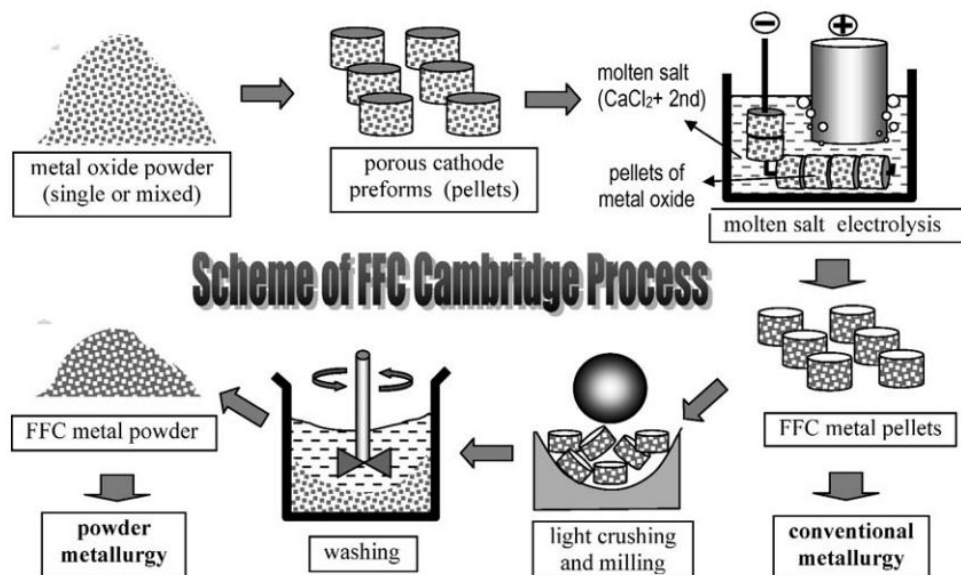
Figure 2.16 – Schematic representation of the stages involved in metal production via electrochemical oxide reduction by the FFC Cambridge Process [121].

As outlined in **Figure 2.16**, a further advantage of the FFC Cambridge Process is its relatively simplistic operation, involving few stages under amenable conditions (temperatures, ambient pressures, etc...). The oxide powders which comprise the feedstock are first pressed or slip cast to form a green precursor, often followed by sintering at temperatures between $900^{\circ}C$-$1400^{\circ}C$ to improve strength for handling and to develop a preferred density and open porosity. The cathode assembly is formed by attaching the preform onto a refractory metal wire, such as molybdenum, tungsten, tantalum, titanium or stainless steels and immersed into the molten salt. A voltage is then applied to the cell below the decomposition voltage of the molten salt but above that for the reduction of the chosen oxide. The advent of the reduction process utilised by the FFC technology was not

without controversy in the early years of establishment. Formerly a debate centred on the precise mechanism of deoxygenation ensued; by either direct electroreduction as championed by the inventors, or by in-situ electro-metallothermic reduction put forward by a competitive operation, namely the Ono-Suzuki (OS) Process[122–133], presented in **Figure 2.17**.
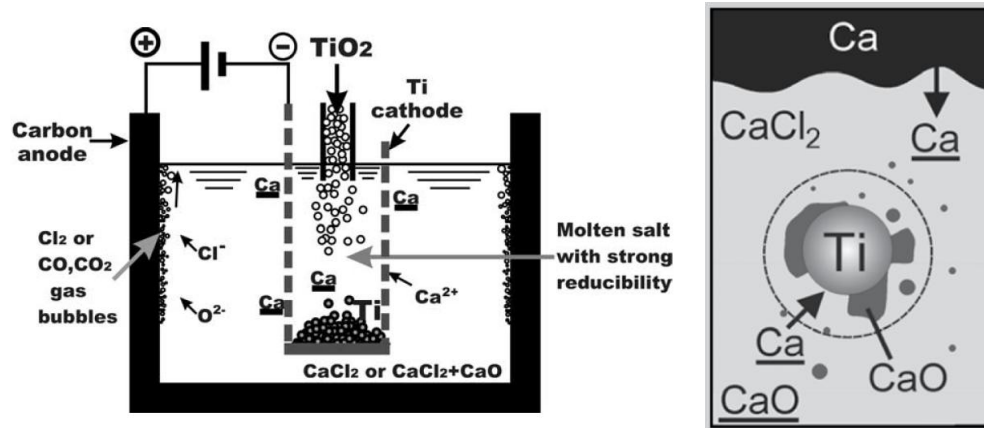
Figure 2.17 – example of the OS Process cell (left) and the specific mechanism of reduction for a titanium oxide precursor (right)[126,134].

The base principle of the OS process is allied to the ability of $CaCl_2$ to dissolve CaO, and hence continue the generation of Ca via CaO decomposition and the reduction of the oxide preform via a metallothermic route. Generic reactions for the both the FFC Cambridge Process and OS Process are given as follows (**Equations 2.20-2.22**),

Direct electroreduction:

$$MO_x + 2xe^- (+ xCa^{2+}) = M + 2xO^{2-} \text{ (or } xCaO) \qquad \textbf{2.20}$$

Electro-metallothermic reduction:

$$xCa^{2+} + 2xe^- = xCa \qquad \textbf{2.21}$$

$$xCa + MO_x = M + xCa^{2+} + O^{2-} \text{ (or } xCaO) \qquad \textbf{2.22}$$
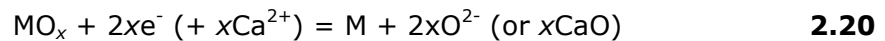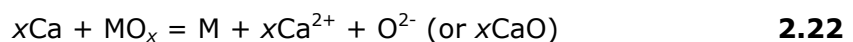
With the OS Process the calcium reductant is theoretically regenerated, meaning the decomposition of the $CaCl_2$ molten salt can be avoided provided a suitable concentration of CaO is introduced into the melt.

However the voltage required to produce the Ca reductant has the capacity to cause anodic production of elemental Cl_2 at low concentrations or indeed precipitate CaO when at elevated levels.

Various authors have independently sought to validate the precise reduction mechanism which occurs under polarised electrodes in molten $CaCl_2$, and using various oxide feeds. In 2006 a group demonstrated that the electrochemical metallisation of terbium oxide (Tb_4O_7) pellets proceeded via the FFC Cambridge Process at 850°C by the application of progressive voltages, see **Figure 2.18**[135]. This work demonstrates that as voltage increased, the reduction speed of the oxide pellet concomitantly increased up until a plateau (at approximately 3.5 V, **Figure 2.18**), believed to be caused by a saturation of produced Ca metal blocking the ionic pathway for O^{2-} diffusion away from the pellet.

If indeed it were the case that a metallothermic-reduction was dominating, than the rate of reduction above the point of Ca formation (once Ca activity reached unity) should be constant and independent of the applied cell voltage. Instead we see an incremental reduction depth at even voltages far below the theoretical decomposition potential of the molten salt, but which is assisted by increasing the cell voltage, i.e. increasing the driving force for the removal of oxygen.
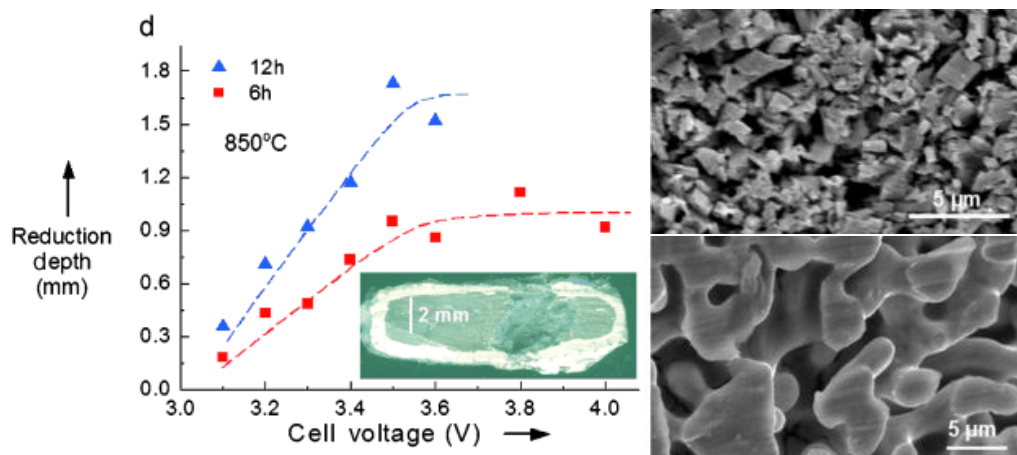
Figure 2.18 – The relationship between applied cell voltage and depth of reduction for a Tb_4O_7 pellet in molten $CaCl_2$ at 850°C following either 6 hours or 12 hours of electrolysis (left). Images of the sintered Tb_4O_7 (right, top) and the produced Tb metal (right, bottom)[135].

An important detail regarding the reduction of insulating oxides at voltages far below the realm of Ca production in molten $CaCl_2$ has been further investigated by the use of chromium sesquioxide (Cr_2O_3). The experimental results of a polarisation curve in a 98 mol % $CaCl_2$, 2 mol % CaO solution using a pseudo graphite reference electrode and current-time plots of Cr_2O_3 are presented in **Figure 2.19**[82]. Reduction was shown to be initiated at a potential more anodic than even -1 V vs. C (+0.4 V vs. Ca/Ca^{2+}), proving the occurrence of electrochemical reductions that bypass or simply do not require the presence of deposited Ca metal. Similarly CV results for TiO_2 and a host of other tested insulating metal oxide materials contradict the necessity of generating a metal reductant[136,137], with the implication of a direct electrochemical method being the overall dominant process.
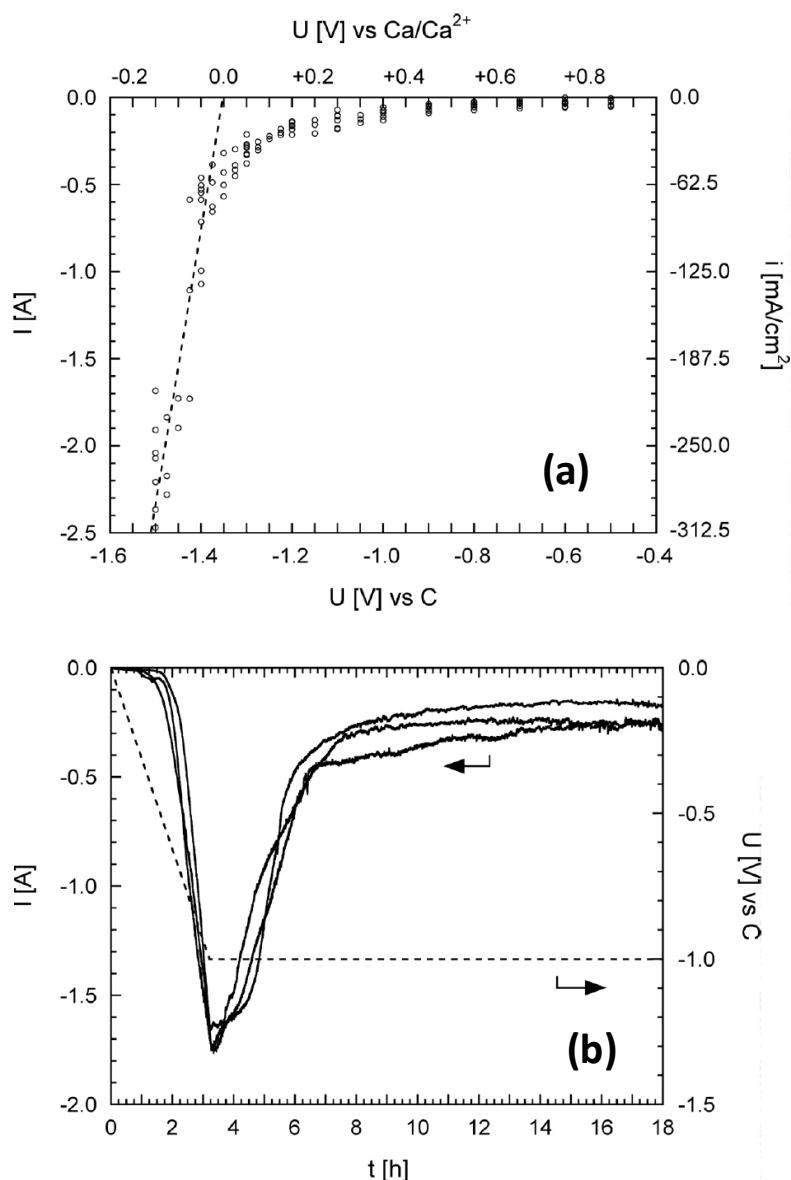
Figure 2.19 – (a) Current/current density vs. Potential curves as a function of working electrode potential vs. a graphite pseudo reference electrode (lower abscissa) and the internal Ca/Ca^{2+} standard (upper abscissa) in molten $CaCl_2$ with a 2 mol % CaO addition at 900°C and under dried argon. (b) Current vs. Time curves obtained during reduction of Cr_2O_3 pellets ramped (-300 mV/h), and then maintained at, -1.0 V vs. a graphite pseudo reference electrode [82].

One such recent and relevant example of the divergent claims made within the literature is for the investigated reduction of NiO, which was reportedly formed by the electrolysis of CaO[132]. This specific example was examined by one of the co-founders of the FFC Cambridge Process[138] and, as supported by reaction thermodynamics (See **Table 2.2**), was found to be

completely reducible at potentials far more anodic (>1 V) than the formation of Ca metal.

Table 2.2 – Oxygen ionisation potentials (E^o) of select metal oxides in an example chloride electrolyte at 800°C and 900°C, calculated using thermodynamic data[120] on the basis $E^o_{Ca^{2+}/Ca} = 0$ V

Electrode Reaction	E^o (V)	
	800°C	900°C
$\frac{1}{2} O_2 + 2e^- = O^{2-}$	2.68	2.62
$NiO + 2e^- = Ni + O^{2-}$	1.97	1.95
$\frac{1}{3} Fe_2O_3 + 2e^- = \frac{2}{3} Fe + O^{2-}$	1.77	1.75
$\frac{1}{3} Cr_2O_3 + 2e^- = \frac{2}{3} Cr + O^{2-}$	1.23	1.21
$\frac{1}{2} TiO_2 + 2e^- = \frac{1}{2} Ti + O^{2-}$	0.76	0.74
$\frac{1}{2} CeO_2 + 2e^- = \frac{1}{2} Ce + O^{2-}$	0.46	0.45
$\frac{1}{2} ZrO_2 + 2e^- = \frac{1}{2} Zr + O^{2-}$	0.38	0.37
$\frac{1}{2} PuO_2 + 2e^- = \frac{1}{2} Pu + O^{2-}$	0.50	0.48
$\frac{1}{2} UO_2 + 2e^- = \frac{1}{2} U + O^{2-}$	0.37	0.36
$2 Li^+ + 2e^- = 2 Li + O^{2-}$	0.36	0.37
$Ca^{2+} + 2e^- = Ca + O^{2-}$	0.00	0.00

The composition of oxides (or alternative reduction targets such as sulphides[139], OCl[140–142], perovskites[81,143,144] etc...) is paramount in both the species produced during the electrochemical reduction cascade and the final metallic product yielded, provided the favourable reaction conditions are present for these processes to occur. As the metal phases begin to form they tend to combine to give their respective alloys, interestingly often at temperatures far below their melting points making the FFC Cambridge Process of topical interest for the fabrication of very high melting 'super-alloys' - for instance W-Ti[145] and Ti-6Al-4V. Specific examples of FFC Cambridge Process application and fundamental electrochemical and physical mechanisms behind its performance are given in the following sections.

2.3.2   The Electrochemical Mechanism

The primary focus for the early years of investigation into the FFC Cambridge Process was to understand the reactions occurring during TiO_2 reduction, whilst simultaneously applying to the process to other commercial ores and oxides. Electrochemical characterisation by Cyclic Voltammetry (CV) was initially conducted on thermally grown TiO_2 scales on a pure Ti rod within $CaCl_2$[136] where it was proposed a series of reactions occur, represented by **Equations 2.23**, **2.24** and **2.17**, coupled with a disproportionation of the titanium sesquioxide (**Equation 2.25**) produced during **Equation 2.23**.

$$2TiO_{2(s)} + 2e^- \rightarrow Ti_2O_{3(s)} + O^{2-} \qquad \textbf{2.23}$$

$$TiO_{(s)} + 2e^- \rightarrow Ti_{[O]} + O^{2-} \qquad \textbf{2.24}$$

$$Ti_2O_{3(s)} \rightarrow TiO_{2(s)} + TiO_{(s)} \qquad \textbf{2.25}$$
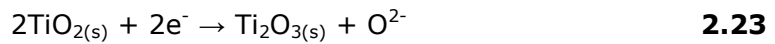
Significantly, the presence of calcium titanates could be observed in the partially reduced TiO_2 samples, suggesting a chemical reactivity between the titanium oxide and CaO, or the intercalation of Ca into the bulk oxide cathode. It was later elucidated that a series of microstructural changes occur during TiO_2 reduction involving calcium intercalation[81].
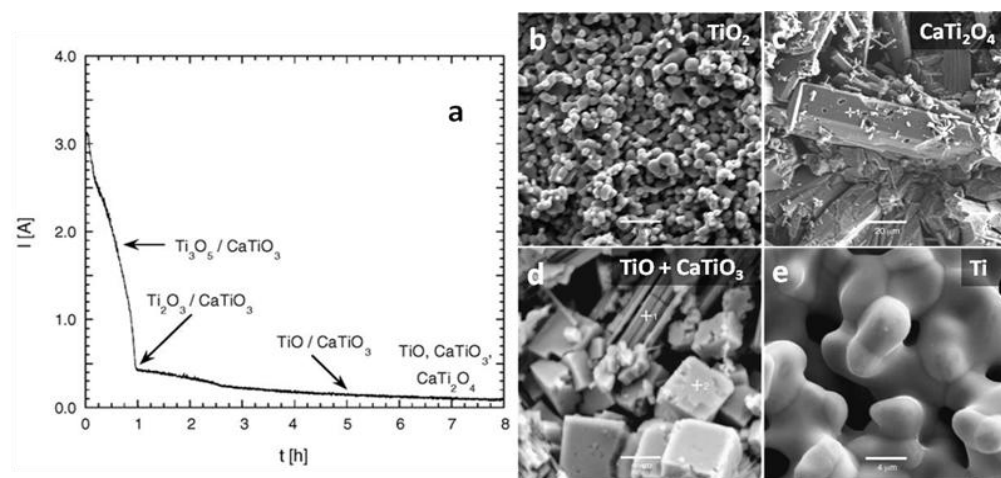
Figure 2.20 – (a) Current-time curve for the electroreduction of TiO_2 in molten $CaCl_2$ at 900°C, with compositional information given. SEM micrographs of preform microstructure after (b) 1 h, (c) 12 h, (d) 52 h and (e) 120 h polarisation[81].

A complete current-time plot from electrolysis for TiO_2 reduction in molten $CaCl_2$ at 900°C over 8 hours is shown in **Figure 2.20a**, coupled with the SEM micrographs of the observed variety of microstructural components produced over a larger reduction duration (**Figure 2.20b-e**).

The results from the 120 hour long TiO_2 electrolysis, including microstructural and elemental analysis, led to the suggested complex reduction pathway (**Equations 2.26-2.32**), involving repeated iterations of calcium inclusion at progressively higher Ti:O ratios.

$$5TiO_{2(s)} + Ca^{2+} + 2e^- \rightarrow Ti_4O7_{(s)} + CaTiO_{3(s)} \qquad \textbf{2.26}$$

$$4Ti_4O_{7(s)} + Ca^{2+} + 2e^- \rightarrow 5Ti_3O_{5(s)} + CaTiO_{3(s)} \qquad \textbf{2.27}$$

$$3Ti_3O_{5(s)} + Ca^{2+} + 2e^- \rightarrow 4Ti_2O_{3(s)} + CaTiO_{3(s)} \qquad \textbf{2.28}$$

$$2Ti_2O_{3(s)} + Ca^{2+} + 2e^- \rightarrow 3TiO_{(s)} + CaTiO_{3(s)} \qquad \textbf{2.29}$$

$$CaTiO_{3(s)} + TiO_{(s)} \rightarrow CaTi_2O_{4(s)} \qquad \textbf{2.30}$$

$$CaTi_2O_{4(s)} + 2e^- \rightarrow 2TiO_{(s)} + Ca^{2+} + 2O^{2-} \qquad \textbf{2.31}$$

$$TiO_{(s)} + 2(1-\delta)e^- \rightarrow Ti_{[O]\delta} + (1-\delta)O^{2-} \qquad \textbf{2.32}$$
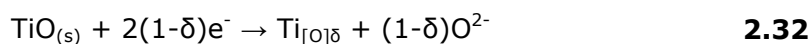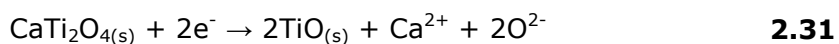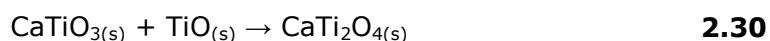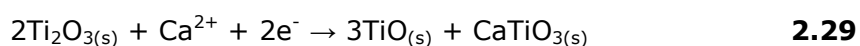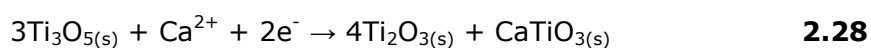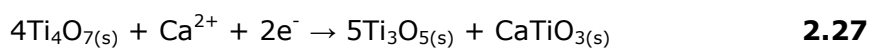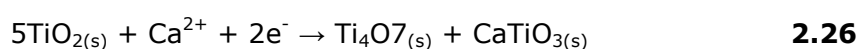
From **Figure 2.20a**, the transition of phases via **Equations 2.26-2.28** appears to occur rapidly despite a significant microstructural and chemical shift, whereas a prolonged period of transformation at a low current response is observed for Ti_2O_3 reduction. The low current coupled with difficulty in final reduction was attributed to the drastic change in crystal structure required from Ti_2O_3 to TiO. $CaTi_2O_4$ reduction to TiO and then to Ti via **Equations 2.31** and **2.32** remain rate limited by the capacity to diffuse oxygen away from the pellet interior.

Useful thermodynamic predictions can be organised in such a way to be visually intuitive whilst helping to predict the reduction hierarchy of a given feed material. These predominance or 'Littlewood' diagrams[146], while only

providing a theoretical approach to conditionally derived species formation, can be readily validated by direct measurements of the oxoacidity of a molten salt melt and consequently may prove powerful tools for investigating reduction behaviours of given materials. For the Ti-O-Ca system, a first juncture was attempted in 2005[147] based on the work of Littlewood, the diagram was later revisited to incorporate specific chloride systems[148] and is shown in **Figure 2.21**.
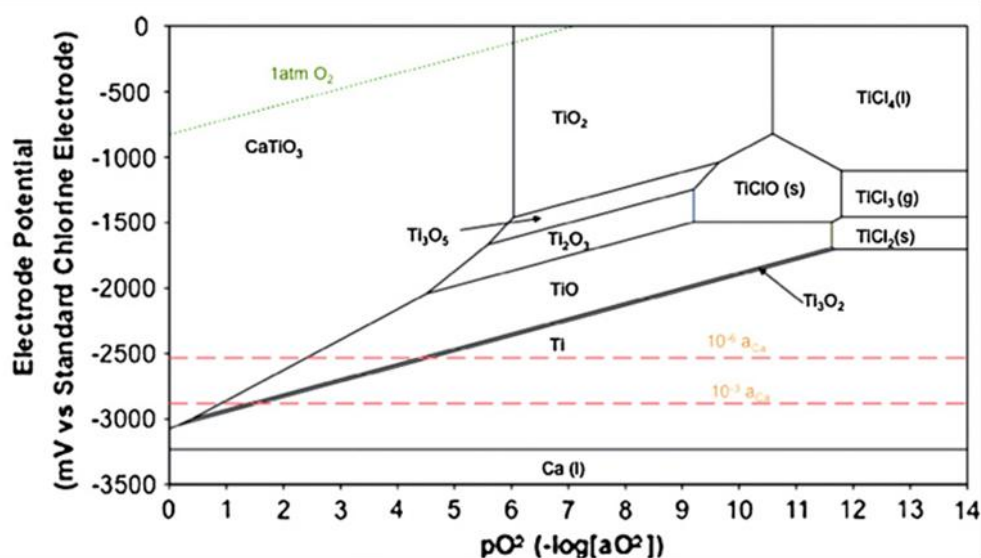
Figure 2.21 – Electrochemical predominance diagram for the Ti-O-Ca-Cl system at 900°C[148].

Figure 2.21 highlights that under high oxygen saturation within the electrolyte and even within the bulk oxide pellet (e.g. pO^{2-} value of 0 to 4.6 at 2.0 V); TiO_2 will indeed chemically react with CaO to form $CaTiO_3$, a material which is broadly stable under a range of ionisation energies and high oxygen activities. What was particularly insightful from this work however was the unequivocal confirmation of the theorised reduction pathway by a live, in-line crystallographic analysis of TiO_2 electrolysis. The resultant XRD spectrum is given in **Figure 2.22a** and inferred atomic oxygen % at different incremental distances from the current collector (i.e. reduction depth) in **Figure 2.22b**.
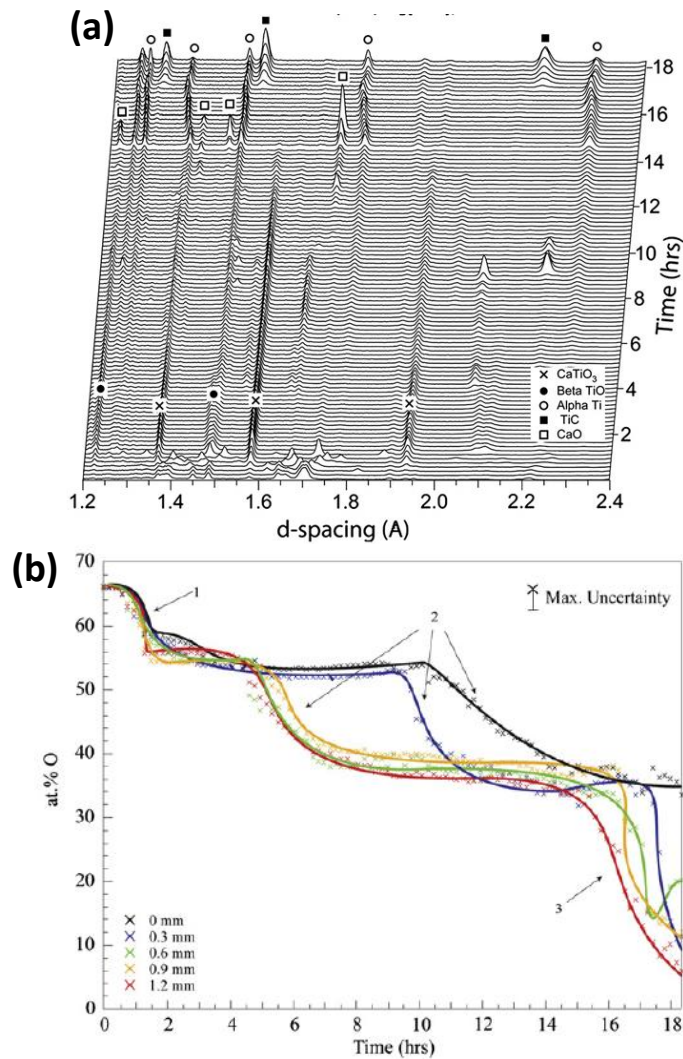
Figure 2.22 – (a) Time resolved XRD spectra of reduced TiO_2 showing phase evolution at 1.2 mm from pellet core (0.3 mm from the surface) and (b) inferred oxygen content of pellet at different depths over the duration of electrolysis[148].

The obvious benefit of in-situ analysis is the removal of external influencing factors introduced following end of electrolysis and before ex-situ analysis, leaving a direct, time-resolved comprehension of the reduction procedure. The voltage was ramped at a rate of 0.5 mV/s up to 3.1 V, yet the presence of calcium titanate could be observed after only 1 hour suggesting the chemical interaction between CaO and TiO_2 is indeed present and at a voltage far below that required for metallic Ca production. The XRD spectra shown in **Figure 2.22a** clearly shows a transitioning matrix of compounds, from an early introduction of $CaTiO_3$ and formation

of partially reduced TiO to the later stage (after 14 hours) production of α-Ti and at extended durations, the appearance of titanium carbide (TiC).

It has been demonstrated that avoiding calcium intercalation during reduction, for those feed materials liable to interact with a molten salt cation, can be partially achieved by premeditated physical manipulation of the pellet properties prior to electro-reduction (i.e. control of pressing and sintering parameters). In one case, TiO_2 precursors were prepared by sintering at 1200 $^{\circ}$C for 2.5 h leading to a porosity of between 15-16 %[149]. This was much less than the 'standard' porosities applied in the region of 25-40 %, for example prepared using PVA/PVB and PVB binders and sintered in air at 1100 $^{\circ}$C for 2.5 h[81]. The current-time curve produced via electrolysis of these dense samples was markedly different in appearance to those of a higher porosity, notably having some of the many current waves predictably observed in standard conditions absent. Ideally the dense pellets restrict a thermodynamically favourable calcium-incorporation due to the lack of void space to accommodate the associated volume change of phases (TiO_2 has an *abc* lattice cell volume of 0.1263 nm^3 whilst $CaTiO_3$ has a volume of 0.4583 nm^3 [150]). $CaTiO_3$ could still be observed in the product samples after electrolysis, however in quantities much less than could be expected given a larger porosity sample. This lower porosity TiO_2 sample is given in **Figure 2.23a** following sintering to yield a dense pellet with a highly interconnected structure.

Figures 2.23b and **2.23c** are optical micrographs following the reduction procedure for the TiO_2 pellet in **Figure 2.23a**, which offer a visual indication as to the species present. The authors apply the images in conjunction with analytical XRD, SEM and EDS for the following arguments: (1) a well-defined reduction pathway occurs for TiO_2 given the used experimental conditions and (2) a lack of significant quantities of $CaTiO_3$

was formed, particularly on the pellet surface. Instead unreduced TiO_2 and highly ordered Magnéli phases are the dominant core feature, for example Ti_8O_{15}, produced via small inclusions of Ca^{2+}, as in **Equation 2.33**
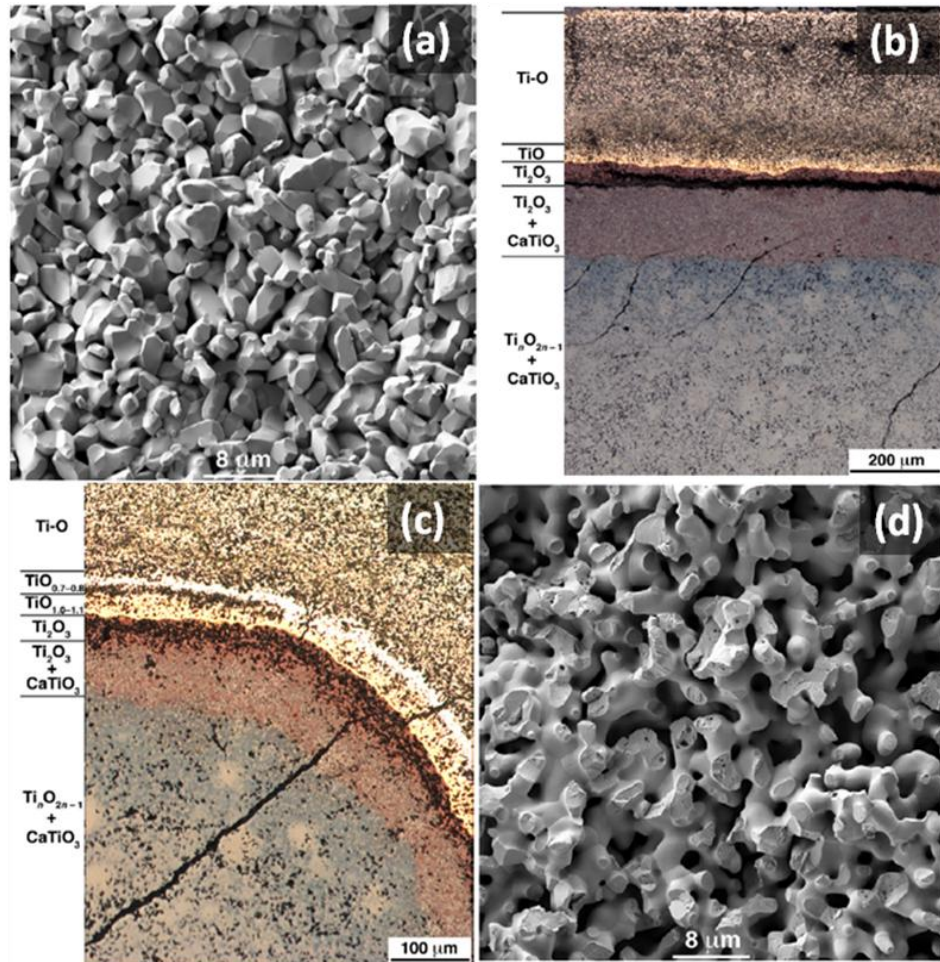
Figure 2.23 – (a) Dense sintered TiO_2 feed prior to electrolysis. (b) and (c) optical micrographs of a TiO_2 sample analysed after 10kC and 20kC charge passed respectively. (d) SEM image of a metallic Ti product with 6200ppm oxygen after electrolysis for 32 hours[149].

$$9TiO_{2(s)} + CaO \rightarrow Ti_8O_{15} + CaTiO_3 \qquad \textbf{2.33}$$

Other works using the TiO_2 benchmark for FFC Cambridge reduction have suggested that an opposite approach may work to increase efficiency, evaluated in terms of total charge consumed versus oxygen removal. In these papers electro-deoxidation improvements could be achieved by increasing porosity[94] or with the ex-situ 'perovskititation' to prevent in-situ formation of $CaTiO_3$[151]. Ex-situ perovskititation was achieved in solid state

by pressing and sintering fine, ball milled powders of TiO_2 with CaO or $Ca(OH)_2$ for 5 hours at 1300°C, as in **Equation 2.34a and 2.34b**;

$$TiO_2 + CaO = CaTiO_3 \qquad\qquad \textbf{2.34a}$$

$$TiO_2 + Ca(OH)_2 = CaTiO_3 + H_2O \qquad\qquad \textbf{2.34b}$$
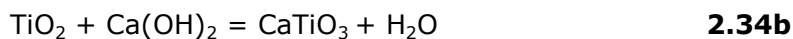
The 'perovskititation' precursors outperformed the pure TiO_2 pellets both by more readily reducing to a pure metallic phase at a lower voltage (from bypassing Ca intercalation) and in much shorter time scales, although during reduction will introduce excess CaO into the electrolyte.

2.3.3   Physical Considerations

Enhancement of internal and surface porosity has been frequently linked to improvements in efficiency of electroreduction. A mechanism has been proposed to consolidate this phenomena, termed the 3-Phase-Interline (3PI) model, it concerns the progression of reduction through an insulating cathode and is illustrated in **Figure 2.24**[121].
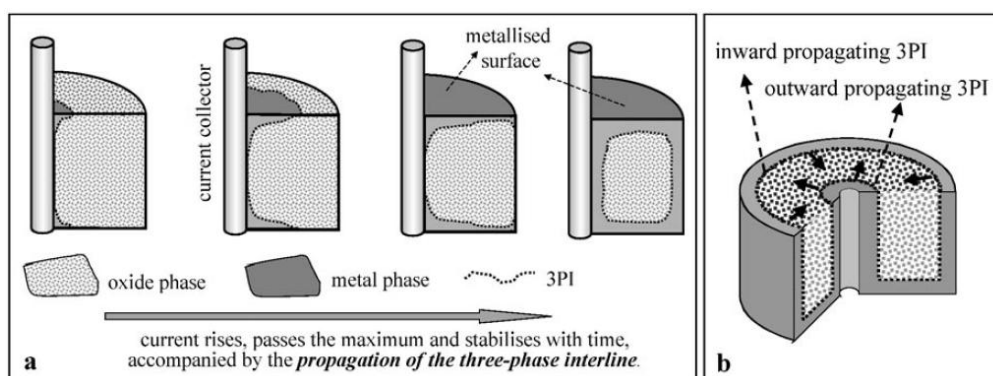
Figure 2.24 – (a) Macroscopic model of the proposed 3-Phase-Interline reduction mechanism[121].

During electroionisation of a given oxide material, three physical regions must be considered on a local scale that determine the viability of reduction beyond the thermodynamic feasibility. These are: (1) an electrical contact to the oxide electrode, (2) the oxide electrode itself and (3) the electrolyte to host and transfer produced oxygen ions. The spatial

region where these three interfacial points converge is known as the three-phase interline. Current understanding, as highlighted in **Figure 2.24**, is that reduction of insulating electrodes begins at the initial 3PI boundary, at the junction between current collector and electrode (metal|oxide phase), provided the electrolyte can infiltrate this region. Reduction progression occurs outwards, as the insulating cathode becomes more conductive the 3PI continually shifts as more of the pellet is reduced[152].

Clearly the porosity is a crucial parameter in the effectiveness of this progression, determining the availability of electrolyte to within the bulk oxide electrode. Equally, the larger the volume of electrolyte within the insulating pellet, the greater the saturation point of oxygen ions and faster the diffusion of oxygen into the bulk electrolyte for discharge on the anode. As discussed above, maintaining a low oxoacidity is paramount to avoid objectionable parasitic reactions that effectively act as electron sinks, limiting reduction efficiency and potentially retarding further reduction. It should be noted here that simply allowing the greatest possible porosity, for instance by using a fugitive porogenic agent, may not guarantee the most effective reduction conditions. Some researchers consider there to be mathematically derived optimal porosity, specific to a given feed oxide[94,153]. Additionally the requirement for mechanical strength of green forms often necessitates sintering, and depending on the intended application metallic phases a porous product may be undesirable (requiring further densification or grinding for conventional powder metallurgy).

In concert with the underlying macroscopic features of insulating feed electro-deoxidation by the FFC Cambridge Process, understanding of the physical transitional changes on the atomic scale have been rigorously investigated[121,154,155]. The microscopic renewal and propagation of the metal oxide surface during TiO_2 electroreduction derives from the removal

of the large oxygen atoms (126 pm for O^{2-} versus 74.5 pm for Ti^{4+} based on a hard-sphere model[156]) leading to the continual aggregation of metal atoms, shown in **Figure 2.25**.
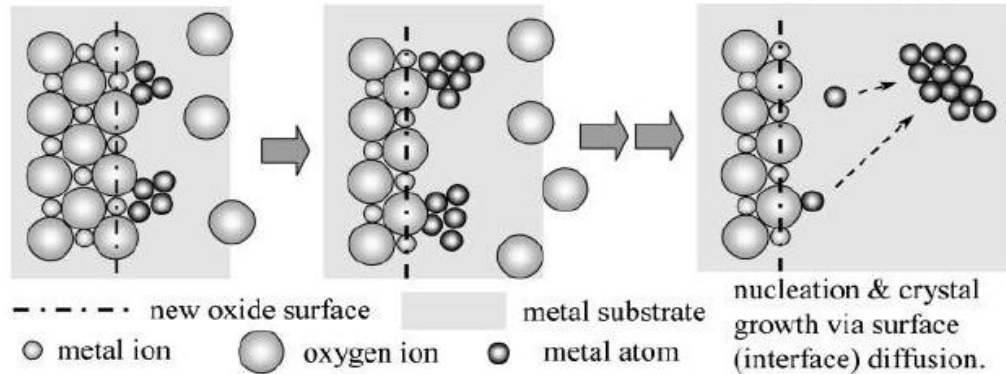
Figure 2.25 – Illustration of the surface diffusion and nucleation of metallic atoms claimed to occur during electroreduction of an oxide precursor[155].

As indicated in **Figure 2.25**, the electroreduction process gradually leads to gaps between the metal clusters and between the produced metal and new oxide surface. A 2D growth model was interpreted based on the requirement of metal atoms to diffuse along the surface (interfaces) as opposed to the unlikely cases of transfer through the molten salt or by solid diffusion. The nucleation of the metallic atoms can be predicted to form spherical particles, as spheres are the least energetic form for liquids and isotropic solids, particularly for solids of a very small size. Therefore metals produced by the FFC Cambridge Process are theoretically more likely to form in spherical or nodular shapes (depending on the shape of the precursor particles), which is in excellent agreement with experimental observations. In the case of Cr_2O_3 nodules were formed when the oxide powders were sufficiently small (< 1-2 μm), however these then coalesced into larger cubic shapes[155]. The change was attributed to the differences in preferential growth of some crystal planes over others due to the variance in atomic packing density and hence surface energies, leading to a conversion of the initial spherical nuclei to more regularly shaped crystals.

In addition to various metals discussed above, the ability to produce semi-conductors has been investigated by electroreduction. Succeeding incipient work of FFC Cambridge Process reduction using solid quartz plates[157], a quartz sheath was formed around a solid tungsten current collector, then subject to polarisation in a three electrode cell at +0.3 V vs. Ca/Ca^{2+} in CaCl$_2$ at 900°C (**Figure 2.26a-d**)[152]. The total extent of reduction was monitored intermittently over a short duration (850s) to assess the rate of 3PI propagation and, indirectly, the conductivity of formed silicon.
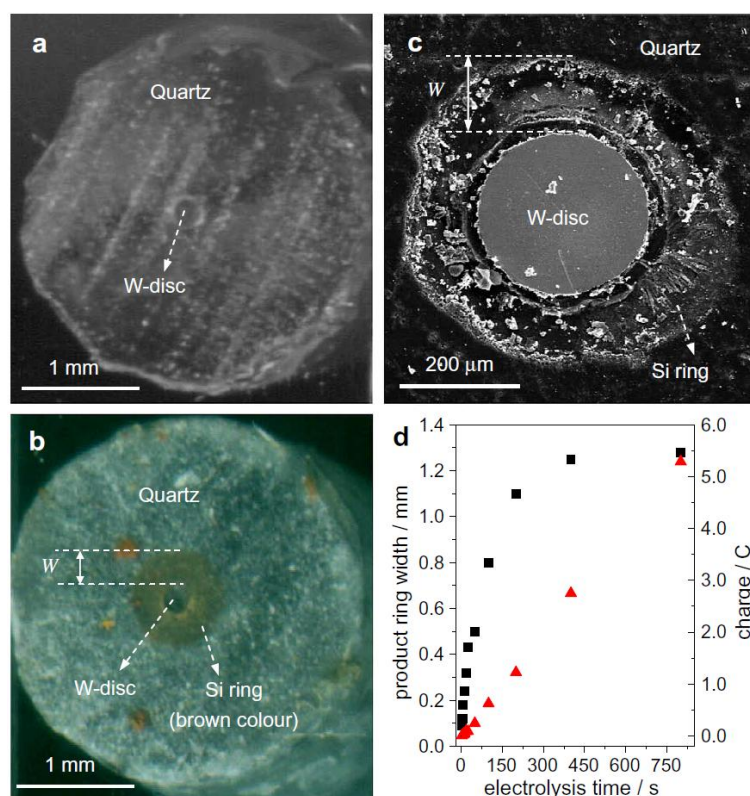
Figure 2.26 – (a) and (b) optical microscope images of the face of a W-SiO$_2$ electrode before and after electrochemical reduction by the FFC Cambridge Process. (c) Higher resolution SEM image of the W-SiO$_2$ electrode following reduction. (d) Plots of charge (triangles) and width of the created Si ring versus time[152].

It's clear from the images taken following reduction (**Figure 2.26b and 2.26c**) that metallisation to a porous silicon ring occurs radially outwards from the current collect at the point of the 3PI. Of particular interest is that following the initial linear relationship between reduction depth and time, a rapid decrease in the rate Si formation occurred after 450 s and at a

distance of approximately 1.2 mm from the W current collector. This was reportedly a consequence of the increase in effective interfacial surface area caused by the rapid removal of oxygen (developing open porosity) coupled with an increase in resistance polarisation through the expansion of generated silicon (at a resistance of 28.2 Ω cm)[158,159].

Collectively the above discussion colludes to the relatively rapid initial reduction of an oxide pellet at the original 3PI interface. This stage proceeds across the outer surfaces, where the rate of reaction is uninhibited by the formation of O^{2-} that can readily and quickly enter the bulk electrolyte phase. However as reduction continues inwards, diffusion of oxygen ions becomes the rate limiting factor, coupled with the non-negligible increases circuit and electrolyte (electronic and ionic) resistance across the reduced or partially reduced regions of the pellet i.e. the iR drop. A considered cathode design is therefore needed in order to maximise electrical contact and to ensure optimal electrolyte saturation, parameters which are examined in Chapter 4. Experimentally this behaviour can be demonstrated in the current-time curves for electrolysis of oxides pellets. An initial high current response is generated during the early stage of electrolysis as this reflects the prompt metallisation of the pellet surface. From this point reduction must continue inwards with a steady decline in reduction surface area accompanied by a decrease in current. Intriguingly, the current-time plots can be vastly different for different materials, even if recorded under identical experimental conditions. Cr_2O_3 for example has been observed to undergo a single-step six electron transfer to give pure Cr metal[160], as by **Reaction 2.35**.

$$Cr_2O_{3(s)} + 6e^- \rightarrow 2Cr + 3O^{2-} \qquad \textbf{2.35}$$
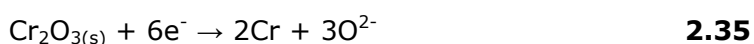
Consequently the lack of suboxide formation and from chromium exhibiting limited oxygen solubility, reduction is controlled by an idealised 3PI

mechanism. More recently, mathematical models were developed in an attempt to ascertain a better appreciation to the rate of oxygen removal and hence improve the commercial desirability of the FFC Cambridge Process[161]. As this was extended to electrodes comprised of solid SiO_2 wrapped in Ni foil, the relationship of a more negative applied potential resulting in faster reduction was only apparent until approximately -0.85 V (vs. Ag/AgCl reference electrode). At more negative potentials than this resulted in a 'cathodic passivation' attributed to a rapid oversaturation of oxide concentration in the local environment, and consequently a precipitation of CaO hindering further reduction[159]. The FFC Cambridge Process' ability to generate metallic forms in such a unique and beneficial way makes this technique ideal to utilise as a means for the selective reduction of various spent fuel components and superior to that of reduction via metals. By avoiding the necessity of metallothermic reduction of target oxides required by current pyrochemical processing, the molten salt electrolyte can be maintained and correspondingly the current efficiency and cost of such a process is more amenable. Investigating application towards nuclear reprocessing is therefore a highly worthwhile endeavour and will be pursued in this thesis.

2.4   Electrochemical Actinide Speciation

The major goal of advanced nuclear energy systems is to have an effective fuel utilisation strategy for waste minimisation and increased energy yields. Here a brief overview of the pyroprocessing approach to LWR spent fuels for the desirable reduction of UO_2 and other TRUs is given, with the recent advances using the FFC Cambridge Process explored. The basics of electrorefining are also covered, including the present operational procedures and inadequacies which remain to be addressed.

2.4.1 Individual and Co-reduction of TRU Oxides

As UO_2 is currently the only natural fuel source for conventional operational nuclear reactors and is by far the most abundant material within spent fuel, a considerable amount of research has been accrued on various aspects of UO_2 to U reduction under transitional conditions. Electroreduction of metal oxides by FFC reduction usually occurs in molten $CaCl_2$ (>800°C), and similarly the drive for commercial pyroprocessing has almost exclusively been using a LiCl electrolyte (~650°C). There are significant tangible benefits of developing a lower melting point system, including the ability to maintain metallic plutonium as a solid (mp: 639°C), and so the LKE (mp: 352°C[162]) has been modelled and experimentally studied as a possible candidate for UO_2 reduction. **Figure 2.27** shows the calculated predominance diagram for UO_2 in 1 wt% Li_2O-LKE at 520°C, in addition to a current-time plot of a pelletised UO_2 cathode reduction with XRD analysis[76].
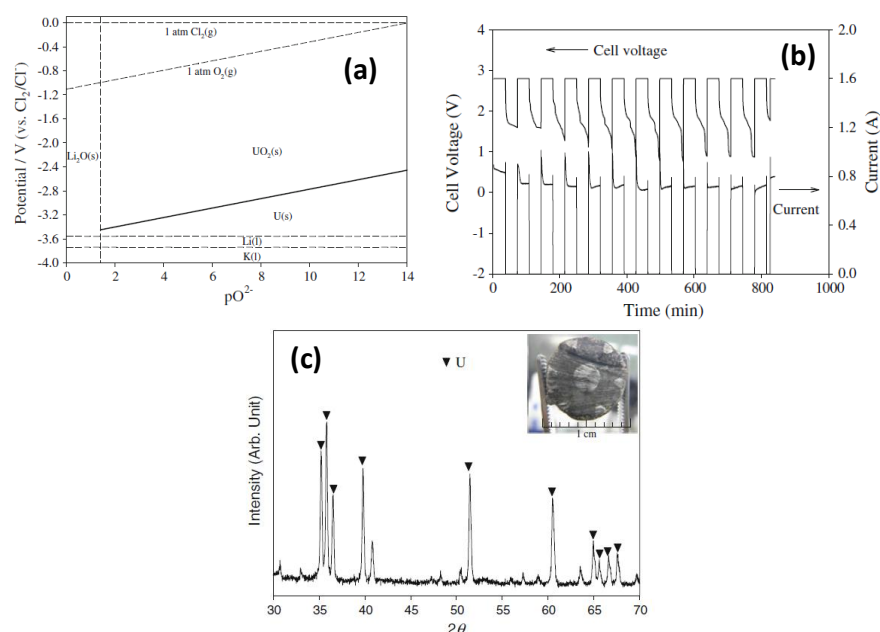
Figure 2.27 – (a) Thermodynamically predicted predominance diagram for U-O in a LiCl-KCl-Li_2O molten salt at 520°C. (b) Plot obtained from the periodically interrupted electrochemical reduction of UO_2 in LKE-1mol% Li_2O and (c) XRD results and image of the U product from (b)[76].

The applied cell voltage in **Figure 2.29b** (2.8V) was carried out in a mode of cyclical interruption, which allows the measurement of the open circuit potential of the cell during reduction and helps gain a better insight into the reaction mechanisms occurring. The authors note that the cathode potential of the cell during the first 600 minutes of reduction was more negative than the Li deposition potential of -1.27 V vs. Li-Pb, and so they claim the reduction of UO_2 to U occurred via a cycling of Li^+/Li (**Equations 2.2** and **2.35,** e.g.[44]).

$$UO_2 + 4Li = U + 2O^{2-} + 4Li^+ \qquad \textbf{2.35}$$
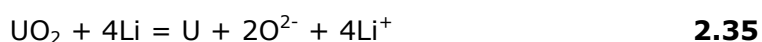
The inability to produce a pure U sample at potentials below Li deposition was also mentioned, despite the predominance diagram in **Figure 2.27a** suggesting the formation of U occurring more favourably than either Li or K metal at nearly all oxygen activities. This would indicate that either the presence and reduction of Li_2O is disruptive to the direct electrochemical reduction of UO_2, the temperature and therefore thermodynamic favourability of UO_2 reduction in LKE at 520^oC is insufficient or the calculations used to produce the predominance diagram was not correct. Others have sought to develop diagrams of the same system (as well as Pu-O) in both LKE and $CaCl_2$, but have produced very different conclusions[75] (see literature for relevant calculations and methodology). In **Figure 2.28a**, the direct electrochemical transition between UO_2 and U in LKE at 500^oC can only occur at pO^{2-} values greater than approximately 7 and at potentials close to the decomposition point of the molten salt.

Comparatively the electrochemical stability of UO_2 in $CaCl_2$ at 800^oC is more favourable for direct reduction (**Figure 2.28b**), being possible according to the available thermodynamic data[120] at any likely oxygen activity within the melt. While it may be possible to electrochemically reduce UO_2 to U in LKE it is clearly more challenging than in $CaCl_2$. One

solution considered in this thesis is the option of avoiding PuO_2 and other TRU oxide reductions but maintaining the ability to reduce UO_2; and so circumventing one of the requirements for operating in lower melting point systems (avoiding liquid Pu formation and the need for a liquid cathode).
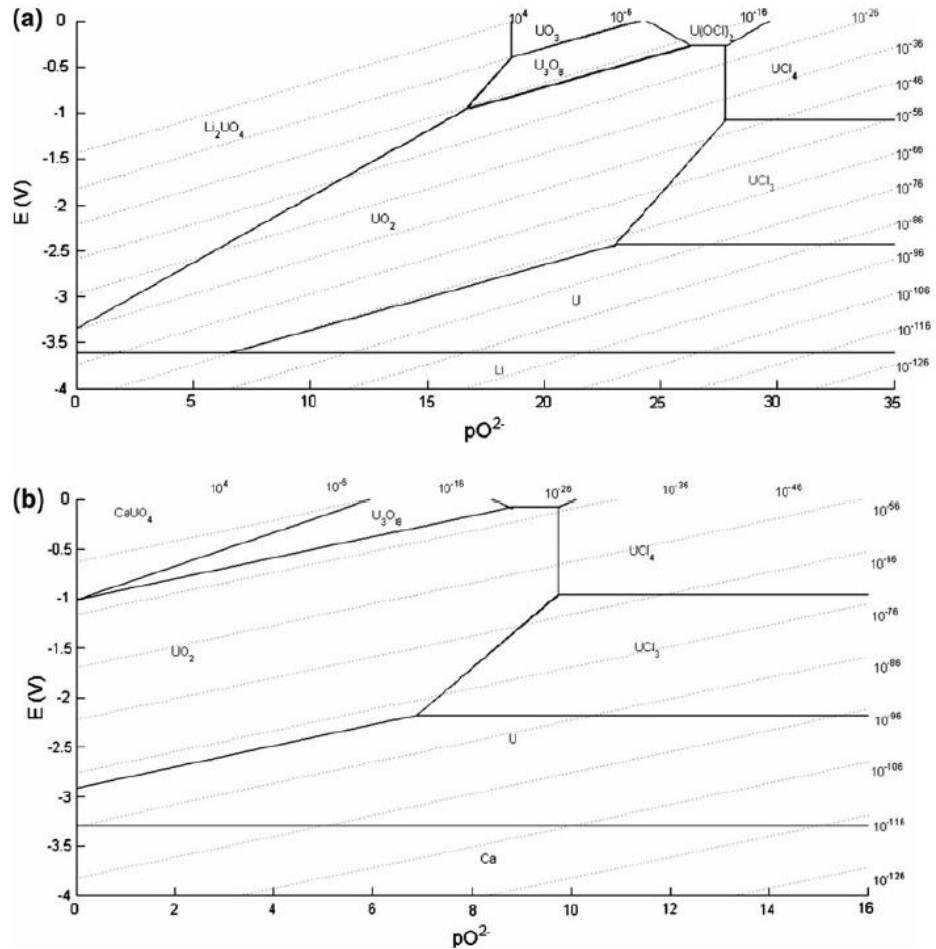
Figure 2.28 – Predominance diagrams of uranium species in (a) LKE at 500°C and (b) $CaCl_2$ at 800°C[75].

Subsequent electrochemical verification of the predominance diagrams above in LKE at 450°C was performed, with the additional benefit of in-line synchrotron Energy Dispersive X-ray Diffraction (EDXD) to monitor elemental shifts in real time[163]. UO_2 was loaded into a Metallic Cavity Electrode (MCE, first reported in[160]) with CVs recorded presented in **Figure 2.29** that evidently suggest the electrochemical reduction of UO_2 is (a) possible in LKE at lower temperatures (peak C1) and (b) is a single step,

four electron transfer process. Linear Sweep Voltammetry (LSV) at a sweep rate of 0.1 mV s^{-1} was used during the in-line synchrotron analysis, results of which are given in **Figure 2.29b**. At a potential of approximately -2.51 V (vs. Ag|Ag$^+$ ref) there is a fundamental transition from UO_2 to U as observed from the intensity shift of each species, occurring in region 'b', approximately 40 mV more positive than Li reduction. The total absolute quantity of U detected however was rather small and this was argued to be a consequence of an increase of O^{2-} ion concentration in the melt from the initial reduction and which were not consumed at the counter electrode.
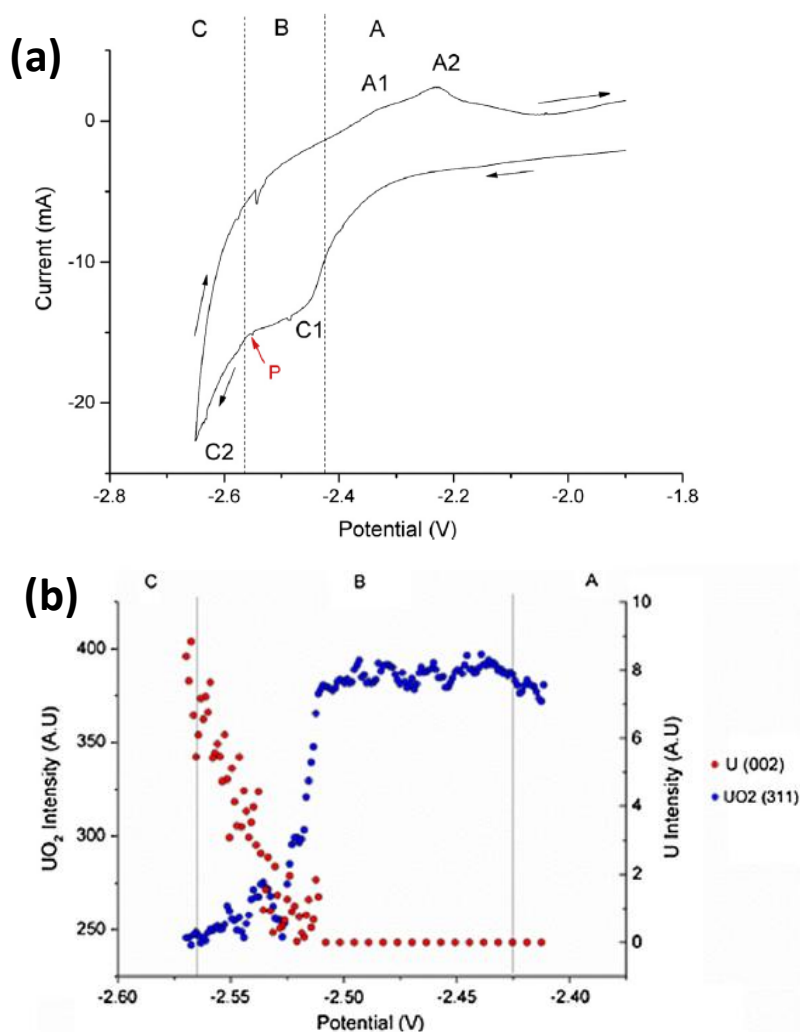
Figure 2.29 – (a) CV of UO_2 filled MCE vs. Ag|Ag$^+$ in LKE at 450°C (10 mV/s) and (b) synchrotron EDXD peak intensities for UO_2 and U during a 0.1 mv/s LSV[163].

Consequently the new pO^{2-} value brought about a discontinuation of UO_2 electroreduction, the root cause of which was suggested to be the tight packing density and low tortuosity of the UO_2 loaded MCE preventing effective oxygen ion diffusion out of the bulk oxide powder.

Other work on pure UO_2 reduction in both $CaCl_2$ and LiCl has produced contrasting results, claiming that in LiCl uranium metal could be produced completely in a potential range of +0.15 V vs. Li^+/Li, and that underpotential deposition of Li was barely observed[35]. The conclusions drawn from using a $CaCl_2$ electrolyte at approximately 800ºC was the unfortunate densification of a surface metallic U skin on the bulk UO_2 pellet, preventing further discharge of oxygen and the full reduction of UO_2. This also corresponded to a higher current efficiency for using LiCl than $CaCl_2$, however there was no further discussion or consideration given to developing a more porous pelletised UO_2 preform to help tackle the issue of coherence in the higher temperature $CaCl_2$ melt. More recently a return to examining the suitability of $CaCl_2$ for UO_2 reduction by the FFC Cambridge Process produced much more favourable results, showing that even highly dense (94 %) UO_2 pellets could be reduced to U up to a thickness of 3 mm and with multiple examples of 1 mm thick UO_2 disk electrodes, reduction proceeded readily[164].

In spent fuel where multiple species are present destined for co-reduction, an introduction of alloying or further structural and solid state diffusion related phenomena may occur. MOX fuel particles (9.45 wt% PuO_2) were pressed into pellets and subject to cathodic polarisation in LiCl at 650ºC, maintained at a voltage below 2.8 V to avoid molten salt decomposition[165]. The electrolysis was performed in 6 cycles of 30 minutes reduction and 30 minutes relaxation, the resultant pellet showed only partial reduction after ex-situ SEM imaging and elemental analysis. The authors recognise the

influence of a propagating 3PI reduction and that the reduction of the grain boundary between particles occurs initially to form a porous and coral-like network structure. U distribution within the pellet remained fairly homogenous, albeit with an expected higher density in the reduced region. Pu however shows pronounced variety, with fine 'spots' in the reduced region at a relatively lower concentration than the original stoichiometry. At the reduced/non-reduced interface there is a thin condensed layer of Pu at a concentration of 1-3 wt% which the authors attribute to the higher rate of reduction for UO_2 vs. PuO_2, excluding and precipitating the Pu to the surface of MOX grains.

An attempt was made to electrochemically reduce highly porous SIMFUEL particles[166], which are characterised by having bulk uranium oxide content with multiple components representative of fission products commonly found in LWR spent fuels. **Table 2.3** highlights the various species and at what concentrations were present in the fabricated SIMFUEL particles at an open porosity of 70.7 % (as in contrast to commercial fuels at 5 % or porous UO_2 pellets at 35-40 %[85,167,168]). Electroreduction progressed in LiCl at 650°C using a variable decreasing voltage between 3.2 V and 3.0 V until either 150 % or 250 % of the theoretically required charge for a full reduction had been supplied. Results suggest a very high reduction extent of UO_2 after 250 % charge supply (**Figure 2.30**) as well as >50 % of the oxide rare earths present. The highly porous nature of the preform was advantageous in reducing the spent fuel surrogate species. However even at 150 % theoretical charge supplied for complete oxide reduction, the majority of lanthanide oxides remained unreduced.

Table 2.3 – chemical composition and surrogated oxides added to UO_2 powder as fission products to form porous SIMFUEL[166].

Impurity groups	Elements in SIMFUEL	Surrogate oxides	Element composition[a] (wt.%)
	U	UO_2	94.459
Dissolved oxides	Y	Y_2O_3	0.084
	La	La_2O_3	0.226
	Ce (Pu, Np)[b]	CeO_2	1.342
	Nd (Pr, Sm)[b]	Nd_2O_3	1.111
	SUM		2.763
Dissolved oxides/oxide precipitates	Sr	SrO	0.150
	Zr	ZrO_2	0.667
	Ba	$BaCO_3$	0.326
	SUM		1.143
Metallic precipitates	Mo	MoO_3	0.624
	Ru (Tc)[b]	RuO_2	0.566
	Rh	Rh_2O_3	0.064
	Pd	PdO	0.290
	SUM		1.544
Oxide/metallic precipitates	Te	TeO_2	0.091

[a] With 60,000 MWd/tU burnup and 5 years of cooling.
[b] Element in parenthesis was replaced by the element in the front of parenthesis.
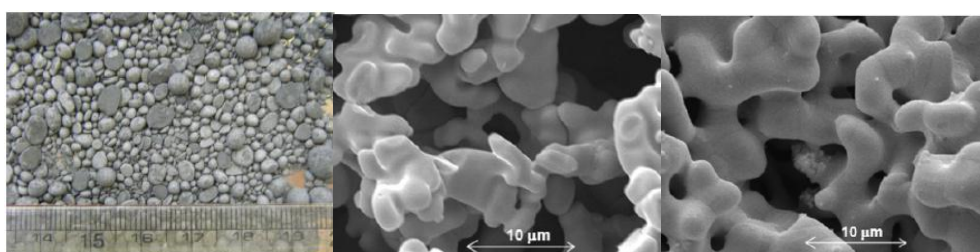
Supplied charge[a] (%)	Fuel	Elements									
		U	Rare earth				Noble metal				
		U	Nd	Y	La	Ce	Zr	Mo	Ru	Pd	Rh
150	Metal (%)	88	6	6	4	5	7	83	36	77	58
	Oxide (%)	12	94	94	96	95	93	17	64	23	42
250	Metal (%)	99.6	53	74	50	51	55	78	86	100	67
	Oxide (%)	0.4	47	26	50	49	45	22	14	-	33

[a] Supplied charge (%) to the theoretical value for the complete reduction of the SIMFUEL particle.

Figure 2.30 – Photograph of SIMFUEL particles after sintering (top left), SEM imaging of highly porous SIMFUEL before reduction (top middle) and after (top right). Post analysis electrochemically reduced SIMFUEL particles (bottom)[166].

2.4.2   Electrorefining of Spent Fuel Species

In a similar manner to electroreduction, research on electrorefining for pyroprocessing has progressed mainly through simplified systems of perhaps two or three metallic species. The fundamentals of nuclear directed electrorefining have been known for some time now, developed

originally by Argonne National Labs for the refining of U-Pu-Zr spent fuels from fast neutron reactors to extract plutonium for weapons manufacture, and later as a power source for domestic deep space satellite programmes. Since the movement towards civil nuclear application, and the adoption of oxide fuels for moderated reactors, electrorefining has been adapted as a secondary step following electroreduction to selectively partition the bulk metallic uranium and other actinide presence in reduced spent fuels.

Traditionally electrorefining has been achieved by placing the pelletised metallic fuels into a perforated anode basket and anodically oxidised by the sequential deposition of U onto a solid cathode, and of minor U quantities (from a gradual decrease in activity) along with other actinides into a liquid Cd cathode (**Figure 2.31**). Noble metals and rare earths remain in the molten salt due to their general redox stability compared to actinides.
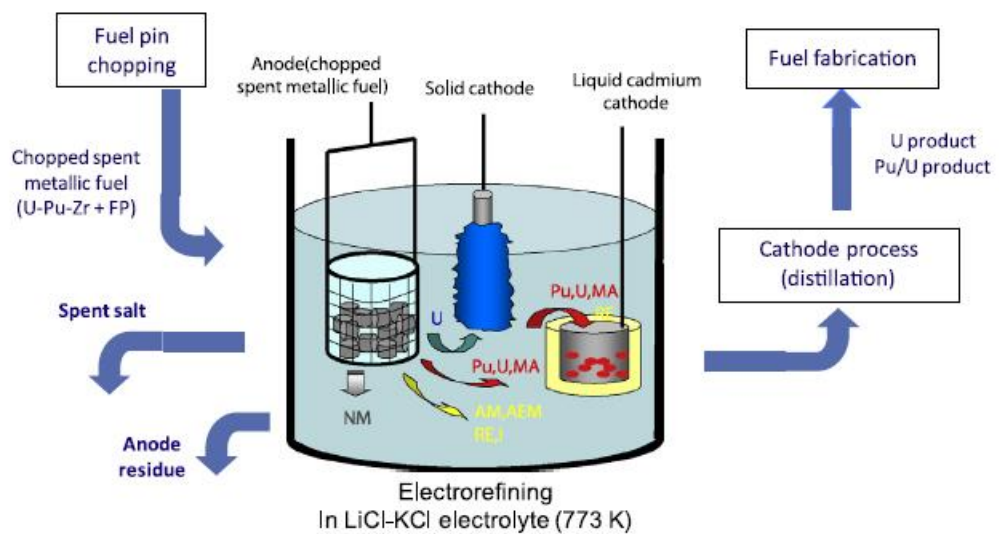
Figure 2.31 – Schematic diagram of a typical electrorefining cell used for metallic fast reactor fuels[169].

A comprehensive electrochemical analysis of the behaviours of U^{3+} ions onto a solid Mo electrode and Liquid Cd electrode has also been performed[170]. **Figure 2.32a** provides an overview of the processes occurring while electrorefining proceeds on both a solid and liquid cathode,

this information was assessed transiently by CV (**Figure 2.23b and 2.32c**), to observe the deposition potentials, but also by Electrochemical Impedance Spectroscopy (EIS) to better appreciate the interfacial processes related to cathodic reduction of U^{3+} ions (**Figure 2.32d and 2.32e**). The CV curves for each electrode are broadly shown to be diffusion controlled, given the linear relationship between cathodic current peak ($I_p{}^C$) and scan rate (v), however the rate of current increase is more nominal for the liquid cathode suggesting a slower diffusion rate of U^{3+}.

Impedance spectra for the U^{3+}/U redox couple on the solid cathode at -1.4 V shows charge transfer begins to take over diffusion based processes and metal ions discharged onto the electrode surface are incorporated into the metal at growth sites along the edges of the nucleus[171]. The features of the liquid electrode are markedly different involving complex aspects of U diffusion into the liquid Cd until a solubility limit is reached, changing interfacial properties (restricted diffusion, 'M' on the equivalency circuit), after which dendritic growth similar to a solid cathode form. The selectivity to deposit U onto a solid cathode versus Ce in an LKE electrolyte at 500°C was investigated via the dissolution of both UCl_3 and $CeCl_3$[172]. CV results in individual melts containing $CeCl_3$ and UCl_3 are shown in **Figure 2.33a** and **2.33b** respectively. The large difference in electrodeposition potentials permitted the use of -1.65 V vs. Ag/AgCl to selectively recover U metal which alloyed with the SS rod (**Figure 2.33c** and **2.33d**).
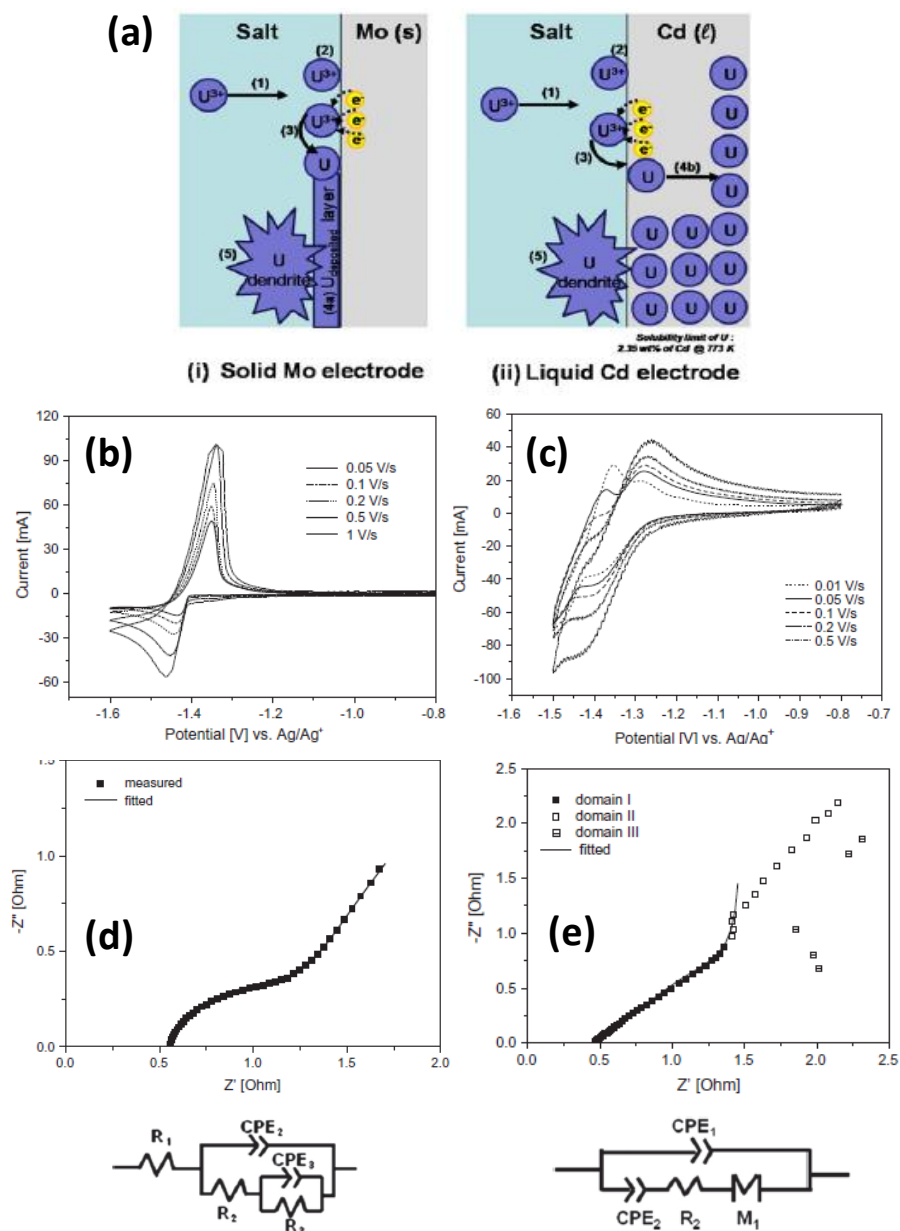
Figure 2.32 – (a) Concept of the molten salt/electrode interfacial processes at a (i) solid Mo electrode and (ii) liquid Cd electrode. (1) U^{3+} Mass transfer, (2) adsorption, (3) charge transfer, (4a) formation of U deposited layer, (4b) atomic diffusion of U, and (5) formation of dendrites on electrode surface. Variable scan rate CVs of 1 wt% (0.167 mol%) UCl_3 in LKE on a (b) Mo electrode, and (c) Cd electrode. Nyquist plots and equivalency circuits for 1wt % UCl in LKE between 5 kHz and 0.1 Hz on (d) an Mo electrode at -1.4 V, and (e) a Cd electrode at -1.37 V[170].
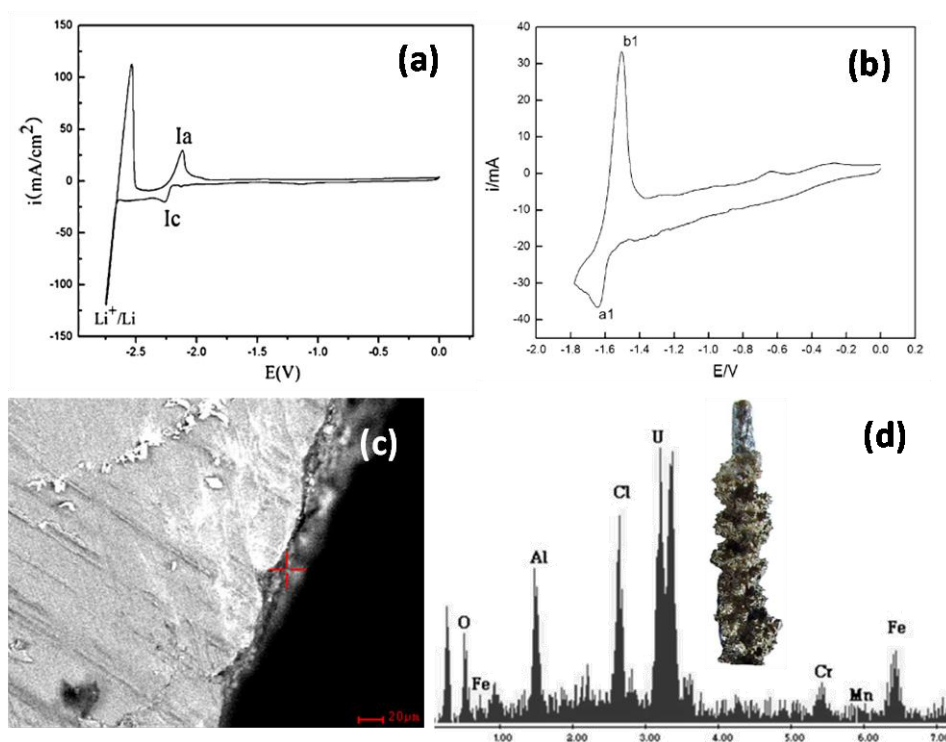
Figure 2.33 – CVs, 100 mV/s at 500°C in (a) LiCl-KCl-CeCl$_3$ (C$_{CeCl_3}$: 2.0 x 10^{-4} mol/cm^3) and (b) LiCl-KCl-UCl$_3$ (C$_{UCl_3}$: 9.1 x 10^{-6} mol/cm^3). (c) SEM image and (d) EDS spectrum of the interface between cathode and deposit, inset in (d) is an image of the removed pure U cathode deposit[172].

Recent advancements in the ability to forego a liquid cathode for actinide accumulation have been made within the specific application of fast reactor fuel production[173]. Speciation of lanthanides and actinides on a reactive solid Al cathode was investigated in LKE at 500°C using 3.176 g of 'METAPHIX-1' irradiated fuel (2 wt% Actinides; Np, Am, Cm, and 2 wt% rare earths; Nd, Ce, Gd, Y, and the remainder U) in a SS basket as the anode. Refining was initiated at a cathodic cut-off potential of U metal deposition (-1.48 V vs. Ag/AgCl, according to the authors), prior to the corresponding start of lanthanide-aluminium alloy formation (-1.35 V for Nd-Al)[174]. Example galvanostatic runs are given in **Figure 2.34**, along with optical microscopy images of the aluminium cathode after those respective runs.
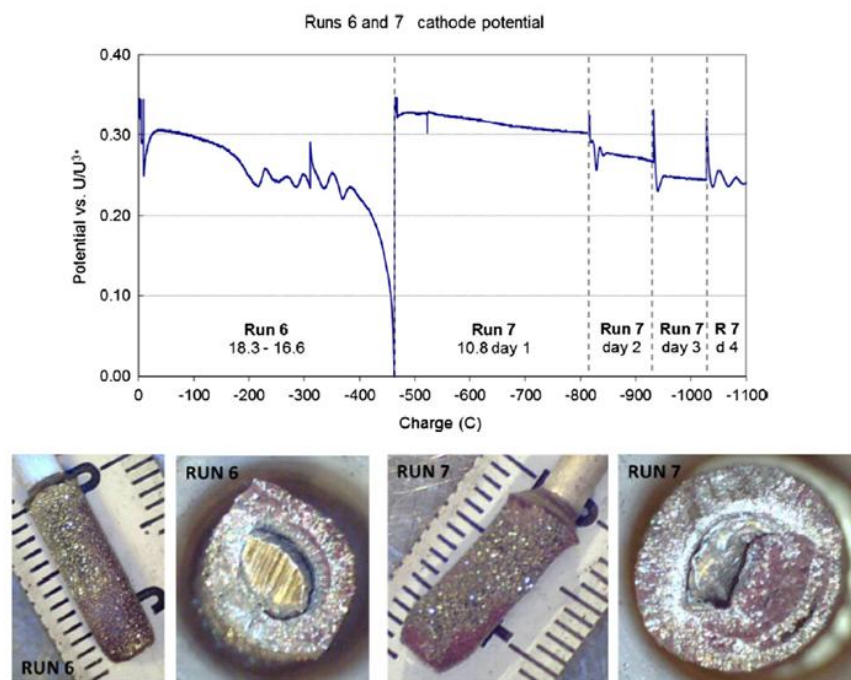
Figure 2.34 – Galvanic plots of cathode potential developments for two select runs by the authors (6 and 7) indicating total charge consumed and duration of each run (top). Optical microscope images of the corresponding $AnAl_x$ alloy deposits on the surface of the Al cathode after electrolysis (bottom)[173].

Maximum attainable deposition thicknesses were also analysed as a function of the current density. The thickest deposits were at the lowest current densities, indicating the need to use a large surface area and thin cathode during electrorefining for larger scale processes. The selectivity was shown to be impressive, where a minimum of 99.89 % of actinide recovery was achieved after a charge passed of 415 C, predominantly in the form of $AnAl_3$ alloys. Whilst the reactivity of Al metal creates the possibility of co-depositing multiple TRU species, it also means a secondary step of electrowinning is still required before further cathode processing. Additionally, assuming the commercialisation of pyroprocessing of LWR spent fuels; the entire method presupposes a fully reduced metallic composite produced from a successful reduction of the oxide spent fuel.

2.4.3   Consolidation of Electroreduction and Electrorefining

Literary work on the prospect of combing electroreduction and electrorefining in the same molten salt system using solid electrodes, maintaining elemental selectivity and proliferation resistance has been notably absent. In essence, the very simple operation could proceed as follows: using a three electrode cell with an oxide spent fuel working electrode and graphite/inert counter electrode, a precise electrochemical reduction is carried out for the production of the desired metal(s) (U, Pu, Np, Zr etc...). The metal/oxide mixture is then subject to a reverse polarisation, where the counter electrode is replaced with a suitable solid metal alternative to for the deposition of ionised metals from the working electrode. **Figure 2.35** gives a simple schematic of the above description for a homogenously mixed two oxide system.
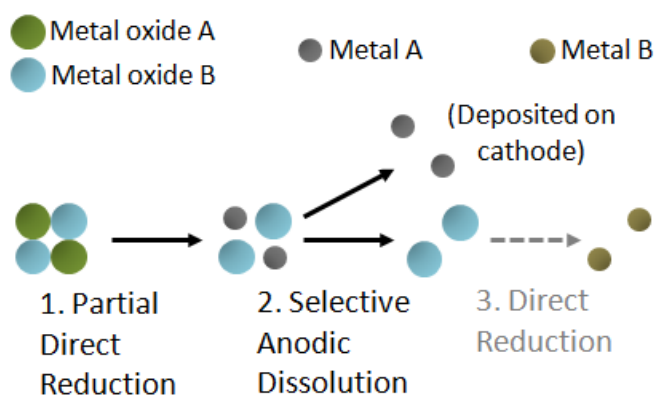
Figure 2.35 – Simple two-oxide representation of the idealised mechanism behind partial direct reduction and selective anodic dissolution partitioning of spent nuclear fuels.

After the initial metal partitioning, the remaining oxides at the working electrode can undergo a second selective reduction for the next desired species (or the co-reduction of U-Pu, for example) to be anodically stripped to a fresh metal counter electrode for recovery. As outlined in the review of electrorefining technology, should the presence of rare-earth FPs prevent a UO_2 specific reduction, then during the reversal of electrode polarisation U

metal (and other actinides) should still be preferentially deposited. The lack of apparent effort into such a method is perhaps due to the relative stage of technological infancy, or the perceived difficulties in applying such precise potentials required for a successful partitioning. Indeed perhaps one of the greatest limiting factors to the development of selective electrochemical reductions comes in the ability to maintain accurate potentials over considerable durations, directly related to the stability of a reference electrode. Being able precisely and selectively partition species from a bulk oxide matrix clearly needs to be examined initially, however the capacity to achieve a high yield recovery of spent fuel species is also an important concern. Should the idealised mechanisms suggested here prove plausible, it could mean a significant leap forward in pyroprocessing in terms of simplification, cost reduction and overall safety.

2.5 Conclusion

The basics of established pyroprocessing technology undertaken in world research institutes have been given in this chapter. Specifically details regarding the current advancements being made towards a better understanding, efficiency and yield of recoverable materials for both current MOX fabrication and next gen fast metallic fuels has been covered. Key considerations in the materials and electrochemical challenges which face the future of pyroprocessing have also been highlighted, lending to the positive prospects of nuclear power as a prominent and stable global energy source. Given such a diverse range of obstacles, the development and adoption of a commercial electrochemical reprocessing technology is not without adversity. However the perceived and partially demonstrated benefits of implementing a pyroreprocessing system discussed here have the potential to be invaluable for short to long term global energy supply.

Chapter 3

Methodology

3.1 Experimental Design

Experimentation using high temperature molten salts presents an immense challenge to materials scientists, and as such the application of suitable materials and the development of appropriate working practices are crucial. It has been nearly 10 years since the first system for molten salt work was installed at the University of Nottingham's Department of Chemical and Environmental Engineering and subsequently the first molten salt experimentation began. Throughout the duration of this research the system in place has been subject to constant critical review, with *ad hoc* optimisation changes to the cell design, operational parameters and electrolysis conditions. Some of the implemented evolutionary changes to both materials and procedures will be discussed throughout remainder of this thesis where appropriate to the specific challenge or situation encountered. Descriptions of the active materials instrumentation and processes performed at the National Nuclear Laboratory (NNL) will also be included in this section where different from those performed at the University of Nottingham.

Electrolytic experiments were performed in a bespoke retort created by rolling 6.55 mm thick 304 SS (A H Allen Steel Services) which was then TIG welded to create a tube of 138 mm inner diameter (ID) and 875 mm in length. A base plate, flange and water cooling jacket made from the same material were all welded to the tube to form the complete retort, and a lid made separately which was manually attached. A crucible containing the dried electrolyte was positioned inside the retort, placed upon a SS stand

to best position the crucible within the effective heating zone of the furnace. Prior to heating, the retort was sealed by placing a rubber or neoprene o-ring between lid and flange and bolted tight by 8, 5 mm hex head bolts. Holes of various diameters drilled into the lid to allow insertion and removal of electrodes, and as viewing windows, were sealed by silicon bungs to prevent gas leaking. Two short SS pipes were also welded perpendicular to the x-y plane of the lid to act as the argon inlet and outlet respectively. These pipes also have specific controlled geometry to provide favourable flow properties within the cell and prevent blockages from salt vapour condensation at operational temperature. During heating and electrolysis all holes were sealed tight, hence the retort hermetically sealed, and subject to a pure argon atmosphere.

The entire retort was placed inside a resistance element heated, raised vertical split-tube furnace (Vecstar Furnaces Ltd.) with a 160 mm bore and 500 mm tube length that is capable of heating to 1200°C. An 8 segment programmable furnace controller (2416CG Eurotherm) was used to control furnace operations. The small gap between furnace and retort was sealed at the top by use of an alumina fibreboard (ZIRCAR Ceramics) to limit heat losses. As the height of the retort was much longer than the furnace, the region of the retort subject to the highest temperature was a significant enough distance from the top or bottom welds, preventing severe corrosion where it is most likely to occur. **Figure 3.1a-c** provides images of the furnace/retort electrochemical experiment setup following the set-up procedure and onset of heating.
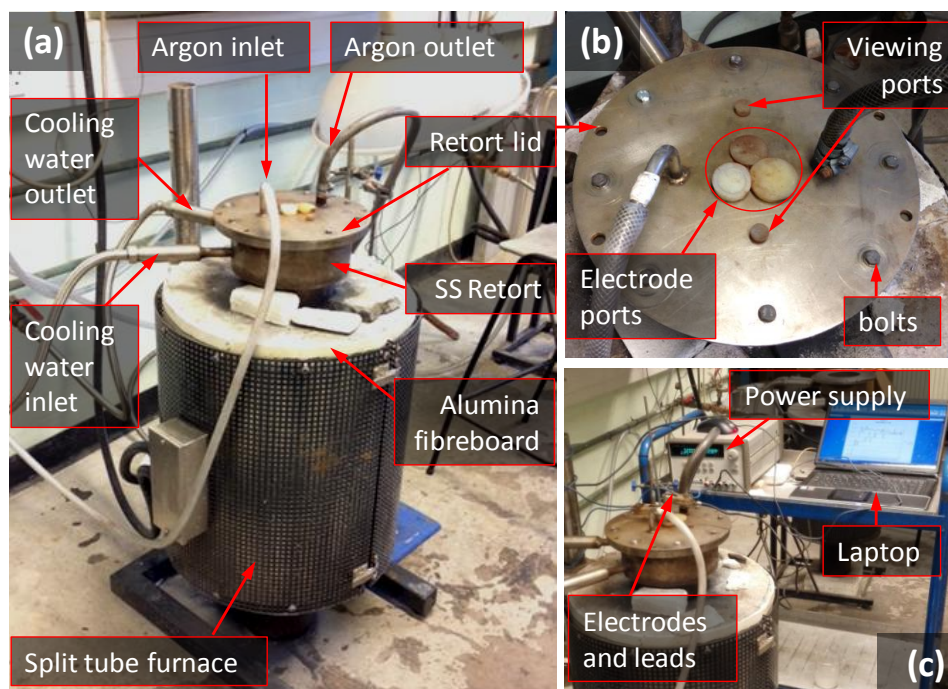
Figure 3.1 – Annotated photographs of electrochemistry setup. (a) Fully sealed retort within the furance during heating, (b) top-down view of the lid showing port orientation and (c) the DC power supply used for electorlytic cleaning of the salt and constant cell voltage electrolysis.

The difference between the real temperature and that displayed on the furnace controller was recorded using a handheld YCT YC-727D thermometer (TC Ltd.) equipped with a 1 m long, 3-mineral insulated thermocouple (310-grade stainless steel K or Pyrosil® insulated type N). This was to allow for accurate control of the electrolyte temperature and mediate the divergence between the controller and electrolyte values. A typical heating profile employed during the heating procedure, and corresponding approximate temperature gradient from within the crucible is shown in **Figure 3.2**. Rest periods were used during ramping, the first to permit several purge cycles of Ar and attain a low oxygen content and the second to slow down the rate of temperature increase of the alumina crucible to prevent thermal stress. The argon used was of a technical grade (99.992 %, Air products Ltd.) and acted as a carrier for anodic gas discharge as well as providing a protective atmosphere.
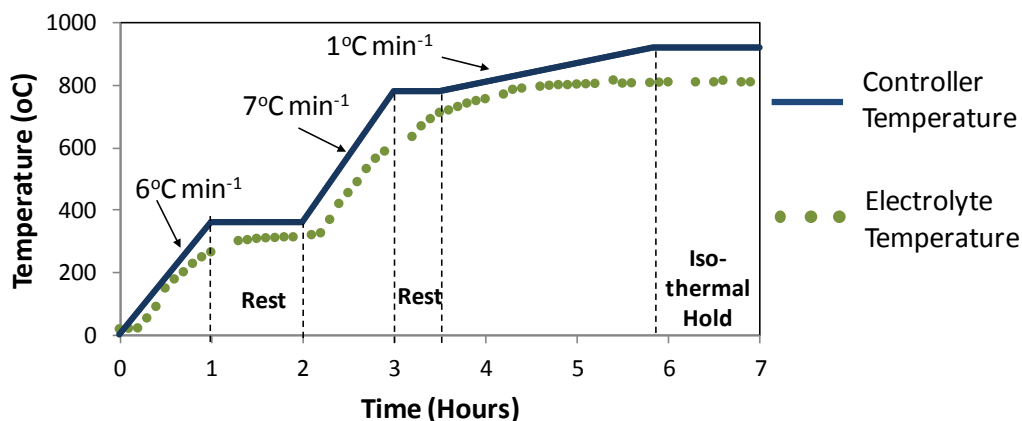
Figure 3.2 – Ramping procedure of the furnace controller and the corresponding temperature profile from within the crucible during heating.

Flow rate of the Ar was controlled by a 2-stage brass regulator (GIS Leengate) from the cylinder itself and a manual 20-200 ml/min Ar calibrated rotameter (Roxspur Measurement and Control). Off gasses were fed via the outlet into a dreschel bottle containing a mineral oil (Labovac 10" mineral oil, Jencons Ltd.), to isolate the system from backflow induced air uptake.

For non-active experiments undertaken at the NNL, a similar set up was administered; however the completed cell/furnace was housed inside a dry box under slight positive (250-500 Pa [1-2 InH$_2$O]) argon pressure with a typical moisture and oxygen content of 40ppm and 4ppm respectively. A copper based catalyst was integrated into the argon circulation as an oxygen scrubber whilst residual moisture was adsorbed via passing the atmosphere through a zeolite based molecular sieve. The retort used was a high integrity cell made from blown quartz (22 mm ID) rather than stainless steel, as to allow visual management of electrodes from outside the dry box under more precise conditions, and the furnace was both shorter and narrower to permit its accommodation. Annotated images of the retort, furnace and drybox used for non-active experiments at the NNL are shown in **Figure 3.3**.
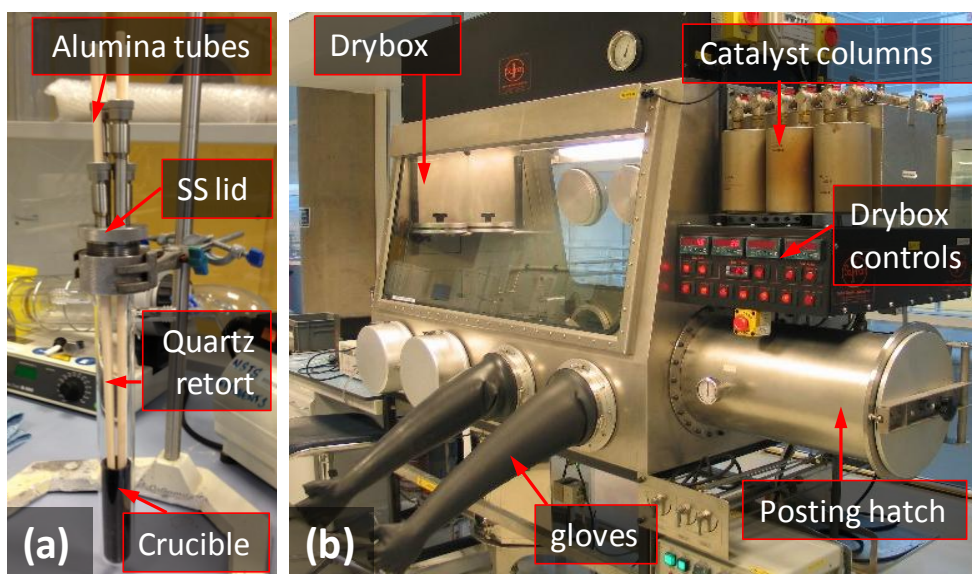
Figure 3.3 – photographs of (a) the completed quartz cell used for electrochemical experiments at the National Nuclear Laboratory. (b) The Saffron^{TM} drybox used to house the furnace and cell under a dry, low oxygen content Ar atmosphere.

3.1.1   Crucibles

In terms of materials, two options were used for crucibles: alumina (99.0 % purity, Almath Crucibles Ltd.) and carbon (both graphitic and vitreous). Steels are a common choice for bulk electrolysis; however the extent of corrosion can be severe and lead to the introduction of and possible contamination by compositional steel elements (Fe, Cr, Ni etc...). A variety of crucible sizes and geometries were also examined (**Figure 3.4**) on their contribution towards electronic conductivity (and hence current efficiency) of the electrolyte during electrolysis, discussed further in Chapter 5.
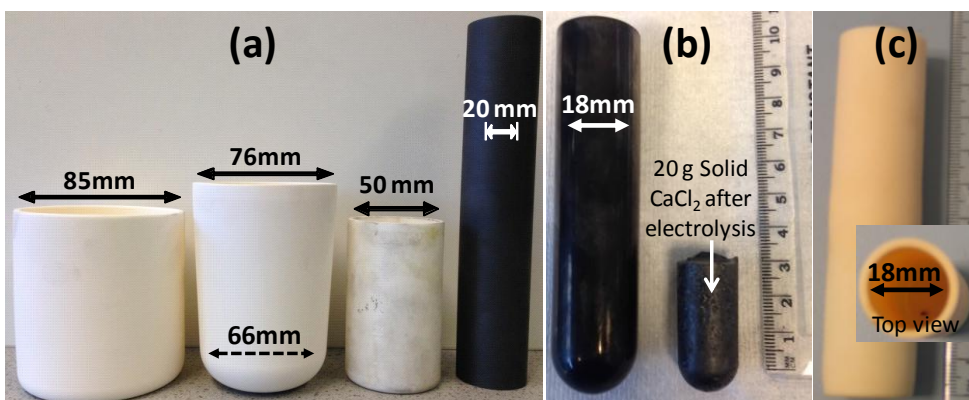
Figure 3.4 –Photographs of the (a) alumina and graphite crucibles (b) vitreous carbon (showing carbon contamination) and (c) narrow alumina crucible.

3.1.2   Counter Electrodes/Anodes

For the vast majority of work performed in this thesis, a 100 mm x 10 mm graphite rod (HK-3, Tokai Carbon Ltd.) was used as both anode and counter electrode. Other grades of graphite rods were tested (HK-1 and HK-75) but were found to succumb to degradation far more readily than HK-3, likely due to a larger grain size and open porosity. The surface porosity can aid anodic gas entrapment, leading to pitting and facilitating capillary flow of salt within the rod, whilst a larger grain size packing meant that carbon particulates were more likely to dislodge. The rods were tapped to fit a 6 mm SS rod of approximately 400 mm length, ensuring good connectivity and low contact resistance which completed the anode/counter electrode assembly (**Figure 3.5c**).

In some select experiments, attempts were made at utilising an inert material as the anode/counter electrode to avoid the issues associated with carbon contamination. A Pt wire (2 mm thick x 50 mm immersion depth, 99.99%, Advent Research Materials) was used during several CV experiments and 'Extremely Low Resistance' ELR SnO_2 rods of 10 mm diameter and 100 mm length (Glassworks Hounsell Ltd.) were employed occasionally during bulk oxide and pre-electrolysis. Finally a unique and bespoke $La_{0.33}Ca_{0.67}RuO_3$ electrode was fabricated in-house based on the suggested doping-induced p-type semi-conductive perovskite structure advocated within the literature, and tailored for specific use within molten $CaCl_2$, all counter electrodes tested here are shown below (**Figure 3.5a-d**).
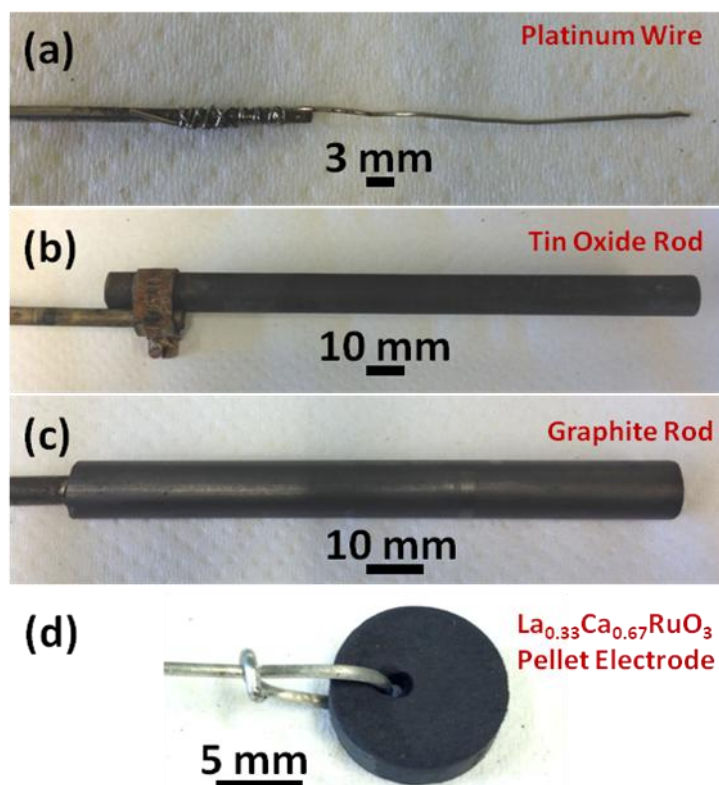
Figure 3.5 – Images of the various sacrificial and trialed inert counter electrodes fabricated and tested for electrochemical measurements in molten $CaCl_2$/LCE. Including (a) a 0.5 mm Pt wire, (b) a 10 mm SnO_2 rod, (c) a 10 mm graphite rod and (d) a 12 mm dia. $La_{0.33}Ca_{0.67}RuO_3$ conductive perovskite electrode.

As was predicted from the previous works available in the literature from various molten salts, both Pt and SnO_2 were found to be unsatisfactory within the $CaCl_2$ melt, even at temperature as low as 810°C. The Pt counter electrode suffered from an apparent lack of electrochemical inertness during anodic sweeps of CV scans and although not directly investigated here, there may have been reactions involving CaO which led to less stable or soluble species (e.g. Ca_4PtO_6[175] or $Ca_2Pt_3O_8$[176]) in a similar mechanism as described in Li_2O containing LiCl melts. The Tin (IV) oxide rods however performed comparatively well in regards to being chemically inert after prolonged exposure to the melt, but suffered from poorer current efficiencies due to limited conductivity. Additionally, as the SnO_2 rods were not fully dense, salt intrusion into the pores of the electrode could not be avoiding and consequently led to frequent stress fractures during salt

solidification making their use both costly and impractical. Further information regarding the custom designed and fabricated $(La_{0.33}Ca_{0.67}RuO_3)$ perovskite inert anode is given in Appendix 2. It is plausible the use of RuO_2 creates the mass manufacture of such an electrode prohibitively expensive; however initial experimental results provided very favourable stability characteristics.

3.1.3   Reference Electrode

To achieve a successful selective reduction it is crucial to have sufficiently accurate potential control, necessitating a mechanically robust and electrochemically stable reference electrode. Pseudo-reference electrodes, (usually in the form of metal wires) have been used in the literature and also infrequently in this work for short durations where the potential creep can be considered insignificant enough that the resultant data be valid (e.g. approximately 30 minutes at a <5 mV shift). The pseudo reference electrode used for this purpose was a 1 mm Mo wire attached to a SS rod 1.5 mm in diameter. For experiments involving larger quantities of oxide feeds, and so longer durations for potentiostatic electrolysis, a functional and unique alumina sealed Ag/AgCl reference electrode was fabricated following a modified description laid out in the literature[177] (**Figure 3.6**).

The performance of the electrode was shown to be more than satisfactory in $CaCl_2$, and surprisingly given the lower operational temperature of 600°C, in the LCE electrolyte - but was investigated further in two regards. Firstly, the internal diameter of the alumina tube was increased to 4 mm from 3 mm, increasing the interfacial area between the internal alumina wall and molten salt by approximately 30 %. The modification was to effectively decrease the overall resistance to ion conduction through the membrane wall, hence improving performance, and to increase the convenience of filling the salt into the tube before melting.
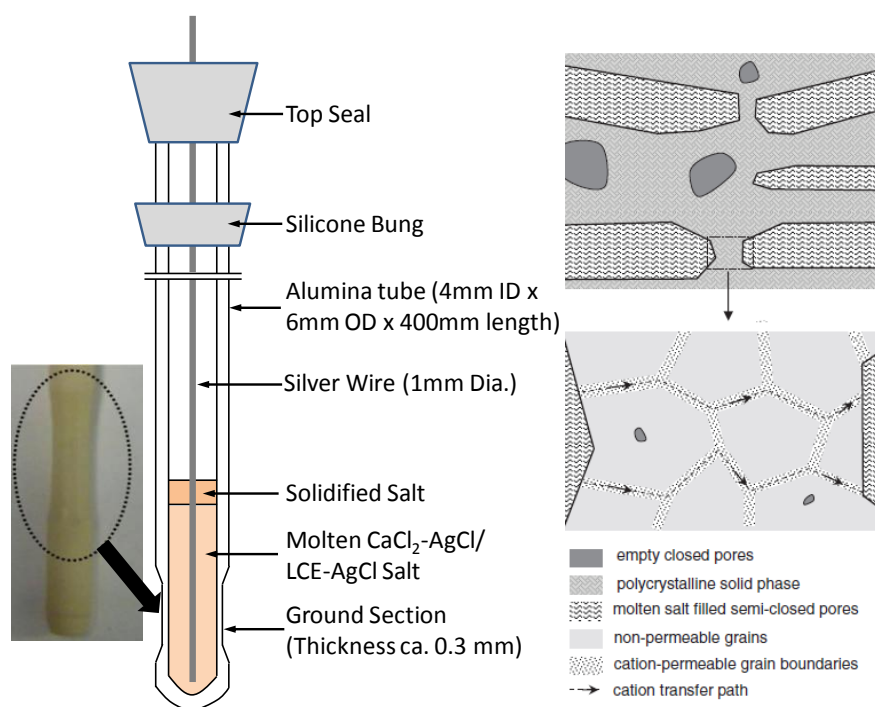
Figure 3.6 – Image and Schematic of Ag/AgCl reference electrode, with illustration of ion conduction mechanism through the alumina membrane[177].

Secondly, it is understood that $CaCl_2$ and AgCl are fully miscible at all compositions above the melting point for $CaCl_2$ (**Figure 3.7a**) so variations in the concentration of AgCl between 1 and 20 mol % were assessed in how the reference potential was affected (**Figure 3.7b**). The results show an approximate linear behaviour between potential shift and the log of Ag concentration.
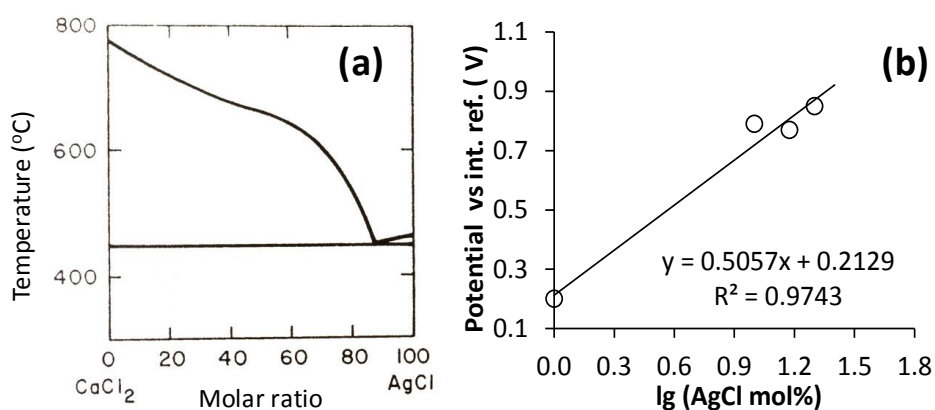
Figure 3.7 – (a) Phase diagram of AgCl and $CaCl_2$[178]. (b) Potential of the alumina membrane Ag/AgCl reference electrode as a function of the logarithm of AgCl concentration in molten $CaCl_2$ at 810°C.

A mullite sealed Ag/AgCl reference electrode was also used in some experiments where the addition of Na doping in the Al_2O_3 crystal structure is believed to aid ion diffusion through the membrane and so further increase electrode performance. Mullite however suffers chemical attack much more readily than alumina and displayed relatively poor survivability within the molten salt over periods of hours to days. Interestingly the extent of chemical attack of mullite was found to be more severe in the lower temperature LCE melt at 600^oC versus 810^oC for pure $CaCl_2$. This may be due to the influence of the smaller effective Li^+ ion size (r_{ion} = 76 pm versus 100 pm for Ca^{2+} [156]) influencing internal intergranular migration behaviour or from potential lattice destabilisation by Na displacement form chemically similar Li^+ ions. **Figure 3.8** highlights the extent of damage on the mullite sealed reference electrode recovered after 24 hours use within the LCE melt at 600^oC. For this reason the ground, alumina sealed reference electrodes were used primarily in three electrode experiments.
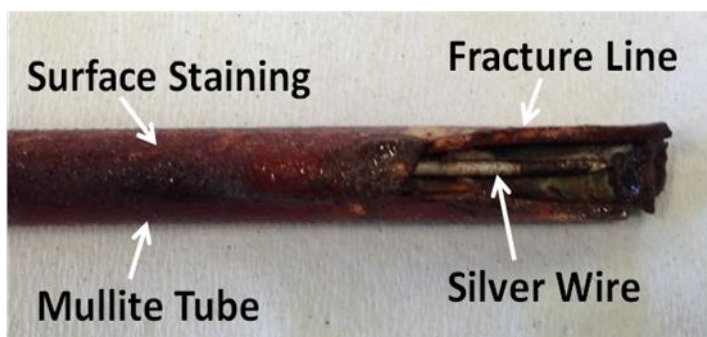
Figure 3.8 – Photograph of Mullite sealed Ag/AgCl reference electrode after removal from the LCE melt following 24 hours of use at 600^oC.

3.1.4 Electrolyte Pre-treatment

In early work performed on the redox characterisation of select metal oxides, factors effecting molten salt electronic conduction and the process of partial direct reduction and anodic dissolution were exclusively performed in a molten $CaCl_2$ electrolyte. Later, where baseline process variables were established and the desire to reduce operation temperature

became more important, a 65 mol% LiCl-CaCl$_2$ eutectic was implemented instead. These salts were chosen primarily because of their excellent stability (w.r.t e.g. CaCl$_2$ = Ca + Cl$_{2(g)}$) visually represented in **Figure 3.9**.
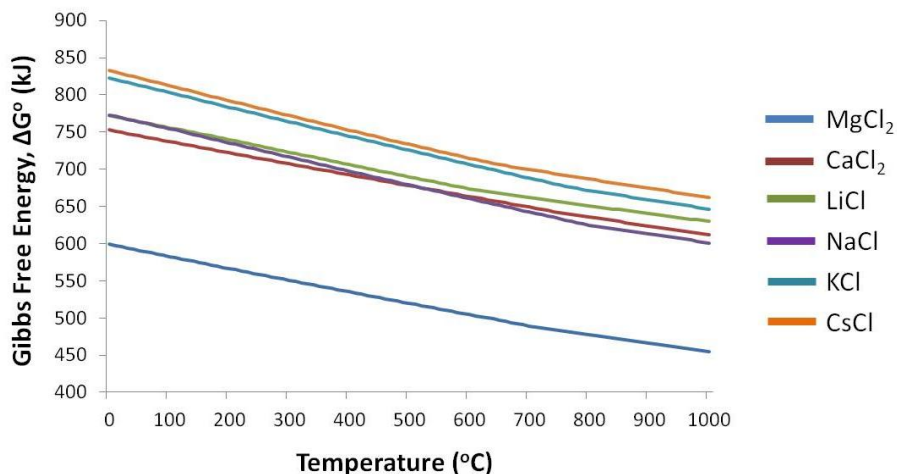
Figure 3.9 – Thermal stability of 'common' molten chlorides used as electrolytes versus temperature. Data obtained from HSC chemistry software[120].

Additional favourable characteristics include relative environmental banality and other crucial thermodynamic considerations which aid the reduction process, such as oxide solubility. Experiment ready CaCl$_2$ was prepared from the dihydrate, CaCl$_2$·H$_2$O (99 %, Sigma-Alridch) by gradual heating at a rate of 1°C min^{-1} under vacuum (ca. -96kPa) where it was held for a period of 20 h. Caution was applied in the heating rate and general pace at which drying took place, as to avoid any potential hydrolysis and the formation of undesirable HCl and excess CaO. LiCl was purchased in an anhydrous form (>99 %, Sigma-Alridch), and both salts stored in a drying oven at 60°C prior to use.

3.2 Metal Oxide Precursors

3.2.1 Feed selection and preparation

The innate difficulties of working with radioactive materials make the investigations designed here challenging without dedicated systems to store, process and dispose of the spent fuel components. Consequently, all

of the work at Nottingham proceeded using analogous electrochemical surrogates, based on the free energies for oxide reduction and redox potentials in solution, as given in **Table 3.1**. Depending on the specific chemical or electrochemical characteristics of the spent fuel to be emulated, it's possible to populate viable surrogate tables with a range of potential candidates. For example, in **Table 3.1** the most suitable electrochemical surrogate when considering actinide species in solution (useful when analysing deposition hierarchy during electrorefining) is entirely different to those for direct electroreduction of actinide oxide species. Similarly the precise defining properties that are to be investigated in a single process can lead to different suitability of a given species.

Table 3.1- Actinide surrogate matrix for spent fuel species and calculated redox behaviour in molten LiCl and $CaCl_2$ using HSC Chemistry[120].

Key Actinide	Melting Point (°C)	Valence *1	Reduction Potential		Oxide Melting Point (°C)	Oxide Reduction Potential	
			LiCl *2	CaCl₂ *3		LiCl *2	CaCl₂ *3
U	1132	+3	1.201	**1.110**	2865	0.028	**0.379**
Pu	641	+3	0.882	**0.787**	2400	0.150	**0.501**
Am	994	+2/	//	//	//	//	//
		+3	0.858	0.774	1000	0.419	0.770
Np	640	+3	1.099	1.016	2547	0.063	0.414
Cm	1345	+3	1.010	0.990	370*4	0.620	0.791
Potential Analogue Elements							
Ce	795	+3	0.625	0.554	2400	0.110	**0.461**
Sm	1077	+2/	-0.023/	-0.059/	2335	0.251	0.100
		+3	0.716	0.617			
La	921	+3	0.565	**0.482**	2315	0.215	0.136
Mg	649	+2	0.915	**0.820**	2852	0.156	0.195
Zr	1855	+4	1.651	1.557	2715	0.036	**0.387**
Ti	1668	+4	1.967	1.850	1843	0.467	0.766

*1In the presence of host metal
*2at 650°C calculated from $E_{Li} = 0V$
*3at 800°C calculated from $E_{Ca} = 0V$
*4Unstable at temperatures above 370°C

La and Mg for instance have a near identical potential difference for deposition compared to U and Pu when in solution (highlighted orange in **Table 3.1**) however the absolute value of the potential for the La and Mg is much less than the actinides. In practice, it is best to have both suitably accurate potential differences and a similar absolute reduction potential for surrogates when considering the possibility of selective partitioning by partial direct reduction. Shared chemical behaviour is also of huge importance as it helps develop a consolidated system where the consequences of species interactions can be measured and used as predictive models for active materials. For this reason CeO_2 was chosen as a surrogate for PuO_2 during electroreduction, and is widely regarded as the only viable candidate for this purpose[179].

It can be argued that with untested novel technologies, the desire to establish process feasibility would allow for the lack of adherence to these rules for initial surrogate suitability. In this manner, a large nobility difference would be useful in order to make partitioning of two oxides relatively more facile. NiO was selected as a counterpart for mixing with CeO_2 for this reason, and partitioning trialled on a 2:1 atomic % ratio in order to assess the ability to selectively remove Ni presence. In later experiments where feasibility had been established, both ZrO_2 and TiO_2 were chosen to replace NiO. ZrO_2 has a broadly similar reduction potential to UO_2, and together with CeO_2 has a nobility difference very near the real binary system of UO_2 and PuO_2 (highlighted blue In **Table 3.1**). However difficulties arising from ZrO_2 reduction due to poorer conductivity of sub-oxide and perovskite intermediates meant TiO_2 was tested as an alternative, where broadly speaking the intermediate oxide phases ($2>\delta>0$, δ = O content) show progressive increases in conductivity. For the various binary oxides used, mixing and homogenisation was achieved

by either pestle and mortar and ball-milling where deemed appropriate. When used, a planetary ball mill (Pulverisette 6, Fritsch) and a set of zirconia milling balls and bowl (250 ml bowl, 1 mm balls, 94.8 % ZrO_2, Fritsch) with the addition of iso-propanol alcohol were employed to grind quantities of up to 30 g of the oxides. On occasion, bulk preparation of TiO_2-CeO_2 pellets (in batch of approximately 50) was achieved by a slip-casting method, which is outlined further in Chapter 4.

For experiments investigating the influence of disrupting electronic field lines on molten salt electronic conductivity, a relatively simple system with well-defined redox behaviour and previous examination was ideally required. Consequently Cr_2O_3, which had been described in the literature as having a basic electrochemical reduction procedure by the FFC Cambridge Process, was used in both CV and constant cell voltage experiments. ZrO_2 also underwent the same analysis by CV to validate any potential findings beyond a single species and as it is more directly relevant to the reprocessing strategy developed here.

3.2.2   Pressing and Sintering

Situations requiring pelletised cathode electrodes were usually approached by the pressing of homogenised oxide powders into green forms using an Atlas power T8 Hydraulic Press (Specac Ltd.) which could be used with a range of bore sized moulds and dies (**Figure 3.10**).

The powder to be formed was added to the appropriate mould, between two SS dies, before a pressing force of between 1-8 tonnes applied in a single axial direction. Sintering was used on all occasions the pressed precursors were produced, as manual wrapping of the pellets to form the cathode/working electrode assembly required a significant structural integrity. The exact temperatures, sintering durations and pressing forces

were varied in an attempt to gain a better understanding of the final density and overall utility of pellets produced via different forming parameters. Throughout these tests no pore forming agents used, deemed unnecessary as the open porosity in even the most onerous conditions was sufficient to yield metallic products following electroreduction.

Figure 3.10 –Specac Ltd. T8 hydraulic press, die and moulds used for pellet synthesis from oxide powders.

3.3   Electrochemical Techniques

3.3.1   Cyclic Voltammetry (CV)

Being one of the most versatile and useful electrochemical analysis techniques, CV was used frequently in this research to determine the potential window of electrolytes, analyse salt purity and give redox characterisations of the various oxides investigated. As mentioned, the cell for CV studies consisted of three electrodes and potentiodynamic control was provided by either a PGSTAT30 Autolab potentiostat (Ecochemie) with 'General Purpose Electrochemistry Software' (GPES), an Ivium stat (IVIUM

technologies) with 'Iviumsoft' software or a 1285-model Solartron potentiostat with 'corrview2' software. Regardless of the potentiostat used, the equipment and software were controlled by a PC where qualitative data was automatically recorded. For potential controlled experiments, the voltage across the working and counter electrodes is adjusted to maintain the potential difference between working and reference electrodes, with the arrangement given in **Figure 3.11**.
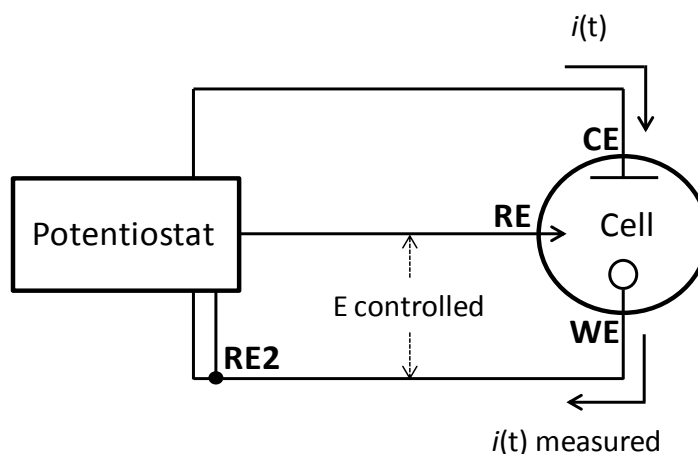
Figure 3.11 – Schematic arrangement for potential controlled experiments, such as cyclic voltammetry or chronoamperometry.

Typically in the CV tests, the potential of the working electrode was set to the open circuit potential (OCP), i.e. the voltage recorded between working and reference electrode under no external electrical loading, and therefore no current flow. From this starting point (E_0), the potential was linearly altered to a second fixed value in the cathodic direction (E_1) at a uniform scan rate (v). The exact end point of the cathodic scan was determined to be when an abrupt, linear and continuous current increase could be observed, understood to be the deposition of the molten salt cation (e.g. $Ca^{2+} + 2e^- = Ca^0$) by the decomposition of the electrolyte. Following the definition of cathodic limit, the scan direction was reversed using the same rate to either the original potential value (E_0) or, should it be desirable to investigate anodic behaviour, potentials more positive than the OCP where

the dissolution of the working electrode can occur (E_2, e.g. $Mo \rightarrow Mo^{3+} + 3e^-$). This reaction is again reflected by a large linear current increase, colloquially termed the anodic 'tail', which completes the defined region of electrochemical stability within a given cell. A simple illustration of potential behaviour versus time is given in **Figure 3.12.**
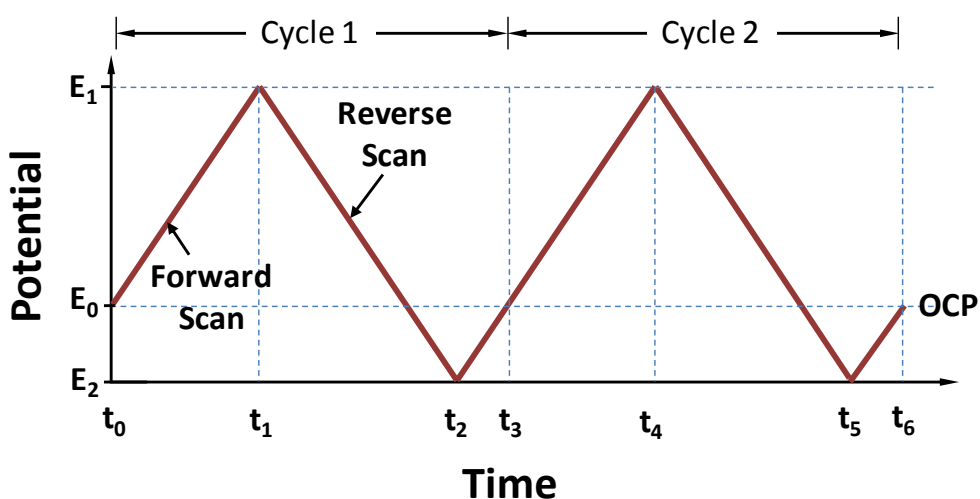
Figure 3.12 – Typical waveform of potential-time signal in a exemplary cyclic voltammetry experiment.

Electro-deoxidation and anodic dissolution of the various species involved in this work can therefore be characterised by CV provided their reaction potentials are within the electrochemical window of the electrolyte. Based on the calculated thermodynamic properties of each of the actinide species and potential surrogates (**Table 3.1**) all of the suggested species can in theory be reduced and refined in both $CaCl_2$ and $LiCl$, with the exception of Sm^{2+}, which was never implemented in these works.

3.3.2   Constant Voltage Electrolysis

During pre-electrolytic cleaning of the molten salt and the electroreduction of single oxide species to metallic phases, it was deemed that a two electrode cell under constant voltage electrolysis was more suitable. There are several reasons for this, including the often limited longevity of reference electrodes, the high currents involved in large scale reduction

making a three electrode cell costly (and the potentiostats having a limited 10A capacity) and general simplicity of operation. The constant DC voltage for these processes was supplied by an E3633A 20A/10A Autoranging power supply (Agilant Ltd.) and is shown in **Figure 3.13**.

Figure 3.13 - Agilent E3633A 20A/10V Autoranging DC power supply.

The voltage selected for experiments was based upon the theoretical reduction voltage and decomposition voltage of the molten salt, but incorporated consideration of the iR drop across the cell, meaning that sometimes a considerable overvoltage was needed. For example voltages in the range of 3.1 and 3.3 V were used for CeO_2, ZrO_2 and CeO_2-ZrO_2 reductions in $CaCl_2$ at 810^oC using a graphite anode as the actual voltage of the cell depends on the current flow, described by **Equation 3.1**. Current response was recorded in 5 s intervals and plotted using a computer.

$$E_{applied} = E_{cell} - iR - \text{overvoltage} \qquad \textbf{3.1}$$

Where E_{cell} is the set cell voltage (V), $E_{applied}$ is the realised voltage across the cell (V) and iR is the voltage loss associated with electron flow through a resistor. In reality this phenomenon can be quite problematic as the resistance across the cell can be assumed to be relatively high (e.g. 0.5 Ω[115]) and also as current is variable as electrolysis proceeds, the influence

of iR drop varies. These issues may be compensated by fixing the potential of the working electrode against a reference redox potential ($H_2|H^+$, $Ag|Ag^+$, $Mo|Mo^{3+}$ etc...), i.e. the application of a third, reference electrode to the cell.

3.3.3 Constant potential Chronoamperometry

To achieve the desired speciation of spent nuclear fuel surrogates, selective reduction of oxide species and anodic dissolution of metallic phases is desired, which in turn necessitates the use of potentiostatic electrolysis in place of constant cell voltage methods. The addition of a stable reference electrode for the experimental duration can help achieve this goal for the reasons outlined above, and becomes integral when considering the marginal differences in theoretical reduction potentials between constituent actinides within spent fuel.

Working electrode potentials were set positive of the reduction limit of the molten salt during reduction, guided by the data obtained from CV studies on the same material, and current responses recorded. In conjunction with ex-situ analysis and the thermodynamic data produced, these current responses could be paired with a given electrochemical reaction for the present species. Kinetic considerations such as electrolysis duration and oxide electrode structure were also incorporated working explantions. A similar approach was taken during anodic electrorefining, however as in theory the only metallic species present should be the desired species for partitioning; the potential for anodic dissolution was frequently set as high as possible to drive a full partitioning between oxide and metal without causing disintegration of the electrode current collector material.

3.3.4   Electrochemical Impedance Spectroscopy (EIS)

With imposed potential sweeps or constant voltage electrolysis operations, electrode conditions within the cell deviate far from equilibrium and so the responses obtained are always transient. This is useful for forcing electrochemical reactions which otherwise are unfavourable, however prohibits our measurement of natural kinetic phenomena which guide understanding of the aforementioned electrochemical processes. It is possible however to perturb the electrode with an Alternating Current (AC) voltage with small signal amplitudes (e.g. ≤10 mV), meaning that the measurements of the dominant physical processes within the system can be performed at or near steady-state conditions[180,181]. EIS is a powerful tool which measures the impedance of a cell in relationship to the frequency change; impedance effectively being the measure of opposition within an electrical circuit to a sinusoidal alternating current. This allows for the inference of information relating to reaction mechanisms, species transport processes and mass or charge transfer, but additionally can be used for the determination of resistance and capacitance of an electrode or cell measured.

Normally, these small perturbations in potential within a linear cell will produce small excitations with a linear response; hence the current response will follow the same sinusoidal pattern of an equivalent frequency, but with a shifted phasor (**Figure 3.14**).

The excitation signal as expressed by a function of time can be defined by, **Equation 3.2**.

$$E_t = E_0 \sin(\omega t) \qquad \qquad \textbf{3.2}$$
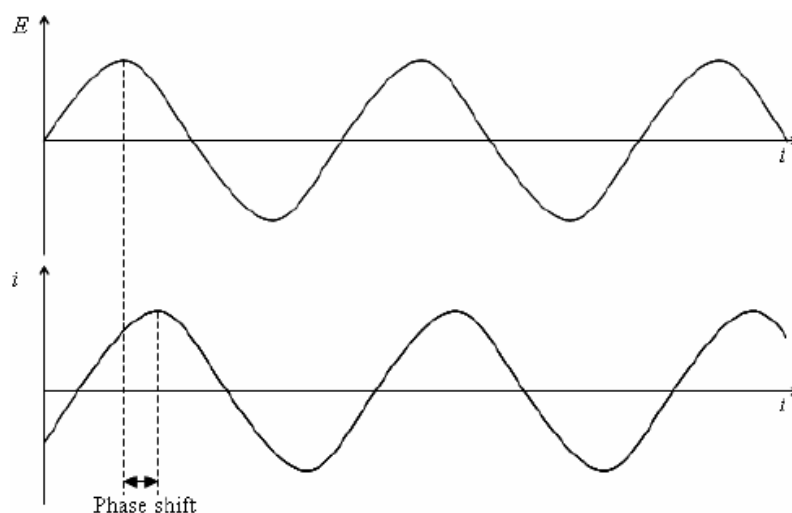
Figure 3.14 – Sinusoidal current response to an applied sinusoidal (AC) potential in a linear system[182].

Where E_t is the potential at time t, E_0 is the amplitude of the signal and ω the angular frequency (ω) in rads^{-1}, related to frequency (Hz) by **Equation 3.3**.

$$\omega = 2\pi f \qquad \qquad \textbf{3.3}$$

The subsequent response signal, i_t, is shifted in phase, Φ, (shown in **Figure 3.14**) resulting in a different amplitude, i_0, expressed in **Equation 3.4.**

$$i_t = i_0 \sin(\omega t + \Phi) \qquad \qquad \textbf{3.4}$$

The impedance of the electrochemical system (Z) can then be expressed in a form analogous to Ohm's Law (R = V/I), given in **Equation 3.5**.

$$Z = \frac{E_t}{i_t} = \frac{E_0 \sin(\omega t)}{i_0 \sin(\omega t + \theta)} = Z_0 \frac{\sin(\omega t)}{\sin(\omega t + \theta)} \qquad \textbf{3.5}$$

Where Z is the impedance (Ω) and Z_0 the amplitude, hence based on **Equation 3.5** impedance is expressed in terms of magnitude, Z_0, and phase shift, Φ. EIS theory then employs Euler's relationship, where phase angles are described in terms of complex functions including real and imaginary parts written in the form $z = x + jy$, with $j = \sqrt{-1}$ and so x and y

the real and imaginary components respectively. Conversion of potential and current response as a function of applied sinusoidal stimulus (originally **Reactions 3.2** and **3.4**) to an electrode now lends to **Equations 3.6** and **3.7** respectively, based on the relationship $e^{jx} = cosx + jsinx$,

$$E_t = E_0 exp(j\omega t)$$ **3.6**

$$I_t = I_0 exp(j\omega t + \Phi)$$ **3.7**

and furthermore to the definition of Z as a complex number, **Equation 3.8**.

$$Z(\omega) = Z_0 exp(j\Phi) = Z_0(cos\Phi + jsin\Phi)$$ **3.8**

As the derived impedance now composes a real and imaginary number, it can be plotted onto an x-(real) and y-(imaginary) axis of an Argand diagram, termed a Nyquist plot and is exemplified in **Figure 3.15**. With the Nyquist plot, the y-axis is defined as negative and each point on the plot corresponds to the impedance at a particular defined frequency. They are by far the most common means of presenting variations of impedance with respect to frequency in systems influenced by reaction kinetics and mass transfer[183]. As with all impedance spectra, the type of impedance response shown in **Figure 3.15** must be coupled with an equivalency circuit which showcases the constituent features of the cell. Here, as a pure resistor is frequency independent (i.e. $\Phi = 0$), the real impedance is directly equal to the resistance at the intercept of the x-axis (Z') and circuit elements can both be readily observed and quantified.

In all cells there will be aspects of uncompensated resistance, which may be poignant to try and remove, however in some circumstances can offer a more suitable ionic environment for favourable electrochemical reactions. This resistance is characterised by solution resistance (R_s).
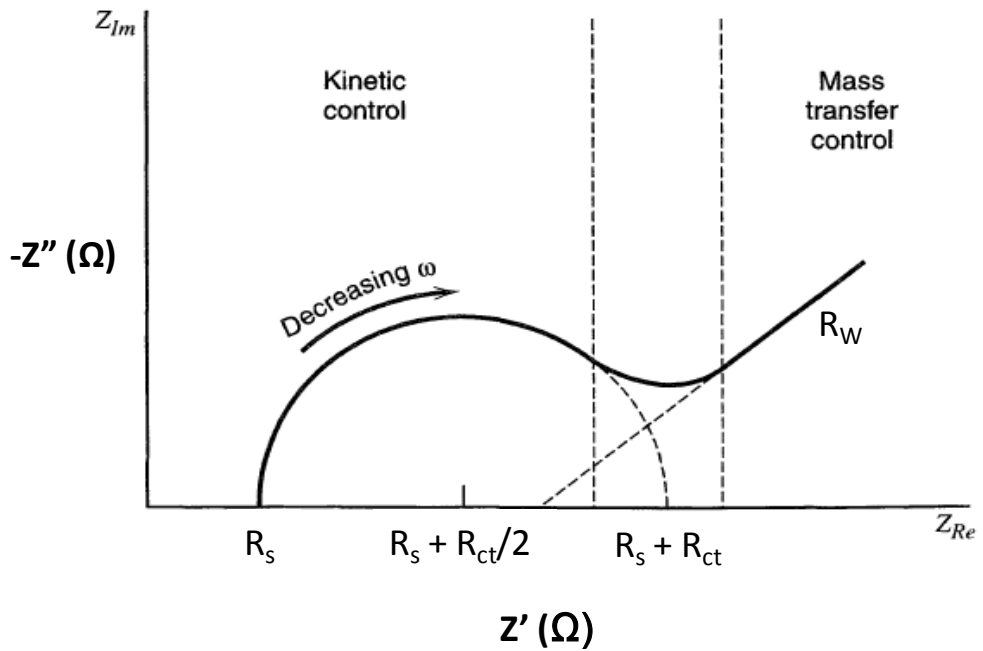
Figure 3.15 – Typical Nyquist plot for an electrochemical system. Modified from[180].

Charge transfer resistance (R_{ct}) when present manifests from a single kinetically controlled reaction at equilibrium, for example R $\rightleftharpoons$ O + ne^- and defines both the curvature and effective diameter of the hyperbolic impedance spectra, so indicating the kinetic favourability of reactions at the electrode|electrolyte interface. Finally capacitance in the form of double layer charging (C_{dl}) is a near ubiquitous feature of impedance spectra produced from absorbed ions on the electrode surface and can be affected by many variables, including electrode potential, temperature, species concentration and etc... In the region controlled by mass transfer, the linear curve leading away from the hyperbolic spectra (low frequency) at a 45° angle is termed Warburg impedance (R_w) and characterises mass transport of species. As EIS was primarily employed here for solid oxide electroreduction or electrolyte resistance characterisation at higher frequency, contributions from Warburg impedance were virtually non-existent, hence will not be considered further. The equivalency circuit for the Nyquist plot above is given in **Figure 3.16**.
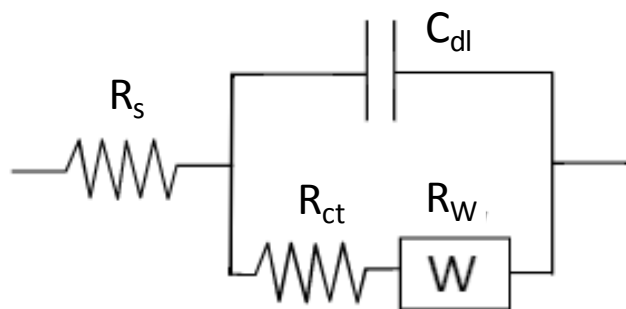
Figure 3.16 – Equivalency circuit for in a typical electrochemical cell as described by the Nyquist plot in Figure 3.15.

Although EIS can be utilised in a number of useful ways, for instance for capacitive measurements of batteries, in this work it was predominantly employed as a creative method of measuring the electrolyte resistance between two fixed electrodes in order to assess electronic conduction through the melt. Further discussion and results are given in Chapter 5. EIS measurements were performed with the PGSTAT30 Autolab potentiostat (Ecochemie) coupled with Frequency Response Analyser (FRA) software and were mostly limited to a frequency range of 100kHz to 10Hz.

3.4   Conventional Analysis

Following electrochemical in-situ analysis and processing of the various oxides used in this research, often ex-situ characterisation of samples, such as morphological variations, elemental composition, phase transitions and crystal structure were required. In these techniques, briefly described below, the broad aim was to supplement the electrochemical data in such a way to establish convincing arguments for the key processes occurring during selective reduction and anodic dissolution investigations.

3.4.1   Scanning Electron Microscopy (SEM)

As a widely used technique in exploring the morphological properties of samples and also in having significant reference in the literature for oxide reduction by the FFC Cambridge Process, SEM was used extensively for this

research. Imaging was performed on a Phillips XL30 FEG instrument with a hairpin thermionic emission source fitted with an EDAX genesis 2000 Energy Dispersive X-Ray (EDS) detector for elemental analysis. Working distances varied depending on sample type (pellet versus powders) and depending of the specific procedure desired. For high resolution and focussed images, a closer working distance of approximately 8 mm was used, whereas for elemental spectral analysis via EDS, a stage height working distance of >10 mm was needed. Secondary Emission-Scanning Electron Microscopy (SE-SEM) was used at an acceleration voltage of between 15-25 kV almost exclusively for these works, as this technique gives the clearest morphological distinction which is useful for visually identifying those axiomatic structures understood to form via FFC reduction as discussed in Chapter 2. Samples were mounted on aluminium stubs using either a sticky carbon pad where sufficient contact could be made, or using a conductive carbon based cement for irregular shaped samples. Non-conductive samples (pure oxide precursors, unreduced samples and some intermediate products) were carbon coated before analysis to avoid excess electron charging during imaging.

Spatially defined elemental analysis by EDS provides impressive utility in combination with SEM; however the determination of oxygen quantity via this method has proven troublesome. Reasons for this include the inherently low detection limit for oxygen at approximately 1 at%, non-specific calibration of the machine which was set to general operation for multiple users, the small atomic size of oxygen and the difficulties of deconvoluting similar emission spectra, e.g. Ti Lα/β (452/458 eV) and O Kα (525 eV). Efforts were made to correct some of these issues by specific calibration and increasing data acquisition durations, as the detection and

accurate quantification of oxygen for some investigations was a fundamental requirement.

3.4.2   X-Ray Diffraction (XRD)

XRD is a method of detecting crystal structures of materials from their specific photon diffraction spectra after being irradiated by x-rays at various angles. The emissions interfere with each other and these patterns are picked up by a specific photo detector to give crystal lattice spectra that can be correlated using a database of known materials. A Siemens D500 advanced XRD with a DG3 Cu-Ka x-ray generator coupled with a goniometer set to rotate at between 0.5-1° 2θ/min with a step size of 0.05^o and range of 10-90° was used on all occasions requiring XRD analysis. Samples were ground into a fine powder by pestle and mortar before loading onto an acrylic sample holder for analysis. Diffraction data was processed with Jade 5.0 XRD analysis software package.

3.4.3   Thermogravimetric Analysis (TGA)

TGA, coupled with heat-flux Differential Scanning Calorimetry (DSC) was performed by an SDT Q600 (TA Instruments) for use in a variety of experiments where mass loss/gain measurements, onset oxidation temperature (OOT) or oxidation activation energy (OAE) were of interest. A typical example was as a means of indirectly measuring extent of reduction of some metallic species by oxidising the produced samples using a precise linear temperature flux and quantifying mass gain attributed to the reformation of oxide species. Similarly where elemental analysis was impossible with traditional means, DSC was used to assess the point of phase transition (e.g. melting) or oxidation and this information used to identify materials present. The advantage of using a combined TGA/DSC (as shown in **Figure 3.17**) is the simultaneous ability to obtain thermal characterisation information in a single step with both accurate heat flow

(W g^{-1}) and mass variation data referenced to a isothemric or ranging temperature.
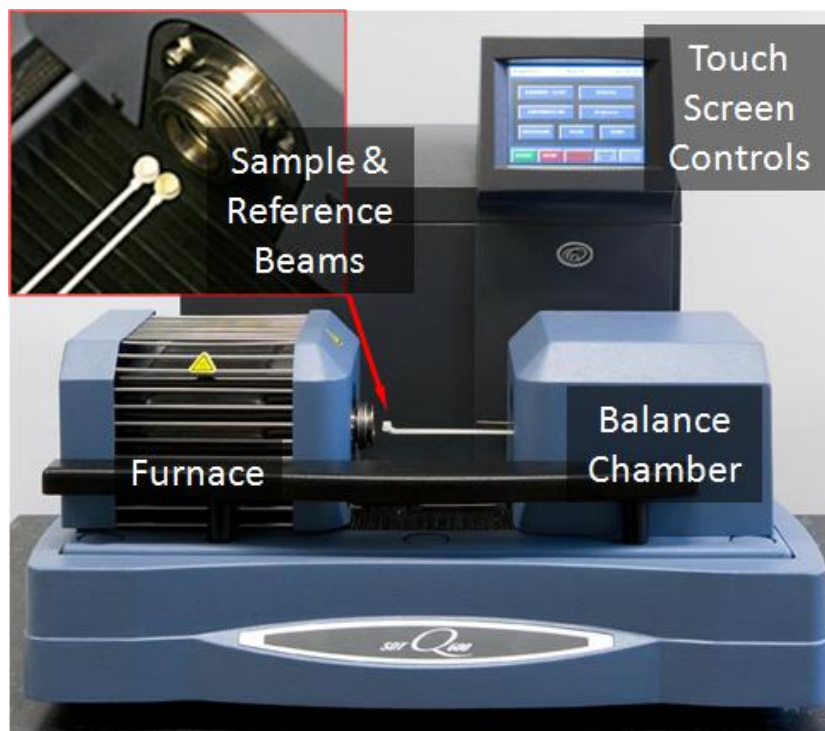
Figure 3.17 – Image of the SDT Q600 TGA-DSC equipment.

In this work, two 90 µL alumina pans were utilised for the sample and as the reference, where up to 20 mg of the sample in form of either fine powder, grains or particulates were used in an inert N$_2$ or compressed air gas flow. Calibration of the machine, required for an accurate heat flux measurements by DSC, was done using a sapphire standard. During heating the sample temperature will lag the reference (empty pan), but during an endothermic or exothermic reaction a response of increased or decreased (respectively) temperature in regards to the reference will be observed. The difference is recorded by the instrument and measured versus time to give heat flow, and any changes in mass can then be attributed to this change.

Chapter 4

Electrolyte and Precursor Processing

This chapter will cover the various nuances involved with preparing the molten salt electrolyte both for bulk electrolysis by the FFC Cambridge Process and precise on-line electroanalysis of the various oxides. Many of the difficulties and limiting factors most associated with molten salt electrochemistry, including aspects of electronic conduction, poor signal responses and unwanted faradaic reactions can be avoided with rigorous and intelligently executed pre-treatments. Additionally, as has been frequently described in the thesis thus far, optimisation of pelletised oxide electrodes for direct reduction is crucial in determining performance as a factor of oxygen removal and current efficiency. Consequently different fabrication methods were trialled here including parameters that influence the porosity, geometry and final electrode assembly in an attempt to improve the overall process and drive towards an industrially acceptable standard.

4.1 Salt Preparation

4.1.1 Thermal Drying and Chemical Treatment

The choice of electrolyte remains of great importance during electrochemical processes. There are several vital criteria which should ideally be met in order to achieve or further optimise a desired process. Firstly, of course, the electrolyte must be stable at the operational temperature, meaning no thermal degradation occurs and the vapour pressure remains low enough to not significantly reduce the quantity of electrolyte over potentially lengthy experimental durations. There must be

good solubility and ionic conductivity for the ions of interest but a limited electronic conductivity (a factor considered in Chapter 5) as well as the electrolyte being preferably non-corrosive, non-toxic, non-reactive and exhibiting a wide potential window. For most electrolytes these properties there exists some reasonable operational threshold for each of these factors. Regarding molten salts, the alkali and alkali-earth chlorides perform very favourably in many of these aspects and so perhaps help to explain their popularity in various ore processing fields for the most challenging metal extractions.

The purity of a molten salt electrolyte is a vital consideration, particularly with direct oxide reduction by the FFC Cambridge Process where the applied overpotentials are often large enough to be close to the decomposition point of the electrolyte. There are often complex issues which can arise from the presence of these impurities, but primarily concerns are focussed on: (1) aspects of reduced process efficiency through parasitic charge consumption caused by ion cycling between electrodes or (2) from the co-deposition of impurities during reduction with the desired product – resulting in a lower quality output should the impurity be incorporated. The $CaCl_2$ used in these experiments, in both its pure form and as a binary eutectic with LiCl, was purchased in the form of dihydrate which was then thermally dried to remove water content and yield an anhydrous salt. Despite both $CaCl_2$ and LiCl then being decidedly moisture free, both are highly hydroscopic to the point of deliquescence and undoubtedly reabsorb moisture during storage, especially in instances involving repeated opening of the storage container. Hence purchasing anhydrous salt in itself is not sufficient enough to guarantee a moisture free melt. When coupled with contamination from metallic ions, oxides and/or hydroxides which are often present in trace amounts (ppm to ppb)

within the salt prior to melting; a pre-treatment method is usually necessitated. Additionally many spent fuel fission product species, for example strontium and caesium oxides, have considerable solubility in molten salts, so the inevitable removal and recycle of salt for extraction of these fission products is a driving force for an industrially accepted treatment process.

The thermal treatment of purchased salt was based upon the understanding that the rapid onset and isothermal drying at elevated temperatures (above 200°C) causes both excess CaO formation, and an agglomeration of salt particles to form a dense mass, preventing further drying. The agglomeration of salt during drying temperatures above 200°C became so severe that the fused clumps required chiselling or crushing to regain any form of utility. An initial ramp at 0.5^{o}C/min up to 100°C with a dwell of 12 hours, followed by a 0.1^{o}C/min ramp to 150°C and dwell for 48 hours was found to produce an agglomeration free, low oxide content and dry salt. Surface area exposure was maximised by using a shallow pan to disperse the salt and heating performed under vacuum (ca. -96kPa) to lower the partial pressure of water and assist the rate of drying.

An accepted protocol for purification of molten salt solvents beyond the thermal removal of moisture is by chemical treatment[184]. Once molten, the salt is sparged with either Cl_2(g) or HCl(g) in order to remove any metallic oxide or hydroxide products from aqueous reactions, for instance by the rapid drying of $CaCl_2$ salt (**Equation 4.1**). In these purification stages, given in **Equation 4.2** and **4.3**, the impurities are removed by evolving gaseous oxygen or water, with the addition of chlorine gas also forming HCl to further remove hydroxide species. A consequence of this method however is the contamination of the melt by the oxidising agents themselves. Indeed in ionic liquids at more modest temperatures the

formation of undesirable trichloride species (Cl_3^-) has been reported extensively using a chlorine sparge under an ambient argon atmosphere[185,186], although their formation at higher temperatures is broadly unknown.

$$CaCl_{2(s)} + 2H_2O_{(g)} \rightleftharpoons Ca(OH)_{2(s)} + 2HCl \qquad \textbf{4.1}$$

$$2Cl_2 + 2MOH \rightarrow 2HCl + O_2 + 2MCl \qquad \textbf{4.2}$$

$$HCl + MOH \rightarrow H_2O + MCl \qquad \textbf{4.3}$$
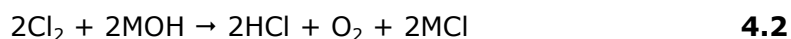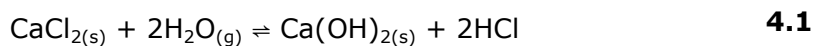
If such a relationship does exist in higher temperature molten salts it raises concerns with regards to the nuclear industry in its capacity to adversely affect molten salt electrochemistry as well as potential impacts in salt containment. Furthermore, with direct reduction by the FFC Cambridge Process a secondary issue persists related to **Reaction 4.1**, where a thermal decomposition of $Ca(OH)_2$ to CaO and H_2O can occur. The additional water vapour is troublesome in its capacity to regenerate the hydroxide but also CaO has significant solubility in molten $CaCl_2$ (ca. 20 %) and is reduced more readily, leading to increased electronic conduction, limited current efficiency and potential contamination of products by Ca metal. The theoretical decomposition voltage of $CaCl_2$ and CaO can be calculated from ΔG^o values, as described by **Equation 4.4** where n is the number of electrons and F the Faraday constant.

$$E^o = \frac{-\Delta G^o}{nF} \qquad \textbf{4.4}$$

This data is plotted against temperature on **Figure 4.1**, highlighting the decomposition of CaO and subsequent production of Ca can occur at voltages as low as 1.63 V at 810°C in the presence of carbon. A similar paradigm exists with the Li_2O-$LiCl$ system and the $LiCl$-$CaCl_2$ Eutectic, albeit with higher stability phases at the lower operational temperature range (500-650°C).
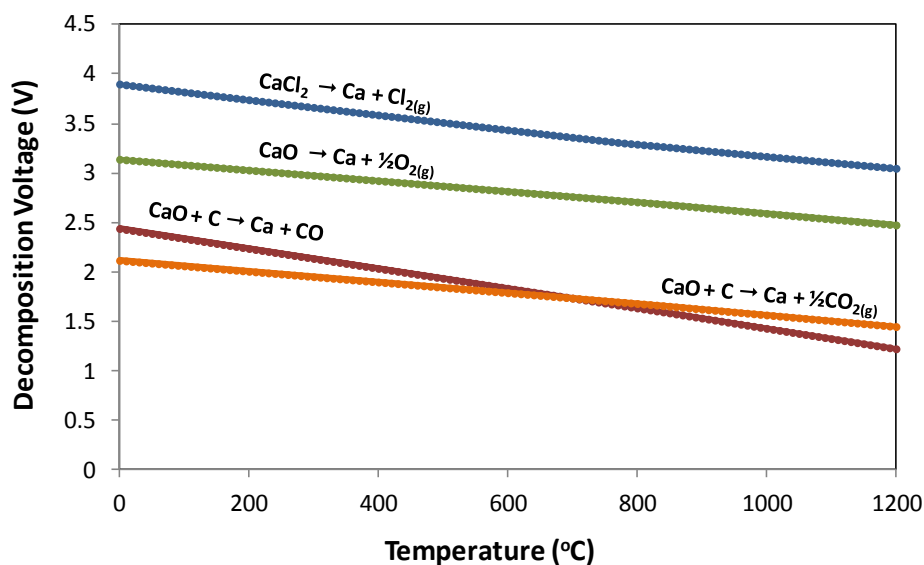
Figure 4.1 – Plot of decomposition voltages versus temperature for pure $CaCl_2$ and CaO.

Clearly it is evident that the performance of electrochemical processes in molten salts can be adversely affected when significant amounts of moisture, oxide, hydroxide or metallic species are present. Besides thermal treatment and chemical cleaning methods discussed above, a direct electrochemical route for salt purification exists termed pre-electrolysis, the utility of which has been outlined previously[136,187].

4.1.2 Pre-Electrolysis

The routine preparation of electrolytes for all aspects of electrochemistry in this work involved the use of pre-electrolysis to remove residual impurities. The basis for the procedure is an application of a modest fixed voltage through the molten salt medium at operational temperature to electrolyse any remaining water and plate feasible chloride or hydroxide based metal impurities. Current-time curves for pre-electrolysis performed overnight at different voltages in 320 g molten $CaCl_2$ at 810°C are shown in **Figure 4.2**, carried out using a 5 mm diameter nickel rod as the cathode and the 10 mm graphite rod anode described previously.
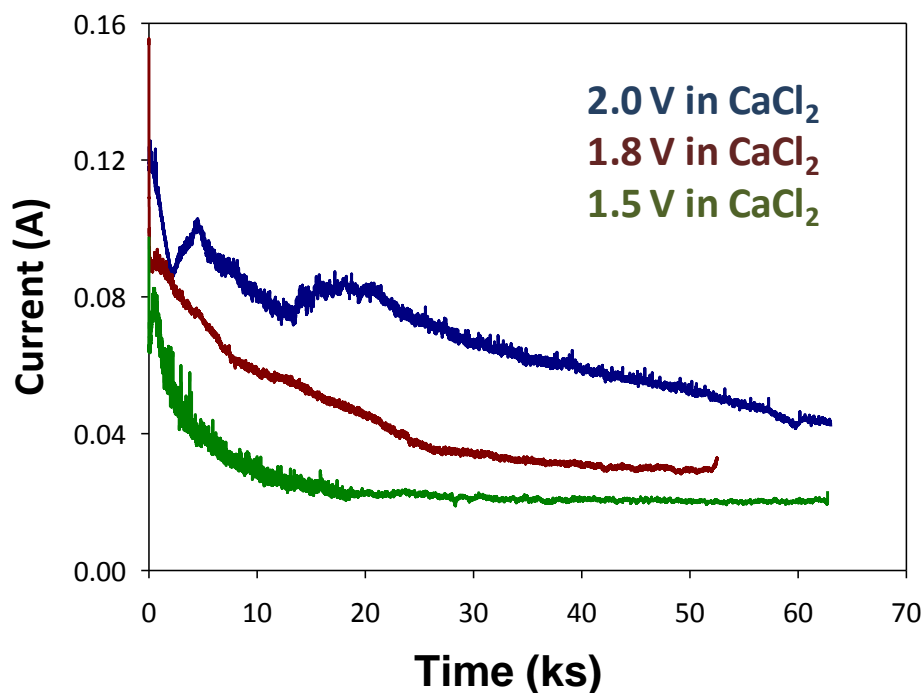
Figure 4.2 –Current response curves from pre-electrolysis at various voltages in 320 g molten $CaCl_2$ at 810°C

As could be expected, the scale of the current responses increases at higher voltages, however the salient features of each curve appears to be unique. At 1.5 V the current displays an idealised behaviour as described by the Cottrell equation. The background current is reached much sooner (ca. 20ks) than at higher applied voltages, indicating an insufficient energy supply for the removal of ambient impure species. Despite theoretically there being no more faradaic reactions occurring at the point where the background current is reached, the small magnitude in current observed (20 mA) is deemed to arise from the multivalent ion cycling between electrodes and from remnants of electronic conduction. Although higher applied cell voltages could increase the driving force for impurity removal, care was taken not to implement such a high cell voltage as to assist the generation of metallic calcium as graphite was used as the anode could assist the decomposition of any CaO resident. The current response recorded at 2.0 V in **Figure 4.2** shows signs of cyclical phenomenon which may be attributed to coupled chemical reactions, for example the formation

and regeneration of carbonate based phases considered unfavourable for efficient operational activity. At 1.8 V slight current peaks are displayed that have similarities to those produced form the adsorption of species onto the electrode surface (electroplating), hence voltages of around 1.8 V were used in $CaCl_2$ pre-electrolysis. Furthermore it is possible that calcium deposition could occur at potentials below the theoretically calculated values for the decomposition of $CaCl_2$, based on the activity of Ca within the melt as described by the Nernst equation, given in **Equation 4.5**.

$$\varepsilon_{Ca} = \varepsilon_{Ca^o} - \left(\frac{RT}{2F}\right)\ln(\alpha_{Ca})$$

4.5

$$\varepsilon_{Ca^o} = -3.27 \text{ V}$$

Where ε_{Ca}^0 is the standard cathodic potential for decomposition of $CaCl_2$ at 810°C (-3.27 V vs. The standard chlorine electrode [S.Cl.E]), ε_{Ca} the calculated cathodic potential including parameters of the unit activity of calcium (α_{Ca}). R, T, n and F retain their usual meanings. The effect of this activity shift of calcium can be considerable, and is explored in **Table 4.1**.

Table 4.1 – decomposition potentials of $CaCl_2$ versus S.Cl.E at various Ca activities at 810°C

Calcium Activity (α_{Ca})	Cathodic Decomposition Potential for $CaCl_2$ (V vs. S.Cl.E)
1	-3.27
10^{-1}	-3.16
10^{-2}	-3.01
10^{-3}	-2.95
10^{-5}	-2.73
10^{-7}	-2.52
10^{-10}	-2.20

In this work the applied voltage of 1.8 V for $CaCl_2$ and 2.6 V for LCE (owing to the lower working temperature and stability of LiCl) proved effective at

removing all bulk contaminant species. This was confirmed by the achieved steady state current responses, from the coated nickel rod following electrolysis indicating metal plating, and also from the lack of sloping or redox behaviour in blank CV scans in the treated molten salts (highlighted for $CaCl_2$ in **Figure 4.3**).
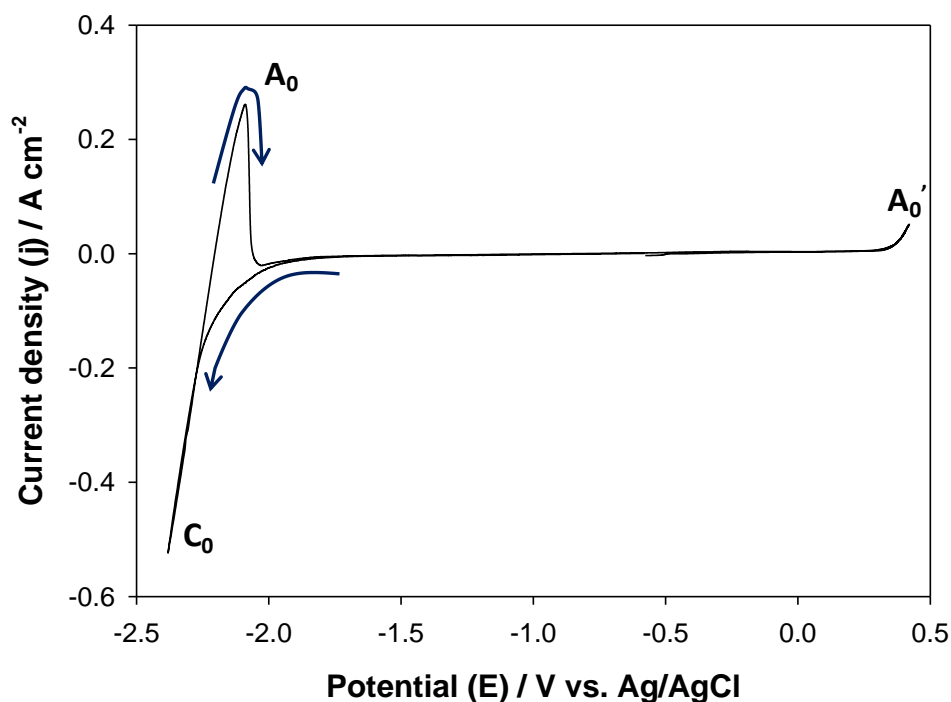
Figure 4.3 – Typical Cyclic voltammogram in $CaCl_2$ at 810^oC showing the working potential range. Scan rate 20 mV s^{-1}, MCE WE surface area: 0.51 cm^2.

The blank Mo MCE CV scan shown in **Figure 4.3** was the first potential cycle and highlights the purity of the melt by a lack of current features in the broad, favourable potential window for electrochemistry. Peaks C_0 and A_0 represent the deposition and anodic stripping of Ca caused by the decomposition of the melt, hence effectively determines the cathodic limit of reduction for oxides. Here, in $CaCl_2$ at 810^oC using a 1 mol % Ag/AgCl reference electrode it was shown to be -2.20 V. Occasionally where different molar concentrations of AgCl were added, the working temperature was varied or a pseudo reference electrode was used the potentials were standardised to this internal reference of Ca/Ca^{2+} which is

an effectively fixed point over short time scales provided the molten salt conditions remain similar. The anodic peak at A_0' represents the anodic dissolution of Mo from the working electrode, and exemplifies the need to use stable refractory materials in WE construction to ensure a wide and stable electrochemical window. It's worth noting here that the presence of peak A_0 is a consequence of the relatively low operational temperature and of the semi-fast scan rate used. The solubility of Ca in $CaCl_2$ can be as high as 4 %[127], so during CV at relatively negative cathodic potentials, and at slow scan speeds, Ca metal has sufficient time to dissolve back into the melt before the onset of reoxidation, leading to an absence of an A_0 peak. This is exacerbated where Ca is in a liquid state, i.e. at temperatures above 842°C, and so be keeping operation temperatures down and scan rates above approximately 10 mV s^{-1} it's possible to retain and observe these transient features of the melt during CV investigations.

4.1.3 Salt Recovery

One of the positive discernible characteristics of FFC based electro-deoxidation is the ability to remove spent salt from the containing vessel, fraction impurities accumulated during electrolysis and reintroduce the clean salt into a new electrolytic cycle. This consideration becomes increasingly paramount when operational scale up to industrial levels is envisioned, when quantities of generated salt solutions will likely necessitate a system for recovery. With molten salt based pyroprocessing of spent fuels, the complexity of a functional method of salt recovery becomes far greater and perhaps given the radiotoxicity of the actinides present, a direct vitrification and waste destination may be a more realistic outcome. However the prospect of salt recovery is hypothetically a possibility by a similar method to the traditional direct reduction process and the presence of actinide and lanthanide species dissolved in the molten

salt can be recovered for burn up in fast neutron reactors. **Figure 4.4** provides an overview of the potential basic strategy of salt reclamation for direct reduction and one for spent fuel speciation from a LWR for a metallic fast cycle application.

Traditional Salt Reclamation Strategy

Modified Salt Reclamation Strategy for Metal Fuel Production from LWR waste
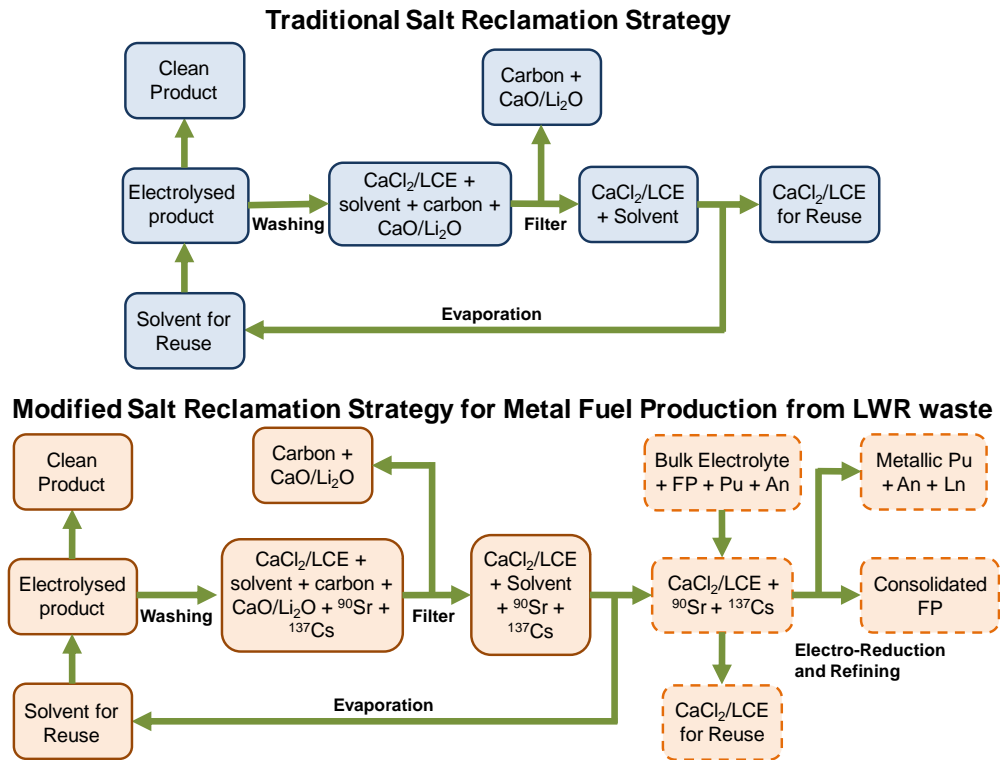
Figure 4.4 – Theoretical examples of how salt reclamation strategies for traditional FFC Cambridge Process electrolysis and for the FFC based processing of spent oxide fuels for fast metallic products may function.

In the former, a simplified physical system can be applied involving the dissolution of salt in a solvent, filtering any particulate carbon or insoluble oxides and then evaporating residual solvent for reuse and leaving a purified metallic electrolysis product and clean salt ready for reintegration. The latter requires a secondary and perhaps even ternary electrolysis cell to electrochemically reduce and refine the various contaminant actinides and FPs, assuming a pure U metal is the electrolysed product. Two crucial FPs are the ^{90}Sr and ^{137}Cs isotopes which are known to have significant solubility in molten salts and represent the primary cause of heat generation, hence specific interest was highlighted to these species in the

flow chart in **Figure 4.4**. In fast reactors using metallic fuels, a tolerable ratio of fissionable actinides and non-fissionable lanthanides can be loaded into the core without halting the fission chain reaction. Of course this is of huge benefit in transmutating those lanthanides which would otherwise be destined for geological storage and which have considerable half lives.

Properties of the solvents used in this work for cleaning of the electrolysed product are given in **Table 4.2**. Dimethyl Sulfoxide (DMSO) was shown to have poor general characteristics for both $CaCl_2$ and LiCl dissolution, however improved when diluted with water to form a protic solvent.

Table 4.2 – Physical properties of solvents used for $CaCl_2$ and LiCl at 20°C.

Solvent	B.P. (^{o}C)	Heat Capacity, C_p (J/mol·K)	Vaporisation Heat, dH_{vap} (kJ/mol)	Salt Solubility (g/100g solvent)	
				$CaCl_2$	LiCl
Water	100	75.4	40.66	74.5	83.5
Methanol	64.6	79.5	35.3	29.2[188]	43.8[188]
Ethanol	78.3	112.4	38.6	25.8[188]	24.3[188]
Dimethyl-Sulfoxide	189	149.4	48.1[189]	unknown	10.2

The reason for identifying DMSO as a potential candidate washing media was because many of the metals likely to be present from an electrochemical reduction of spent fuels (particularly lanthanide species) are chemically reactive with water and oxygen. This was experienced most obviously when recovering samples of produced metallic cerium which would react vigorously in water to produce hydrogen bubbles and cerium hydroxide. Consequently finding a solvent which could remove the salt residue without oxidising the produced metallic forms was imperative. The small dilution factors of water added to DMSO was found to slow down the oxidation procedure, but not completely avoid it, and at the same time the

rate of salt dissolution was slow. As such for samples involving cerium presence in its metallic state ethanol was nearly always used, and for all other less reactive materials a slow washing method in water was used.

Although water is a preferential solvent for the process of salt recovery in terms of salt solubility, the two alcohols examined have more favourable enthalpies of evaporation, heat capacities and boiling points. Replacing the use of water to wash salts in an industrial setting also has the benefit of avoiding formations of hydrated $CaCl_2$/LiCl, which could further complicate the process and increase costs of a water based leaching.

4.2   Oxide electrode Preparation

4.2.1 Feedstock Characterisation and Processing

The unique nature of the proposed process in this thesis requires a rational and intelligent approach to an optimised feedstock preparation. In electrochemical processes the electrolyte is often utilised to solvate desired species so they can travel through the melt via a combination of diffusion, convection and migration before undergoing an electrochemical reaction at the electrode interface. With transition metal oxides (i.e. some of the surrogate materials selected here), and indeed some actinide and lanthanide oxides, the solubility in molten chloride melts is marginal. Fortunately, the solubility of oxide ions in molten chloride melts is much more substantial, and forms the basis of solid oxide reduction via an applied cathodic potential (i.e. the FFC Cambridge Process).

The use of oxides in this manner holds both considerable advantages to a condensed reprocessing technology but also some limitations which require attention. Firstly the form of the spent fuels from civil thermal nuclear reactors is an agglomeration of oxides, and whilst various processes exist to convert oxides to more soluble species (for instance via chlorination)

these hold such serious implications with regard to cost and safety that their application towards nuclear materials is broadly restricted. Secondly the ability to maintain the position of product species in solid state, particularly considering the fissile nature of those actinides within spent fuel, is a huge boon for process control and for accurately developing quantised flow sheets for an industrial method. Thirdly, oxides can be manipulated into preforms with specific properties, such as size, density and porosity which facilitate improved reduction kinetics through inter-particulate contact lowering resistance when attached to conductive current collector. Finally, as a point of scrutinising the potential for technological maturity, the capacity to bridge batch reprocessing to a continuous one is far more likely using a standardised oxide pellet configuration. As such it seems intuitive to keep spent fuels within an oxide form for reprocessing to produce metallic phases for GENIV reactors.

The general process of reduction covered within the literature is one of direct full reduction of single or multiple oxides metallic phases, whereas here initial attempts to illicit a partial reduction of a single species in a binary matrix were pursued. Consequently there may be interactions prior to alloying between any potential intermediary sub-oxides, and include the formation of chlorine containing or cation intercalated species. There potentially also may be an initial co-oxide formation which would otherwise be avoided at potentials significant enough for a full reduction. These cases more generally highlight the fundamental concept in oxide electroreduction that the starting properties of the preform will directly influence the ability to produce a desired metallic product. Careful characterisation of feedstock materials prior to electrode fabrication is therefore paramount, as is the method of fabrication and post-reduction ex-situ analysis as a means of interpreting the potentially complex interactions during partial reduction.

Engineering homogenous preforms which permit optimised, repeatable reduction with recoverable yields remains a considerable challenge requiring investigation. Oxides have been mixed previously with the sole intention of the production of alloys by the FFC Cambridge Process e.g. NiTi[190], Ti-10W[191], Ti-15Mo[192], Zr-2.5Nb[193], Co-Cr[194] etc..., but as yet none with the intent of a partial reduction of mixed oxide feedstock. In this work various binary oxides were prepared through either simple mixing via pestle and mortar or through ball milling. The stoichiometry for surrogate materials tested was either in a 2:1 or 1:1 atomic ratio, as to more readily identify individual redox reactions during electroanalysis. Investigation using MOX fuels contained 5 at% Pu, which is a higher concentration than produced in a typical LWR spent fuel but was important again to identify and relate potential electrochemical reactions during CV. For auxiliary investigations of molten salt conductivity improvements and for identifying the characteristics of direct reduction, single oxide powders and pellets were prepared. **Table 4.3** gives an overview of the various feed oxides and their properties used for electrochemical reduction in these studies.

Table 4.3 – Information regarding various oxide feedstock materials for reduction

Feed Oxide	Supplier	Purity (%)	Particle Size (µm)	Density (g/cm^3)
NiO	Sigma-Aldrich	99.99	<2*	6.67
CeO$_2$	Sigma-Aldrich	99.9	<5	7.65
ZrO$_2$	Sigma-Aldrich	99	5	5.68
TiO$_2$$^{\#}$	Sigma-Aldrich	99.8	<0.3	3.78
Cr$_2$O$_3$	Acros organics	99	<5*	5.22
PuO$_2$	Sellafield Ltd.	>99	10†	11.50
5%MOX	Sellafield Ltd.	>99	~10†	11.00

#In Anatase form †Estimated from literature[195] and from previous samples

Sieve analysis cross-referenced to SEM imaging was performed on those powders which were supplied with no information regarding particle sizes,

indicated by (*) where 99.99 wt% was the designated threshold for sieve retention. Spent fuels following voloxidation typically have over 99% of the fuel particles reduced to <44µm[196], providing suitability for a pelletisation procedure. Pressing and slip casting of the oxides where possible was examined following this consideration and are discussed below.

4.2.1.1 2NiO-CeO$_2$ Morphology

The as-received particles of NiO consisted of approximately uniform, near spherical morphologies with an estimated average diameter of one micron (**Figure 4.5a**) Conversely the unmodified CeO$_2$ powders were on average larger, far more angular and with a greater range of sizes (**Figure 4.5b**).

Figure 4.5 – SE-SEM images of supplied powders of (a) NiO under 6000x magnification and (b) CeO$_2$ under 2400x magnification, with (c) the mixed 2NiO:CeO$_2$ at 3000x magnification, and (d) the EDS analysis of sample (c). All samples were manually pressed into the cavity of a Mo MCE prior to imaging.

The powders of NiO and CeO$_2$ were mixed in a 2:1 stoichiometry and gently ground by dry pestle and mortar, the resultant mixture displayed in **Figure 4.5c**. Elemental analysis by EDS (**Figure 4.5d**) revealed a near perfectly predicted stoichiometry, suggesting a satisfactory homogenisation and

distribution of the individual oxides. Additionally much of angularity of the CeO$_2$ presence had been mitigated after a short (<10 minutes) grinding procedure. The binary mixture as prepared was used either directly by manual pressing between two glass slides into an Mo MCE to form the loaded cavity electrode for CV investigation, or pelletised for bulk electrolysis (see **Figure 4.6**).

Figure 4.6 – Photographs of 2NiO-CeO$_2$ WE electrodes: (a) The 2NiO-CeO$_2$ powders on a glass slide for manual pressing into (b) an empty Mo MCE electrode to produce (c) the oxide loaded MCE. (d) Pressed powders using a 5 mm die at 1.5 tonnes and after sintering in atmosphere at 900°C for 2 hours. (e) The final working electrode for pellet electrolysis using Mo mesh and binding wire.

The most common means of achieving pelletisation employed here was by uniaxial cold pressing in a hydraulic press using SS dies and moulds. Envisioning a larger scale application, automated pressing systems capable of mass production in either batch or continuous routes are commonplace; however lab scale operations typically involve small batch units where green form properties can be readily altered. With spent fuel head-end

processing, any stage involving pelletisation would require integration into a mechanical system free from human presence, owing to the intrinsic dangers of high ionising energy at close proximity. The addition of binders has been considered here but generally was found to be unnecessary owing the high quality of preforms from the hydraulic press at low pressing force (1-2 tonnes), potentially assisted by the excellent particle properties of NiO in producing stable green forms.

4.2.1.2 ZrO_2-CeO_2

As the same CeO_2 feed was used throughout all investigations it was not necessary to re-characterise the powders prior to mixing. An SEM image of the ZrO_2 as-received is shown in **Figure 4.7** (top) and highlights the large and irregular unit particle sizes. The powders for the ZrO_2-CeO_2 binary were mixed in a 1:1 Atomic stoichiometry by vigorous shaking in a sealed container (**Figure 4.7,** middle). It appears the action of hand mixing was sufficient enough to shear some of the CeO_2 powders into smaller grains which, probably by an electrostatic interaction, then coated the outer surface of the ZrO_2 particles. Dry ball milling was deemed necessary in this instance due to the generally large and discontinuous sizing of the two constituent oxides and additionally ball milling has the advantage of thoroughly homogenising the oxide matrix. Powders recovered after grinding at 600 RPM for a total of 45 minutes were much more ordered and uniform, possessing an average diameter of approximately 200 nm (**Figure 4.7,** bottom).

Figure 4.7 – SEM images of as-received ZrO_2 powders (top), following hand mixing with CeO_2 to form ZrO_2-CeO_2 (middle) and after ball milling (bottom).

The prepared powders were then considered suitable for use in either MCEs or for pelletisation. XRD was also performed to characterise crystal structure of the binary oxides after ball milling and additionally following the sintering procedure (**Figure 4.8)**. Predictably, no contaminating species or chemical interaction between oxides (for instance co-oxide formation) had occurred during the process of milling. Indeed even during sintering for 2 hours at $1000^{o}C$ it appears that both oxides are relatively stable (undergoing no phase transitions) and chemically inert to each other even at elevated temperatures and durations.

Applied pressing force was varied when using the ZrO_2-CeO_2 binary powders to create cold pressed pellets revealing a lamination effect at higher pressing forces (greater than 2 tonnes) when a 5 mm die was used.

Figure 4.8 – XRD patterns for raw and ball milled ZrO_2-CeO_2.

This lamination caused shearing to occur in the green forms, making the calculation of porosity impossible and more importantly causing the pellet integrity to fail during sintering. The cause of these incumbent laminar cracks during die pressing have a duel origin; firstly a concentration of tensile stress at the upper edge of the pelletised form and a rebound effect during die retraction, both illustrated in **Figure 4.9**.

Subsequent efforts utilised a much more modest force of, again, between one and two tonnes with resultant pellets exhibiting much better cohesion and stability. Sintering was performed for 2 hours as before, but at $1000^{\circ}C$ in an attempt to increase interconnectivity of oxide grains as well as mechanical strength, at the expense of a marginally diminished porosity.

Figure 4.9 – Mechanism for the formation of laminar cracks during die pressing of ceramic materials, (a) initially from pressure release by the upper punch and (b) then from material rebound at the top of pellet[53].

Table 4.4 outlines the theoretical porosity from various pressing characteristics used for a batch of the ball milled and non-ball milled ZrO_2-CeO_2 powders followed by uniform sintering to all samples.

Table 4.4 – pressing and sintering characteristics for both ball milled and hand mixed ZrO_2-CeO_2 powders.

Pellet Sample	Weight (mg)	Milling	Pressing Force (tonnes)	Sintering Parameters		Porosity (%)
				Temperature (°C)	Duration (h)	
1	103	None	1.0	1000	2	59.8
2	121	None	2.0	1000	2	56.7
3	109	Ball Milled	1.0	1000	2	51.1
4	125	Ball Milled	1.5	1000	2	48.9
5	117	Ball Milled	2.0	1000	2	49.4

Fortunately due to the definitive geometry of final cold-pressed pellet preforms their theoretical porosity (φ_t) was calculated based on the calculated mass of a fully dense pellet of the same dimension (M_t) given the materials average density (ρ), as described in **Equation 4.6**.

$$\varphi_t = \frac{M_t - M}{M_t} \times 100 = \frac{\rho r^2 h\pi - M}{\rho r^2 h\pi} \times 100 \qquad \textbf{4.6}$$
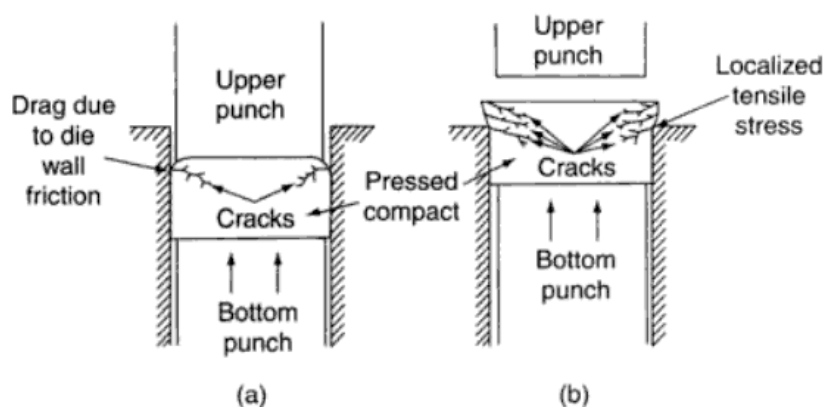
Where M represents the weighed mass of the pellet (mg), r its radius (mm) and h the pellet height (mm). All ball milled samples were shown to be

consistently less porous than the non-milled counterparts. The ordered packing density coupled with a better intra-particle contact during sintering of the milled powders most likely assisted this observation, however even the lowest porosity observed (48.9%) is still substantial enough to permit ingress by the molten salt during electrolysis. Images of the pressed but unsintered ZrO_2-CeO_2 pellets at 2 and 4 tonnes are shown in **Figure 4.10**, along with a completed modified working electrode arrangement.

As a progressive design from the $2NiO$-CeO_2 pelletised working electrode, the arrangement shown in **Figure 4.10** was implemented in an effort to (1) increase metal|oxide contact area and hence encourage more rapid 3PI reduction and (2) to orientate a larger surface area to face the counter electrode during electrolysis.
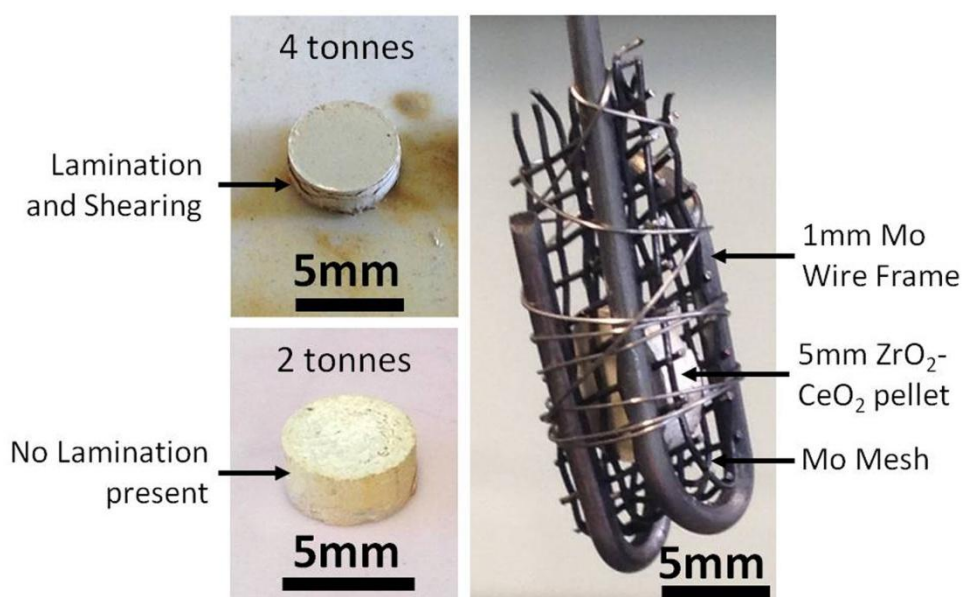
Figure 4.10 – photos of green ZrO_2-CeO_2 pressed at 4 tonnes (showing lamination) and 2 tonnes (left) and the produced Mo wire/mesh working electrode.

The latter addition may seem academic but becomes an important consideration when identifying the effects of the electronic field influences between electrodes and through the molten salt electrolyte, which should provide greater oxygen ion transfer kinetics towards the counter electrode. The porosity data and trends obtained for the smaller 5 mm pellets were

shown to be transferrable when the scale was increased to a 13 mm die and mould. At an identical sintering profile, and at pressing forces between 1 and 3 tonnes the porosity varied between 51.5% and 47.6%, suggesting the pressing parameters as a function of force applied per unit area had less contribution to porosity than, for instance, the sintering methodology.

4.2.1.3 TiO$_2$-CeO$_2$

Whereas the two previous binary oxides were used to investigate direct reduction and the possibility of partial reduction and selective dissolution in CaCl$_2$, the TiO$_2$-CeO$_2$ oxide system was used exclusively in the LCE melt. Preparation of the oxides were performed in much the same way as before, however the anatase TiO$_2$ morphology from Sigma-Aldrich was already favourable in terms of being homogeneously spherical with particles sizes bordering on nanoparticle range (0.1-0.4 nm) and broadly displaying a lack of agglomeration, as shown in **Figure 4.11**. Mixing between TiO$_2$ and CeO$_2$ was once again performed by hand after weighing the appropriate quantities of the oxides and preceded wet ball milling. Isopropyl alcohol (C$_3$H$_8$O) was used as a lubricant during the milling process, dissipating the powders to help prevent agglomeration in the final product[197].

15000 x magnification   60000 x magnification

5µm   1µm
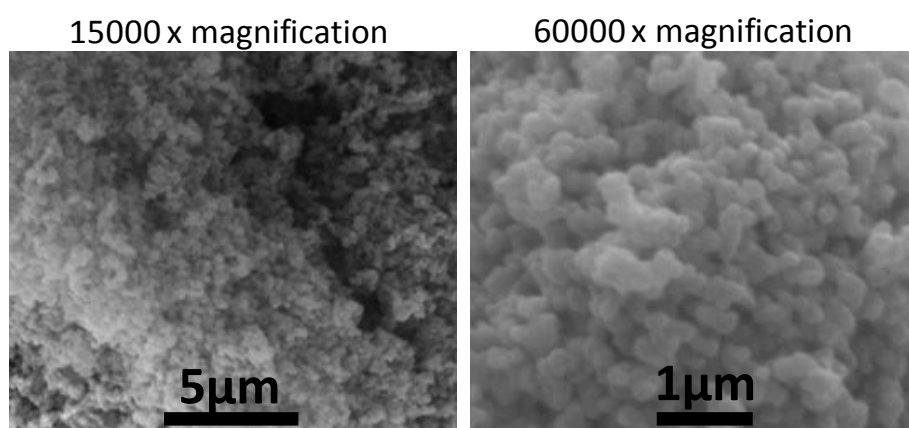
Figure 4.11 – SEM imaging of the unmodified Sigma TiO$_2$ anatase feedstock.

The use of ZrO$_2$ as a milling material was acceptable for these powders as the Mohs hardness for ZrO$_2$ (8.2) is far greater than for TiO$_2$ anatase (6-

6.5) or CeO_2 (6.0) and so abrasion or exfoliation of the milling set should not occur to introduce contamination. This was confirmed by EDS analysis of the precursor materials revealing a stoichiometric ratio of Ti, Ce and O. TiO_2-CeO_2 powders retrieved from milling at 600 RPM for 1 hour (0.5 h clockwise and 0.5 h counter clockwise) were washed with deionised water and left to dry in a drying oven at 60°C for approximately 48 hours.

4.2.1.3.1 Cold-Pressing

Pelletisation was performed in two ways for the preparation of the TiO_2-CeO_2 binary as both a larger quantity of material for experimentation was required and it afforded an opportunity to investigate how head-end processing can influence spent fuel treatment. Firstly, as with the other oxides, cold pressing was employed using a larger die of 13 mm. Parameters such as force applied, sintering temperature and sintering duration were altered to assess how the final porosity of the pellet was affected. Considering the implication of maintaining an open porosity for permitting effective electrolyte impregnation and to avoid concentrations of oxygen ion accumulation (frequently outlined within the literature), an intrinsically high porosity should be beneficial. However it is also of fundamental importance to adequately contain desirable spent fuel components, making a high mechanical strength oxide electrode also a requisite. Furthermore due to the nature of the process under investigation, where parts of the oxide are to be deliberately partitioned, a highly interconnected and durable preform is also coveted. **Table 4.5** outlines the results of theoretical porosity analysis from implementing variations in pressing forces (2-6 tonnes) and in sintering parameters (1000, 1100 and 1200°C for 3, 5 and 7 hours).

Table 4.5 – Porosity data for pressed pellet investigations with applied sintering.

| Applied Force (tonnes) | Sintering Temperature (°C) / Duration | | | | | | | | |
| | 1000 | | | 1100 | | | 1200 | | |
	3h	5h	7h	3h	5h	7h	3h	5h	7h
2	46.55	46.26	48.46	47.83	46.12	45.15	33.08	31.53	22.13
3	43.41	46.29	49.11	42.90	42.30	34.69	32.28	36.53	27.74
4	43.50	43.59	47.05	48.81	36.87	43.77	28.08	34.39	36.11
5	47.30	43.80	41.47	52.22	43.20	37.38	33.40	35.34	33.59
6	45.86	41.91	42.76	45.39	41.89	36.94	30.84	39.57	37.43

It was found using the larger 13 mm die and programmable forces of up to 6 tonnes for the CeO_2-TiO_2 binary led to no obvious delaminating or cracking events. The effective pressure given the increased surface area (1.131 cm^2) at 6 tonnes pressing was calculated to be 520MPa, whereas at 2 tonnes force with the smaller 5 mm die (0.196 cm^2), the effective pressure was 1GPa, hence it is reasonable to observe functional preforms at such applied forces for these investigations. A screening test using significant variations in total oxide powder mass was performed prior to the porosity analysis in an attempt to optimise the final geometric properties of the pellets. It was discovered that the final height of the pellets after sintering had the strongest influence on the degree of shearing lamination, as seen in **Figure 4.12**, realised as a function of the oxide mass prior to pressing.
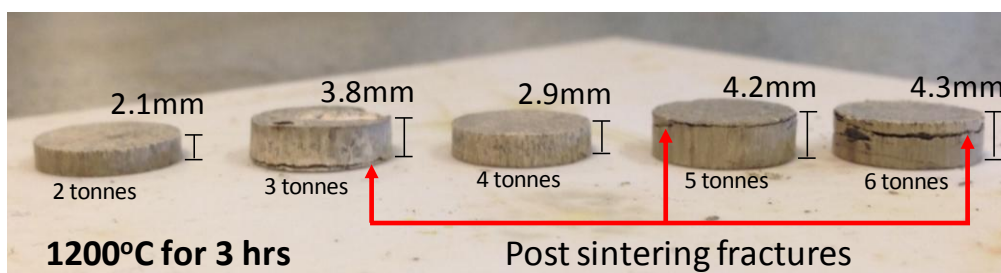
Figure 4.12 – Photograph of pelletised ZrO_2-CeO_2 by hydraulic pressing under different forces and using different quantities of initial oxide powders.

Iterations of pellet height were tested under identical sintering conditions and although those heights assessed weren't continuous, a repeatable observed feature was the development of stress fractures of the pellet preform after sintering at heights of 3.8 mm and greater. Yet the general relationship between the applied pressure and the resultant theoretical porosity after sintering is seemingly random, shown in **Figure 4.13** (top).
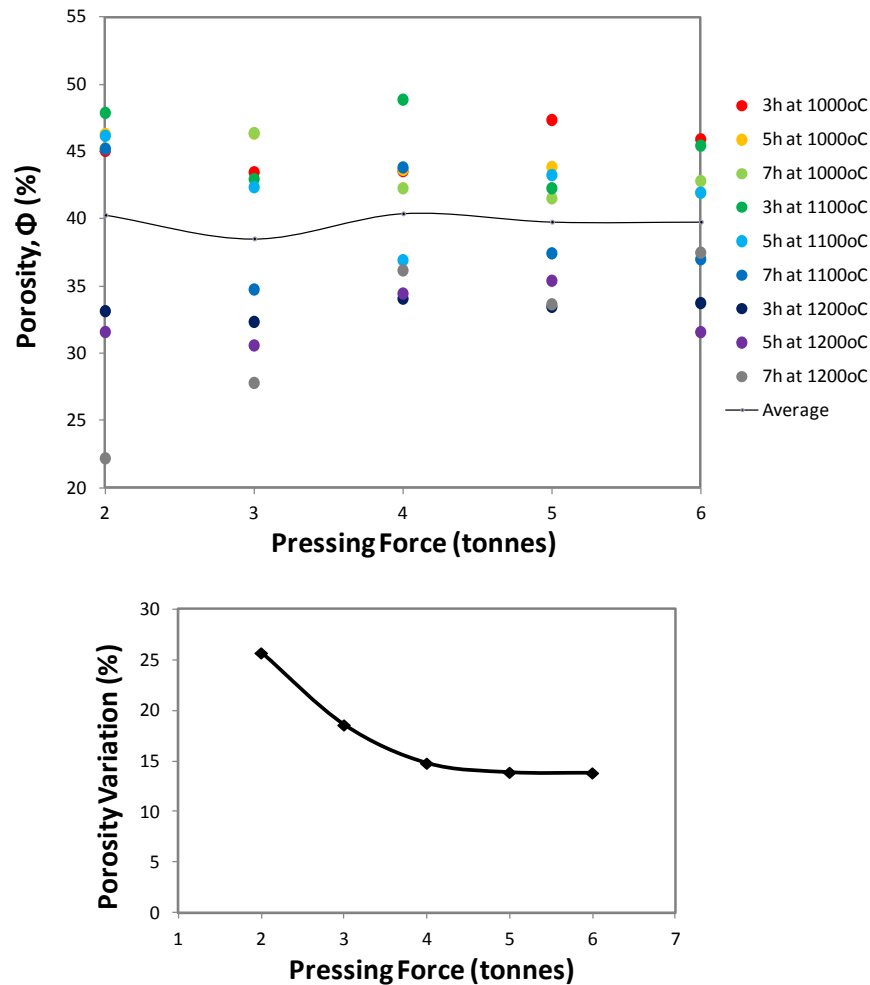
Figure 4.13 – Plots of the relationship between applied pressing forces for ZrO_2-CeO_2 pellets and the resultant porosity after sintering under various conditions (top) as well as the variation in porosity data versus pressing force (bottom).

Whilst it may be expected the pellets yielded from higher formation forces during pressing may have a more densely packed structure, this was not the case here, or the influence of sintering overtly normalised open porosities across all sintering parameters. The only consistent trend was a

gradual decrease in porosity variation or spread as pressing forces were increased, culminating in what appears to be a plateau at between 5 and 6 tonnes (**Figure 4.13**, bottom). At lower applied forces during cold pressing the oxide particles will likely have an overall poorer interconnectivity, or there may be aspects of relaxation after the plunger is released from the hydraulic press. Consequently sintering at lower temperatures for shorter durations may produce relatively loosely consolidated pellet forms compared to the effects of sintering at higher temperatures to expedite the inter-particle grain boundary growth. At much higher pressing forces the influence of sintering, whilst still a key influencing factor, will likely contribute less to the divergence of porosity due to better initial packing.

Solid state sintering is a technique for densification in ceramic processing and is diffusion controlled, proceeding by the differences in free energy between the surfaces of adjacent particles. The required activation energy is provided by heating and allows for an initial rearranging of particles to form bridges or necks to neighbouring particles, developing grain boundaries. This phase is considered the first stage of sintering and is likely the stage many of the samples prepared by the methodology outlined in this thesis lies, occurring at only moderate temperatures and durations. A second stage then proceeds termed an intermediate sintering, particle centres move closer to each other and porosity is gradually eliminated resulting in shrinkage of the final preform. It is worth noting here that even under the most extreme sintering conditions applied (7 hours at $1200^{\circ}C$) the largest shrinkage that occurred in ZrO_2-CeO_2 pellet diameter was 1.1 mm, or an equivalent of 8.5%, suggesting that phase two sintering was indeed present but its extent was relatively limited. There is also a third stage, where a more complete densification and exclusion of remaining pore spaces via vacancy diffusion occurs through the growth of grain

boundaries. Given ideal conditions a near full densification of initial powders can occur (**Figure 4.14**). As the aim of reduction by the FFC Cambridge Process is to avoid the excessive densification and subsequent shrinkage of pelletised oxide powders, the lack of late stage 2 or stage 3 sintering is consequently very desirable.
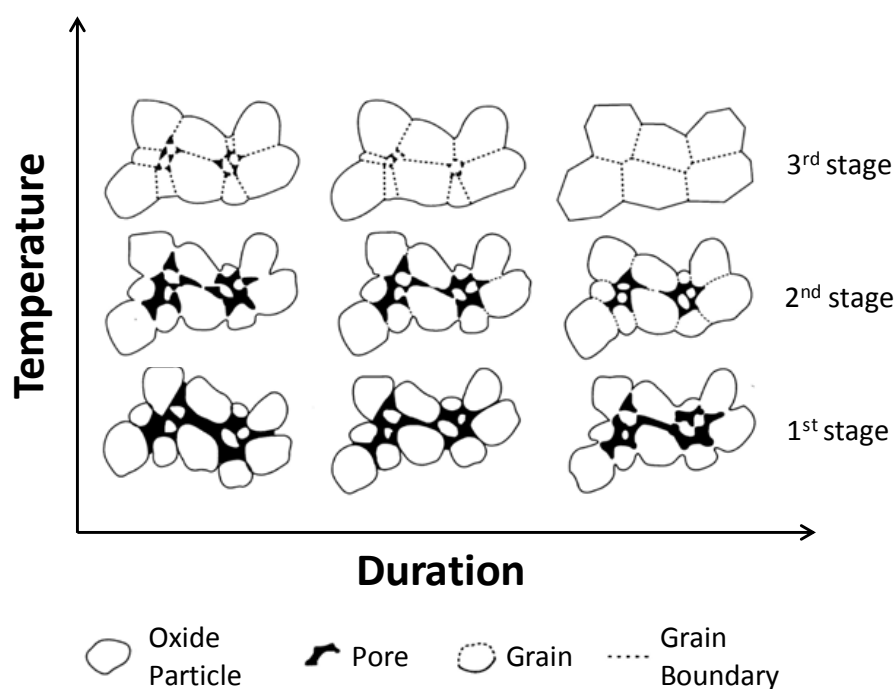
Figure 4.14 – Schematic illustration of the solid-state sintering process with regards to arbitrary sintering temperature and time increases (reproduced from[198]).

Should substantial in-situ sintering occur of the ceramic or metallic phases, the reduction process becomes retarded due to the cessation of oxygen diffusion out of the bulk phase (or significantly limited to transport through the solid phase of those metals that form M[O] solid solutions). Additionally, entrapment of electrolyte could potentially lead to a favourable formation of intercalated phases which are more thermodynamically stable or can lead to contamination of the final product.

The significance of sintering on the green pellet forms were also interesting in its discrete effects on appearance, as shown in **Figure 4.15**. The clear divergence in theoretical porosity between 1100°C and 1200°C is

accompanied by a marked darkening of the pellet from an off-white colouration to a shade of brown and this feature is more apparent at longer sintering durations. This phenomenon wasn't observed during the sintering processes employed for the ZrO_2-CeO_2 at temperatures of up to 1100^oC, indicating the aesthetic variations result from the presence of TiO_2.
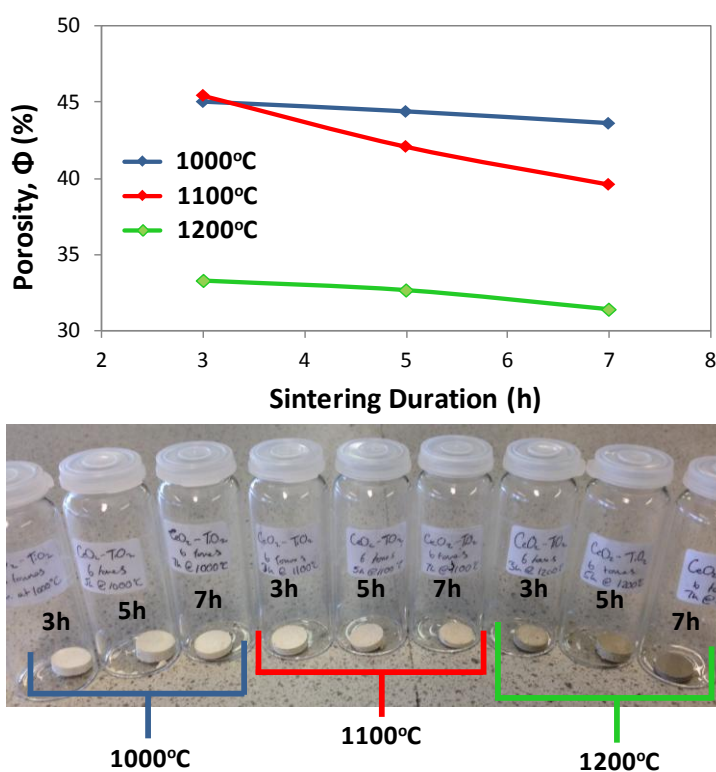
Figure 4.15 – Effect of sintering temperature and duration on the final porosity of ZrO_2-CeO_2 pellets with a photo of the produced pellets after sintering. Note the colouration shift from lighter preforms on the left to darker further right.

There is a point of crystal transition in TiO_2 from anatase to rutile at elevated temperatures, the exact point of which is a source of continued debate[199], however it is generally agreed the transition to rutile is complete by 900^oC. As the change in appearance observed here happens most significantly between 1100^oC and 1200^oC, it would appear to not be directly caused by a TiO_2 crystal phase shift. Impurities however do influence the exact point of the phase transitions and as 50 % of the pellet was CeO_2, the possibility of significant inhibition of crystal structure change for TiO_2 warranted investigation. XPS of TiO_2-CeO_2 pellet surfaces prepared from

sintering at 1000°C for 3 h, 1100°C for 5 h and at 1200°C for 7 h is shown in **Figure 4.16** and reveals no shift in binding energy for either the O1s (ca. 530eV) line, OKLL (ca. 960eV) lines or the Ti2p (ca. 459eV) line.
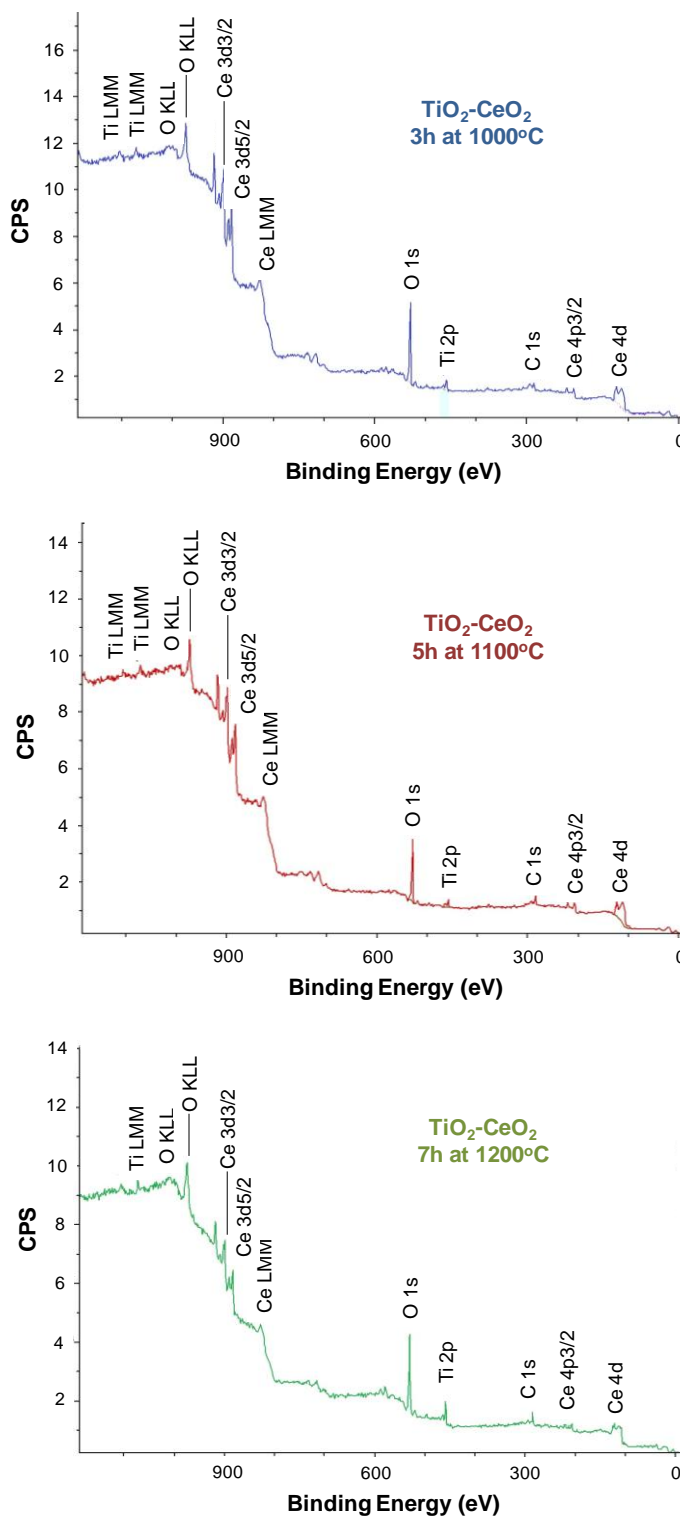
Figure 4.16 – XPS spectra for cold-pressed TiO_2-CeO_2 pellet surfaces prepared under different conditions: 3h at 1000°C (top), 5h at 1100°C (middle) and 7h at 1200°C (bottom).

Peak energy levels for Ce and Ti also remain broadly identical between samples, however the O spectra for the pellet sample sintered for 7h at 1200°C shows slightly more intense responses, and this is coupled with an over stoichiometric recorded O at%, from 68% to 71%. Work has previously covered the prospect of conductivity shifts via oxygen vacancies or titanium interstitials in (non-stoichiometric) rutile TiO_2 at elevated temperatures (800°C to 1100°C)[200,201]. Conversely the effect of TiO_2 over oxidation has received sparse attention within the literature. When anatase TiO_2 was doped with Ce for the development of a new adsorbent material for Thiophene ($Ti_xCe_{x-1}O_2$), it was noted by DFT calculations that Ceria acted as an 'oxygen reservoir' to form O-rich sites[202]. However as no co-oxide formation could be detected by XPS or XRD and no colour shift was observed during sintering of ZrO_2-CeO_2 at similar temperature ranges, evidence supports a chemical transition in the TiO_2 rather than ceria.

The prospect of over oxidation is intriguing, as non-stoichiometric over-oxidised UO_{2+x} has been investigated in its electrical properties and shown to offer substantial increases in conductivity (**Figure 4.17**)[203]. These increases would allude to a more amenable initial electroreduction paradigm, potentially increasing current efficiency and facilitating swifter pyroprocessing. Further consideration on the general possibility of preparing metal oxides for FFC reduction via this approach is interesting in its simplicity and relative ease, however wasn't pursued further here as access to active materials was lacking, particularly large enough quantities for subsequent analytical techniques.
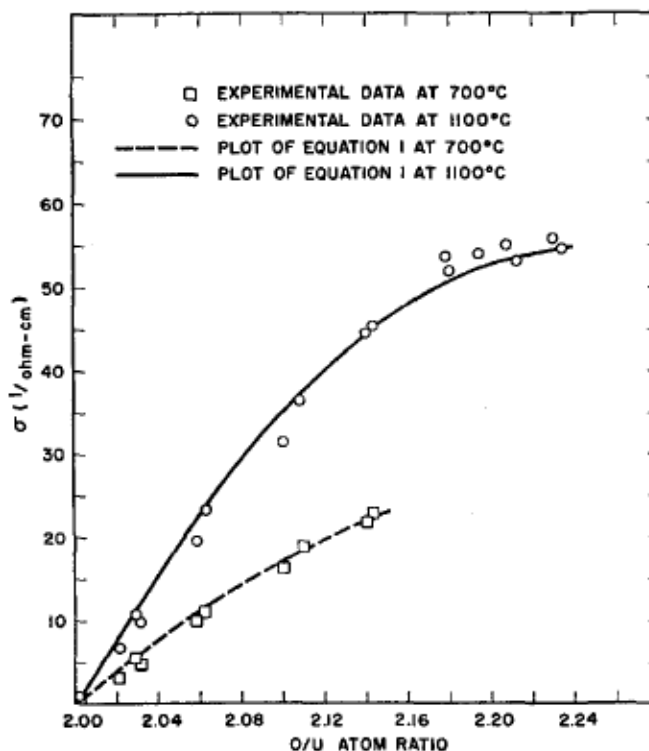
Figure 4.17 – Conductivity changes of non-stoichiometric UO_{2+x} (where $0 \leq x \leq 0.24$) at 700°C and 1100°C.

The lack of significant peak shift in the XPS data indicates that there is no chemical difference between samples (i.e. the rutile transformation must be nearing completion when sintering at 1000°C for 3 hours). This is supported by the very marginal shift to lower binding energies for the Ti2p spectra from around 459eV to 458.6eV observed as sintering time and duration increased[204].

Given that the open porosity of samples sintered at 1200°C was consistently less than 40%, coupled with the introduction of parameters beyond the capacity to investigate within this thesis and a desire to limit energy consumption, only pellets produced via sintering at 1000°C and 1100°C were used for electrolysis experiments. Overall the cold-pressed pellets after sintering at intermediate temperatures showed excellent porosity characteristics and mechanical integrity when producing the working electrodes.

4.2.1.3.2 Slip Casting

Several batch production runs of slip cast TiO_2-CeO_2 were trialled as an alternative method to cold-pressing for the rapid forming of homogenously mixed oxide powders. Solid slip casting is a traditional method for ceramic particles involving the mixing of particles in a liquid suspension (termed a slip) which is poured into a mould were the liquid is gradually removed by capillary action from the pores within the mould. The slip is continually added until the mould has been completely filled with the drained and semi-compacted ceramic green form, which is then left to further dry and contract slightly ready to be removed from the mould. Preparation of an effective and well dispersed slip was accomplished through ultrasonication to encourage suspension in deionised water at a 2:1 mass ratio, ensuring a non-viscous solution. Another key factor which influences suspension characteristics is the electrical surface charge of particles and the surrounding solution, quantifiable by the measurement of zeta potential.

It is possible to modify particle surfaces within the slip to give like charges and repulse each other, hence avoiding agglomeration build up. However the use of deionised water and vibrational dispersion proved to be simple and more than adequate in achieving a satisfactory slip suspension. In an effort to adhere to the realisms of safety concerns from potential airborne contamination, ball milling wasn't applied for oxide preparation and instead the slips were produced from powders as-received. The mould was fabricated from plaster of paris ($CaSO4_2 \cdot H_2O$) and designed to batch produce 50 slip cast pellets (**Figure 4.18a**), with an approximate final diameter of 8mm and height of 3 mm.
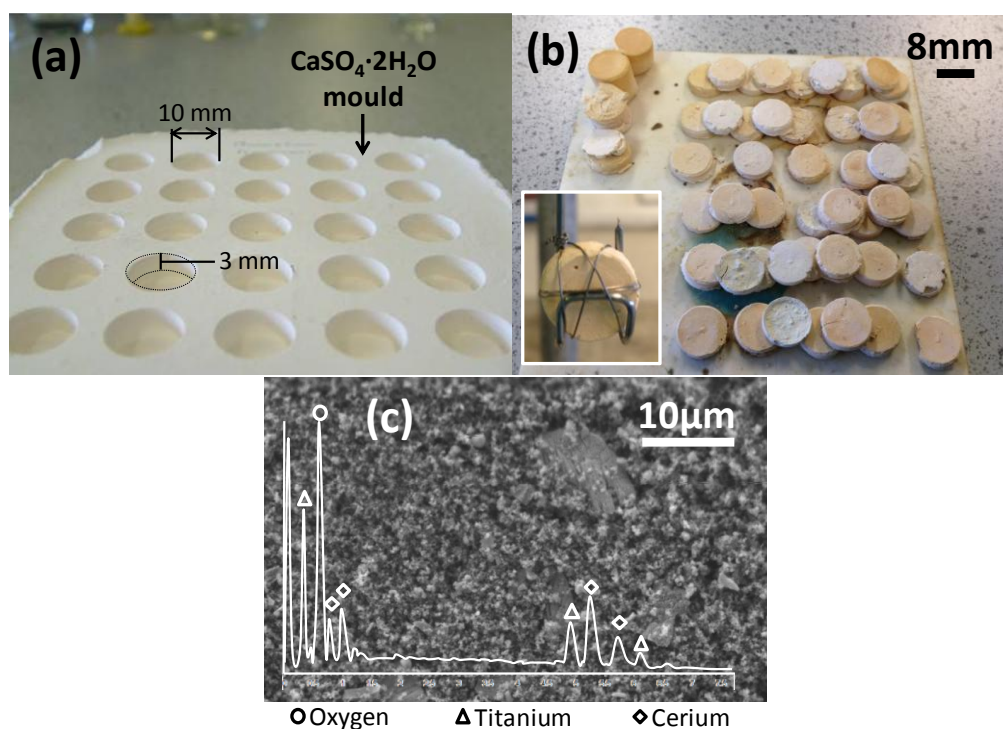
Figure 4.18 – (a) image of the plaster of paris mould used to slip cast TiO_2-CeO_2 binary oxides (b), and (c) SEM and EDS analysis of pellet surfaces from (b).

The produced slips were generally very uniform and released well from the mould. An image of the recovered green forms from two batches is shown in **Figure 4.18b**, with SEM and EDS analysis (in **Figure 4.18c**). Dimensional consistency of these slip cast pellets were not as ideal as those produced from die pressing and included uneven textures and an nonconformity in thickness. The base causes of these observations were likely a combination of uneven drainage of the slip through the mould and an uneven rate of pouring into the cavity. An automated solution which could apply pressure to the slip reservoir should in theory mitigate both of these issues.

A random selection of 20 slip cast pellets were then subject to a base sintering programme of $1000^{\circ}C$ for 2 hours in order to compare the effects of densification between slip and pressing based preforms. **Figure 4.19** highlights the substantial amount of shrinkage experienced after a relatively rapid sintering procedure, equivalent to between 37% and 49%.
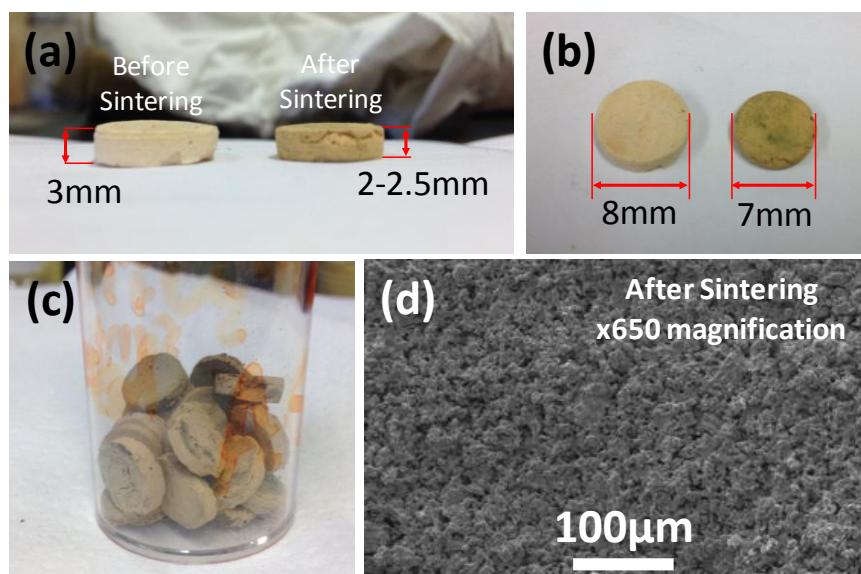
Figure 4.19 – Before and after sintering photographs of the slip cast TiO_2-CeO_2 pellets with dimensional variation (a) side view and (b) plan view. (c) Image of sintered TiO_2-CeO_2 pellets and (d) SEM image of the sintered surface from (c).

The cause of extraordinary decrease in volume is likely a function of the lack of pressing force applied during forming, hence the act of sintering introducing considerably more grain boundary growth. The density of these sintered slip cast pellets are also more in line with what has been measured from the die pressed pellets under similar conditions. Additionally the same colour shift, albeit to a lesser extent, was shown to occur when sintering the slip cast pellets at a much more modest temperature of 1000°C compared to the 1100°C to 1200°C required for the die pressed forms.

The mechanical integrity of the sintered slip cast forms exhibited great promise and required significant effort to snap by hand. Overall the mass production of pelletised oxide forms by slip casting had proved successful using an extremely simple manufacturing methodology that yielded a 100% recovery rate. Further investigation of larger slip cast forms from a ternary oxide composite (TiO_2-Al_2O_3-V_2O_3) are explored in Appendix 1.

4.2.1.4 PuO_2 and MOX

The active materials used at the NNL facility were supplied by Sellafield Ltd. originating from their reprocessing actions. The pure PuO_2 is isolated from recent spent MAGNOX fuels (MAGNOX being a graphite moderated obsolete reactor developed by the UK and using Mg-Al clad fuels) via aqueous processing. The PuO_2 in the MOX makeup however is sourced from the Thorp facility as Sellafield dealing with oxide spent fuels from a variety of UK and international inventories, and is combined with depleted UO_2 which is a by-product of the enrichment process.

The age of the material is of critical importance owing to the radioactive decay of fissile materials introducing contaminants into the fuel matrix. Although there are systematic methods of accurately predicting the fuel composition at a given decay time from knowing the exact original composition and the axiomatic half-life of unstable isotopes, the decay products are still undesirable from a point of fission energy yield and frequently a higher radioactive output. The PuO_2 provided for these studies were obtained from a reprocessing plant less than two years ago, so the potential contaminants are predicted to be in the region of ppb to ppm. As such the likelihood of observing transient redox features during CV investigations of non Pu/U base species is very low. Particle sizes of the materials here could not be directly verified as electron or optical imaging was not available and the powders were confined to the working glove box. However batch samples of MAGNOX produced PuO_2 have been imaged elsewhere and are shown in **Figure 4.20**[195]. The SEM images here show square particles at around 2 μm thickness or crystallites with truncated square profiles or square pyramid forms. All have reasonable porosity; apparently developed by a loss of escaping gases during calcination.
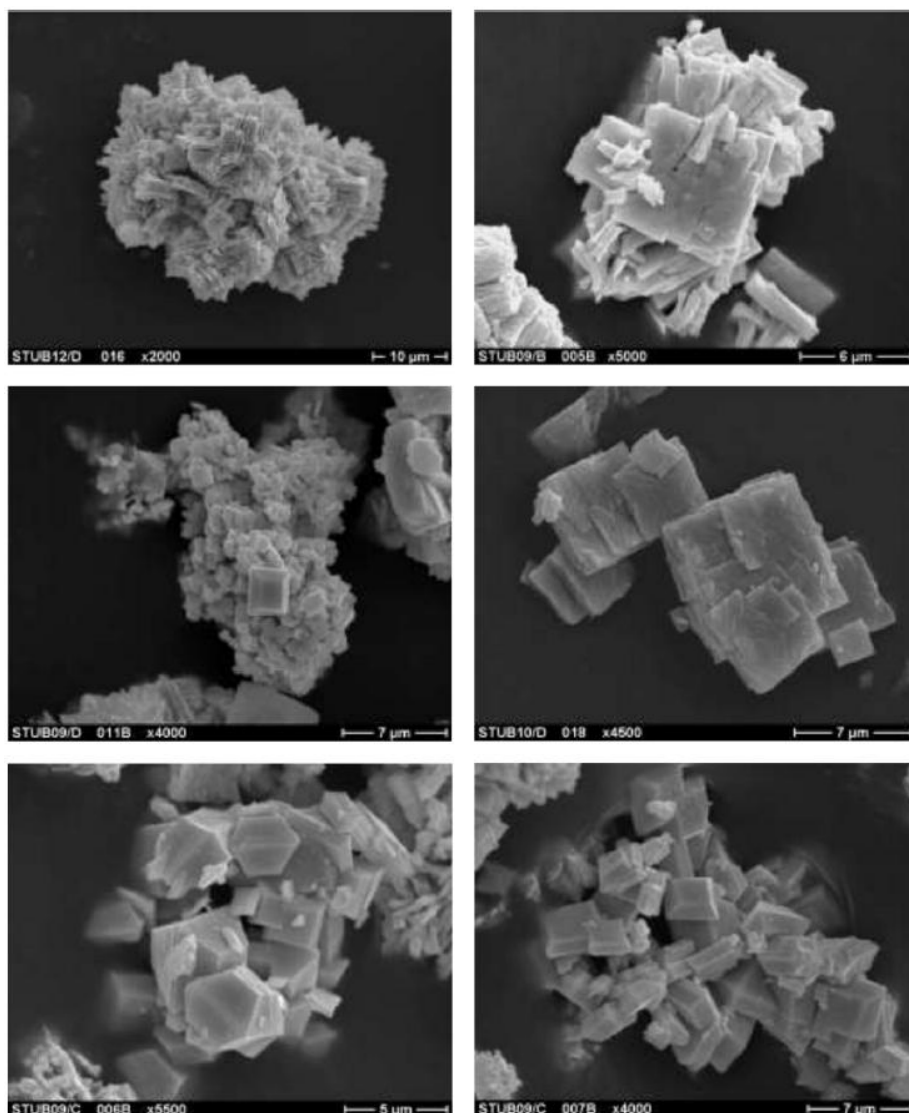
Figure 4.20 – Various SEM images of MAGNOX PuO_2 obtained from a single production batch[195].

Other researchers have concluded that PuO_2 can take various forms including densely packed spherical particles with high specific surface area (SSA)[205], but the final appearance appears to be in accordance with the specific parameters used during production. This is usually from the calcinations of plutonium oxalate, where factors such as calcination duration and temperature as well as the oxalate production factors (Pu concentration, acidity etc...) directly influence the morphological features of the produced powders. Essentially this allows for pre-selection of features for PuO_2 production from spent fuels. The basic characteristics of

PuO$_2$ here show broadly similar angular crystal structure to the CeO$_2$ powders purchased commercially and used for partitioning experiments; however the discrepancies in particle sizes may well contribute to a divergence in observable features during CV or other electrochemical investigations. In the conceived functional pyroprocessing methodology, the PuO$_2$, UO$_2$ and other actinides will be used directly from the reactor and so any structural features associated with the aqueous separation technologies, such as precipitation and calcination, will become redundant. However as currently the only readily available means of isolating PuO$_2$ comes from PUREX and its derivatives, the characteristics of the feed material used was tied to these properties of production.

4.3   Conclusions

The logical development of an electrochemical pre-treatment methodology for both CaCl$_2$ and the LCE molten salts has been explored in this chapter. Using the hydrated form of CaCl$_2$ offers benefits in terms of lessening process costs, but even when anhydrous CaCl$_2$ and LiCl are used their hydroscopic nature necessitates a drying procedure be applied. The effects of excess moisture within the FFC Cambridge Process cell can be severe, including high temperature corrosion and reducing electrolysis current efficiency by increasing ambient background currents.

By avoiding the use of chemical oxidants to remove oxide and hydroxide species, issues associated with unfavourable chemical regeneration of the oxidising agents can be avoided. The 'pre-electrolysis' option pursued for this work has been optimised for each molten salt system and shown to perform remarkably well in removing redox active contaminant species as exemplified by the wide and stable potential windows observed during CV. Background currents during pre-electrolysis at 1.8V in CaCl$_2$ and 2.6V in LCE were shown to reach low and stable levels after being performed

overnight and avoided the reduction of any present CaO within the melt or the dynamic evolution of carbon particulates from the graphite anode. A theoretical basis for an integrated salt recovery methodology was also explored, as to recover the electrolyte for reuse which can help limit the costs of a pyroprocessing system. The nuclear orientated paradigm likely dictates spent salt from electrolysis be classified as a high level waste (HLW), however recovery and purification of crucial spent fuel actinide contaminants is still a necessity and a pragmatic means of achieving this through an additional electroreduction and refining was explored.

Morphological characterisation of all oxides both as-received and in composite binary form (where applicable) was performed by SEM and accompanied by EDS and XRD analysis to confirm stoichiometry. The variation amongst the commercial powders was often vast so homogenisation proved vital for standardising size distributions of oxide particles as well as ensuring thorough mixing. The active PuO_2 and MOX powders could not be directly analysed due to procedural restrictions, however previous analysis of powders from the same fabrication facility was provided. By using ball milling, spherical powders as small as 200 nm could be produced which proved helpful in the successful pelletisation of the CeO_2-ZrO_2 binary.

Aspects of the pelletisation process were assessed in their influence on final porosity, a factor known to directly affect the reduction extent or even capacity of the FFC Cambridge Process to yield metals. Pressing force during cold pressing had no discernible affects on final porosity, however did decrease the spread of porosity values as higher forces were used. The effect of high force on pellet stability was more apparent however with lamination occurring on green forms at forces of 1GPa. Furthermore the final height of the sintered TiO_2-CeO_2 forms were found to directly influence

extent of mechanical failures experienced, with those below 2.9 mm found to experience no apparent shearing or cracking.

Sintering temperature was shown to have a discontinuous influence on the TiO_2-CeO_2 binary oxides between 1100^oC and 1200^oC, where porosity was on average around 15% lower. No chemical shifts however could be observed for any of the oxides studied following sintering, suggesting no thermally induced co-oxide or over oxidation states formed. A batch method for slip casting the TiO_2-CeO_2 was developed and found to be amenable compared to the cold pressed fabrication methods in terms of producing durable forms. Optimisation of fabrication methods should be seen as an imperative step towards the eventual adoption of a more sustainable pyroprocessing technology and the work here has explored various simple methods to improve the quality of starting materials. Electrolyte conditioning for the energy efficienct electrolysis of metal oxides is considered more in Chapter 5, whereas the reduction and partitioning characteristics of the preforms produced here are explored in Chapter 6 and Chapter 7.

Chapter 5

Enhancing Electrolyte Ionicity

5.1 Introduction

Ideal electrolytes for the FFC Cambridge Process require kinetic conditions which enhance ionic transfer of O^{2-} ions (i.e. electrolytic conduction), whilst having as feasibly low as possible electronic conduction. Electronic conduction within molten salts represents a source of considerable energy consumption and remains a fundamental barrier towards the high current efficiency of various industrial processes and refractory methods, such as molten salt electrowinning and electrorefining[92,151,206–208]. Concordantly the wider acceptance and industrial application of the FFC Cambridge Process is dogged by issues relating to unacceptable levels of current efficiency, historically less than 30% for TiO_2 reduction[81,209]. Presenting both technological and theoretical concerns, the understanding of electronic transport phenomena within an electrolytic cell is a requisite for optimal performance not only FFC based reduction but of all molten salt electrochemistry.

In Chapter 4, exploration into the use of pre-electrolysis as a method of removing metallic contaminants was given. This is a significant first step in removing impurities which can contribute to electron mobility, a prominent cause of undesirable background currents that arise during electrolysis as discussed below. This chapter goes further and considers an inherently elegant yet imperative case of optimised cell and electrode design, with the aim of limiting aspects of electron mobility with molten salt electrolytes to both reduce energy consumption and speed up electrochemical processes.

152

5.2 Improving Electroanalytical Techniques

5.2.1 Sources of Electronic Conduction

Previous research has been able to demonstrate that the origins of background current generated via electronic conduction in molten salt electrolytes are likely quite diverse. For example it was established that the redox active multivalent metal complexes Ta(V)-Ta(IV) and Nb(V)-Nb(IV) provided a means of 'electron-hopping', which directly contributed to the semi-electric nature of the investigated CsCl-NaCl eutectic[210]. The form this mechanism manifests is visualised in **Figure 5.1** and exemplified in **Equation 5.1** for Ta complexes, given a solvated metallic state within the molten salt.
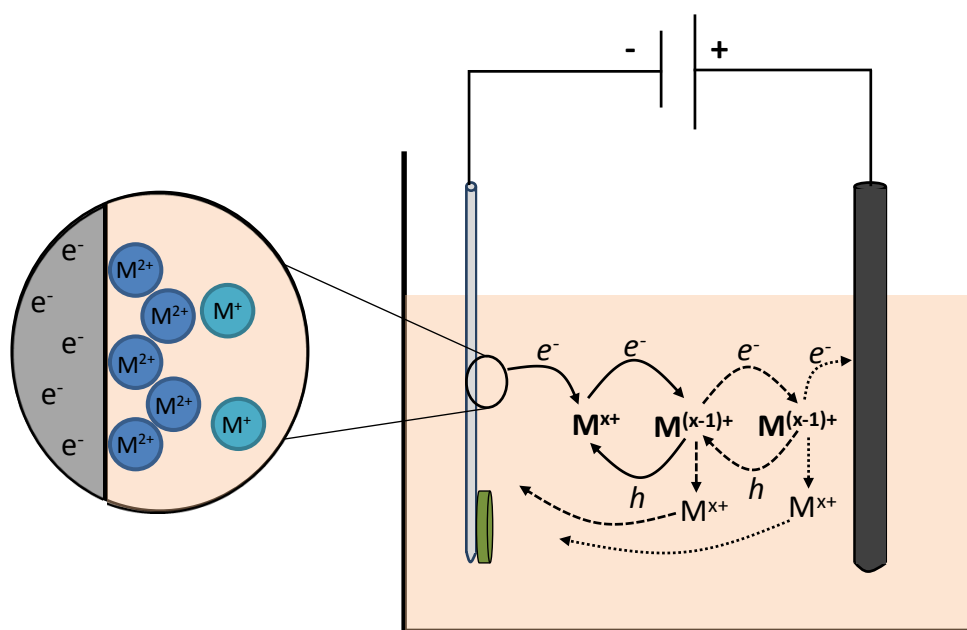
Figure 5.1 – Mechanism of electron hopping in metal (M) rich molten salts.

$$_A Ta(V) + {_B}Ta(IV) \rightleftharpoons {_A}Ta(IV) + {_B}Ta(V) \qquad \textbf{5.1}$$
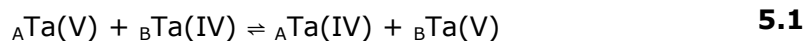
This example is specific to the case of an intentional addition of soluble metal containing species to the electrolyte for electroreduction, whereas the process being developed here uses a solid oxide feed out of solution. Additionally the combined thermal-electrochemical dehydration and cleaning procedure applied to the electrolyte should leave impurities mostly

absent, and CaO presence below 0.1%[136]. However, if the salt was inadequately cleaned then hydrolysis could occur and lead to further CaO formation which is problematic as the decomposition voltage of CaO is approximately 2.7 V at 810°C. Under the typical applied cell voltages, or potentials given a reference redox reaction, the reduction of Ca^{2+} to a lower valence state may be possible. Additionally the use of a carbon anode further reduces the necessary cell voltage for Ca^{2+} reduction by lowering the anodic discharging potential of O^{2-} ions to form CO_2 or CO. Hence the presence of Ca^{2+} ions not only lowers current efficiency from being a source of electron consumption via side reactions, but also (assuming the produced Ca is not consumed by the oxide electrode to form intermediate compounds) it can increase electronic conduction through dissolution into the molten salt and occurrence of electron hopping, by **Equation 5.2**.

$$_ACa(I) + {}_BCa(II) \rightleftharpoons {}_ACa(II) + {}_BCa(I) \qquad \textbf{5.2}$$
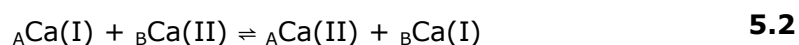
Where the presence of Ca(I) can be associated with either underpotential deposition on the electrode interface or via disproportionation, i.e. $Ca^0 + Ca^{2+} \rightleftharpoons Ca^+ + Ca^+$. Consequently it can be concluded that the miscibility of molten metals within their constituent metal halide complexes itself contributes to increased electronic conduction[206], which in electrochemical processes is generally caused by a high overpotential reducing the disassociated alkali/alkali-earth/transition metal ions.

Secondly if the applied voltage is considerable enough, the electrolytically mediated decomposition of molten chloride salts will lead to the discharge of anodically generated chlorine, facilitating a transformation from non-metallic to metallic states. The metallic forms produced dissolve into the molten salt and act as electron sinks or centres for immobilisation, but moreover can effectively introduce 'vacancies' within the melt that are

thought to cause shifts in electronic conduction through localised defects. For example in molten monovalent metal salts, features such as F-centres (electron trapping in anionic vacancies to maintain charge neutrality) and bipolarons (atomic lattice distortions to screen electron charges) have been described[210]. These states exist only on the picosecond timescale but can cause troublesome potential fluctuations during data recording of electroanalytical processes[211–213] (signal noise during voltammetry for instance) and are difficult to remove. Detailed quantum modelling of excess electrons in molten salts via molecular dynamics (MD) and Monte-Carlo simulations have been considered further elsewhere[214,215] to describe these effects. Clearly there is a dynamic characterisation of the molten salt conductivity, determined as a function of its composition[216] and characterised by the equilibrium of mobile and localised electrons[217]. The relationship of excess electrons in an electrolyte can be described by a function of electronic and ionic conductance, as shown by **Equation 5.3**, and identifies a key parameter of improving electrolyte ionicity to a more ideal condition is to limit electronic conduction.

$$t_e^o = \frac{\sigma_e}{\sigma_t} = \frac{\sigma_t - \sigma_i}{\sigma_t} \qquad \textbf{5.3}$$

Where t_e^o is the transport number of electrons, σ_e, σ_t and σ_i the electronic conductivity, total conductivity and pure (ionic) conductivity respectively[218]. Limiting aspects of electronic conduction will increase the total resistance of the cell, however in doing so improves efficiency by limiting undesirable parasitic sub-reactions. The effects of this approach can be clearly demonstrated in the aesthetic change in CV curves where the change in current response per unit change in potential is limited in those electrolytes with better ionic to electronic conduction ratios, where charge transfer is better represented by the desired faradaic reaction(s) rather than background processes (e.g. **Figure 5.2**).
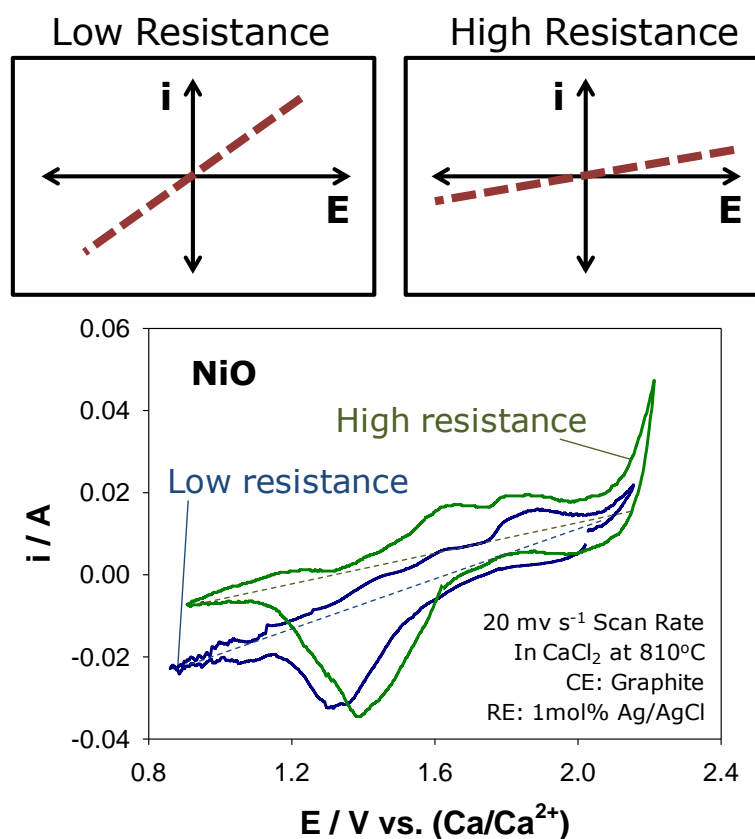
Figure 5.2 – Diagrams of the expected current response from sweeping potential in low and high resistance electrolytes (top). CV plots of NiO demonstrating the slope of the current response of the first cycle is less in a higher resistance melt.

Beyond the previously described electrochemical methods of limiting electronic conduction via the electroplating of impurities, a physical alteration of electronic field lines in the cell may offer a simple, immediate and effective improvement to electrolysis experiments. By interrupting the field by which solvated species migrate, it is believed that the mean free electronic pathway will also be disrupted, shifting focus to a more ionically dominated conductivity.

5.2.2 Manipulation of Electric Field Lines in CaCl$_2$

5.2.2.1 Molten Salt Electronic Field Structure

In a two electrode cell under polarisation there is a dominant conductivity that converges and diverges between the electrodes to form a predictable yet electrodynamic field. Test particles of unit charge within the field

experience a Lorentz force, determined by the strength of the field and distance away from the test charge, i.e. how large the polarisation energy is and how far away from the electrodes a particle (or solvated species) is. **Figure 5.3** gives a schematic representation of how these fields likely manifest in two dimensions in unmodified and interrupted two electrode electrochemical cells under polarisation.
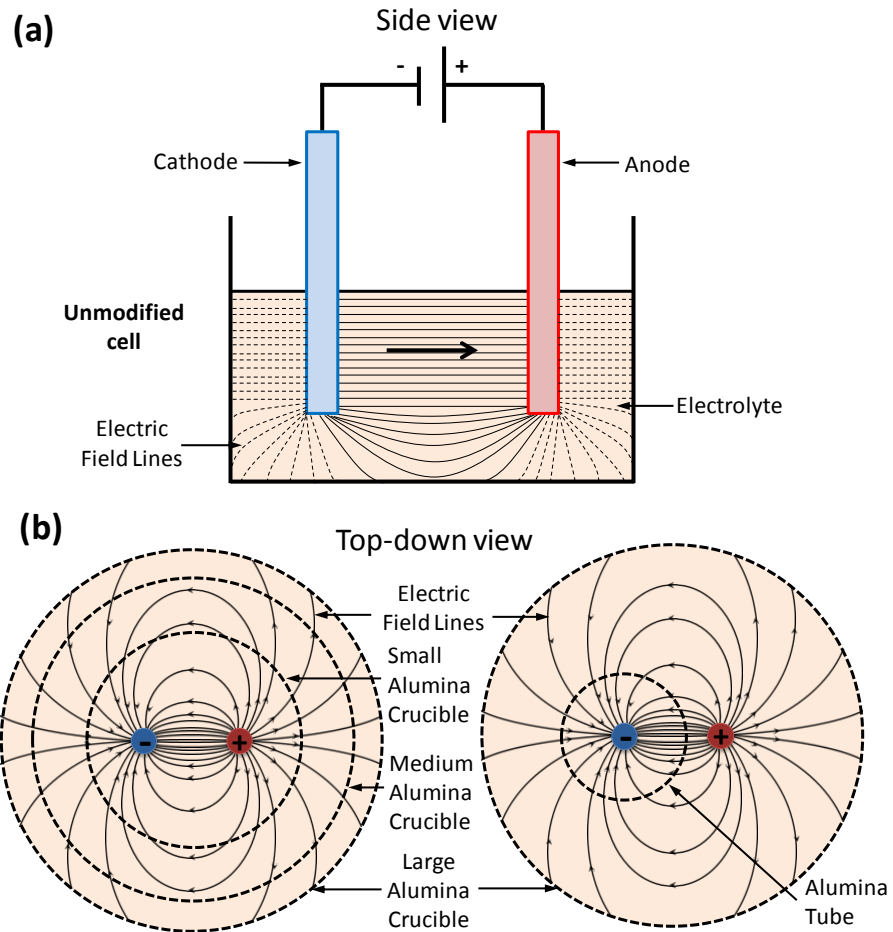
Figure 5.3 – (a) Side view of an unmodified two electrode cell experiencing polarisation and how electric field lines may manifest. (b) The same cell from (a) from a top-down perspective, including a scale presence of non-conductive barriers (smaller alumina crucibles and tube) which would interrupt field line provided the position of the electrodes remained constant.

In **Figure 5.3a**, the strongest Lorentz forces will be experienced in the region directly between electrodes where the field structure is at its most dense, as denoted by solid black lines. By reducing the immersion depth of the cylindrical electrodes the effective surface area decreases and is

understood to limit the influence of iR drop and diffusion dependant responses, for example the fabrication of planar microelectrodes ($20\mu m^2$) have demonstrated enhanced electroanalysis properties in LKE molten salts[219]. Reducing the total quantity of molten salt can perhaps have an even greater benefit as the effective surface area may decrease by a comparative amount as raising the electrodes, however the lesser salt quantity reduces the physical space for the electric field to persist hence increasing electric resistance, and the use of smaller quantities of molten salt is of course economically preferable. **Figure 5.3b** outlines how given the static position of the cathode and anode, the electric field structure could be interrupted by the inclusion of non-conductive barriers in addition to the benefits of limiting molten salt quantity. Here the extent of field lines are interrupted when narrower non-conductive crucibles are used, theoretically providing the same type of decrease in electric conductivity as minimising salt quantity.

The alumina crucibles selected and assessed for this hypothesis were outlined in Chapter 3 (**Figure 3.4**) with total capacities of 399 g (large), 320 g (medium) and 60 g (small), in addition to a narrow graphite crucible with capacity of 44 g. These capacities were also approximately halved for the medium (167 g), small (30 g) and graphite (22 g) crucibles to assess the change in molten salt impedance via a decrease in salt quantity. In later studies an alumina tube (19 mm ID, 3 mm wall thickness; Almath Crucibles) was inserted into the largest alumina crucible and used to house the working electrode for CV investigations or oxide pellet during direct reduction. A hole (10 mm diameter) was drilled at 5 mm above the base of the tube and below the salt meniscus to allow the migration of O^{2-} anions through the melt, and two holes drilled higher up the tube to equilibrate pressure and permit complete argon saturation of the cell.

5.2.2.2 Impedance Effects from Varying Molten Salt Quantity

In molten alkali chlorides containing surplus transition metal species, the Wagner-Hebb polarisation method is often employed as a means of measuring partial electronic conductance[206,217]. However owing to an origin in solid state measurements and inherent difficulties in the interpretation of achieved results as previously reported[220,221], EIS was instead used to assess electronic resistance in the melt. The electrolyte or more generally the solution resistance (R_e) is directly measured via EIS at high frequencies and is effectively the reciprocal of total electrolyte conductivity (σ_t) when corrected for the electrical resistivity, ρ ($\Omega \cdot m$), area of electrode interfaces, A (m^2), and the distance between electrodes ℓ (m), as in **Equations 5.4** and **5.5**.

$$\rho = 1/\sigma_t \qquad \textbf{5.4}$$

$$R_e = \rho \frac{\ell}{A} \qquad \textbf{5.5}$$

There are some considerable limitations with the above simplifications, crucial among which is that for the relationship between total conductivity and electrolyte resistance to hold, a uniform current density must be present across the conducting material. For conductors such as metal wires, this approximation is virtually true, however due to the nature of electric fields the field strength and therefore density will be much weaker at distances radially away from the electrode surface. In regular solid conductors when an AC signal is passed, such as in the usage of EIS applied here, a 'skin effect' inhibits current flow in the centre of the material due to eddy currents caused by changing magnetic fields. In reality this means the geometrical cross section area deviates from the effective one, making the resistance higher. In the case of molten salts where conductivity occurs through a liquid medium this effect can be self correcting due to counter diffusional processes across chemical potentials.

The applied perturbation potential during EIS is required to be insignificant (0 V [OCP] in these investigations) so to not introduce redox activity and influence the molten salt quantity/crucible geometry parameters being investigated. In an attempt to mitigate the concern of current density fluctuation, the measurements of impedance here were made via a bespoke conductivity probe using two 1 mm diameter Mo wires in a duel bore alumina tube at 5mm immersion depth with a short working distance of 10 mm (**Figure 5.4a**).
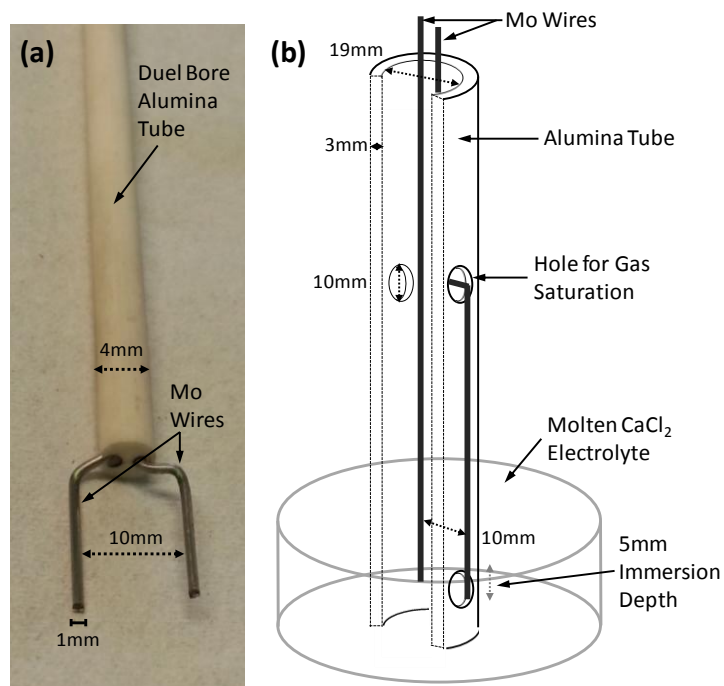
Figure 5.4 - (a) Image of the conductivity probe used for EIS measurements and (b) the modified design for EIS measurements when using the alumina tube.

Where the alumina tube modification was implemented EIS measurements were performed using two 1.0 mm Mo wires, one placed inside the tube and one outside with the drilled hole between them (**Figure 5.4b**). Immersion depth and separation distance of the Mo wires were kept identical.

Impedance measurements of pure molten salts can be expected to form an equivalency circuit of electrolyte resistance in series with a Voigt-like

element[183], however as metal impurities often exist which lead to faradaic reactions the circuit can often be more suitably characterised by a Randles type element[222] which includes aspects of Warburg impedance. Ohmic resistance in parallel to the Voigt or Randles element is interpreted as the electric resistance within the molten salt[217] (see **Figure 3.16**). In either case it is the electron impedance through the electrolyte which determines the ratio of electric to ionic conduction, and so ultimately the overall current efficiency. Assuming an equivalency circuit of electrolyte resistance in series with a Voigt element the molten salt impedance can be calculated by **Equation 5.6**.

$$Z = R_e + \frac{R_t}{1 + j\omega R_t C_{dl}} \qquad \textbf{5.6}$$

Where Z is the impedance, R_e the electrolyte resistance, R_t the charge transfer resistance between the electrode and electrolyte, ω the angular frequency and C_{dl} the double layer capacitance. Electrolyte resistance represents the real part of the equation and is frequency independent, hence can be measured directly using EIS at the intercept of the curve where the imaginary value equals zero. Whilst it is difficult to identify the source of conductance within the melt it remains much easier to quantify the electric resistance via impedance measurements, hence focus is given to electrolyte characterisation by the latter.

Nyquist plots as measured by EIS in the various crucible sizes and molten salt quantities at 810°C (using electrochemically pre-treated salt, 1.8 V for 18h) are shown in **Figure 5.5**. Each measurement was over a frequency range of 100 kHz to 10 Hz and the resultant average form three consecutive experiments, each with identical recording parameters. At all crucible capacities and salt quantities, including where an alumina tube was used in the largest crucible, the impedance spectra showed a partial hemi-spherical or hyperbolic shape at the chosen frequency range.

- • Medium Alumina - Full (310g)
- ○ Medium Alumina - Half Full (167g)
- ◆ Small Alumina - Full (60g)
- ◇ Small Alumina - Half Full (30g)
- ▲ Small Graphite - Full (44g)
- △ Small Graphite - Half Full (22g)
- ■ Large Alumina - Without Tube Full (399g)
- □ Large Alumina - With Tube Full (399g)
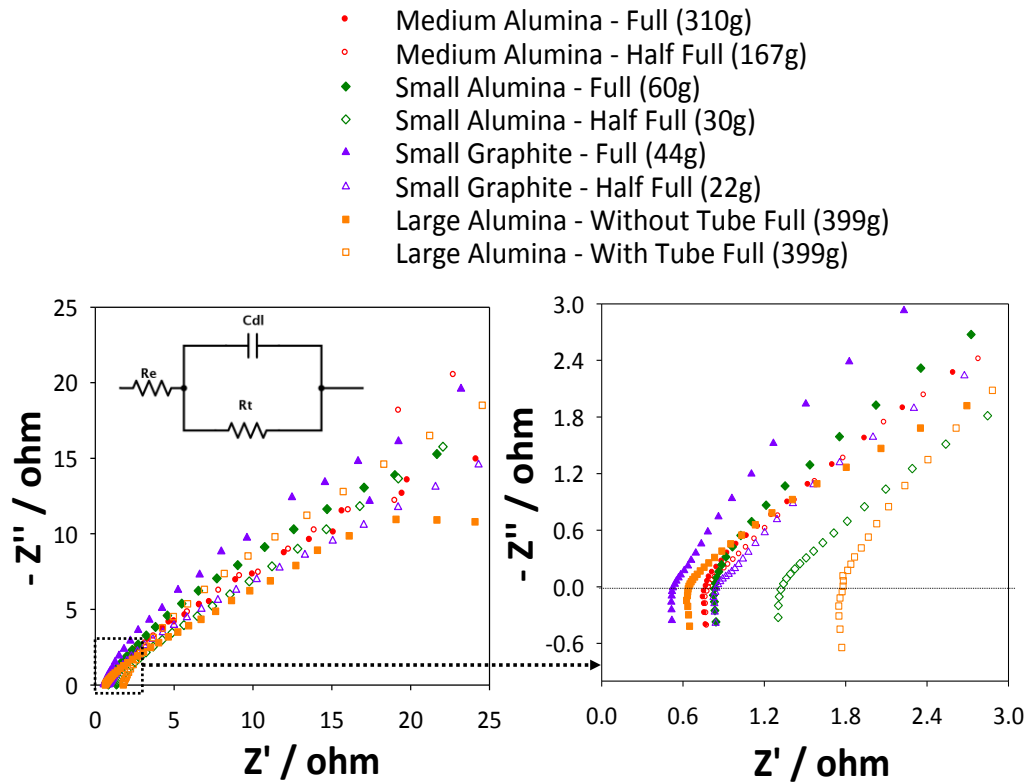
Figure 5.5 - Nyquist plots showing the impedance of various molten $CaCl_2$ weights in a range of crucible sizes at 810°C at full range (left) and scaled (right) to better observe solution resistance (R_e). Recorded with a Mo working electrode at a 0V bias potential (0.33 cm^2 surface area, 10 mm working distance). Inset is the equivalency circuit diagram based on impedance spectra.

The lack of a full semi-circular section on the spectra in **Figure 5.5** is an indication that the initial pre-electrolysis was effective in removing metal impurities that invariably lead to increased conductivity as described by Warburg impedance; specifically the diffusive transport of electro-active species. When considering the application of a 0 V bias potential during EIS measurements, the lack of definable charge transfer resistance (R_{ct}, by the presence of full hemi-spherical spectra) isn't unsurprising. Consequently any shift in electrolyte resistance when maintaining all other parameters is an effective shift in field structure due to the reduction in salt quantity. Crucibles with large quantities of molten salt (399 g and 320 g) showed the least electronic resistance (R_e value of 0.64 Ω and 0.78 Ω respectively), as shown in **Figure 5.6**.
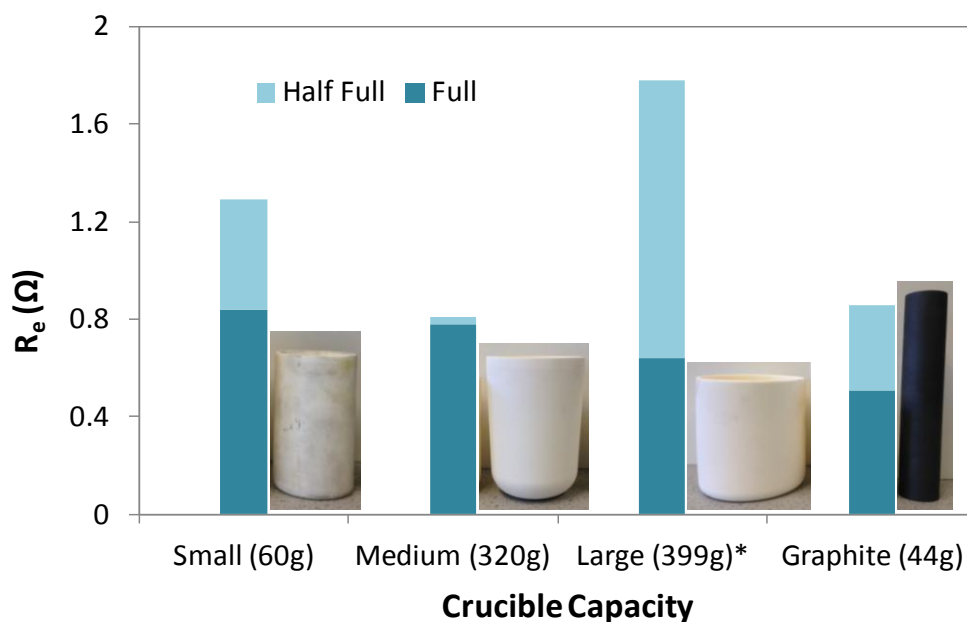
*The weight of salt in the large crucible was kept consistent and instead an alumina tube was inserted around the cathode for the 'half full' measurement.

Figure 5.6 – Plot of the average EIS recorded electrolyte resistance (R_e) versus various molten salt quantities in different capacity crucibles or designs.

Despite a usual focus of electronic conduction between fixed electrodes during polarisation, the higher weights (i.e. larger volumes) of ambient electrolyte permitted a greater degree of electron freedom via broad, uninterrupted electric field lines in the bulk electrolyte. Cell designs which utilise large volumes of supporting electrolyte are therefore subject to higher electronic conductance, a requirement for greater orders of electron hopping and subsequent current inefficiencies. It was the full graphite crucible (44 g of $CaCl_2$) which provided the least electronically resistive conditions (R_e value of 0.53 Ω). The small interior diameter of the graphite crucible most likely facilitated a favourable electronic conductive pathway through the crucible itself, negating any potential benefits to electronic resistance of using such small electrolyte quantities.

Once the electrodes were polarised during EIS measurement rapid species accumulation occurs via migration through the electrolyte that then supports electron diffusion through an established chemical potential.

Owing to unavoidable difficulties of positioning the conductivity probe within the graphite crucible, it's probable this arrangement allowed electron transfer on the electrode interface closest to the wall of the crucible. However an increase in electronic resistance was still observed when the salt volume was halved in accordance with results from the tested alumina crucibles. While it would appear that conflicting mechanisms exist where improvements to the electrolyte resistance were mitigated by the presence of a more direct electronically conductive pathway through the graphite crucible. Consequently in all future experiments the use of the graphite crucible design was avoided. In *ad hoc* CV measurements, the quality of signal response as a function of the change in current per unit change in potential was much poorer, likely from contributions of direct electronic conduction discussed here. Recorded R_e values are presented in **Table 5.1**.

Table 5.1 – Cell parameters, EIS derived electrolyte resistance and total conductivity for various quantities of molten salt in different crucible geometries.

EIS run	ℓ (cm)	A (cm^2)	R_e (Ω)
Small Crucible - 60g	1.0	0.66	0.84
Small Crucible - 30g	1.0	0.66	1.34
Medium Crucible - 320g	1.0	0.66	0.78
Medium Crucible - 167g	1.0	0.66	0.81
Large Crucible - 399g	1.0	0.66	0.64
Large Crucible - 399g With Sheath	1.0	0.66	1.78

Complementary to the impedance data for each molten salt quantity, current-time plots were produced by constant voltage electrolysis following pre-electrolysis in the small (60 g CaCl$_2$) and large (399g CaCl$_2$) crucibles as well as the large crucible with the alumina tube modification around the

cathode. A Mo cathode and graphite anode were employed and electrolysis was ran at 2.9 V until steady state currents were reached (**Figure 5.7**).
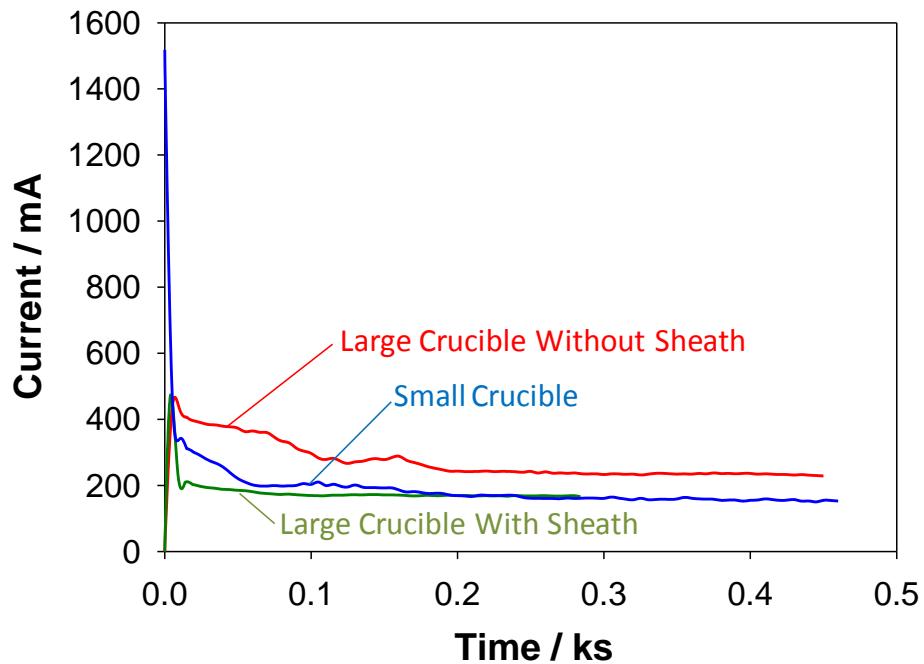
Figure 5.7 – Current versus time curves using a Mo MCE cathode and graphite anode for three different cells using pure, pre-treated molten $CaCl_2$.

Cumulative passed charge Q is automatically processed from the current-time plots by $I = dQ/dt$ and was used to calculate the electron diffusion coefficient, D_e, within the melt from **Equation 5.7**[206],

$$D_e = \frac{Il^2}{(Q - It)^3}$$
$\quad$ **5.7**

where I is steady-state current (A), ℓ the distance between electrodes (m), t the time taken to reach steady state (s) and where Q was the charge passed (coulombs) - measured after the background current was met[206]. The mobility of electrons, u_e, within the molten $CaCl_2$ can then be defined by a variation of the Nernst-Einstein equation (**Equation 5.8**),

$$u_e = \frac{D_e F}{RT}$$
$\quad$ **5.8**

where F, R and T all represent their usual definitions. The relationship between the total weighed $CaCl_2$ in each experiment versus the measured

electronic resistance by EIS polarisation is shown in **Figure 5.8a**; omitting resistances measured from electrolytes in the graphite crucible. A modest yet obvious increase in electrolyte resistance was observed as the total quantity of salt decreased, although it would appear that much of the perceived influence occurred at the extreme ends of measured weights. The nature of the molten salt electronic states was addressed by the partial measurement of electron mobility and diffusion coefficients which, plotted against the electrolyte resistance (R_e), are shown in **Figure 5.8b**.
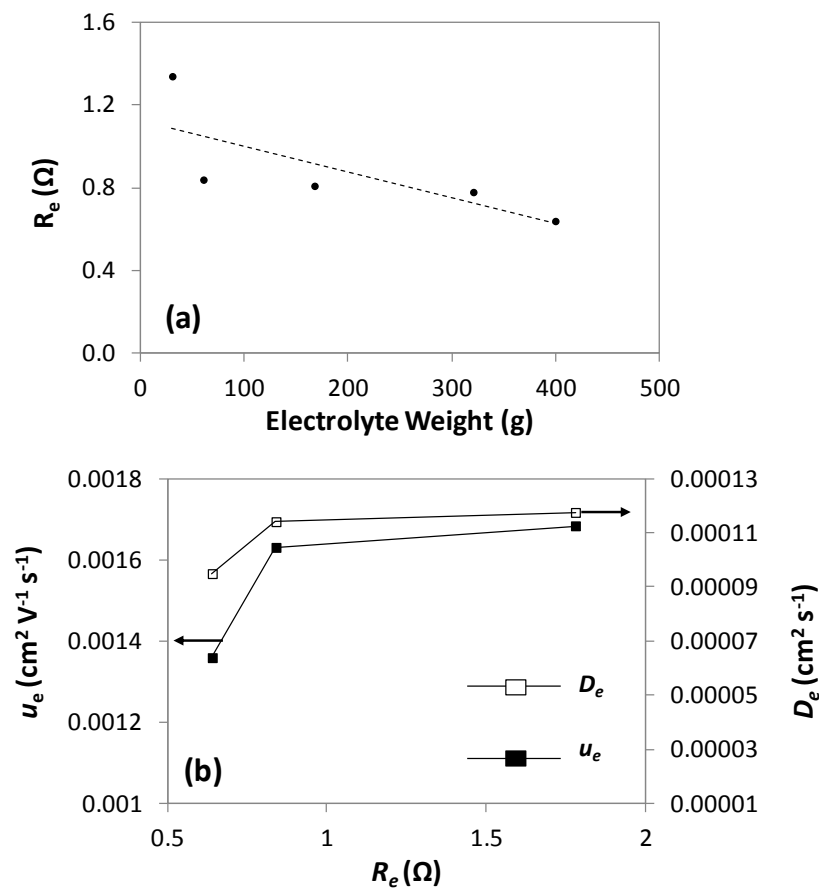
Figure 5.8 - (a) Dependency of $CaCl_2$ electrolyte resistance on the total weight of electrolyte and (b) the relationship of the electron diffusion coefficient (D_e) and electron mobility (u_e) to the electrolyte resistance (R_e).

Rather interestingly there was an apparent nominal increase in the dynamic electron states when the measured electrolyte resistance increased. A possible explanation for this observation is an unaccounted effect of crucible geometry on electronic field line strength. The perceived

change in electronic states should be small given the changes in mobility, and so it is probable that electrons remained relatively immobile within the melt over various R_e values. At the same time however the change in density of field lines induced by limiting the crucible size (salt weight and volume) benefited the prominence of ionic fidelity over electronic conduction via a spatial limitation in electron conductivity centres.

The diffusive process of electrons in molten salts has been frequently modelled as the 'jumping' between two sites in very short time scales (i.e. the formation of F-centres and through intervalance charge transfer of multivalent charge carriers)[223,224]. Given the comparatively small diffusive transport of electrons observed, an order of magnitude less than reported elsewhere for NaCl-Na (D_e = 9.4 x 10^{-3} cm^2 s^{-1} at 920 ^{o}C)[206] and KCl-K (D_e = 3 x 10^{-3} cm^2 s^{-1} at 277 ^{o}C)[72] solutions, it is likely only insignificant quantities of free calcium or other metal species were present within the molten salt. The Nyquist plot in **Figure 5.5** also confirms the lack of metallic impurities as achieved by pre-electrolysis treatment, which is in accordance with the electron diffusion values. Cumulatively this suggests an infrequent occurrence of such hopping events brought about by an electrolyte deficient in centres for localisation.

Elsewhere it has been shown that the addition of multivalent metals species in mixed fluoride salts actually increased the electronic resistance of the melt through the formation of stable solvated ion complexes (M_n^+-F_n^-)[225]. A similar conclusion was made when considering various chloride systems, such as Na+NaCl, Cd+$CdCl_2$ and Bi+$BiCl_3$, where each displayed a diminishing trend of solute resistance attributed to electron immobilisation in the covalent bond of neutral metallic dimers, i.e. M_2^0 [226]. Although no direct experiment was performed where metallic Ca was added to the electrolyte, after prolonged CVs using a sufficiently negative cathodic

potential beyond that of metallic Ca deposition, an increase in slope of subsequent scans was always present. It could be inferred that the accumulation of electrochemically produced metallic Ca has detrimental effects on the quality and response of qualitative electro-analytical processes, where electronic conduction is presented as a function of Ca activity and/or the concentration of multivalent impurities. If the formation of Ca_2^0 did occur in the molten $CaCl_2$ at 810^oC under these conditions, it could be either in quantities too modest to provide a tangible contribution to a R_e decrease or ephemeral and non-stabilising. What is more probable however, given the high thermodynamic stability of $CaCl_2$, the engineered deficit of CaO and the operational temperature of these experiments, is that Ca_2^0 specifically did not exist within the melt.

5.2.2.3 The Importance of Cell Design and Crucible Geometry

The insertion depth of the conductivity probe remained constant at all salt quantities, meaning the distance from the tip of the probe to the base of the crucible would have fluctuated based on the original salt height; a parameter not intrinsically tied to the weight itself but rather the shape of the crucible used. Most remarkably when a alumina tube modification was implemented in the largest alumina crucible, a 174.7% increase in resistance was observed despite no change in the total weight of $CaCl_2$. This considerable deviation can be explained by the perceived rather than actual reduction in electrolyte volume and applied physical limitation of the electric field lines within the small interior diameter (19 mm) of the alumina tube. Additionally, as the only spatial region for electron diffusion and species migration comes from the small hole below the surface of the molten salt, the effective cross sectional area of the housed electrode is limited and field lines from the rear surface of the both electrodes are subdued. The theoretical value of the cell constant (K) may therefore shift

when using the non-conducting sheath and different crucible sizes even though no absolute changes to electrode area (A) and distance between electrodes (ℓ) occur. All electrolyte resistances, electron diffusion coefficients and mobilities measured are shown in **Table 5.2**.

Table 5.2 - Electrolyte resistance (R_e), electron diffusion coefficient (D_e) and electron mobility (u_e) as functions of the mass of molten $CaCl_2$ (M) in an assortment of crucible sizes.

Crucible		M (g)	R_e (Ω)	D_e (cm^2 s^{-1})	u_e (cm^2 V^{-1} s^{-1})
Graphite (20/10/200)*		22	0.86	-	-
		44	0.53	-	-
Small Alumina (50/2/90)*		30	1.34	-	-
		60	0.84	1.14×10^{-4}	1.63×10^{-3}
Medium Alumina (76/3/108)*		167	0.81	-	-
		320	0.78	-	-
Large Alumina (85/4/100)*	Without Tube	399	0.64	9.48×10^{-5}	1.36×10^{-3}
	With Tube	399	1.78	1.17×10^{-4}	1.68×10^{-3}

*Numbers in brackets are in mm for the maximum internal diameter /wall thickness /height of the crucible.

To assess how the interruption of electric field lines influence the current response of electrolytic processes, CVs of ZrO_2 using different salt weights and of Cr_2O_3 using the alumina tube sheath in the largest crucible with identical salt quantities were performed.

5.2.3 Limiting Electronic Conduction during CV

5.2.3.1 Effect on ZrO_2 Features

An initial comparative was made to better define the relationship between the quantity of molten salt and the solution resistance by using the redox behaviour of ZrO_2 in the medium sized alumina crucible (320 g $CaCl_2$) and a small alumina crucible (60 g $CaCl_2$). The relative positions of the ZrO_2 loaded Mo MCE, graphite counter electrode and Ag/AgCl reference remained unchanged for each weight volume chosen. Present on a blank

CV curve (**Figure 5.9**) in 60 g of $CaCl_2$ at 810°C when scanned to very cathodic potentials (more negative than -2.18 V vs. Ag/AgCl) is the cathodic cross-over loop, a behaviour attributed to the deposition of Ca onto a foreign (Mo) substrate[136].
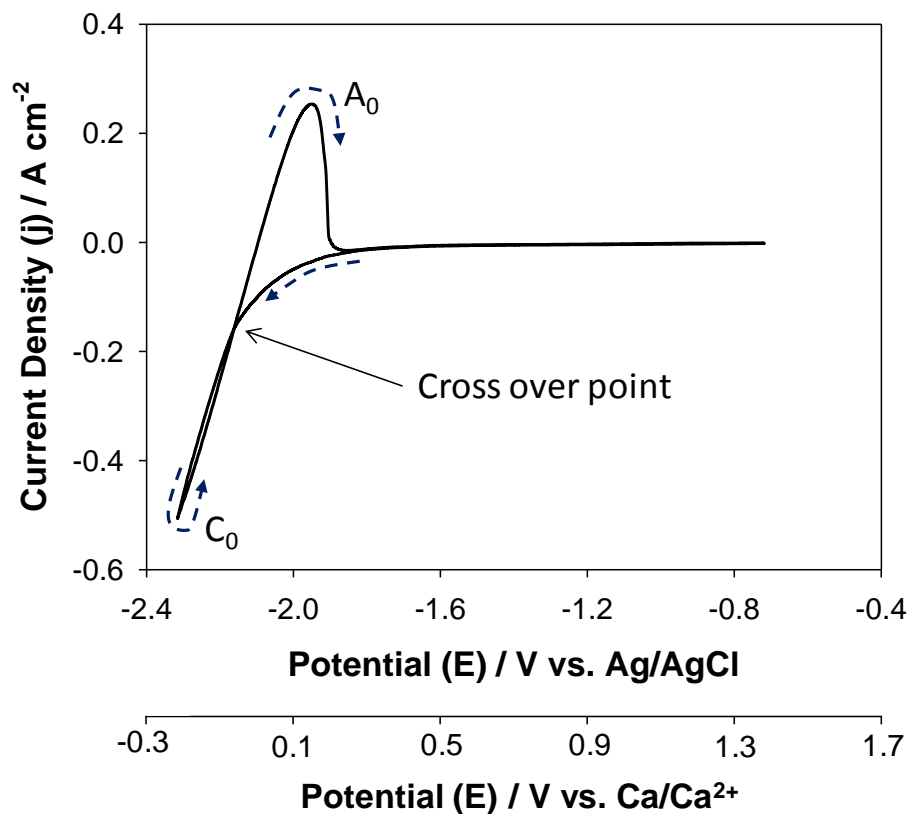
Figure 5.9 – Typical cyclic voltammogram of $CaCl_2$ at 810°C using a blank Mo working electrode. Inset is a second abscissa below the primary showing potential in relation to Ca stripping (Ca/Ca^{2+}) at -2.1 V vs. Ag/AgCl.

The blank CV in **Figure 5.9** along with all over CVs in this chapter were scanned at a rate of 20mv s^{-1}. For the measurement, the open circuit potential (OCP) was first recorded in the melt at equilibrium after all electrodes were immersed, and then used as the starting potential for voltammetry. As with the blank CV scan in **Figure 4.3**, the continuously increasing reduction peak at C_0 and the peak labelled A_0 are ascribed to the decomposition of the electrolyte and stripping of Ca metal respectively. It is thought the onset of the approximately exponential current increase leading to peak C_0 (at around -2 V) is caused by a reduction of the Ca^{2+}

ions to Ca^+ and Ca_2^{2+} ions, i.e. $Ca(I)$[227]. This is considered to be a phenomenon of 'underpotential deposition' of Ca^{2+} species, believed to be a property of the relatively high Ca solubility (1.5-3 %) in its molten chloride. Electrochemical processes which require the use of a molten salt electrolyte at high voltages may therefore suffer from non-ideal behaviour at prolonged electrolysis times, particularly in terms of achieving a low background current. A typical oxidation or stripping peak for Ca in $CaCl_2$ was recorded and labelled A_0. The onset potential for this reaction was occasionally used as a means of standardising redox potentials when different reference reactions, membrane materials or molar concentrations of reactant were used, with the scale shown on the secondary abscissa in **Figure 5.9**. Each ZrO_2 loaded MCE, measured in their respective crucibles and volumes of $CaCl_2$ electrolyte are shown in **Figure 5.10**.
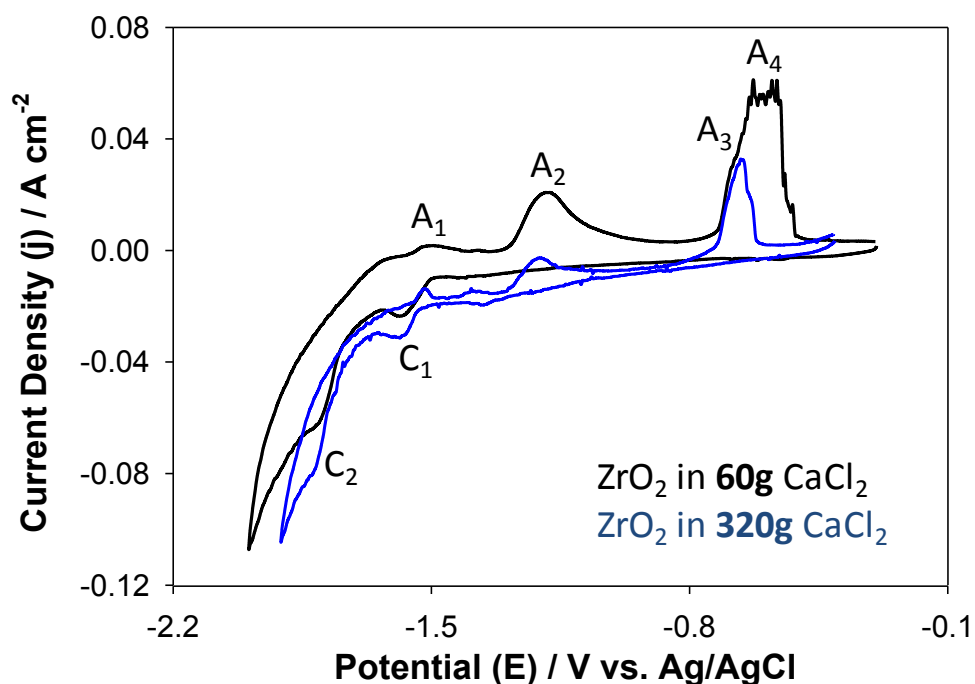
Figure 5.10 – CV scans of two ZrO_2 filled MCEs under identical conditions but in two different $CaCl_2$ masses: 320g (blue curve) and 60g (black curve).

When the ZrO_2 loaded MCE was measured in 60 g of salt, two cathodic peaks appeared at -1.54 V (C_1) and -1.75 V (C_2) which clearly are not visible from the blank scan, the second being obscured slightly by the

partial reduction of Ca^{2+} to Ca^+ [228]. These two peaks have been attributed to the two stage de-oxidation of ZrO_2 to Zr [227] by **Equation 5.8** and **5.9.**

$$C_1: \quad xZrO_2 + 2(x\text{-}1)e^- \rightleftharpoons Zr_xO + (2x\text{-}1)O^{2-} \qquad \textbf{5.8}$$

$$C_2: \quad Zr_xO + 2e^- \rightleftharpoons {_x}Zr + O^{2-} \qquad \textbf{5.9}$$
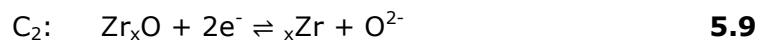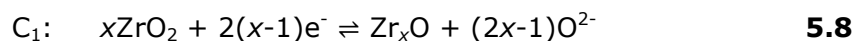
The two-stage full reduction is significant for ZrO_2 as a surrogate material as it deviates from the understood single step, four electron transfer reduction for UO_2 to U metal. However previous works of ZrO_2 reduction in pure $CaCl_2$ at 850°C have suggested the intermediate, Zr_xO, is metastable and undergoes disproportionation to ZrO_2 and Zr. Further insight into this observation from scans performed here is given in Chapter 6 for the ZrO_2-CeO_2 experiments.

Anodically, four current peaks exist at -1.55 V (A_1), -1.29 V (A_2), -0.73 V (A_3) and -0.68 V (A_4) corresponding according to thermodynamic calculations to the partial and full reoxidation of produced zirconium metal (i.e. the reverse of the above reactions); and at more anodic potentials, the chlorination of metallic zirconium to the dichloride and tetrachloride either directly or via a conversion of remaining Zr **Equations 5.10-5.13,**

$$A_1: \quad xZr + O^{2-} \rightleftharpoons Zr_xO \; 2e^- \qquad \textbf{5.10}$$

$$A_2: \quad Zr_xO + (2x\text{-}1)O^{2-} \rightleftharpoons {_x}ZrO_2 + 2(x\text{-}1)e^- \qquad \textbf{5.11}$$

$$A_3: \quad Zr + 2Cl^- \rightleftharpoons ZrCl_2 + 2e^- \qquad \textbf{5.12}$$

$$A_4: \quad Zr + 4Cl^- \rightleftharpoons ZrCl_4 + 4e^- \qquad \textbf{5.13a}$$

$$ZrCl_2 + 2Cl^- \rightleftharpoons ZrCl_4 + 2e^- \qquad \textbf{5.13b}$$
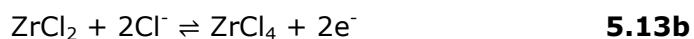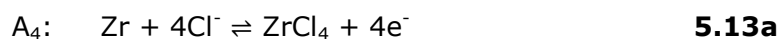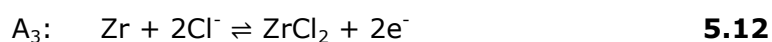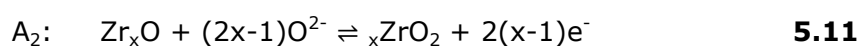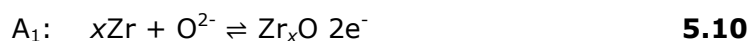
The gaseous phase of zirconium chlorides at the operational temperature yields the current fluctuation observed at peak A_4, resulting from the volatile release on the working electrode.

The overall slope of the CV in the larger weight of $CaCl_2$ is greater than in the smaller weight CV scan (5.2° vs. 3.3° slope angle), attributed to a smaller electrolyte resistance. As mentioned, the quality of the salt in both

experiments appears unchanged, including the presence of species to act as electron centres for electronic conduction. By physically restricting the field lines between static polarised electrodes, ionic migration of O^{2-} becomes a more dominant process and the influence of the broad exchange of free electrons in the melt relatively decreases by merit of **Equation 5.3**. This mechanism is illustrated from the change in appearance in the CVs in **Figure 5.10** and general aesthetic superiority to those from the literature[227]

5.2.3.2 Effect on Cr_2O_3 Features

The highest electrolyte resistance encountered by EIS measurement was by implementing an alumina tube sheath around the working electrode in the largest crucible and salt weight tested. This design merited further investigation by CV to see whether similar improvements in current response could be observed in relation to the large difference in electrolyte resistance. CVs of Cr_2O_3 loaded Mo MCEs are shown in **Figure 5.11**, which used an identical weight of salt (399 g), temperature (810°C) and scan rate (20 mV s^{-1}) for each scan, but with some experiments recorded using the alumina tube shielding the working electrode. Here the prominence of sloped behaviour from large $CaCl_2$ volumes, as compared to an environment of restricted electric field lines (by the presence of the non-conductive alumina tube) is clearly exemplified.

Redox features displayed on the CV obtained in the crucible without an alumina tube present are obscured by the higher increase in current per unit increase in potential, similar to the results obtained from ZrO_2 analysis. As a result charge transfer reactions become increasingly difficult to distinguish or even identify clearly from CV data alone. This is particularly apparent in **Figure 5.11a** where the Cr_2O_3 CV using the alumina tube (blue curve) clearly shows two reduction peaks on the

forwards scan believed to be an initial Ca^{2+} intercalation (C_1, **Equation 5.14**), followed by a direct, single step reduction from Cr_2O_3 to Cr (C_2, **Equation 5.15**)[121,160].

$$Cr_xO_y + Ca^{2+} + 2ne^- \rightleftharpoons CaCr_xO_z + (n-1)O^{2-} \qquad \textbf{5.14}$$

$$Cr_2O_3 + 6e^- \rightleftharpoons 2Cr + 3O^{2-} \qquad \textbf{5.15}$$
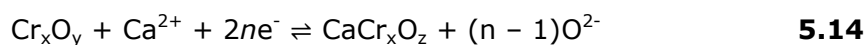
For **Reaction 5.14**, $z = y - (n-1)$. When n = 1, y = z and **Reaction 5.14** doesn't remove oxygen from the system, but instead can be compared to lithium intercalation within a discharging lithium-ion battery.

Alternatively the first cathodic peak (C_1) may represent the electroadsorption of Ca^{2+} ions onto the oxide layer within the MCE rather than intercalation, plausible owing to the small current response, short scan duration and the relatively large ionic radius of Ca^{2+} (1.0 Å).

Despite applying a more cathodic potential limit in the ZrO_2 CV scans, no such electrochemically mediated Ca intercalated phenomenon was shown in the current response. Ca intercalation is a known process in pellet scale electrolytic reduction of ZrO_2 to form meta-stable compounds[83], however given the relative conductance of the chromium oxide and insulative properties of ZrO_2 plus correspondingly a more negative $E^o_{810^oC}$ for ZrO_2, their respective reductive mechanisms likely differ. During the second scan, current for the C_1 peak decreases substantially (see **Figure 5.11b**), probably owing to the decrease in abundance of metal oxide via dissolution of formed $CrCl_2$ and $CrCl_3$, see A_2 and A_3, and the non-wettability of Cr metal to Ca. In the same CV, where the cell lacking the alumina sheath was used, the resultant curve (green) shows a far poorer current responses i.e. the detail is insufficient to make conclusive assessments regarding redox reactions.
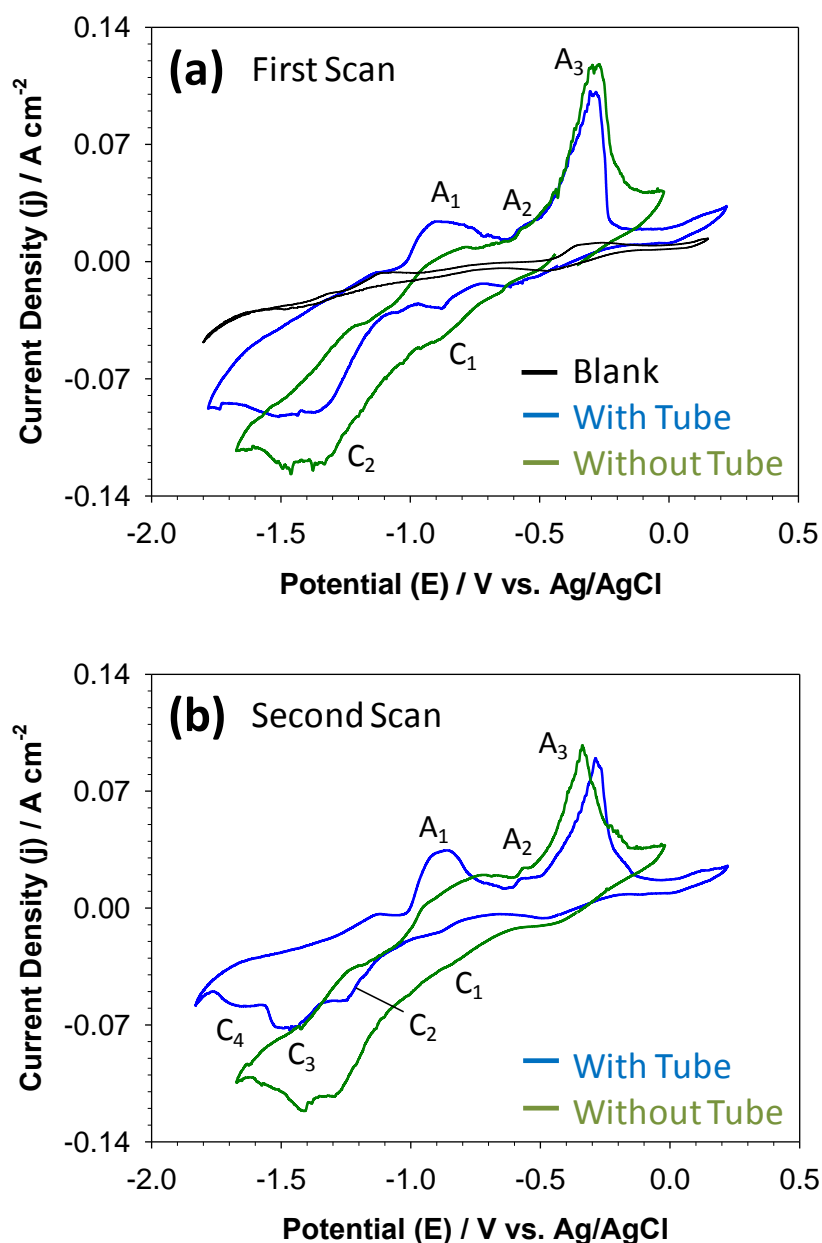
Figure 5.11 – CVs of Cr_2O_3 loaded Mo MCEs in 399 g $CaCl_2$ at 810°C recorded in an unmodified cell (green curve) and one with an alumina sheath (19 mm ID) covering the WE (blue curve). (a) is the first scan and (b) the second scan.

This relationship is similar to that presented in ZrO_2 cyclic voltammetry, but the difference in slope angle between the two Cr_2O_3 cell configurations is far greater (32.5° compared to 8.7°), representative of the larger R_e difference presented in **Table 5.1**. During the second scan (**Figure 5.11b**) a third cathodic peak manifests at approximately -1.37 V (C_3). During constant cell voltage electrolysis of Cr_2O_3 pellets conducted elsewhere in

the literature it was suggested that partially reduced chromium oxide intermediates such as CrO and Cr_2O can form[154], yet these are apparently unstable at the operational temperature used here so it would seem that their formation is unlikely in the context of high temperature microgram quantity voltammetry. The two additional cathodic current peaks revealed on the second CV scan (C_3 and C_4) are therefore likely to represent the reduction of the Ca intercalated oxide phase and perhaps the reduction of residual $CrCl_x$ species. For instance $CaCr_2O_4$ reduction to Cr metal was calculated to occur at +778 mV vs Ca/Ca^{2+} in $CaCl_2$ at 900°C which, when accounting for the 90°C temperature difference, fits exceptionally well with the onset peak at C_3 (assuming a -2.19 V $CaCl_2$ decomposition potential). Three anodic oxidation reactions can be seen on curves for both the first and second scans (A_1, A_2, and A_3) which represent the oxidation back to Cr_2O_3 (where O^{2-} ions are available) and the chlorination of produced Cr metal to di- and –tri chloride[120], **Equations 5.16-5.18**.

$$A_1: \quad 2Cr + 3O^{2-} = Cr_2O_3 + 6e^- \qquad \textbf{5.16}$$

$$A_2: \quad Cr + 2Cl^- = CrCl_2 + 2e^- \qquad \textbf{5.17}$$

$$A_3: \quad Cr + 3Cl^- = CrCl_3 + 3e^- \qquad \textbf{5.18}$$
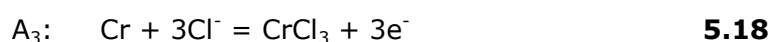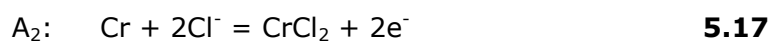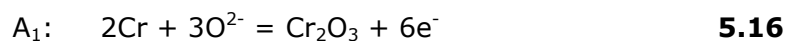
A second CV of Cr_2O_3 was performed using the alumina tube modification at a scan rate of 50 mV s^{-1} for more cycles, shown in **Figure 5.12**. After the eighth scan, the current response was almost identical to that of the blank Mo scan in the same potential region, suggesting the original Cr_2O_3 material from the electrode was no longer present. It's probable that during successive scans an incremental amount of material was being lost due to destabilisation of the MCE cavity, caused by the reduction process removing oxygen ions and the anodic formation of soluble chromium chlorides. As the scan rate was relatively quick it is expected that for $CrCl_3$ in solution there would exist a relatively static reversible redox reaction.

The current emphasis on the leeward peak at C_1 during successive scans in **Figure 5.12** provides tangible evidence of the reduction of the chloride to Cr metal on the surface of the Mo MCE, coinciding with thermodynamic predictions (**Equation 5.19**).
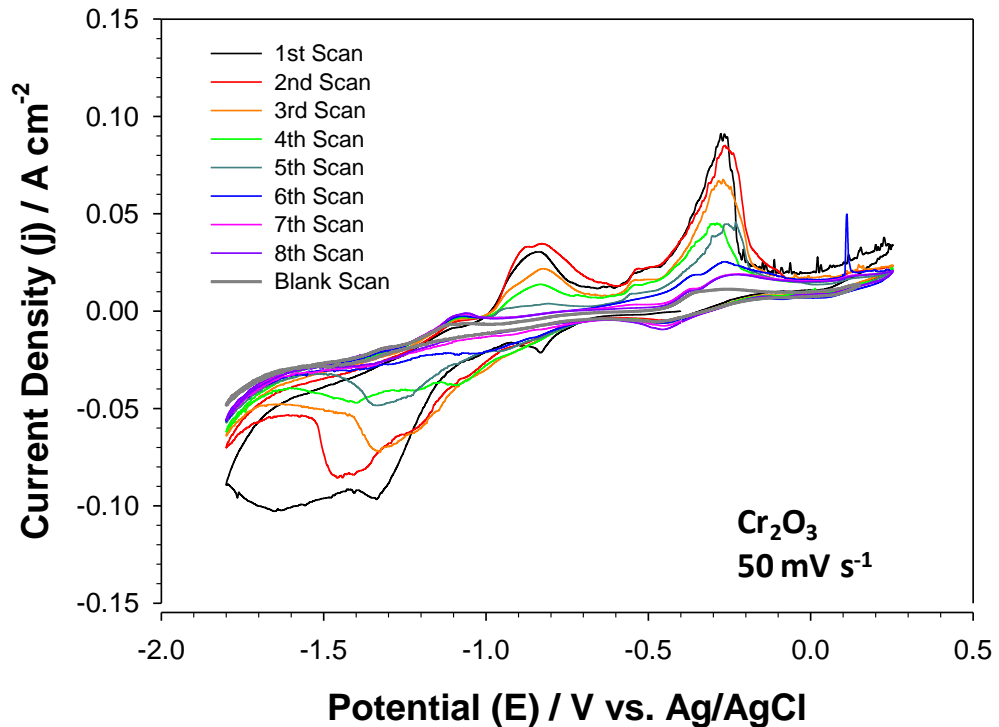
Figure 5.12 – 50mV s^{-1} CV of the Cr$_2$O$_3$ loaded Mo MCE in molten CaCl$_2$ at 810°C.

$$CrCl_3 + 3e^- = Cr + 3Cl^- \qquad \textbf{5.19}$$
$$E^o{}_{810°C} = +1139 \text{ mV vs. Ca/Ca}^{2+} (-1.061\text{V vs. Ag/AgCl})$$
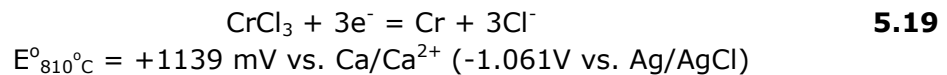
During the reverse scan the first anodic peak, A_1 (attributed to Cr oxidation back to Cr$_2$O$_3$) is present on all cycles until the seventh and could contribute to the material loss on the electrode surface and cavity as the reformed Cr$_2$O$_3$ sinks to the base of the crucible. Consequently on each cycle more of the unreduced oxide may be lost from the cavity due to constant reversing polarisation. Whilst this issue may not be relevant for direct reduction investigations from an oxide to a metallic phase it does highlight the need for understanding how successive reduction and dissolution operations may affect electrode stability, for instance during the pyroprocessing paradigm being invested in this work. As a side note, in

Figure 5.12 the overall slope of each curve diminishes over successive cycles. This is a general behaviour of FFC Cambridge Process CVs where a gradual increase in electrolyte resistance develops from the decrease in oxygen activity via reduction and discharge at the anode, despite an increase in conductivity of the working electrode due to metallisation. Evidently the use of the alumina tube for these experiments using small quantities of metal oxide powders has considerably improved the perceived usefulness of the produced CV scans.

5.3 Current Efficiency Optimisation

5.3.1 Cathode Design

Although the FFC Cambridge Process has been promoted as a viable electro-deoxidation technology for the production of metals[136,160] and valuable alloys[229,230] with low oxygen presence, uptake and wider industrial application is hindered by poor current efficiencies[87,231]. Following the association of an improved electrolyte ionicity with the implementation of a cathodic sheath during CV studies, an approach was taken to further investigate how the current efficiency of a scaled up direct reduction of Cr_2O_3 would be affected by the use of this cell design.

Identical preparation procedures were followed for the CV investigations as before, including pre-electrolysis using a Ni rod cathode and graphite counter electrode at 1.8 V for 16 h. The immersed section of Ni rod following pre-electrolysis typically possessed a dull grey coating from the minor quantities of metallic impurities present in the $CaCl_2$ which are readily electroplated by the applied voltage. In required experiments, the cathode sheath was then ready for insertion into the cell until contact with the base of the crucible was achieved and the machined hole was facing the position of the graphite anode (**Figure 5.13a**). Approximately 1 g of Cr_2O_3 powder as received was weighed out and cold pressed into cylindrical

forms using a 13 mm die subject to 2 tonnes of force to yield green forms approximately 1.5-2 mm thick.
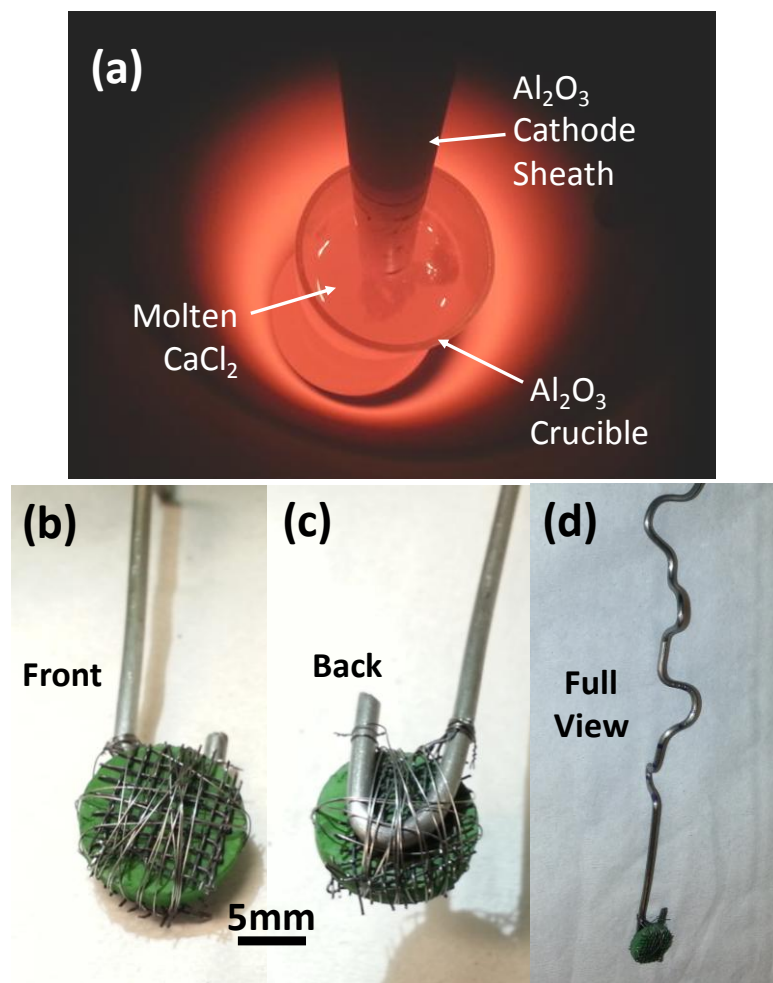
Figure 5.13 – Images of (a) the electrolytic $CaCl_2$ containing cell with the cathodic sheath design at 810°C following pre-electrolysis. (b), (c) and (d) show the assembled Cr_2O_3 pelletised cathode for use in direct reduction investigations.

These were then sintered at 900°C for 2 h, sandwiched between two 10 mm x 10 mm sections of Mo mesh and attached to a Mo current collector using 0.1 mm Mo wire (**Figure 5.13b-d)**. The Mo current collector was carefully shaped in the upper region above the molten salt so that after being inserted into the alumina sheath, the contact points between current collector and tube prevented movement of the oxide pellet whilst in the melt. This was deemed necessary to avoid the potential contact between cathode and alumina sheath within the electrolyte, where the reduction of Al_2O_3 to Al metal has been known to occur via 3PI reduction. As Al melts at

$660^{\circ}C$, the result would be a partial or even total dissolution of the sheath and contamination of the electrolyte following Cr_2O_3 electro-deoxidation.

For similar reasons a careful depth measurement for the immersion of the cathode was imperative, as to not permit cavity formation in the crucible base should they come into contact, causing the molten salt to drain away.

Despite a very amenable strength achieved from the pressing and sintering programme applied for the Cr_2O_3 pellets, they were shown to have a very large 63% porosity, perhaps a consequence of the short sintering duration coupled with slow inter-particle grain boundary growth. As mentioned previously, the pellet was orientated perpendicular to the lube length and directly facing the graphite anode. This was in an attempt to improve reduction kinetics by exposing the largest surface area possible to small hole in the base of the tube. For the reduction experiment involving an unmodified cell, the Cr_2O_3 pellets were attached in an identical way to a straight Mo wire and immersed to an exact height, at an exact distance to the graphite anode achieved when using the alumina sheath.

5.3.2 Direct FFC Reduction of Cr_2O_3 in $CaCl_2$

5.3.2.1 Influence of a Cathodic Sheath on Current Efficiency

Constant cell voltage electrolysis was performed on the ~1 g sintered Cr_2O_3 pellets at a voltage of 2.9 V, as selected based on the previously well-defined redox behaviour characterised by CV. The reduction potential identified from CV for the supposed direct single step oxide to metal reaction was around -1.4 V vs Ag/AgCl, or +0.6 V vs. Ca/Ca^{2+} internal reference. The applied 2.9 V is approximately 0.37 V positive of the internal reference, hence should be adequate to initiate reduction whilst providing a suitable overpotential to compensate for iR drop and avoiding salt decomposition. The electrolysis experiments for when the cathodic

alumina sheath was implemented and in the unmodified cell were both terminated after 6 hours, as a stable background current could be observed in each indicating an End Point Of Reduction (EPOR). The produced current-time plots are given in **Figure 5.14** with the total charge consumption and theoretically derived required charge for each pellet included, given the measured pellet weight prior to reduction.
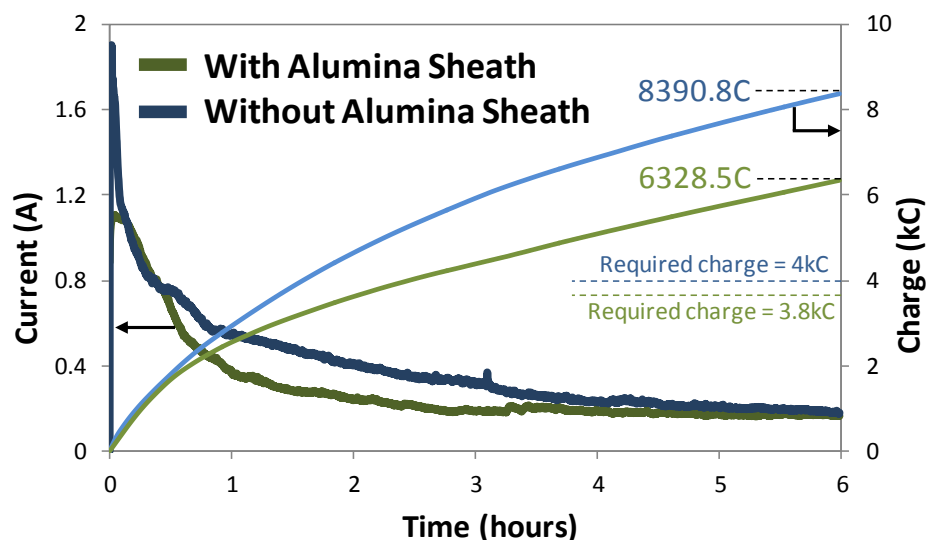
Figure 5.14 - Current-time plots and cumulative charge obtained from constant cell voltage electrolysis of Cr_2O_3 pellets in 399 g molten $CaCl_2$ at 810°C for 6 h in an unmodified alumina cell (blue) and one with an alumina sheath (green).

In **Figure 5.14**, the peak current obtained using the alumina sheath modification is far smaller and the background current reached sooner than observed in the unmodified cell. Accordingly the cumulative charge passed was only 75.4% of the total consumed in the cell without the sheath modification. Yet the background current following completion after 6 h was shown to be near identical for both designs (165 mA with the sheath vs. 170 mA without). Prior to the Cr_2O_3 electrolysis, a bare Mo wire 2 mm in diameter was used as a cathode for a blank electrolysis at 2.9 V, with the aim of determining the background current (**Figure 5.15**).
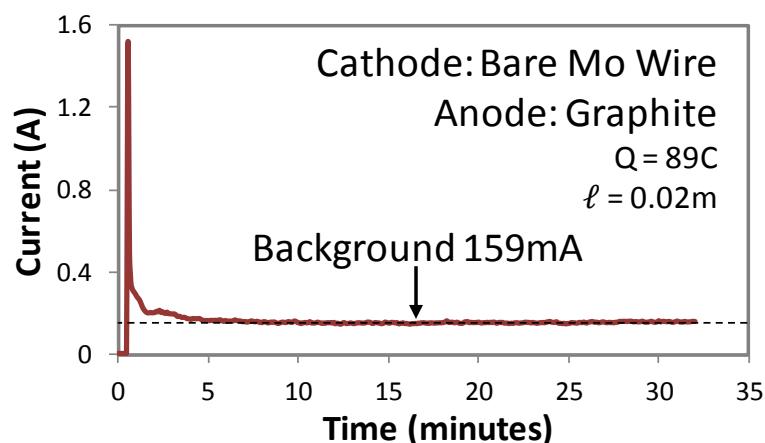
Figure 5.15 – Electrolysis current-time plot for a bare Mo wire cathode and graphite anode in 399 g of pre-treated $CaCl_2$ at 2.9V.

The current response in **Figure 5.15** reached a plateau after just 5 minutes, which reveals that (1) the salt was indeed adequately cleaned prior to its use as an electrolyte and (2) the applied voltage was nominal enough to not induce any significant and unwanted redox reactions. The background current observed for the blank Mo wire was 159 mV, which is close enough to those for the Cr_2O_3 pellet electrolysis investigations to suggest the EPOR was actually reached. Although great care was taken to normalise all parameters not being directly investigated, the small difference in background currents could simply derive from the slight deviation in surface area of the cathode assembly.

The distinctive initial currents for the Cr_2O_3 reduction curves in **Figure 5.14** are a consequence of the differing kinetics during the first 30 minutes of oxygen removal, understood to be by the usually rapid surface metallisation at the triple phase interface. The presence of the alumina sheath effectively limits the ionic migration within the molten salt to the remaining uninterrupted field lines existing directly between the cathode and anode and prevents oversaturation of O^{2-} within the bulk oxide phase (and hence CaO formation) by slowing the rate of electro-deoxidation. Later in the electrolysis a more rapid fall in current was observed when the

sheath modification was used. This is considered an indicator of a more direct reduction of Cr_2O_3 by the interruption of indirect diffusive ionic pathways, facilitating the bypass of potential Ca intercalation events, and crucially by removing a source of short circuiting the cell from a presence of floating carbon (sees section 5.3.2.2).

During constant cell voltage electrolysis it is plausible that some Ca formation occurs where a high voltage (2.90 V at 810°C) was used close to the thermodynamic value for the molten $CaCl_2$ decomposition (3.27 V at 810°C) and above that for CaO decomposition (2.71 V at 810°C). Similarly in CV studies when characterising the deposition potential for Ca during the blank scan, unavoidable Ca metal formation occurs whilst Cl_2 gas is anodically discharged. The addition of excess Ca can be rationalised as a non-stoichiometric compound $Ca_{1+\delta}Cl_2$ where δ = $nCa/nCaCl_2$ with n representing the number of moles of the constituent compounds[232]. Excess electrons will form an equilibrium with electron holes in the non-stoichiometric $CaCl_2$ compound, but as the concentration and activity of Ca metal increases the mole fraction of electrons x_e, defined as $2x$ = $2\delta/(1+\delta)$, also increases[218]. The lack of electron transport within the various molten salt weights tested here (derived by the low D_e values) could be inferred as representing a low concentration of CaO which otherwise would contribute strongly to the transport of electrons.

Example images of the Cr_2O_3 precursor pellet and yielded products following reduction using the alumina sheath are shown in **Figure 5.16** and highlight the apparently near complete metallisation after the 6 hour electrolysis duration.
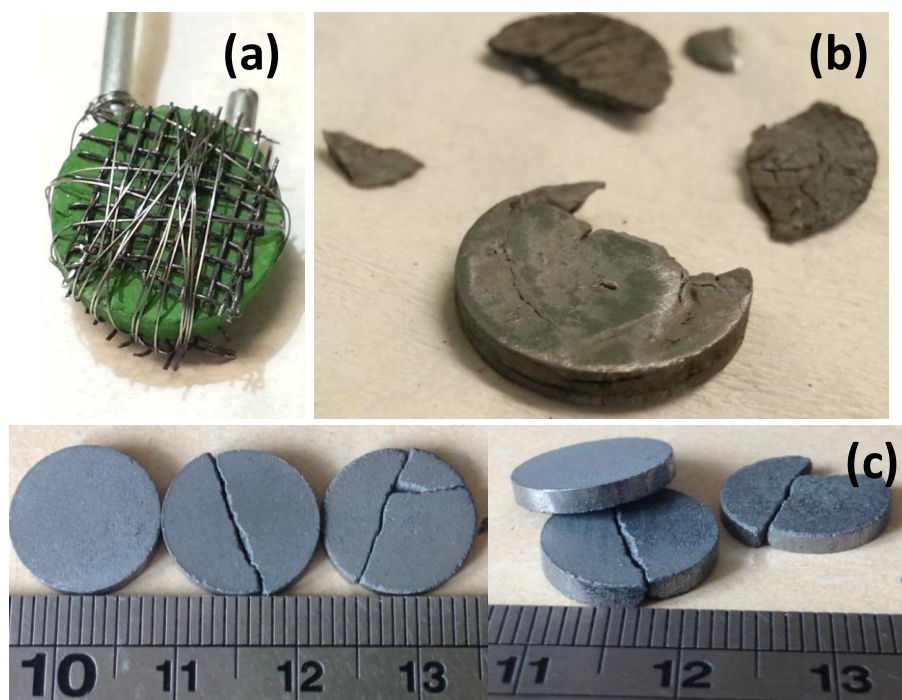
Figure 5.16 – (a) photograph of Cr_2O_3 cathode assembly prior to reduction and (b) following electrolysis at 2.9 V for 6 hours in molten $CaCl_2$ using a cathodic sheath. (c) cold-pressed pellets forged from Cr powder.

After washing the removed cathode in water for 48 h, the appearance of both products were broadly similar, displaying a dark grey colouration with minor shrinkage, however once unwrapped the form tended to break along developed surface cracks under light manual handling (**Figure 5.16b**, following polishing). From an accumulation of several electrolysis experiments on identical oxide pellets using the alumina sheath over the cathode, the collection of metallised forms were lightly ground using a pestle and mortar into a coarse powder and cold-pressed using the 13 mm die into small buttons (**Figure 5.16c**) these presented a much more obvious metallic lustre and were found to be mechanically robust, suggesting a certain ductility that highlights the low oxygen presence of the FFC produced forms. SEM images of the pellets before and following electrolysis can be seen in **Figure 5.17**. Morphologically the as-received Cr_2O_3 powders have a non-uniform particle size and geometry (a particle distribution around 0.2 to 2 µm), whereas both produced samples following

184

constant voltage electrolysis display a more regular distribution and are comparable to those shown and described elsewhere[121,154].
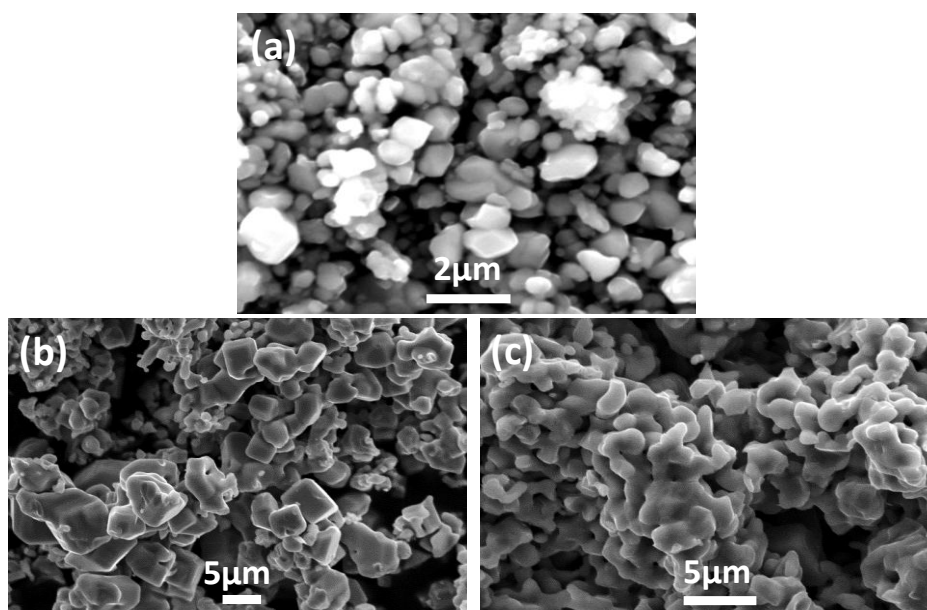
Figure 5.17 - SEM micrographs of (a) Cr_2O_3 powder (carbon coated), (b) following constant cell voltage electrolysis at 2.9 V at 810°C for 6 h in 399 g $CaCl_2$ and (c) after electrolysis under the same conditions but with a modified alumina sheath.

The SEM images reveal a clear transition in the before to after reduction appearance, but more significantly there is a large discrepancy between the morphology and degree of interparticle coalescence of the two reduced samples. The sample that was reduced in the unmodified cell displays more angular and cubic grains with low order grain boundary growth whereas those produced when the alumina sheath was employed exhibit a much greater extent of cohesion and are visually much more similar to other metals produced by the FFC Cambridge Process. The difference can readily be attributed to a higher presence of oxygen content (i.e. lower extent of reduction) which prohibits the formation of low surface energy isotropic solids and coalescence into the characteristic metallic nodular shapes. Where the alumina sheath was implemented the extent of reduction due to improved appropriation of charge transfer and optimised kinetics was clearly favoured.

The total extent of oxygen removal was characterised by TGA after repeated washing in water for 48 h (**Figure 5.18**). Homogenously milled samples of the reduced, vacuum dried pellets were heated at 20 ^{o}C/min up to 1000 ^{o}C in air flow and held for 2 h, after which the maximum mass gain was attributed to the extent of reoxidation.
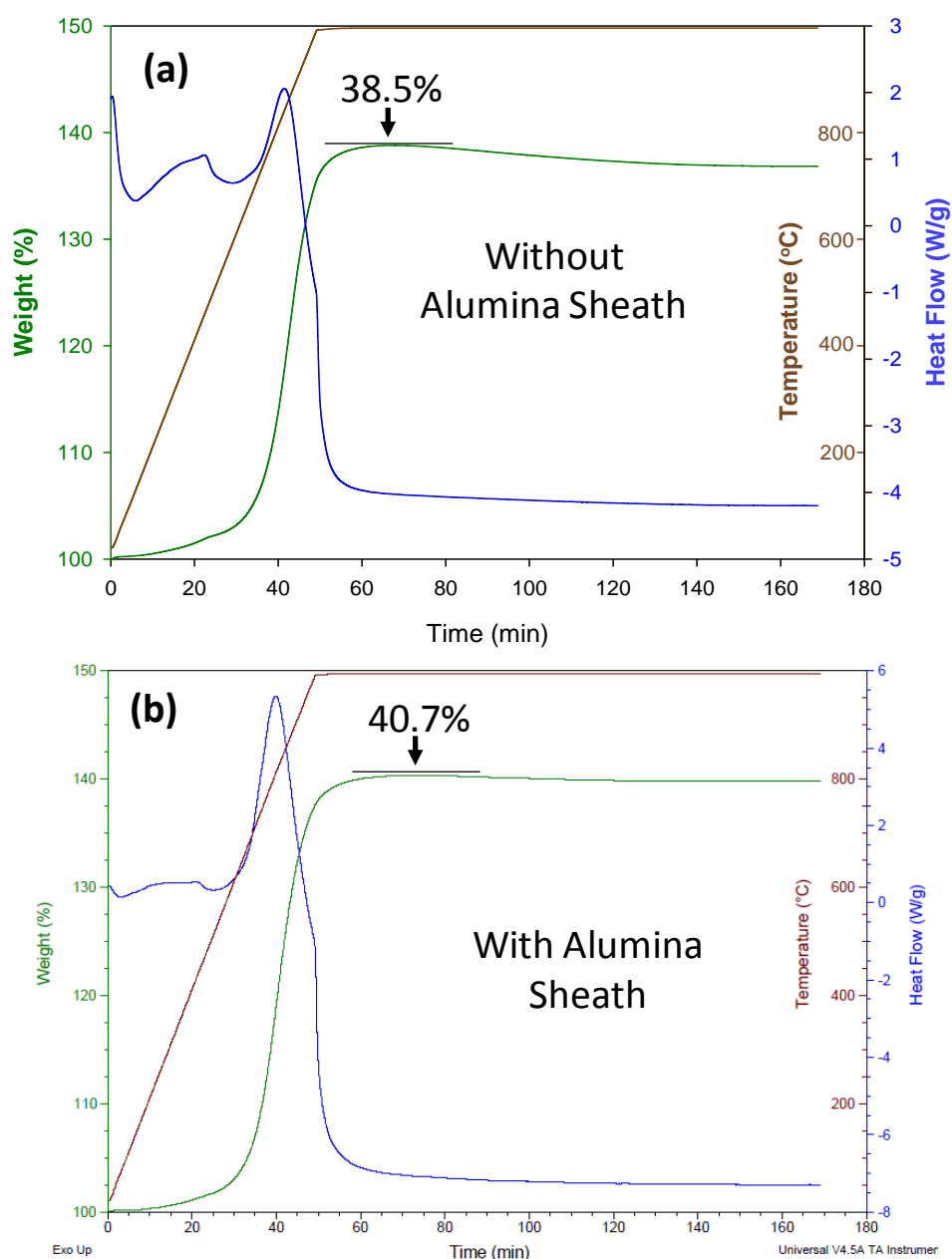
Figure 5.18 – TGA-DSC analysis of reduced Cr_2O_3 samples at 2.9 V in $CaCl_2$ using (a) an unmodified cell and (b) one with an insulating cathodic sheath.

The sample taken from the design using the sheath showed a larger total mass increase of 40.7 %, compared to 38.5 % for without. The theoretical

stoichiometry of a full oxidation of pure Cr metal would induce a mass increase of 46 %, suggesting neither sample was fully reduced during the constant cell voltage electrolysis, likely as a consequence of the relatively low operational temperature and much shorter duration than typical FFC based reduction (900-1000°C for >24 h). What is evident however is that by the addition of an electrically insulating cathodic sheath, a smaller charge is consumed for a more complete reduction in the given electrolysis time due to improvements in electrolyte ionicity and lack of parasitic ion cycling (i.e. carbonate cycling; see section 5.3.2.2). This can be physically seen in the SEM images of the two Cr_2O_3 pellets, where the less reduced product processes a more cubic morphology representative of a partial reduction[121].

The results of this implemented alteration are reflected in the relative improvements in the uncompensated current efficiency (60.19 % vs. 47.66 %) for the modified and standard cell respectively, based on TGA derived oxygen removal data. Results for the two Cr_2O_3 pellet reduction experiments are collated in **Table 5.3**.

Table 5.3 – Features of 6 hour electrolysis experiments on two Cr_2O_3 pellets at 2.9 V using an unmodified crucible containing 399g $CaCl_2$ and an identical cell with an alumina cathodic sheath.

Design	Cr_2O_3 Pellet Mass (g)	Pellet Porosity (%)	Total Charge Passed (Q)	Back-ground Current (mA)	Oxygen Content (%)	Oxygen Removal (%)	Current Efficiency (%)
Unmodified Crucible	1.05	63.3	8390.8	170	1.87	94.1	47.66
Cathodic Sheath	1.00	63.0	6328.5	165	1.11	96.5	60.19

Typically a prolonged electrolysis time is required for metals produced by the FFC Cambridge process to achieve low oxygen content. During constant cell voltage electrolysis using the cathodic sheath, a more rapid attainment

of a background current was achieved (after approximately 3 h, **Figure 5.14**) following the initial kinetically limited surface metallisation phase. It seems probable that this is caused by a more consistent rate of oxygen removal from the metal oxide cathode when compared to the unmodified cell. The final stage of reduction is characterised by a much slower diffusion of oxygen from the mostly Cr rich cathodic product, suggesting that a lower oxygen content was observed in the experiment implementing the alumina sheath from the earlier attainment of a stable background current. Accordingly the evidence suggests this phenomenon is facilitated by the restriction of electric field lines to the section of electrode interfaces which directly face one another. As to why there is considerable decrease in total charge passed compared to the unmodified crucible design, this may be a quantitative response of the physically limited spatial region for electron hopping and localisation and certainly will reflect the reduction of carbon interference to the electrolysis procedure.

5.3.2.2 Carbon Contamination

It is possible, and has been reported several times elsewhere[72,158,233,234], that the anodically formed CO_2 gas on the graphite anode can react with dissolved O^{2-} ions to form CO_3^{2-} by **Equation 5.20.**

$$CO_{2(g)} + O^{2-}_{(diss)} \rightarrow CO_3^{2-} \qquad\qquad \textbf{5.20}$$

The produced CO_3^{2-} can then migrate to the cathode and undergo reduction to form elemental (usually amorphous) carbon that floats atop the molten salt and regenerate the oxygen anions according to **Equation 5.21.**

$$CO_3^{2-} + 4e^- \rightarrow C + 3O^{2-} \qquad\qquad \textbf{5.21}$$
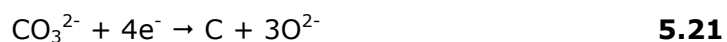
This cycling will again promote a lower current efficiency via an electronically conductive mechanism through the electrochemically generated surface carbon to short circuit the cell, as well as potentially contaminating the cathodic product. The relatively sharp fall in current

early in the unmodified Cr_2O_3 current-time plot, coupled with the image of the as removed pellets shown in **Figure 5.19a** and **5.19b** suggests that **Reactions 5.20** and **5.21** are present in the unmodified cell but have a limited influence throughout the duration of electrolysis in the cell using the alumina sheath. In addition to providing a physical barrier to carbon ingress, data here implies that either less carbonate ions are formed or that their subsequent access to- and reduction on the cathode is restricted.

The cause of this behaviour may have an explanation in the relatively slow initial electro-deoxidation of the oxide pellet when the alumina sheath was used. More vigorous reactions taking place on the anode can cause a dislodgement of carbon particles (resulting in floating carbon particulates often seen in the non-modified experiments) which in turn can hinder the free escape of produced CO/CO_2 via entrapment in formed pores.
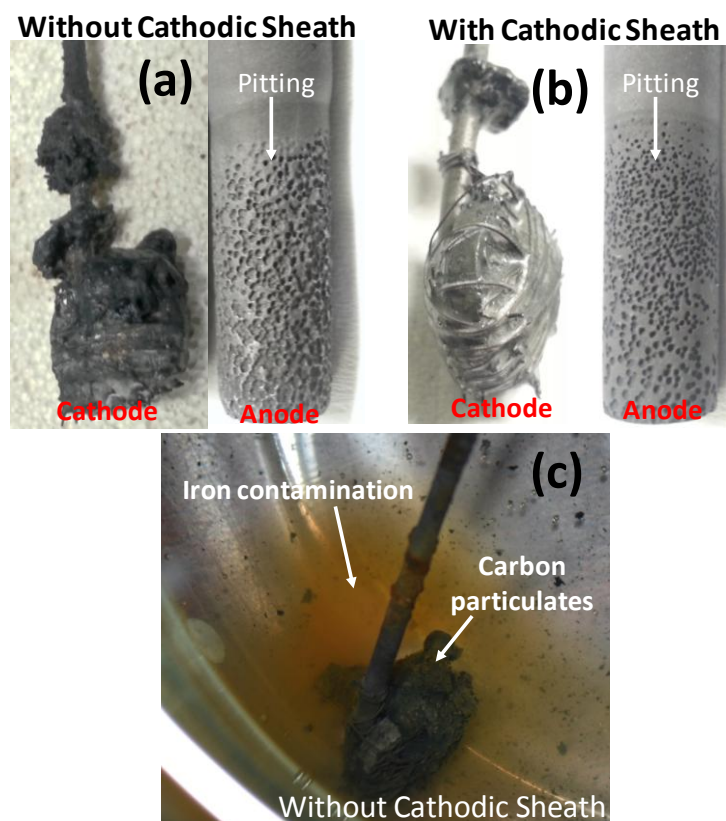
Figure 5.19 – Photographs of the cathode and anode following electrolysis of Cr_2O_3 at 2.9 V in molten $CaCl_2$ at 810°C (a) in an unmodified cell and (b) when using a cathodic sheath. (c) The cathode from (a) after 15 minute's immersion in water.

The initial controlled release of oxygen anions from the interior of the alumina tube, brought about by limiting electric field line density, will retard the degeneration of the carbon anode and by association reduce the scale of **Equation 5.20** through a limited trapping of anodically formed gasses. This idea is supported by not only the difference in charge consumption between the two electrolysis experiments, but also the different condition of the graphite anode after the Cr_2O_3 reduction (**Figure 5.19a** and **5.19b**). The extent of pitting is far more severe in the unmodified cell despite identical electrolysis durations, applied voltages and only a 5 % difference in initial oxide weight.

The cathodes equally display a large aesthetic difference, with the frozen salt encrusted on the unmodified cell cathode being completely saturated with carbon particulates from either the direct inclusion by carbonate ion reduction (**Equation 5.21**) or adhesion from the accumulation of floating carbon particulates on the surface of the molten salt. Where the alumina sheath was used a combined effect of a physical barrier to carbon ingress from the molten salt, a reduced carbon presence from the suppression of carbonate ion formation and an improved current efficiency left salt surrounding the cathode much purer with no visible contamination. An additional beneficial effect was also observed, as seen in **Figure 5.19c**, where the cathode from the unmodified cell exhibit a release of iron rich salt during the washing procedure (thought to be introduced from the degradation of the stainless steel retort wall during operation), whereas the sheathed cathode did not. It is not apparent why the presence of the alumina barrier would have prevented the ionic migration of Fe^{n+} species to the cathode during reduction; however EDS analysis suggests both samples had no alloying or iron presence in the final product which perhaps

suggests the species were mostly insoluble and again the physical restriction of the alumina wall was sufficient to prevent ingress.

The presence of floating carbon powders on the surface of molten salt will undoubtedly contribute to some of the latter deviations in current shown by the plots in **Figure 5.14** (after 1 h electrolysis time). Specifically the hole at the base of the sheath, while permitting oxygen anion transport, restricts the surface electron conduction via the floating carbon contaminants from the bulk of the salt to the interior of the tube. Although not a static process, the surface carbon can act as a direct electronic pathway bypassing the application of electrons to the electro-deoxidation of the cathodic product. By removing the possibility of short circuiting the cell, charge is consumed solely for the metal oxide reduction (and background current consumption) hence the relatively rapid acquisition of a stable background current when the nonconductive alumina tube was used. The results of this proposed mechanism are reflected in the relative improvements in uncompensated current efficiency for the modified and standard cell respectively (60.19 % vs. 47.66 %).

Furthermore the traditional ore refining route of Cr_2O_3 consists of either a direct carbon reduction at a ratio of $3C:Cr_2O_3$ to form the metal and carbon monoxide, or blended with aluminium metal (pure of scrap sources) and ignited. Both methods require temperatures in excess of 2000°C and with carbothermic reduction the presence of carbon as a contaminant is notoriously difficult to remove below 0.1%. Conversely with Al assisted reduction the process is rather energy intensive and becomes redundant considering global Al production is now met by the electrochemical Hall-Héroult process. A method of producing chromium metal in bulk, at less than half the conventional industry temperature and without a chemical

reductant as demonstrated by FFC based reduction here is therefore certainly worthy of further academic and perhaps commercial investment.

5.4   Conclusions

A simple yet significant relationship has been proposed between the extent of electric conduction within molten salt electrolytes and the range and density of uninterrupted electronic field lines. Through considered control of crucible geometry, essentially by eliminating the redundancy of excess electrolyte with the use of smaller crucibles, it was found possible to reduce overall charge consumption of electrolytic processes. Electrolyte resistance, as intrinsically related to electronic conductivity was measured by EIS and shown to increase under identical measurement conditions when only the total mass of molten salt decreased. This was qualitatively assessed by CV investigations of ZrO_2 and Cr_2O_3 with a metallic cavity electrode, and found to improve both the appearance and resolution of redox features when less supporting electrolyte was used.

The largest divergence and subsequently the best improvement (179% increase in R_e) came when an identical amount of salt was used, but when a narrow 19 mm alumina cathodic sheath was implemented to restrict field line influence. In commercial application where larger quantities of oxide are fed into the system, the use of small quantities of electrolyte is prohibitive; hence understanding this relationship is particularly useful. The experimental findings presented provide an insight into the often underappreciated effects of electronic conduction in molten salt processes and a physical mechanism for alleviating this influence forwarded. These considerations when coupled with the electrochemical pre-treatment of molten salts are of fundamental importance in the optimisation of reprocessing technologies on an industrial scale.

The considered relationship between electronic conduction and restricted influence of electronic field lines was further analysed by use of the cathodic barrier in bulk reduction of Cr_2O_3 pellets. These experiments not only proved useful for indirectly improving current efficiency by increasing electrolyte resistance but also directly by both the control of carbon formation and removing its contact with the cathode. Extent of oxygen removal (96.5% vs. 94.1%) and current efficiency (60.19% vs. 47.66%) simultaneously improved respectively when using the cathodic sheath compared to without, at an electrolysis voltage of 2.9 V for 6 h using a relatively low operational temperature (810°C). One of the major drawbacks with industrial processing, and indeed with the wider adoption of the FFC Cambridge Process, is the difficulties in achieving high current efficiencies. Results presented here give a key insight into the practical benefits gained by the understanding and control of the electronic conductivity of the molten salt electrolyte. Tangible improvements in final product purity from restricting the effects of carbonate ion cycling, a more extensive electro-deoxidation by improved charge appropriation and more prominent pathways for oxygen ion discharge undoubtedly can lead to more favourable efficiency and economic performance of an FFC based industrial process.

Chapter 6

Electrochemical Partitioning of 2NiO-CeO$_2$

6.1. Introduction

Partitioning of homogenously mixed metal oxides using a single electrolyte and in solid phase presents a potentially unbridled processing route for actinide recovery from current LWR spent fuel. Such a technology, if implanted successfully, could dramatically reduce the cost of treating nuclear wastes, introduce safer fuel cycles and extend the lifetime of virgin resources by thousands of years. Hence developing the framework and feasibility basis of metal oxide partitioning process is a worthy endeavour. Work presented in this chapter covers a series of investigations aimed at forwarding this cause, using an initial binary of 2NiO-CeO$_2$ as a simplified surrogate system with favourable thermodynamic properties for the selective removal of Ni.

Specifically this chapter will therefore consider the following:

1. The base thermodynamic properties of the NiO-CeO$_2$ system and how the reduction of an oxide to its metallic state is influenced by the metal-to-oxide volume ratio.

2. Constituent oxide characterisation by CV, and crucially characterisation of the binary phase to confirm thermodynamic predictions and assess which, if any, interspecies effects are exhibited (e.g. alloying).

3. Applying the detailed redox information acquired to a proof of concept attempt at partitioning Ni from CeO$_2$ in pellet format using partial direct reduction and selective anodic dissolution.

The issues associated with using ceria (specifically the formation of unwanted intermediates) will also be discussed, including how this may affect an analogous pyro-process using live spent fuel given the predicted similar electrochemical behaviour of CeO$_2$ to PuO$_2$.

6.2. Thermodynamic and Kinetic Considerations

6.2.1. Standard Reduction Potentials

In order to establish the feasibility of partitioning by selective reduction and anodic dissolution, it is necessary to consider the electrochemical reduction of the individual metal oxides. The standard reduction potential is calculated to establish the relative ease, or more appropriately the work required, to reduce an oxide to its metal. The same standard reduction potential (E^o) which was used to determine the various electrolyte stabilities in Chapter 4 is applied here, given in **Equation 6.1** as a function of the Gibbs free energy change (ΔG^o) of the reaction being considered.

$$E^o = -\Delta G^o/nF \qquad \qquad \textbf{6.1}$$

Based on **Equation 6.1**, the standard reduction potentials for anodic and cathodic half cell reactions can be calculated. The common anodic reactions based on the use of a graphite anode at 850°C in CaCl$_2$ are given in **Table 6.1**. As shown in **Table 6.1** two of the viable anodic reactions are either the discharge of chlorine ions (through direct decomposition of the salt) or oxygen ions, resulting in the generation of either molecular chlorine gas or of oxygen, carbon dioxide or carbon monoxide. The standard potentials calculated for each indicate the favoured production of either CO or CO$_2$, which is evidenced by the gradual mass loss from the carbon anode over electrolysis durations. Under all experimental conditions, no excess CaO was added to the melt and so minor chlorine evolution may have occurred during the initial onset of reduction where no available O^{2-} ions were present in the melt to balance the anodic half cell reaction.

Table 6.1 – Standard reduction potentials for various anodic half-cell reactions feasible in the molten CaCl$_2$ melt as calculated from thermodynamic data[120] at 850°C given that $E_{Ca^{2+}/Ca}$ = 0 V

Half-Cell Reactions	Standard Potential (E^o / V)
$2Cl_2 + 4e^- = 4Cl^-$	3.231
$O_2 + 4e^- = 2O^{2-}$	2.626
$CO_2 + 4e^- = C + 2O^{2-}$	1.626
$2CO + 4e^- = 2C + 2O^{2-}$	1.535

With some metal oxides such as TiO$_2$ that have a distinguishing calcium uptake as an intermediate reduction phase, the majority of calcium must come from the calcium chloride if a very low CaO content is maintained; an undesirable consequence of attempting to utilise a pure electrolyte. Where quantities of metal oxide being reduced are small enough this extent of nascent Cl$_2$ production will be marginal. With application to nuclear reprocessing however, an engineered solution of either molecular scrubbers to adsorb free Cl$_2$ or in finding a suitable CaO concentration within the electrolyte to prevent its formation is required.

The cathodic half cell reactions for all of the various metal oxides relevant to the partitioning of 2NiO-CeO$_2$ are presented in **Table 6.2**, with the assumption that NiO undergoes a single step, 2-electron transfer and the viable intermediate species for CeO$_2$ during cathodic polarisation are defined by the Ce-O-Cl predominance diagram[235]. The information combined in **Tables 6.1** and **6.2** were calculated against the internal Ca^{2+}/Ca redox couple ($E_{Ca2+/Ca}$) and assume all reactants and products are at unit activity under standard atmospheric pressure[110,236]. The ease of reducing NiO to its metallic state is apparent from this data, at potentials far more anodic than any Ca forming reactions.

Table 6.2 – Standard reduction potentials (E^o) for relevant cathodic reactions as calculated by available thermodynamic data at 810°C[120]

Half-Cell Reactions	Standard Potential (E^o / V)
NiO + 2e$^-$ = Ni + O^{2-}	2.554
2CeO$_2$ + 4e$^-$ = Ce$_2$O$_3$ + 2O^{2-}	2.108
Ce$_2$O$_3$ + 6e$^-$ = 2Ce + 3O^{2-}	0.689
CeO$_2$ + CaCl$_2$ + e$^-$ = CeOCl + CaO + Cl$^-$	2.161
CeOCl + 3e$^-$ = Ce + O^{2-} + Cl$^-$	0.658
CeO$_2$ + 4e$^-$ = Ce + 2O^{2-}	1.044
CaCl$_2$ + 2e$^-$ = Ca + 2Cl$^-$	0.000

The phase diagram for the Ni-O system is shown in **Figure 6.1** and highlights that below the melting point of Ni (1440°C) where minor NiO-Ni miscibility occurs, there is no suboxide formation at <50 at% O[237].
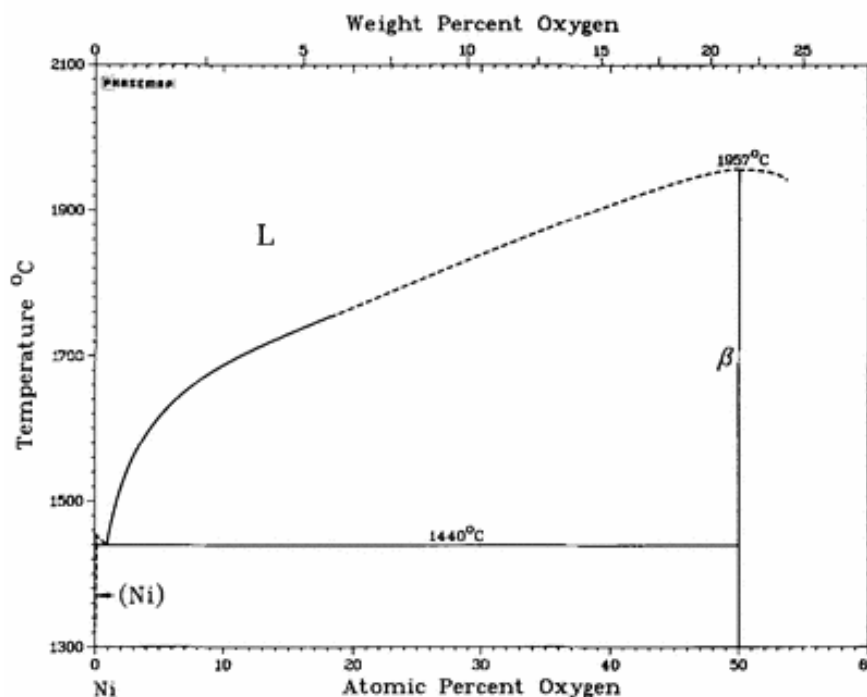
Figure 6.1 – Stability phase diagram of the Ni-O system [237].

When assuming a single direct reduction of CeO$_2$ to Ce, there is a theoretical 1.51 V nobility difference between this reaction and the direct reduction for NiO. This large divergence was the basis for selecting NiO as

197

a counterpart surrogate for CeO$_2$ (representing PuO$_2$). However according to the predominance diagram for the Ce-O-Cl system various electrochemically stable intermediate species exist in the Ce(III) state. The formation of Ce$_2$O$_3$ for example is theoretically only 446 mV more negative than NiO reduction, and CeOCl only 393 mV more negative, hence the desired partitioning between oxide-metal phases whilst still possible becomes more challenging. Consequently, following cyclic voltammetry the defined reduction potential for NiO was applied with precision and care in an attempt to avoid the partial reduction of CeO$_2$ for partitioning.

Considerations also need to be given regarding the chemical properties of the possible intermediates, for example the solubility of the Ce(III) species in particular was found to be problematic in experiments without very exact potential control. In the context of fully understanding the system, a full reduction of both counterparts was trialled using cathodic potentials beyond the theoretical reduction point of both oxides (and beyond Ce$_2$O$_3$ or CeOCl) to consider the prospect of alloying. In the benchmark ANL process a direct reduction of all spent fuel species by a Li reductant is the base process, so evaluating the prospect of electrochemical reduction as a more effective alternative is of great importance in of itself. The kinetic barriers to electrodeoxidation are also crucial and the basis for the oxide-to-metal molar volume ratio as a determining factor in the ease of reduction will be covered in the next section.

6.2.2. Oxide to Metal Molar Volume Ratio

According to the 3PI theory, during electroreduction of a metal oxide by the FFC Cambridge Process the initially formed metal layer must be sufficiently porous to allow molten salt access to the underlying oxide and establish new 3PI boundaries. This is generally the case when it is expected that the removal of oxygen from the solid oxide will leave vacancies in the

produced porous metal. This could only be true however if the molar volume of the metal, $V_m = M_m/\rho_m$, is smaller than that of its oxide, $V_o = M_o/n\rho_o$, where the subscripts 'm' and 'o' represent the metal and oxide respectively, V is the molar volume, M the molar mass, ρ the density and n the number of metal atoms in the oxide formula (e.g. n = 1 in TiO$_2$, n = 2 in Cr$_2$O$_3$). The phenomenon of the metal-to-oxide ratio was first publicised in 1923 and became known as the Pilling-Bedworth Ratio (PBR)[94,238], explained in **Equation 6.2**.

$$PBR = V_m/V_o \qquad\qquad \textbf{6.2}$$

Should the PBR be greater than unity, i.e. the removal of oxygen doesn't cause a decrease in the total volume of the yielded metal then the removal of O^{2-} ions to the bulk electrolyte to be discharged on the anode becomes impeded and similarly fresh electrolyte ingress to continue the electrodeoxidation ceases. The result is a retardation of reduction following the initial surface metallisation. In part it is possible to experimentally manipulate the porosity of the initial feedstock which can mitigate situations where reduction doesn't cause a decrease in atomic packing density. However a certain density is required to achieve a mechanically robust metal oxide feedstock so the metal-to-oxide ratio must also be reliably factored. There are also considerations required where intercalation events can cause a significant volume expansion and effectively halt further reduction in a similar manner. The calculated PBRs for the various feeds used throughout this work are shown in **Table 6.3.** In all examples given, the PBR value is less than 1, suggesting all are candidates for the successful electrodeoxidation procedure by the FFC Cambridge Process.

Table 6.3 – Metal-to-oxide molar volume ratios for metal oxides used in these works and some known partial reduction intermediates under standard conditions.

Metal Oxide/ Metal Pair	n	M_o (g/mol)	ρ_o (g/cm^3)	M_m (g/mol)	ρ_m (g/cm^3)	PBR
NiO/Ni	1	74.693	6.67	58.693	8.91	0.588
Cr$_2$O$_3$/Cr	2	151.99	5.22	51.996	7.19	0.497
CrO/Cr	1	67.996	4.89	51.996	7.19	0.520
CeO$_2$/Ce	1	172.115	7.65	140.116	6.76	0.921
Ce$_2$O$_3$/Ce	2	328.24	6.20	140.116	6.76	0.783
ZrO$_2$/Zr	1	123.218	5.68	91.224	6.49	0.648
Zr$_3$O/Zr	3	289.672	6.60	91.224	6.49	0.961
TiO$_2$/Ti	1	79.866	4.23	41.867	4.50	0.493
Ti$_2$O$_3$/Ti	2	143.76	4.49	41.867	4.50	0.581
TiO/Ti	1	63.866	4.95	41.867	4.50	0.721

Those with particularly low values, such as Cr$_2$O$_3$ and NiO are more readily reduced to their metallic phases than those closer to unity. Interestingly nearly all examples which have partial reduction products (TiO$_2$, Cr$_2$O$_3$ and ZrO$_2$) show incremental difficulty of reduction due to the volume expansion of produced intermediates. However this is frequently offset by increases in the conductivity brought about by reducing the oxide content of each phase. Band structures calculated from semi-local Density Function Theory (DFT) can be used to assess the conductivity of each phase and help visualise the fall in band gap at incremental reduction stages. The example for TiO$_2$/Ti$_2$O$_3$/TiO reduction hierarchy is shown in **Figure 6.2a-c** respectively, with the corresponding crystal structures of each given.
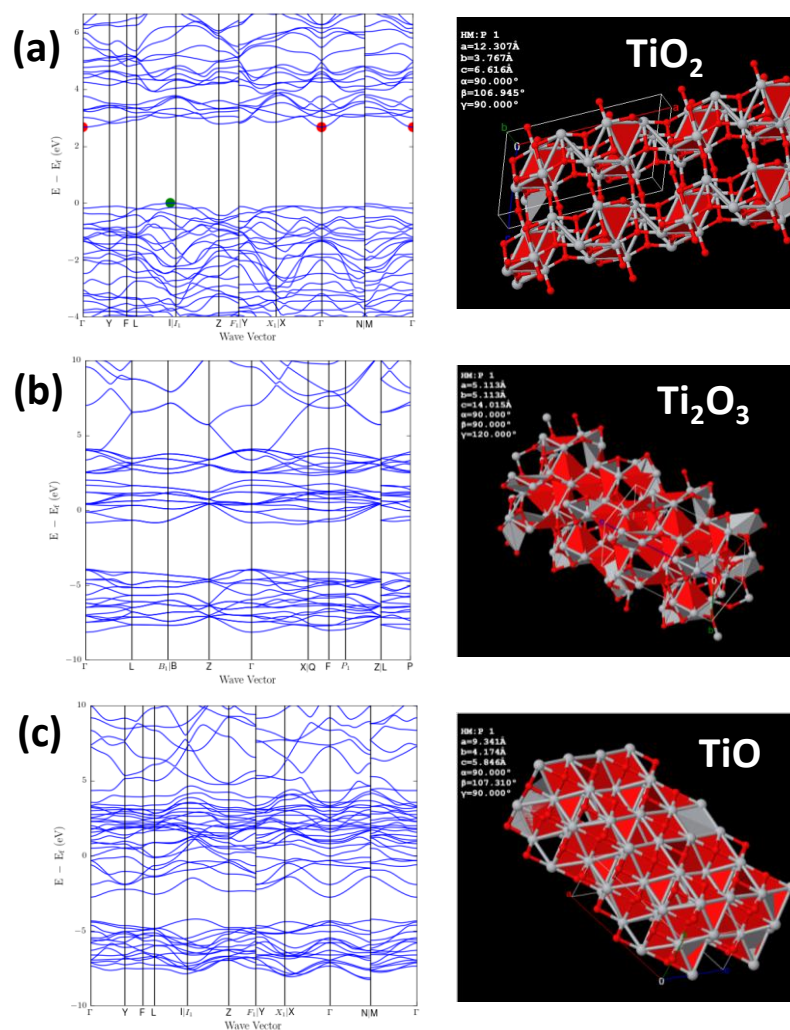
Figure 6.2 – Semi-local DFT derived band structures and crystal structure for (a) TiO₂ [anatase], (b) Ti₂O₃ and (c) TiO under standard conditions[150].

Clearly whilst the information given by the PBR values are a great indicator of whether or not electrodeoxidation will proceed on a given metal oxide feed, it is limited in application when used alone where other kinetic factors also contribute to the electrochemical precedent. The data in **Table 6.3** is also presented at standard conditions, i.e. 25°C and so at elevated temperatures where there is a shift in crystal structure, the results may differ. Additionally when a liquid metal is produced and adheres to the oxide a more challenging environment manifest for the continued removal of O^{2-} ions, as with Ce (melting point of 795°C). Even when this isn't applicable and the PBR data predicts an identical value, the effect of high

temperatures will induce sintering, especially on the metallic phases which nearly always have lower melting points than their constituent oxides.

Another kinetic consideration with the Ti-O and Zr-O systems is that their metallic states can dissolve oxygen to form solid solutions. While the metal-to-oxide ratios suggest reductions become sluggish when TiO or Zr$_3$O intermediates are produced, the reduction process could be accelerated by O diffusion through the metal phase itself. The opposite relationship occurs during the reduction of CeO$_2$ to Ce$_2$O$_3$, where crystal volume apparently collapses. In this particular example, additional difficulties arise as will be discussed later in this chapter and in Chapter 7. Throughout this work, efforts were made to try and mitigate some of the difficulties in reduction outlined when calculating PRB values by increasing feed pellet porosity. Details into these endeavours were given n Chapter 4. Based on the PBR calculations all of the oxides employed in this research could be feasibly reduced, albeit with various difficulty. Where selective reduction of a single species in binary phase is concerned, the removal of oxygen from a relatively easily reduced oxide (NiO for example) may assist the improved kinetics for reduction of the other species through an electro-catalytic route of electron spill over (section 6.3.2.1). This feature, whilst beneficial for direct electro-deoxidation, is actually undesirable for the desirable selectivity being invested here. Cyclic voltammetry studies were performed on the NiO, CeO$_2$ and 2NiO-CeO$_2$ feeds to better comprehend the deoxidation process provided by the information in this section.

6.3.Cyclic Voltammetry Investigations

6.3.1.Studies of Constituent Oxides

Blank CVs using unloaded Mo MCEs have been previously displayed in this thesis and will only be included here where a comparison is useful to highlight the oxide based redox reactions being considered. As standard

the counter electrode used was a graphite rod, however the reference electrode was a freshly fabricated 10 mol% Ag/AgCl sealed in ground alumina. The calcium deposition potential was newly defined as -2.25 V in this case and was found to be highly stable for the duration of experiments, having no more than 5 mV cathodic potential shift over the course of three days. The potential (E) of the Ag$^+$/Ag^0 redox couple can be calculated by the Nernst equation to confirm experimental validity (**Equation 6.3**). Further, as the activity of Ag^0 is 1 and activity coefficient of AgCl close to 1, **Equation 6.3** can be simplified to **Equation 6.4** to include the mol fraction of AgCl used in the reference electrode, x_{AgCl}.

$$E\left(\frac{Ag^+}{Ag^0}\right) = E^0\left(\frac{Ag^+}{Ag^0}\right) + \frac{RT}{nF}\ln\left(\frac{\alpha_{AgCl}}{\alpha_{Ag^0}}\right) \qquad \textbf{6.3}$$

$$E\left(\frac{Ag^+}{Ag^0}\right) = E^0\left(\frac{Ag^+}{Ag^0}\right) + \frac{RT}{nF}\ln(x_{AgCl}) \qquad \textbf{6.4}$$

Using **Equation 6.4**, the reference potential of the redox couple was calculated to be -1.034 V vs. Cl$_2$/Cl$^-$ for the 10 mol % AgCl concentration. This was equivalent to an approximate deviation of just 6 mV from the thermodynamic predictions given in **Table 6.4** (-1.034 + -2.25 = -3.284).

Table 6.4 - Thermodynamic calculations of cell voltages for the reduction of relevant oxides and the associated potentials (vs. Ag/AgCl) at 810°C

Reduction reactions	ΔG^o (kJ)	Half Cell Reduction Potential (V)	Potential (V) vs. Ag/AgCl
2NiO = 2Ni + O$_2$(g)	282.7	-1.47	-0.43
4CeO$_2$ = 2Ce$_2$O$_3$ + O$_2$(g)	454.9	-1.18	-0.14
2CeO$_2$ + 2CaCl$_2$ = 2CeOCl + 2CaO + Cl$_2$(g)	434.5	-1.51	-0.47
CeO$_2$ = Ce + O$_2$(g)	865.6	-2.24	-1.20
Ce$_2$O$_3$ = 2Ce + 1.5O$_2$(g)	1504	-2.60	-1.56
2CeOCl = 2Ce + O$_2$(g) + Cl$_2$(g)	1522	-2.63	-1.59
CaCl$_2$ = Ca + Cl$_2$	634.2	-3.29	-2.25

Reaction data in **Table 6.4** suggest that both NiO reduction to its metallic phase and the partial reduction of CeO$_2$ to Ce$_2$O$_3$ or CeOCl are relatively thermodynamically favourable and should be achievable at low applied potentials. While this may provide benefits in terms of energy consumptions of reduction, the issues in achieving efficient partitioning arises when excess electrons are consumed by the reduction of CeO$_2$ as opposed to directly for NiO. The theoretically predicted potentials as above were tested by CV to either confirm or refute these predictions.

6.3.1.1. Cyclic Voltammetry of NiO

Voltammetry of NiO in a CaCl$_2$ electrolyte has been examined previously within the literature, however one goal of the work was to assess influences of molten salt conductivity on redox activity and in this regard some key qualitative detail was lacking[160]. In this work NiO CV was investigated for the purpose of defining redox reactions and crucially the precise onset point of reduction which is necessary to achieve a selective partitioning process. Prior to scanning, NiO loaded MCEs were slowly inserted into the electrolyte to be used as working electrodes. In early studies the full working potential window was scanned to assess all potential deviations from the effective baseline of a blank Mo MCE. Later, for ease of presentation and to highlight significant information, the CV range was limited to the region of specific Ni-O reactions only, which were observed to be between -1.2 V and 0.2 V vs. Ag/AgCl.

The NiO redox behaviour in **Figure 6.3** has a considerable reduction bias in terms of charge consumption, indicative of reaction irreversibility. This can be considered a consequence of the relatively superior kinetics for electrodeoxidation, such as the high conductivity of NiO compared to other metal oxides and the favourable porosity and geometry of the MCE working electrode. Hence, an optimal environment for ion diffusion was achieved

facilitating low O^{2-} anion concentrations within the electrode cavity and so preventing NiO reformation during the anodic sweep.
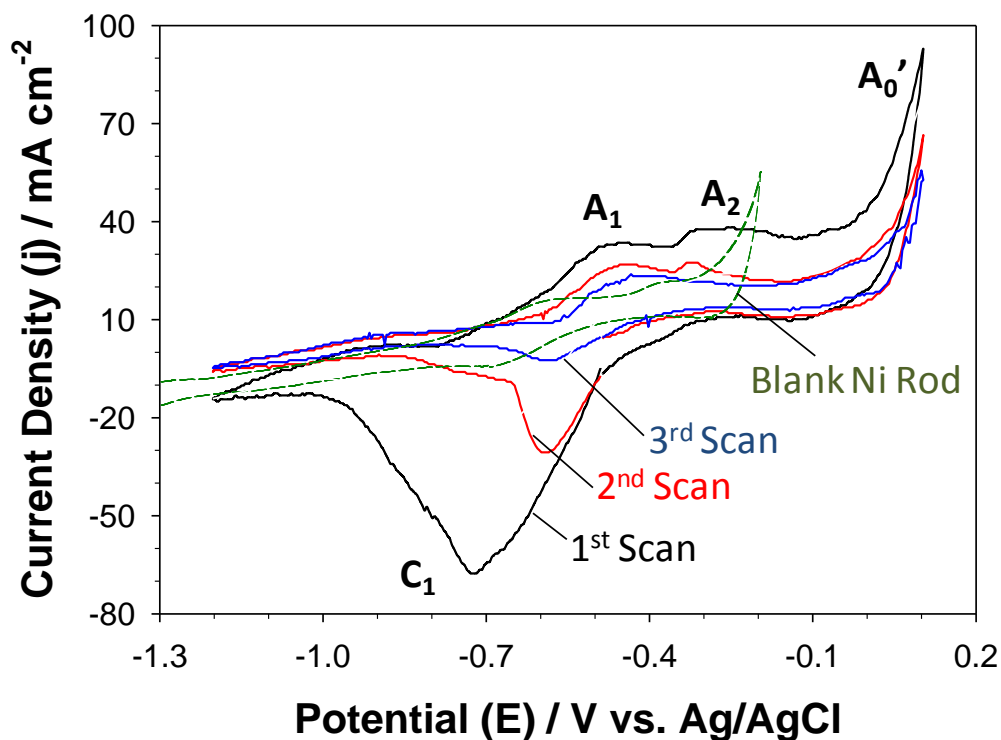
Figure 6.3 – Consecutive CV cycles of NiO in CaCl$_2$ at 810°C using the Mo MCE (1 cm immersion depth 0.51 mm cm^2 surface area, 20 mV s^{-1} scan rate). Overlain is a separate scan of a pure Ni rod (4 mm diameter, 1 cm depth, green curve).

Typically with CV scans of NiO at 20 mV s^{-1} and a potential window of 1.4 V, redox features subsided significantly after the first cycle, and by the third onward became static which is considered to be the cyclic dissolution and deposition of produced metallic Ni following a complete reduction. The sole, relatively large cathodic current peak (C$_1$) is therefore attributed to the single step direct reduction to Ni metal, **Equation 6.5**, as confirmed by thermodynamic predictions (predicted onset of reduction at -0.43 V, versus actual onset at approximately -0.49 V).

$$C_1: \quad NiO + 2e^- = Ni + O^{2-} \qquad \qquad \textbf{6.5}$$
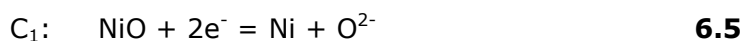
Additionally a direct reduction investigation by chronoamperometry was carried out on a NiO loaded MCE working electrode at -0.68 V vs. Ag/AgCl, followed by SEM analysis to experimentally confirm reduction (**Figure 6.4**).
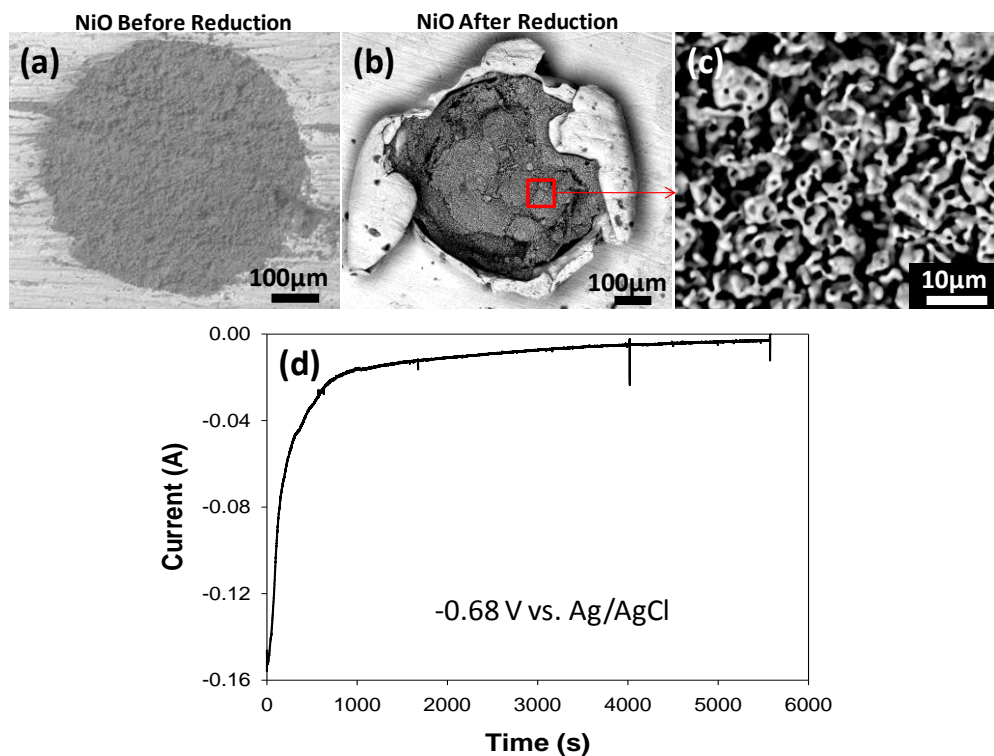
Figure 6.4 – SEM micrographs of (a) a NiO loaded MCE, (b) the MCE after direct chronoamperometry at -0.68 V vs. Ag/AgCl and at higher resolution (c). The current-time curve after approximately 1.6 h is shown in (d).

Supporting elemental analysis by EDS confirmed a less than 1 at% O content following reduction but with minor Mo contaminations, likely introduced during the loading procedure which involved manual pressing by glass slides. After 1.6 hours the NiO contained within the cavity had apparently undergone a complete reduction to Ni and had developed a complex yet relatively uniform porosity.

By using a pure Ni rod as a working electrode during CV, the exact point of anodic stripping for Ni metal could be confirmed as peak A$_2$ in **Figure 6.3**, represented by **Equation 6.6**. Similar to the cathodic counterpart, the current peak at A$_2$ diminished to a relatively stable background current by the third cycle which represents the reversible plating and stripping of Ni. The anodic peak at A$_1$ also showed a successive decrease in current intensity to a background level. Due to the relatively small size of the current response its likely this is represented by the reoxidation of Ni to

NiO, where O^{2-} availability is the limiting factor from the gradual discharge to CO/CO$_2$ at the anode and so decreases on each cycle as reduction progresses further (**Equation 6.7**).

$$A_2: \quad Ni = Ni^{2+} + 2e^- \qquad \textbf{6.6}$$

$$A_1: \quad Ni + O^{2-} = NiO + 2e^- \qquad \textbf{6.7}$$
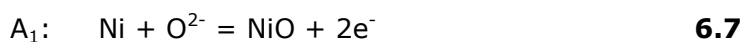
A distinct appearance was observed when increasing the scan rate of CV on the NiO containing MCE from 20 mV s^{-1} to 50 mV s^{-1} (**Figure 6.5**). Between the first subsequent cycles, a considerable peak separation of C$_1$ in the cathodic direction could be clearly observed. It seems the increase in the rate of potential change negatively influenced the electrode kinetics such that overcoming the initial energy barrier between the conducting MCE and insulating NiO became more difficult. Or in other words the initial electron transfer at the 3PI is better served at slower scan rates due to a greater allotted time to overcome the energy barriers present.
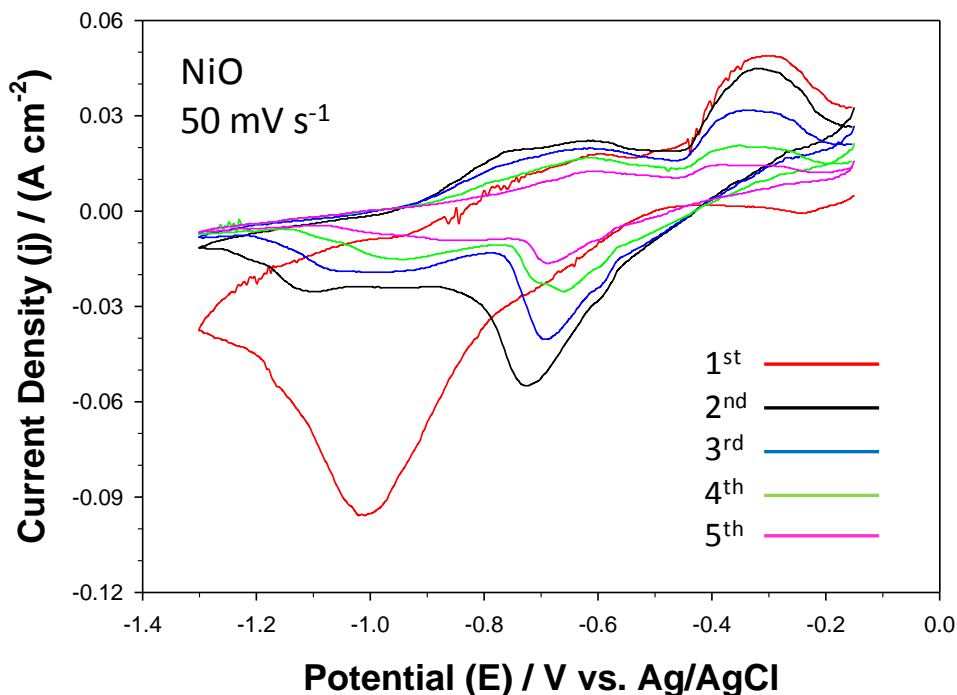
Figure 6.5 – CVs of the Mo/NiO working electrode recorded in a potential range of -1.3 V to -0.1 V vs. Ag/AgCl at 810°C. Scan rate: 50 mV s^{-1}

This explanation is supported by the positive shift in the C$_1$ peak on the successive CV cycles, as the initial metallisation decreases the effective 3PI surface area and assists further electron transfer to the remaining oxide. Additionally the development of open porosity from O^{2-} removal and low energy state orientation of Ni metal phases will further amplify the positive feedback mechanism of FFC based reduction in MCE cavities.

According to CVs of NiO in molten CaCl$_2$ at 810°C, the onset for reduction can be as positive as -0.49 V vs. Ag/AgCl. However in less ideal conditions with poorer kinetics, for example with bulk electrolysis of larger oxide quantities, a greater overpotential (η) is usually necessitated to ensure the process can both continue and progress at a satisfactory rate. With the envisioned pyroprocessing method being considered, difficulties arise when the extent of the required overpotential overlaps with the region for reduction or partial reduction of the other oxides present in the spent fuel matrix. For the 2NiO-CeO$_2$ binary, and also for utility in mixtures with ZrO$_2$ and TiO$_2$, pure CeO$_2$ CV investigations were also performed to investigate the prospect of this reductive overlap.

6.3.1.2. Cyclic Voltammetry of CeO$_2$

CV investigation of CeO$_2$ is very sparse within the literature, predominantly owing to the intrinsically stable properties of lanthanide oxides which makes their electrochemical reduction difficult. Studies using soluble Ce containing species such as CeCl$_3$ in molten salts are more numerous and have highlighted the redox reactivity of Ce(III)-Ce^0 to be at very cathodic potentials close to the respective decomposition points of the electrolytes used. Indeed some authors have concluded that the electrochemical conversion of the oxide to metallic Ce is not possible under normal circumstances and instead a metallothermic reduction using Ca or Li (in the case of LiCl containing electrolytes) is the primary mechanism[239–241]. Work

here attempted to assess the validity of these claims by investigating CeO$_2$ redox behaviour in molten CaCl$_2$ at 810°C.

For a direct CeO$_2$ reduction, the thermodynamically predicted required potential is much more negative than for NiO (-1.20 V vs. −0.40 V), and closer to the potential for Ca^{2+} deposition (-2.25 V). However consideration must be taken of the viable intermediates (Ce$_2$O$_3$ and CeOCl) of which both are more favourably formed and more electrochemically stable. In the CV scan for CeO$_2$, the only observable oxidation peak present (A$_1$) is 400 mV more positive than the observed Ca oxidation (**Figure 6.6**). The presence of an oxidation peak at such anodic potentials suggests it is indeed possible to produce metallic Ce with a separate stripping peak to Ca. This was tested further by limiting the cathodic potential to 100 mV more positive than for calcium reduction and holding the potential for 60 seconds, still the cerium oxidation peak could be observed (inset, **Figure 6.6**).
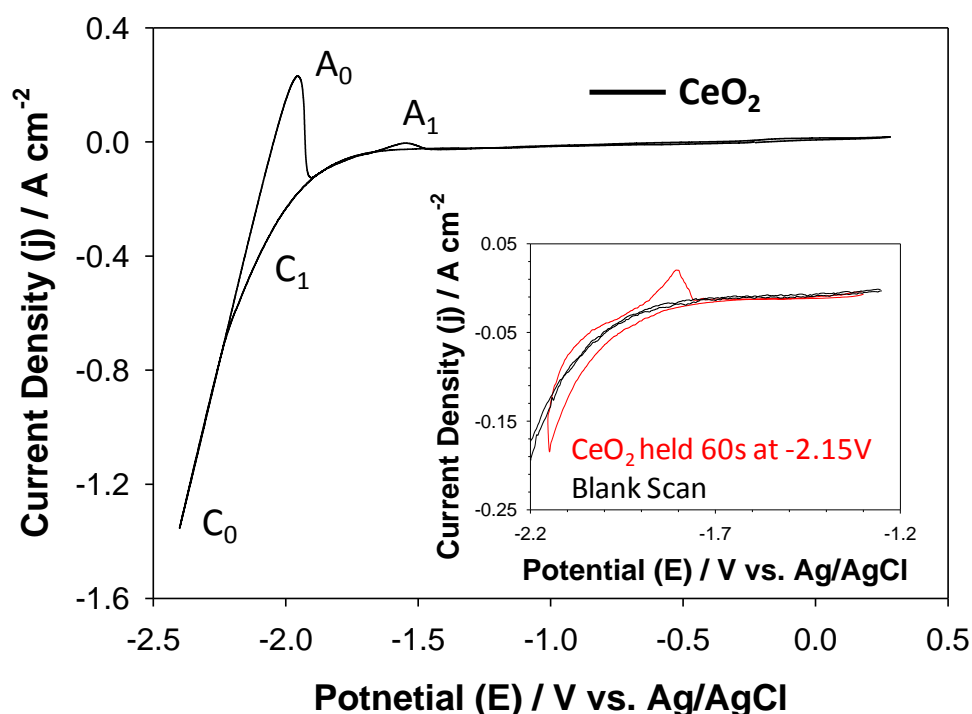
Figure 6.6 – CV of CeO$_2$ scanned across the full potential window in molten CaCl$_2$ (-2.4 V to 0.3 V). Inset is CVs of pure CeO$_2$ and a blank Mo MCE scanned over a narrower potential window, with the CeO$_2$ scan having been paused at the cathodic limit for 60s before continuing. Scan rates: 20 mV s^{-1}.

Unfortunately at this potential range and temperature it proved impractical to collect fully reduced samples using the CeO$_2$ loaded MCE working electrode design as metallic Ce resides in its liquid phase and is believed to fall from the electrode due to loss of mechanical integrity. The single oxidation peak present on the CeO$_2$ CV inset in **Figure 6.6** is thought to be the formation of CeCl$_3$ (A$_1$, **Equation 6.8**), a soluble product in molten CaCl$_2$ which could also help to explain the complete material loss within the MCE after scanning to such negative potentials during cycling.

$$A_1: \quad Ce + 3Cl^- = CeCl_3 + 3e^- \qquad \textbf{6.8}$$
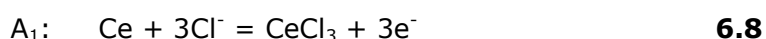
Although no obvious reduction peak could be seen in the pure CeO$_2$ CV scan at these ranges besides that for CaCl$_2$ reduction, it is clear that the predicted thermodynamics in **Table 6.4** indicate an initial one electron transfer reaction occurs at a relatively positive potential, forming either Ce$_2$O$_3$ or CeOCl (-0.14 V/-0.47 V vs. Ag/AgCl respectively). Presence of an oxidation peak for Ce metal on the anodic sweep of CeO$_2$ CVs highlights a full reduction must occur on the cathodic sweep and is apparently masked by the initial underpotential reduction of Ca^{2+} to Ca$^+$. Correlating the onset potential for the reduction of the Ce(III) species is therefore very difficult, however thermodynamic predictions suggest the dominant reaction is for a full CeOCl reduction to metallic Ce, with an onset 30 mV more positive than that for the Ce$_2$O$_3$ reduction. Hence the current increase at peak C$_1$ is attributed to the full reduction of produced CeOCl (**Equation 6.9a**) or even the direct reduction of CeO$_2$ not converted in the cumulatively small duration of the cathodic CV sweep (**Equation 6.9b**).

$$C_1: \quad CeOCl + 3e^- = Ce + O^{2-} + Cl^- \qquad \textbf{6.9a}$$

$$CeO_2 + 4e^- = Ce + 2O^{2-} \qquad \textbf{6.9b}$$
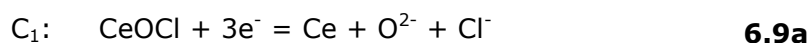
The CeO$_2$ loaded MCEs were scanned to progressively more positive potentials in order to discern the exact point of reducibility and confirm

that the intermediates produced could be independently reduced without decomposing the electrolyte. **Figure 6.7** shows two overlain CV scans from different CeO$_2$ containing MCEs scanned to slightly different cathodic potentials (-2.10 V and -2.05 V) and each held for 30s at the cathodic limit. Here it's clear that even at -2.10 V (150 mV more positive than Ca^{2+} reduction) Ce can be produced, evidenced by the oxidation peak presence. The second experiment using a slightly more positive cathodic limit presents a much more modest current increase at anodic peak A$_1$. It is possible, and indeed likely that the current response here is a remnant of Ce lost to the electrolyte during the previous scan. Consequently for the purpose of maintaining a conservative analysis the limit of Ce production via electrochemical reduction of CeO$_2$ was set to +150mV vs. Ca/Ca^{2+}.
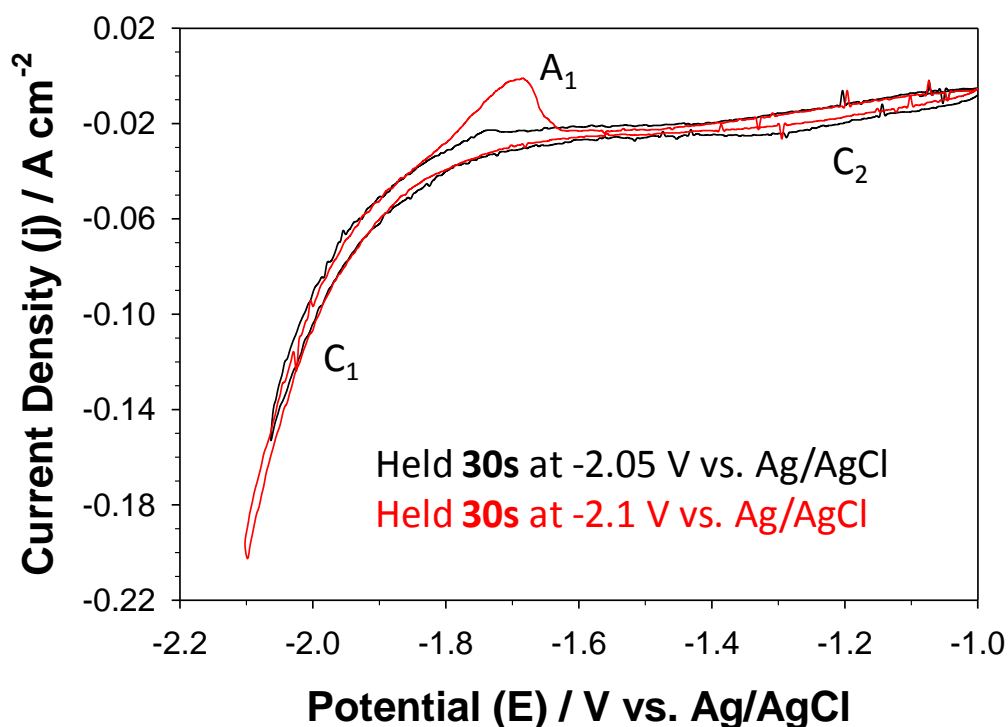
Figure 6.7 – CVs of CeO$_2$ loaded Me MCEs in molten CaCl$_2$ at 810°C, one scanned to -2.1 V (red curve) and the other to -2.05 V (black curve) but both held for 30s before the return sweep.

Interestingly on both of the CV curves in **Figure 6.7** a second reduction peak appeared at more positive potentials, termed C$_2$. Although the

theoretical formation potential of both CeOCl and Ce$_2$O$_3$ is far more positive than shown in **Figure 6.7**, there may be kinetic effects driving the slow reaction and additionally the onset potential of C$_2$ is not clearly defined. Indeed as will be discussed in the next section, the formation of CeOCl is an apparently rate limited process depending on the availability of free Cl$^-$ ions, and so Peak C$_2$ is attributed to its formation (**Equation 6.10**).

$$2CeO_2 + CaCl_2 + 2e^- \rightleftharpoons 2CeOCl + CaO + O^{2-} \qquad \textbf{6.10}$$
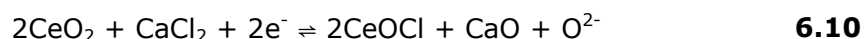
The magnitude of peak C$_2$ is very marginal, which perhaps explains the reason for its presence not being directly obvious for the CV scan presented in **Figure 6.6** (i.e. the current scale when incorporating the cathodic tail was too large). Crucially however, it is paramount to define the point of onset for CeOCl formation and whether or not it falls within the potential range for NiO reduction. Electroanalysis for the binary 2NiO-CeO$_2$ will be given in the next section; along with ex-situ imaging and elemental mapping to support these CV derived discussions.

6.3.2. Electrochemical Behaviour of 2NiO-CeO$_2$

6.3.2.1. Cyclic Voltammetry of 2NiO-CeO$_2$

The binary oxide feed was prepared by manual mixing as described in the methodology chapter prior to loading into the MCE and insertion into the molten CaCl$_2$. Performing CV on 2NiO-CeO$_2$, shown in **Figure 6.8**, revealed a unique electrochemistry to either constituent oxides, with an additional oxidation peak at −1.25 V vs. Ag/AgCl (peak A$_2$) absent in both pure NiO and CeO$_2$ cycles. The cause of this current increase is likely by an anodic dissolution of CeNi$_x$ alloy phases produced by scanning to a relatively negative cathodic potential (-2.2 V vs. Ag/AgCl in this instance). The direct electrochemical formation of the CeNi$_5$ alloy for the purpose of hydrogen storage is a process that has been previously demonstrated via the use of the FFC Cambridge process[242]. If confirmed, the presence of alloy

dissolution would correspond to a complete reduction of at least some of the CeO$_2$/CeOCl, though the presence of Ni metal may provide electro-catalytic assistance in lowering the energy barrier for electron transfer to the insulating oxides or even as a direct oxygen scavenger, reducing the oxygen partial pressure within the MCE cavity and facilitating a more favourable removal of O^{2-} ions. In an similar conclusion, hydrogen reduction of Gadolinium Doped Ceria (GDC) as measured by Raman Spectroscopy was found to be assisted by the presence of NiO/Ni, due partly to a hydrogen spillover mechanism and partly in avoiding intermediate phase formations[243]
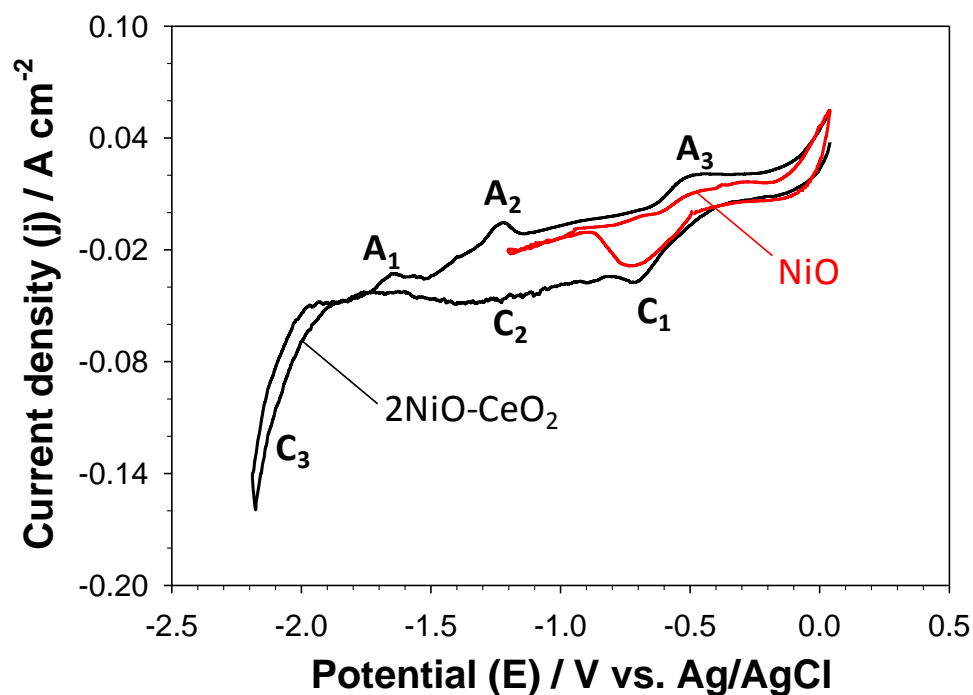
Figure 6.8 – 1st cycle CV scan of the stoichiometric 2NiO-CeO$_2$ overlain with a pure NiO CV. Scan rate: 20 mV s^{-1}.

The first anodic peak on the return scan at −1.75 V vs. Ag/AgCl (A$_1$) could correspond to a shifted potential for Ce^0 oxidation to Ce$^{(III)}$ (observed in **Figure 6.7** at −1.9 V) indicating an increased difficulty for electron transfer caused by a morphological shift and/or intermediate phase transition not present in the pure CeO$_2$ CV scan. Alternatively Ce and Ni are known to form a broad range of solid solutions besides CeNi$_2$ incorporating higher Ni

stoichiometry as illustrated by the Ni-Ce phase diagram in **Figure 6.9** and this peak may represent the dissolution of one of these compounds from an incomplete reduction of CeO$_2$ or a lack of free Ce presence. In some CV experiments on 2NiO-CeO$_2$ using a slower scan rate (<10 mV s^{-1}) peak A$_1$ could not be readily identified, suggesting the latter explanation is the cause of the current peak as the increased duration at more cathodic potentials may facilitate a more complete CeO$_2$/Ce$^{(III)}$ reduction.
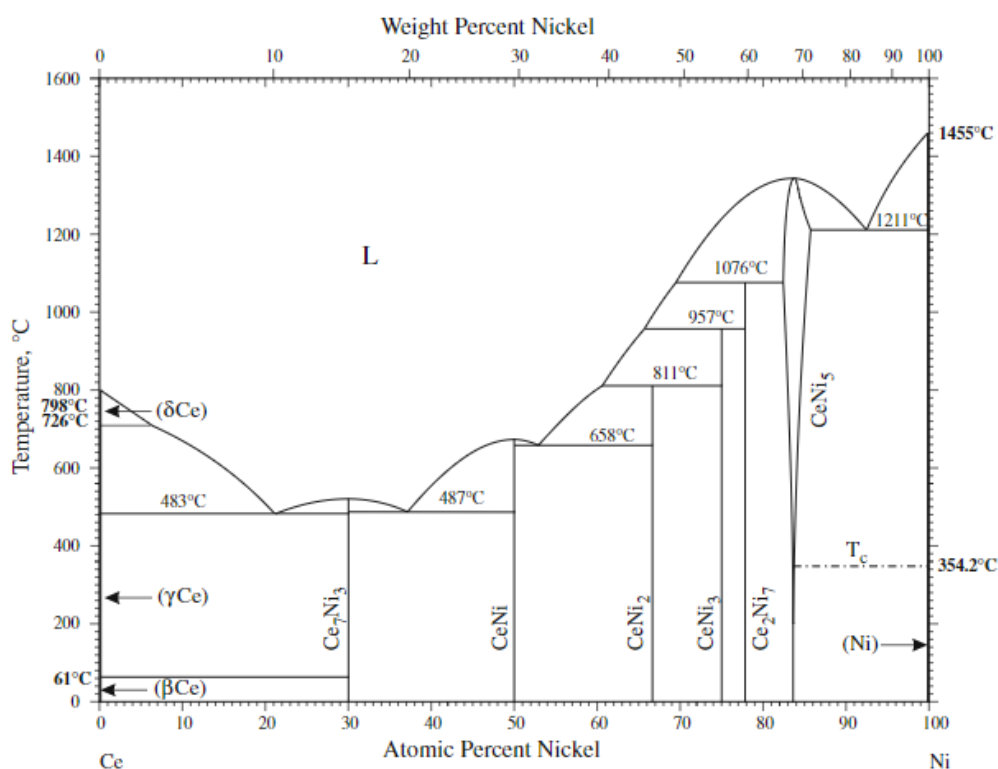
Figure 6.9 – Phase diagram of Ce-Ni [244].

The cathodic behaviour of the CV in **Figure 6.8** within the region for a full CeOCl reduction (more negative than -1.8 V vs. Ag/AgCl) is clearly distinct to the pure CeO$_2$ scan, which appears to be caused by the presence of metallic Ni aiding the reduction to Ce and subsequent alloying. Additionally, due to their being a lesser absolute quantity of each component within the binary oxide mixture compared to the pure oxide scans the magnitudes of current peaks in **Figure 6.9** are slightly smaller than those in **Figures 6.6** and **6.8**. After the initial reduction peak (C$_1$), determined to be the single

214

step NiO reduction to Ni reaction (highlighted by the overlain NiO CV scan) a broad but shallow current increase exists (peak C$_2$). It was believed that this could be attributed to the formation of the initial CeO$_2$ intermediate reduction product, Ce(III). To investigate this the binary oxide mixture was loaded into an MCE, immersed in the molten salt and scanned using CV to a potential within the range of the C$_2$ peak (−1.0 V vs. Ag/AgCl). The produced curves are shown in **Figure 6.10a** following 10 cycles, where a modest current increase is shown on the first scan at approximately -0.4 V on the cathodic sweep and -0.5 V on the anodic, corresponding well to the reduction of NiO and oxidation of Ni shown in **Figure 6.8**. A clearly distinguishable secondary current increase was shown on the cathodic sweep following the NiO reduction, attributed to the C$_2$ reaction.
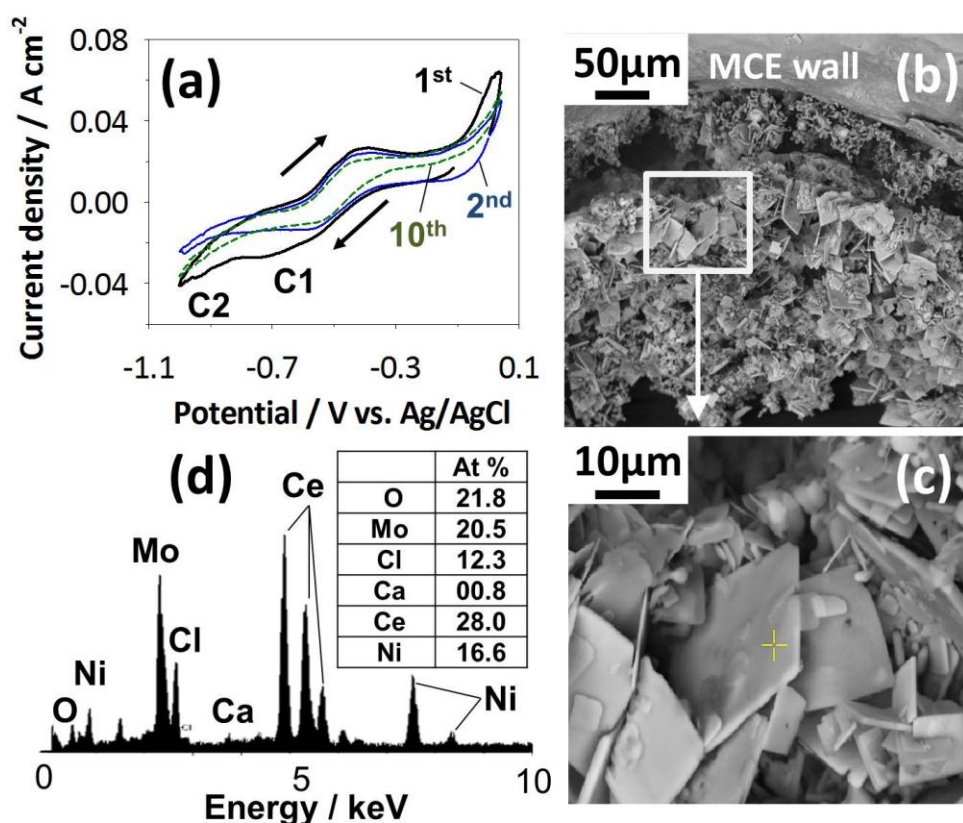
Figure 6.10 - (a) 1st, 2nd and 10th CV curves of 2NiO-CeO$_2$ scanned to a cathodic limit of -1.0 V vs. Ag/AgCl at a 20 mV s^{-1} scan rate with labels (C1 and C2) indicating the two reduction peaks present. (b) and (c) show SEM images of the Mo MCE interior after washing and (d) gives EDS spot elemental analysis results on one of the crystallites from (c).

Following gentle washing in water for 1 h, SEM imaging was performed on the MCE following CV (**Figure 6.10b**) and with higher resolution (**Figure 6.10c**). Encased in the periphery of the electrode cavity is a nodular structure, judged to be metallic Ni by EDS analysis and by the morphological similarities to metals produced by the FFC Cambridge Process (i.e. those in Figure 6.4). This small remaining presence of Ni either hadn't been anodically stripped in the relatively short cumulative time for oxidation or had been continuously redeposited on the return cathodic scans. The unique, quasi- two dimensional and plate-like crystallites in the centre of the cavity (**Figure 6.10c**) had a suggested stoichiometry of CeOCl (**Figure 6.10d**), an electrochemically viable reduction product of CeO$_2$, given by the simplified full cell **Equation 6.11**.

$$4CeO_2 + 2CaCl_2 + C = 4CeOCl + 2CaO + CO_2$$
$$\Delta G^o_{810^\circ C} = 248.06 \text{ kJ}$$

6.11
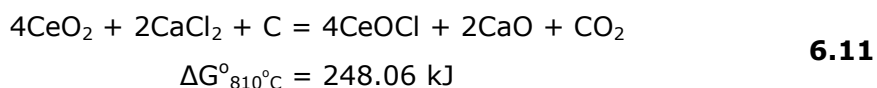
With the ΔG value being calculated based on available thermodynamic data[120]. Much of the content from the interior of the cavity had been lost as seen via SEM imaging, either through the washing procedure or destabilisation of the packed cavity from the extensive morphological change during reduction. Performing CV on the pure CeO$_2$ in the region of CeOCl formation resulted in a complete loss of material in nearly all attempted experiments, suggesting that the presence of Ni in the periphery of the cavity aided stability in providing atomic scaffolding for CeOCl.

6.3.2.2. Concerning CeOCl Formation

Validation of the **Equation 6.11** by crystallographic or spectroscopic techniques such as XRD or XPS proved difficult with these MCE samples owing to the small absolute quantity of materials (<1 mg), however has been performed elsewhere in the literature on the same precursor materials and under similar conditions[242]. In the cited study, electrolysis of 5NiO-CeO$_2$ pellets of 2.5 g mass were performed in molten CaCl$_2$ at

1000°C, with samples taken at 1, 2, 4, 6, 8, and 12 h for XRD. The presence of CeOCl was observed in the first sample (at 1 h) and present until a final complete alloy formation of CeNi$_5$ was detected after 12 h. Initial NiO content was shown to be completely replaced by Ni after around 4 h, whereas both CeO$_2$ and CeOCl were detected up until 8 h which is an indicator of the relative ease of reduction for NiO and follows closely the observed electrolysis route for species formation shown here by CV within the MCE. CeOCl formation by **Equation 6.11** has been suggested to form via the coalescence of Cl$^-$ anions over the bulk CeO$_2$ structure, gradually discharging O^{2-} anions in the form of CaO[245], which may help explain the coexistence of CeO$_2$ and CeOCl phases within the NiO-CeO$_2$ pellet study discussed above as oxygen saturation within the bulk oxide pellet can act as a rate limiting factor to further CeOCl accumulation. CeO$_2$ was not observed in the MCE studies from **Figure 6.10** as apparently a complete conversion to CeOCl could be achieved from the relatively open porosity and small initial quantity of oxide material.

Thermodynamic calculations presented in **Table 6.4** however predict that the more favourable reaction in this system is the production of the intermediate oxide (IO), Ce$_2$O$_3$. The process of IO formation is largely dependent on how durable they are and can remain on the working electrode. At very negative polarisation energies for instance a full reduction to a final product (Ce^0) could be facilitated avoiding their accumulation. As the desired process being considered here is one of selective reduction involving a precise and limited applied potential, intermediates are still viable products, however questions are raised regarding their stabilities. For example the Ce$_2$O$_3$ intermediate phase has been shown to be unstable in both LKE and CaCl$_2$-NaCl[246], and in specific

oxobasic conditions can readily undergo a chemical reaction to produce the oxychloride phase as described by **Equation 6.12**.

$$Ce_2O_3 + CaCl_2 = 2CeOCl + CaO \hspace{2cm} \textbf{6.12}$$

At unit oxygen activity, **Equation 6.12** is not spontaneous at the operational temperature used ($\Delta G^o_{810^oC}$ = 94.54 kJ). A positive Gibbs free energy value indicating that an energy input is still required for the formation of CeOCl from Ce$_2$O$_3$ in CaCl$_2$ at 810°C. Whilst the Gibbs free energy for formation (ΔG_f^o) of CeOCl is believed to be positive[247] and the reaction of Ce$_2$O$_3$ in the free presence of chlorine is viable (ΔG_{810oC} = -35.96 kJ), the cathodic potential in all performed experiments was precisely controlled to be more positive than that for CaCl$_2$ decomposition at approximately –2.25 V; hence avoiding formation of free Cl$_2$. Based on the operational parameters, the empirical EDS evidence from this study and XRD analysis from elsewhere in the literature, it is reasonable to conclude the pathway for CeOCl formation denoted in **Equation 6.12** can be disregarded and that instead the formation of CeOCl is shown to be electrochemical.

Reasoning similar to this can be helpfully visualised by the aid of predominance diagrams, which have been produced for Ce-O compounds[246] and also for the active U-O and Pu-O phases[75] revealing a large region of stability for both CeOCl and PuOCl. Understanding the route of formation in the surrogate is therefore very significant in application to pyroprocessing. Regardless of its origins, the production of CeOCl is parasitic to the overall current efficiency of the partitioning process. Moreover the materials characteristics of CeOCl, such as morphology and electronic and chemical stability, are entirely dissimilar to CeO$_2$. Its formation therefore should be avoided in order to produce a successful and precise NiO separation.

Other works investigating the Ce-O system in molten chloride melts have drawn similar conclusions in that CeO$_2$ is the only stable solid Ce(IV) state, but exclusively exists as Ce(III) within the molten salt[246], apparently in the form of CeO$^+$. However the cited work contradicts other published data on the solubility of CeOCl, suggesting instead Ce$_2$O$_3$ is solubilised and CeOCl is the resultant precipitated form of Ce, being both solid and stable in the melts that were tested (LKE and equimolar CaCl$_2$-NaCl). Although the electrochemical data acquired through CV as presented above suggest a direct formation of CeOCl when correlated to the thermodynamic predictions, the fact that Ce$_2$O$_3$ phases appeared absent could be indicative of its solubility in the molten CaCl$_2$ at 810°C, rather than its lack of formation.

During a direct reduction investigation of a 2NiO-CeO$_2$ loaded MCE using chronoamperometry at a cathodic potential in region for the proposed CeOCl formation, but not for CeOCl reduction (-2 V), a complete loss of Ce containing species was observed via SEM (**Figure 6.11**) and EDS.
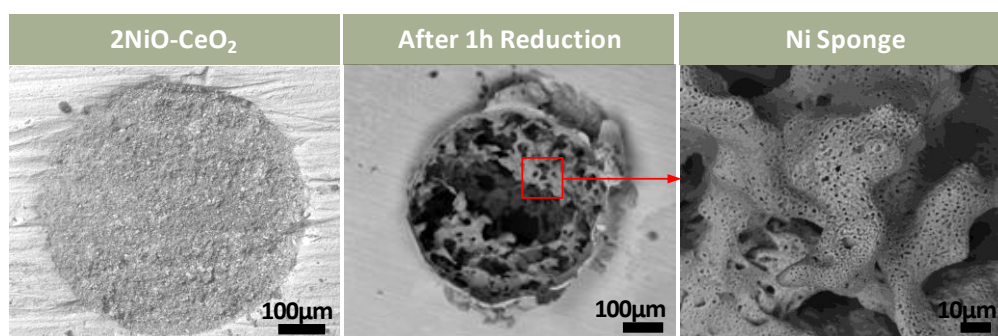
Figure 6.11 – SEM images of the 2NiO-CeO$_2$ loaded MCE (left) and after 1h chronoamperometry at -2.0 V vs.Ag/AgCl (centre) with higher resolution (right).

The applied potential wasn't sufficient enough to reduce any theoretically formed CeOCl and induce alloying with Ni, hence why only pure Ni could be identified by elemental analysis. However the complete loss of Ce via the dissolution of CeOCl into the molten salt is theoretically plausible. Similarly a complete dissolution of Ce$_2$O$_3$ without precipitation of CeOCl an

alternative possibility as the extended duration and favourable oxide ion diffusion may facilitate Ce(III) to remain in solution. No literature exists on the extent or absolute quantitative solubility of CeOCl in molten CaCl$_2$, although some works involving other general LnOCl (Ln = lanthanide) in CaCl$_2$ has suggested that all exhibit at least partial solubility to exist as LnO$^+$ within the melt e.g. La and Nd shown in **Figure 6.12a** and **6.12b**. Furthermore the stability of this phase is intrinsically related to the oxygen activity, with other works modelling and experimentally deriving that for the PuO$_2$/PuOCl/Pu$_2$O$_3$ system in both CaCl$_2$ and KCl-NaCl, Pu(III) is unstable within the electrolyte; precipitating as PuOCl at higher oxygen activities (**Figure 6.12c**).
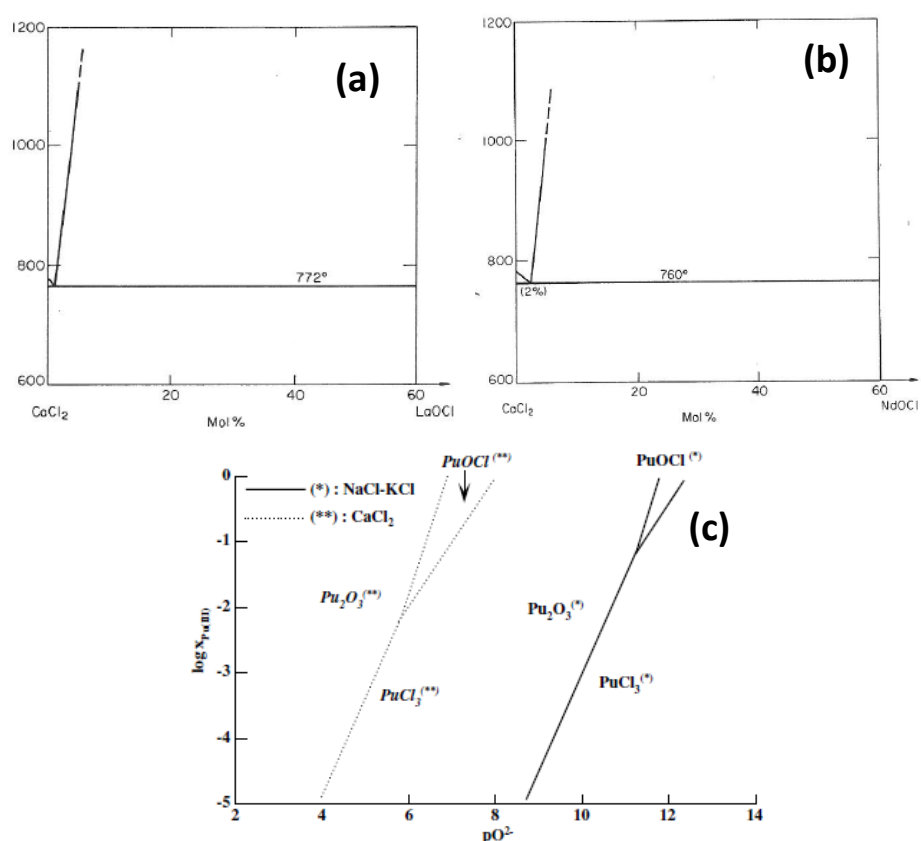
Figure 6.12 – Phase diagrams of (a) CaCl$_2$-LaOCl and (b) CaCl$_2$-NdOCl. (c) Solubility of Pu(III) calculated in CaCl$_2$ and NaCl$_2$-KCl as a function of pO^{2-} at 800°C[248,249].

When electrolysis was conducted at relatively cathodic potentials and for sufficiently long durations it appears the CeO$_2$ partial reduction product will

be solubilised into the molten salt, provided the kinetics are favourable enough to support a low oxygen activity around the working electrode. In the CV experiment presented in **Figure 6.10**, the constant and rapid anodic cycling likely facilitated the retention of oxygen activity surrounding the cavity of the MCE, so even though only a marginal quantity of initial CeO$_2$ was present the development of CeOCl crystallites was supported, rather than dissolution into the CaCl$_2$. It proved beyond the scope of this thesis to construct and deploy a dedicated oxygen sensor for the purpose of determining oxygen activity, though it is technically feasibly using an Yttrium Stabilised Zirconia Membrane Electrode (YSZME) with platinum as the O$_2$ catalysing material. The issue arises both in the difficulty of manufacture and maintaining stability and accuracy due to the poor conductivity of YSZ to O^{2-} ions in CaCl$_2$ at 810°C, further exacerbated in the lower temperature LCE melt (at 600°C).

A few explanations exist as to why there was no current increase correlated to Ce(III) formation observed within the potential window for Pure CeO$_2$ prior to the main reduction peak at approximately -1.6 V. As the anodic peak from the same CV (**Figure 6.8**) is relatively small in magnitude it is possible some of the loaded oxide powders were lost prior to the start of electrochemistry which may explain the apparent lack of other initial reduction currents predicted at more positive potentials. Additionally CeOCl formation is rate limited by the presence of free Cl$^-$ ions and the kinetics of O^{2-} mass transport out of the oxide working electrode, factors that may be assisted by the initial reduction of NiO increasing open porosity.

Despite the complications developed by the CeOCl presence, thermodynamic data in **Table 6.4** and the clear reduction peak separation observable in both 2NiO-CeO$_2$ CV scans at approximately −0.8 V (peaks C1 and C2 in **Figure 6.10**) suggest that a NiO only reduction and partitioning

is still achievable with precise potential control. An attempt at partitioning NiO from CeO$_2$ was made using pelletised electrodes based on the accumulation of these empirical and theoretical findings.

6.4. Bulk Partitioning of Ni from 2NiO-CeO$_2$

6.4.1. Potentiostatic Electrolysis

The Mo MCEs proved to be an excellent working electrode for transient electroanalytical characterisation. The application towards partial direct reduction and anodic dissolution however necessitates some material removal via partitioning, and so may induce mechanical failure of the remaining oxide present within the MCE electrode, preventing sample recovery. To assess the proposed technology using the electrode potentials defined by earlier CV investigation a series of metal oxide pellets were produced with the purpose of enhancing sample recovery, permitting bulk analysis and to better emulate how the idealised final process for spent fuel reprocessing would operate. A series of potentiostatic electrolysis experiments were performed on small (5 mm dia.) cold-pressed 2NiO-CeO$_2$ pellets which had been subject to sintering at 1000°C for 3 h. The various conditions of each experiment are outlined in **Table 6.5**, along with the parameters of each oxide pellet used prior to electrolysis.

Table 6.5 - Operational parameters for individual chronoamperometry experiments on 2NiO-CeO$_2$ pellets. E1 represents an attempt at partitioning Ni, with E2 and E3 investigating direct reduction at key cathodic potentials.

Experi-ment	Pellet Dimension diameter x height (mm)	Pellet Weight (mg)	Reduction potential (V vs. Ag/AgCl)	Oxidation potential (V vs. Ag/AgCl)	Total Duration (mins)	Product colour
E1	4.9 x 1.6	125	- 0.65	+ 0.01	60 (30/30)	White
E2	4.9 x 1.6	120	- 0.81	-	30	Grey
E3	4.9 x 1.4	108	- 2.15	-	60	Grey

After electrolysis the pelletised working electrodes were raised above the salt and left to cool under constant argon flow within the retort before being removed and washed in hydrated DMSO for 2 days for imaging and analysis. The hydrated DMSO proved much more effective as a non-oxidising solvent than pure DMSO, facilitating a complete dissolution of adhered CaCl$_2$ following the 48 h of contact at a sufficiently facile rate as to not destabilise the product. Securing the pellets with a 1 mm gauge Mo mesh and thin (0.1 mm) wire proved to be a favourable fixture which did not inhibit CaCl$_2$ ingress to the pressed and sintered pellets. This arrangement benefits from providing multiple contact points between mesh and pellet for electron transfer and reduction via the 3PI model. Using a larger quantity of the metal oxide also helps visually identify any changes to the bulk oxide electrode and better represents the requirements for an eventual spent fuel reprocessing technology. To determine the feasibility of partitioning Ni an initial experiment (E1, see **Table 6.5**) was performed in which a reduction potential of -0.65 V and oxidation potential of +0.01 V vs. Ag/AgCl were applied in succession for 30 minutes each. It was important to determine whether any removal of NiO was a consequence of the partial direct reduction and, in particular, the anodic dissolution aspect so a second experiment (E2) with a reduction only electrolysis was carried out for 30 minutes at a more negative potential (-0.81 V). This is beyond the theoretical threshold for Ce(III) phase production and was selected to investigate this phenomenon as a source of CeOCl accumulation from CeO$_2$ partial reduction.

The cathodic current-time plots for both E1 and E2 are shown in **Figure 6.13** (top) and anodic counterpart for E1 given below. In both experiments the reduction current initially increased to a peak after 150 s, however the magnitude of the peak of E2 is greater than E1 (250 mA vs. 130 mA).
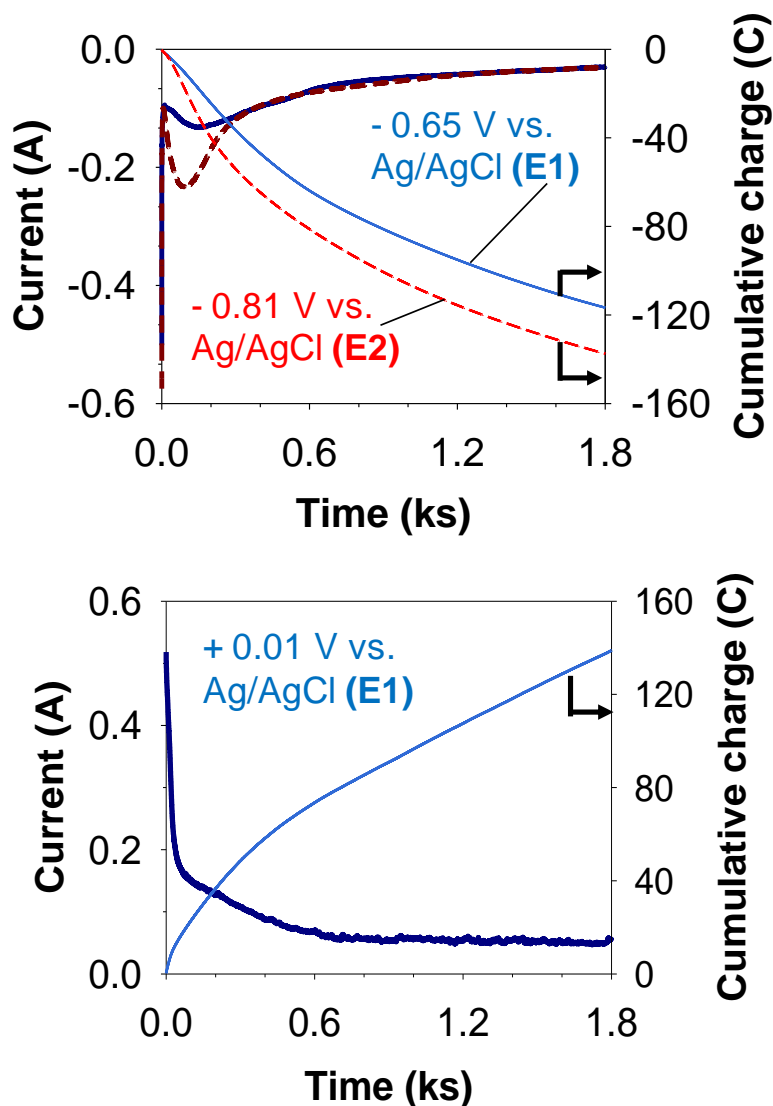
Figure 6.13 – Current-time curves and cumulative charge for the potentiostatic electrolysis experiments E1 (blue) and E2 (red) in molten $CaCl_2$ at 810°C. The reduction current profiles for the two applied cathodic potentials (- 0.65 V and - 0.81 V, 30 minutes each) are shown on the top plot and oxidation profile (for E1 only at + 0.01 V for 30 minutes) is shown on the bottom.

It is thought that this difference could be due to a secondary reaction taking place in the E2 reduction not occurring during the E1 potentiostatic electrolysis experiment, induced by the modest negative shift in applied potential (-160 mV). Despite the more negative applied potential in E2, both currents reached an identical steady state value after approximately 1.7 ks. An additional reduction only investigation was carried out at a more negative potential of -2.1 V (E3) for a longer duration using the same small

2NiO-CeO$_2$ pellets, with the intent of considering the electrochemical reducibility of CeOCl in a bulk oxide pellet. Although CeOCl has been observed within the MCE following CV as shown in **Figure 6.8**, at more cathodic potentials a full loss of Ce species was instead noticed. However as the total mass of the 2NiO-CeO$_2$ was sub-mg during the MCE study, the pelletised electrode offers a better opportunity to assess solubility in bulk oxide with effectively less favourable reduction kinetics in terms of diffusive capability of O^{2-} ions. Furthermore, as CeO$_2$ is an electrochemical surrogate for Pu, and both Ce and Pu form oxychlorides[247], this knowledge will help better understand phase stability in an active spent fuel system.

The current profile for the E3 potentiostatic electrolysis (**Figure 6.14)** shows a larger background current, expected due to the more negative applied potential; however with no obvious current peaks. In theory the applied potential of -2.10 V should be sufficient to reduce both oxides to metallic phases and subsequently induce alloying, particularly given the benefit of an initial onset of NiO reduction lowering the potential of forming alloy phases. However, due to Ce(III) formation and associated iR drop of using a larger surface area metal oxide working electrode, the supplied energy might not have been adequate enough for this full alloying to occur.
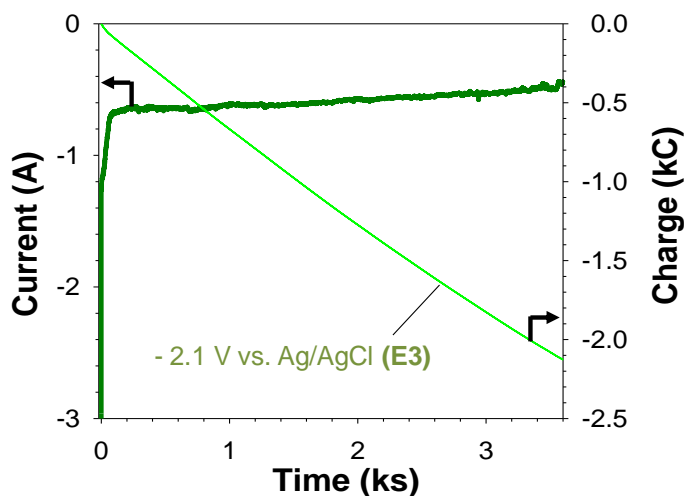
Figure 6.14 - Potentiostatic electrolysis experiment (E3) current and charge plots from 2NiO-CeO$_2$ reduction at -2.1 V. Duration: 60 minutes in CaCl$_2$ at 810°C.

Additionally, it is possible that some of the mixture was non-homogenously distributed through the bulk of the pellet. Morphology changes during a preferential reduction of NiO may cause an uneven distribution or a loss of contact between the packed powders and so the predicted Ni$_2$Ce alloy may not form. At the operational temperature of 810°C a broad range of atomic ratios exist in the liquid alloy phase according to the Ce-Ni phase diagrams available in the literature (see **Figure 6.9**) which could have been lost from the working electrode via gravity or a partial dissolution into the molten salt. All bulk oxide electrolysis experiments were carefully removed from the molten salt and were subject to ex-situ analysis to gauge morphological and composition changes which may have occurred.

6.4.2. Characterisation of Electrolysis Products

Products from experiment E1 and E2 were imaged and analysed by SEM and EDS on the pellet surface, with the results presented in **Figure 6.15**.

1 – Oxygen, 2 – Nickel, 3 – Chlorine, 4 – Calcium, 5 – Cerium
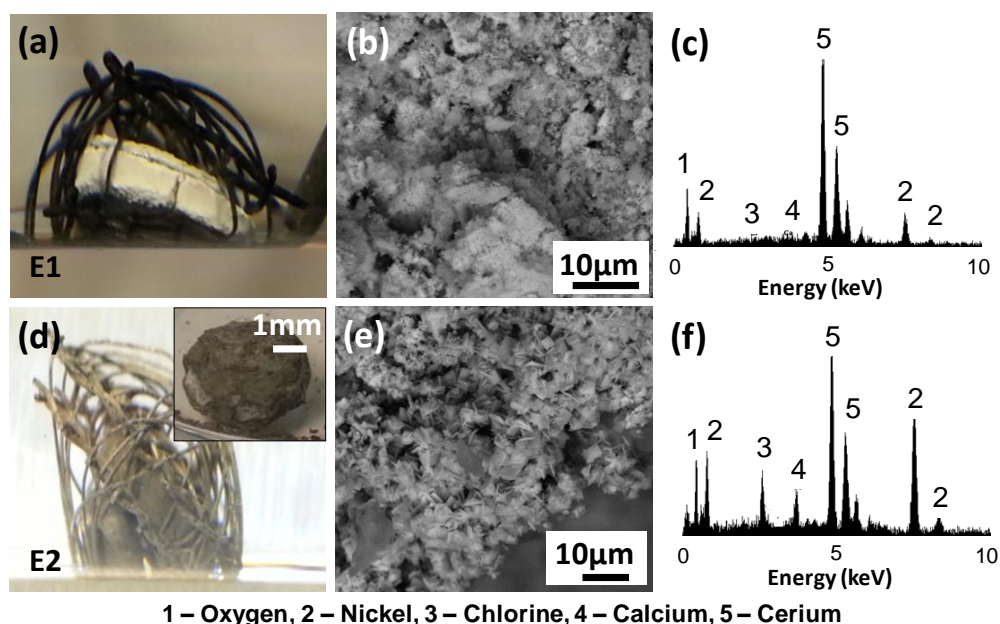
Figure 6.15 - (a) photograph of the pellet product from the E1 experiment of 2NiO-CeO$_2$ applying a reduction −0.65 V and oxidation at +0.01 V respectively, including (b) SEM imaging of the pellet surface and (c) the elemental profile from a full frame analysis of (b). (d) The photographs of the E2 reduction only 2NiO-CeO$_2$ pellet at −0.81 V for 30 minutes with (e) the SEM image of the pellet surface and (f) elemental profile for (e). Both E1 and E2 were performed in CaCl$_2$ at 810°C.

Quantification of the elemental spectrums obtained from EDS is presented in **Table 6.6** for E1 and E2, as well as for E3 and the original stoichiometry. An obvious first observation is that following washing in DMSO to remove solidified CaCl$_2$, is that the colour shifted in both samples from green (owing to the NiO presence in 2NiO-CeO$_2$) to white in E1 and grey in E2 (**Figures 6.15a** and **6.15d** respectively).

Table 6.6 - EDS results for three consecutive chronoamperometry experiments on 2NiO-CeO$_2$ pellets at various reduction potentials in molten CaCl$_2$ at 810°C.

Experiment	Relative Elemental Composition (atomic %)				
	O	Ca	Cl	Ni	Ce
Original	67.0	00.0	00.0	22.9	10.1
E1	64.5	00.4	00.5	07.9	26.7
E2	43.0	02.6	08.2	31.2	15.0
E3	18.6	01.1	06.8	66.3	07.2

SEM analysis of the E1 product (**Figure 6.15b**) reveals a relatively homogenous morphology, lacking the previously observed metallic Ni and CeOCl phases from CV investigations. Full frame EDS of the same image confirms a pure oxide stoichiometry however crucially the Ni presence, which was originally in a 2:1 ratio to cerium, had decreased by 85 % (**Figure 6.15c**, **Table 6.5**). The partitioning process by partial reduction and anodic dissolution had apparently been successful in selectively removing nearly all NiO from the surface of the pellet following just 1 hour of electrolysis, hence contributing to the white aesthetic observed after washing. The lack of metallic Ni, both from visual inspection by SEM and from EDS supported an exclusive oxide stoichiometry suggesting a complete anodic dissolution and consequently that the charge supplied during reduction was the limiting factor for a more complete Ni removal. Understandably this was a consequence of limiting the reducing potential to best avoid CeOCl formation, whereas the oxidising potential (and therefore

ionising energy) was only restricted by the point of Mo dissolution (at approximately +0.1 V). Also apparent is the significant shrinkage of the pellet which displayed cracking along the stress points of the cylindrical disk, seemingly caused by a loss of both O^{2-} anions during reduction and Ni^{2+} cations from anodic dissolution.

In **Figure 6.15e**, the bulk pellet following reduction only chronoamperometry at -0.81 V had a very similar appearance to the MCE cavity interior in the CV investigations of 2NiO-CeO$_2$ scanned to a cathodic limit of −1.0 V (see **Figure 6.8**). Elemental analysis was performed after washing and grinding of the pellet and indicates that the bulk stoichiometry is still that of CeO$_2$, but with a significant presence of CeOCl and some metallic Ni. CeOCl presence in this sample confirms the initial reduction CeO$_2$ at relatively positive cathodic potentials and is likely the cause of the disparity in cathodic charge consumption between E1 and E2 (**Figure 6.13**). However SEM and elemental EDS analysis alone cannot alone distinguish whether the source of CeOCl is from a direct reduction and dissolution via **Equation 6.11**, or a dissolution of Ce$_2$O$_3$ and a precipitation of the crystalline CeOCl. The dispersed metallic Ni throughout the bulk of the pellet is expected to be the cause of the grey coloration. According to these results the potentials acquired from the MCE design during CV can be appropriately applied to the sintered pellet samples with predictable results obtained. Although the morphological and microstructural states influence the electrochemical behaviour, it is shown to be negligible in these bulk pellet examples against the MCE design, suggesting insignificant differences in precursor characteristics despite divergent electrode fabrication techniques (e.g. pellet sintering). These findings also highlight the critical importance of being able to provide a stable reference electrode for this type of partitioning electrolysis, particularly for extended durations.

For the E1 experiment the reduction and oxidation durations were arbitrarily chosen at 30 minutes each. Consequently only 77.6 % of the theoretical required charge for a full reduction of all present NiO was supplied. Following washing and collection from the Mo mesh for ex-situ analysis, the pellet readily cleaved along the fracture lines to reveal a thin veneer of the Ni depleted white crust with the bulk of the core remaining green in colour. Both crust and core were analysed by SEM and EDS (**Figure 6.16**) and confirmed the large percentage removal of Ni from the crust (85 %). It is worth noting that due to difficulties whilst mounting the crust sample for SEM, elemental analysis was performed on the inner surface of the crust section which had been in contact with the NiO rich core. Undoubtedly this would have left an elemental bias towards Ni from contamination and so the extent of partitioning in reality may have actually been significantly higher within the crust than was recorded.

Morphological variance between both crust and core is shown to be marginal as any formed Ni metal was evidently completely removed via anodic dissolution i.e. essentially comparing variances in NiO/CeO$_2$ concentration. In addition CeOCl could not be detected in either section, emphasizing the success of a selective reduction to NiO only. However, in failing to provide the required columbic charge for a full NiO reduction the core of the pellet remained in the original 2Ni:Ce stoichiometry. Besides the limited duration of reduction other kinetic factors may have influenced the lack of partitioning within the bulk pellet, including porosity, geometry and homogeneity of precursor particle size.
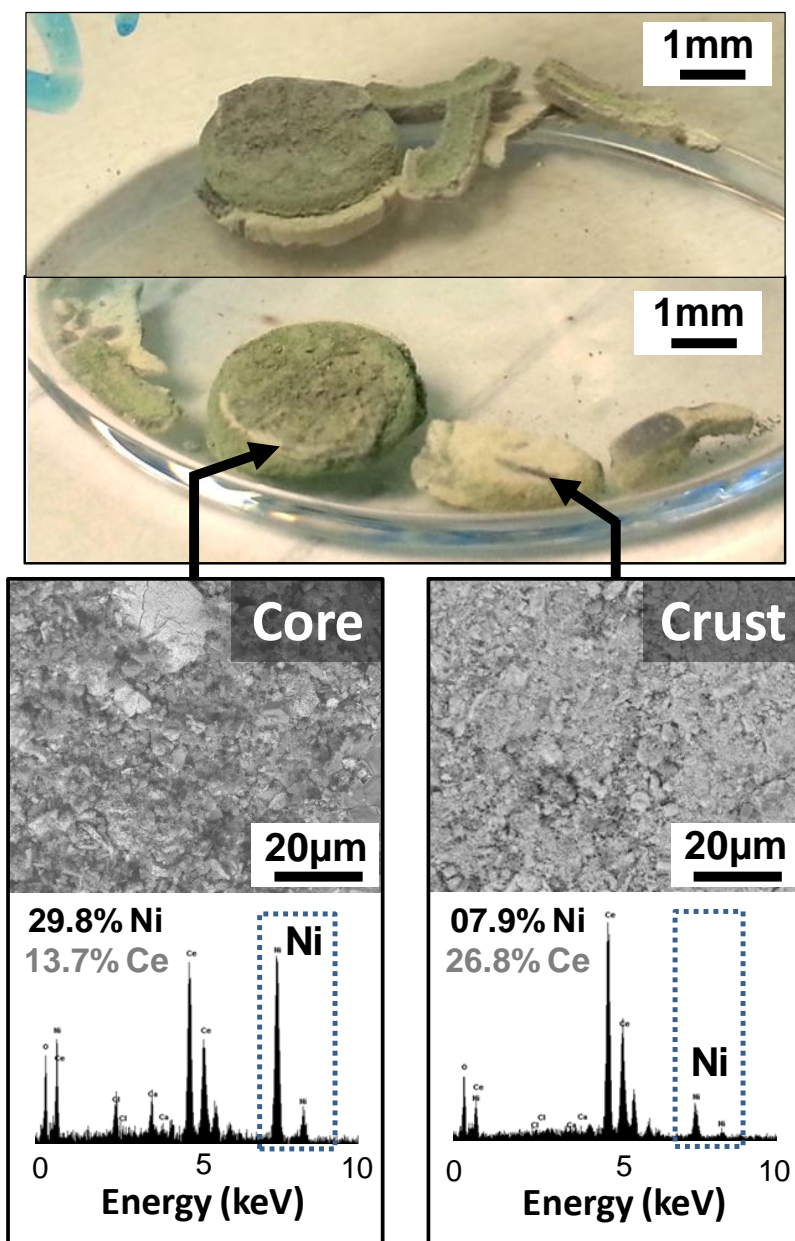
Figure 6.16 – Photographs of the recovered 2NiO-CeO$_2$ pellet after partial reduction and anodic dissolution in CaCl$_2$ at 810°C. SEM and EDS elemental analysis for the crust and core sections following direct reduction at -0.65 V and dissolution at +0.01 V are given and highlight the change in atomic Ni presence.

These parameters comprise an optimisation requirement which is crucial in the progression of partitioning into more analogous spent fuel surrogates; with a potential application for not only the nuclear field, but also in wider materials processing.

The product recovered from the E3 experiment was noted in having an appearance aesthetically similar to the partial reduction product of 2NiO-CeO$_2$ from E2; however most of the Ce presence in the E3 electrolysed pellet had been removed (**Table 6.5**). Consequently it is unlikely that an alloying did occur to form a liquid phase as Ni would have simultaneously been lost from the pellet bulk in stoichiometric quantities. Due to the likelihood of Ce(III) being partially soluble within the molten CaCl$_2$ electrolyte, the route of Ce loss may be via gradual dissolution. Alternatively, CeOCl can undergo a second phase transition under particularly oxobasic conditions (a high pO^{2-}) to form the soluble CeCl$_3$ via **Equation 6.13**, with calcium providing a transport vector for O^{2-} ions.

$$CeOCl + 2Cl^- = CeCl_3 + O^{2-} \qquad \textbf{6.13}$$
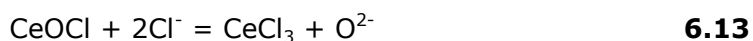
In this case, regardless of the source of CeOCl presence, a gradual dissolution could still occur when the oxygen activity of the electrode and electrolyte gradually decreases. Over the course of the extended 1 hour electrolysis, some Ce may have been lost via a partial reduction of CeO$_2$ to CeOCl, then a staggered chemical shift to CeCl$_3$. A photograph and SEM image of the E3 experimental product is shown in **Figure 6.17** and reveals a dense Ni metal frame with sporadic CeOCl crystallites on the surface.
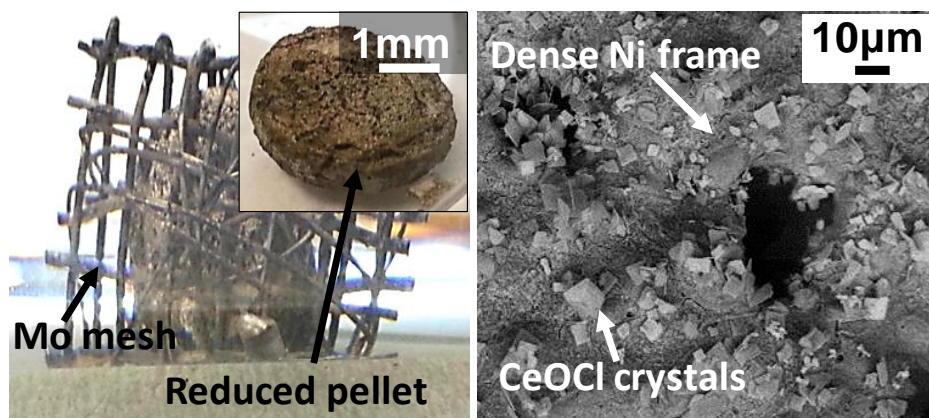
Figure 6.17 - Photograph of the E3 2NiO-CeO$_2$ pellet following reduction at -2.1 V for 60 minutes at 810°C in molten CaCl$_2$ (left) and a high resolution SEM of the E3 pellet revealing the Ni frame covered with sporadic CeOCl crystallites (Right).

Based on the Cl:Ce presence from EDS analysis, CeOCl appears to be the near exclusive phase of Ce in this experiment, suggesting a complete transition from CeO$_2$ to Ce(III). However there remains a great deal of ambiguity within the wider literature regarding the solubility and general fate of Ce(III) compounds. Empirical data from transient studies here might suggest a direct reduction of CeO$_2$ to CeOCl while other studies have linked the presence of CeOCl in electroreduction investigations as a precipitate from the formation and dissolution of Ce$_2$O$_3$ [246,247] apparently highly dependent on the electrolyte used. It has been suggested that CeOCl itself like other lanthanide oxychlorides in molten chloride salts has a partial solubility in CaCl$_2$ [250] which may explain why a smaller quantity of CeOCl was found in the E3 sample after a longer duration of electrolysis. Conversely it could be the redox equilibria of pO^{2-} was conducive enough to permit only a fraction of the solubilised CeO$^+$ ions to precipitate as CeOCl. Ultimately though the lack of a full removal of Ce from the pellet is intrinsically tied to the limited experimental duration and it could be expected that a full dissolution be achieved at longer electrolysis times.

Elsewhere in the literature it has been suggested that the dominant route for CeOCl formation during electrochemical reduction of CeO$_2$ may actually be purely chemical via an interaction between produced metallic Ce, unreduced CeO$_2$ and CaCl$_2$ [247], according to **Equation 6.14**.

$$CeO_2 + 3Ce + 2CaCl_2 = 4CeOCl + 2CaO \qquad \textbf{6.14}$$

Equation 6.14 may help to explain why no metallic Ce was observed in the E3 experiment, and indeed why no alloying occurred. However as CeOCl has been a common observation in these investigations at potentials as positive as −0.81 V vs. Ag/AgCl where Ce^0 would not be a viable reduction product, the direct electrochemical route appears to be the more plausible.

In applying a large overpotential to the 2NiO-CeO$_2$ binary, beyond that for NiO reduction only, it appears that a reverse separation process can be achieved whereby at moderately cathodic potentials the chemical condition of the molten salt dictates a Ce(III) intermediate formation followed by non-selective removal by dissolution. Concerning the analogous nuclear materials in CaCl$_2$ at 810°C (assuming CeO$_2$ acts as an appropriate chemical as well as electrochemical surrogate for PuO$_2$), this mechanism translates to a loss of Pu into the molten salt at moderate to negative reduction potentials. In such a case a secondary salt distillation stage may be necessitated to remove Pu for fast reactor preparation or for geological storage but also in such a scenario the desired component for fuel reintegration (e.g. uranium) remains on the working electrode in metallic form for recovery. Investigating the use of more negative potentials to fully reduce CeOCl into metallic Ce, coupled with the use of a basket working electrode or the use of a lower melting point eutectic molten salt could avoid the loss of Ce to the melt at the expense of lowering current efficiency and reaction kinetics. Practicality and safety may dictate that a lower melting point eutectic be necessitated to avoid any formation of liquid Pu within an industrial setting and so further investigation to the application of molten salt assisted partitioning in such a eutectic is encouraged and will be considered somewhat in Chapter 7.

For the 2NiO-CeO$_2$ binary on a feasibility basis, it has proven possible to selectively remove the NiO without involving any electron transfer to CeO$_2$ via the application of very precise potentials. In a more analogous partitioning exercise, using real nuclear materials, the nobility difference between transuranic oxides becomes more nominal. The formation of intermediates (i.e. X$_2$O$_3$ or XOCl, where X = Ce/Pu) would appear to be unavoidable and hence partitioning by partial direct reduction and anodic

dissolution much more difficult. However in both cases presented here, proliferation resistance remains prominent as Ce (as a surrogate for Pu) is left in a condition unsuitable for weapon fabrication.

6.5. Conclusions

Feasibility of a solid state, single electrolyte partitioning methodology using the FFC Cambridge Process has been considered in this chapter. Using CeO$_2$ as an electrochemical PuO$_2$ surrogate and a NiO counterpart to act as a favourable target for removal, successful selective partitioning was achieved. Comprehensive thermodynamic analysis of the constituent oxides was made, coupled with various kinetic considerations such as the metal-to-oxide ratio (PBR) and referencing optimal oxide parameters discussed earlier in Chapter 4. They revealed that NiO theoretically is much more favourable to reduction than CeO$_2$ with a direct two electron transfer reaction to pure Ni metal, as supported by the Ni-O phase diagram.

Initial electroanalysis by CV characterised the redox activity of both constituent oxides in the molten CaCl$_2$ electrolyte at 810°C and additionally the binary 2NiO-CeO$_2$. Empirically derived reduction potentials for NiO and for Ce(III) were found to coincide very well with their theoretically calculated formation potentials, confirming the relative ease of reducing NiO as compared to species in the Ce-O system. CeO$_2$ was found to be the only stable solid Ce(IV) phase, undergoing an initial reduction to Ce(III) at around -0.80 V vs. Ag/AgCl, more negative than the direct reduction of NiO at -0.41 V vs. Ag/AgCl. When the binary 2NiO-CeO$_2$ loaded MCE was scanned using CV a unique anodic redox paradigm was observed and was judged to be due to an anodic stripping of an alloyed phase, likely Ni$_2$Ce, formed due to the very negative cathodic limit (+ 50 mV vs. Ca/Ca^{2+}).
CeOCl was consistently a dominant presence in CeO$_2$ containing samples. Evidence presented here suggests that CeOCl is likely quasi-stable under

234

specific oxygen activities and given the availability of free Cl$^-$ ions. These parameters are often not met in MCE investigations due to the favouring kinetics and hence (coupled with the partial solubility of Ce(III) phases) a complete loss of Ce was shown in some direct reduction experiments.

Pellet scale reduction and partitioning investigations of the 2NiO-CeO$_2$ binary were conducted in molten CaCl$_2$ at 810°C as to better emulate the engineering and chemical challenges associated with scale up pyroprocessing. In a novel proof of concept investigation using carefully identified redox potentials from CV, 85 % of Ni presence was removed from a surface veneer of the 2NiO-CeO$_2$ pellet. This was achieved after 1 hour by applying a successive reduction potential of -0.65 V vs. Ag/AgCl and +0.01 V vs. Ag/AgCl for anodic dissolution. This reduction potential was shown to avoid any parasitic electron transfer to CeO$_2$, as the bulk phase remained unreduced as concluded by EDS results.

Direct reduction only experiments at both a marginally more negative applied potential (-0.81 V vs. Ag/AgCl) and at a potential significant enough to theoretically induce alloying (-2.15 V vs. Ag/AgCl) were additionally carried out. At -0.81 V, the dominant Ce phase present was CeOCl but the Ce:Ni ratio remained in the same 1:2 range, suggesting little or no dissolution had occurred or a complete precipitation of the Ce species in solution manifested. However at -2.15 V for 60 minutes, only insignificant quantities of Ce could be observed which was correlated to the longer duration and high ionisation energies helping to taper oxygen activity surrounding the bulk electrode, hence encourage a dissolution of Ce(III) species. Interestingly no alloying occurred even at this very cathodic potential, suggesting some effects of iR drop were apparent resulting in insufficient overpotentials being applied.

Chapter 7

FFC Based Electrochemical Pyroprocessing

7.1.Introduction

The fundamental partitioning methodology developed in Chapter 6 has hinted at a great potential and intrinsic value in the broader materials processing field, for example in purification of oxide phase ores or slags. However for a direct application towards spent nuclear fuel treatment, a better surrogacy system with carefully selected chemical and electrochemical similarities would require investigation. Of course, this would naturally progress to an assessment of laboratory scale active spent fuel components in initially simplified systems, gradually working towards a directly applicable technology. Significant difficulties arise at this stage owing to the hazards of working with radioactive isotopes and developing suitable engineering systems.

Having gained an understanding of the capacity for solid state oxide partitioning using a $2NiO-CeO_2$ binary in molten $CaCl_2$ electrolyte, a next evolutionary stage was to apply this to more appropriate surrogates. The oxides chosen for this purpose were again CeO_2, but the inclusion of ZrO_2 to represent UO_2 - coinciding with their theoretical electrochemical similarities. Hence consideration of ZrO_2 and the ZrO_2-CeO_2 binary will be covered in this chapter and how the ability partition is affected by the much more marginal standard half cell potential difference between them. The chemical properties of ZrO_2 are however quite dissimilar to UO_2 and in particular the conductivity of the oxide preform is much poorer, making partial reduction more difficult. TiO_2 was chosen to replace ZrO_2 in binary

with CeO$_2$ and again assessed, but utilising the lower melting LCE electrolyte as to avoid the formation of liquid Ce (Pu) in a full reduction scenario.

Finally, following an appreciation of how the direct electrochemical analogues behave during the developed partitioning methodology, application towards spent fuel species; PuO$_2$ and 5% PuO$_2$ MOX will be given. CVs of sub-mg quantities of each are provided and discussed to consider both how well the surrogates used in this thesis fare to active materials and whether the proposed pyroprocessing technology could be technologically viable.

7.2. Partitioning of Zr from ZrO$_2$-CeO$_2$ in CaCl$_2$

7.2.1. CVs of ZrO$_2$ and Stoichiometric ZrO$_2$-CeO$_2$

7.2.1.1. ZrO$_2$ Redox Chemistry

Fundamental analyses of pure ZrO$_2$ loaded Mo MCEs were provided in Chapter 5 for the validation of electrolyte conductivity improvements, including discussion on the probable redox reactions occurring. Here further qualitative review of the electrochemical reactions is given and how those reactions integrate into the paradigm of a direct UO$_2$ reduction, including the ability to partition reduced Zr from the CeO$_2$ counterpart.

Figure 7.1 shows first and second CV cycles of ZrO$_2$ loaded MCEs scanned in CaCl$_2$ at 810°C. During the second cycle at a full potential range, as presented in **Figure 7.1a**, a third cathodic peak can be seen at approximately -1.45V (C$_3$) not present on the first scan. In all CV experiments performed this was a universal feature only appearing on the second and subsequent CV scans. It was thought that this peak may represent the reduction of anodically produced ZrCl$_x$ gasses (peaks A$_3$ and A$_4$) that had volatilised but were unable to escape before the return

cathodic CV sweep. To assess this, the anodic potential limit was maintained at a point prior to the perceived chlorination potentials represented by peaks A_3 and A_4 (**Figure 7.1b**), determined to be -0.95 V.
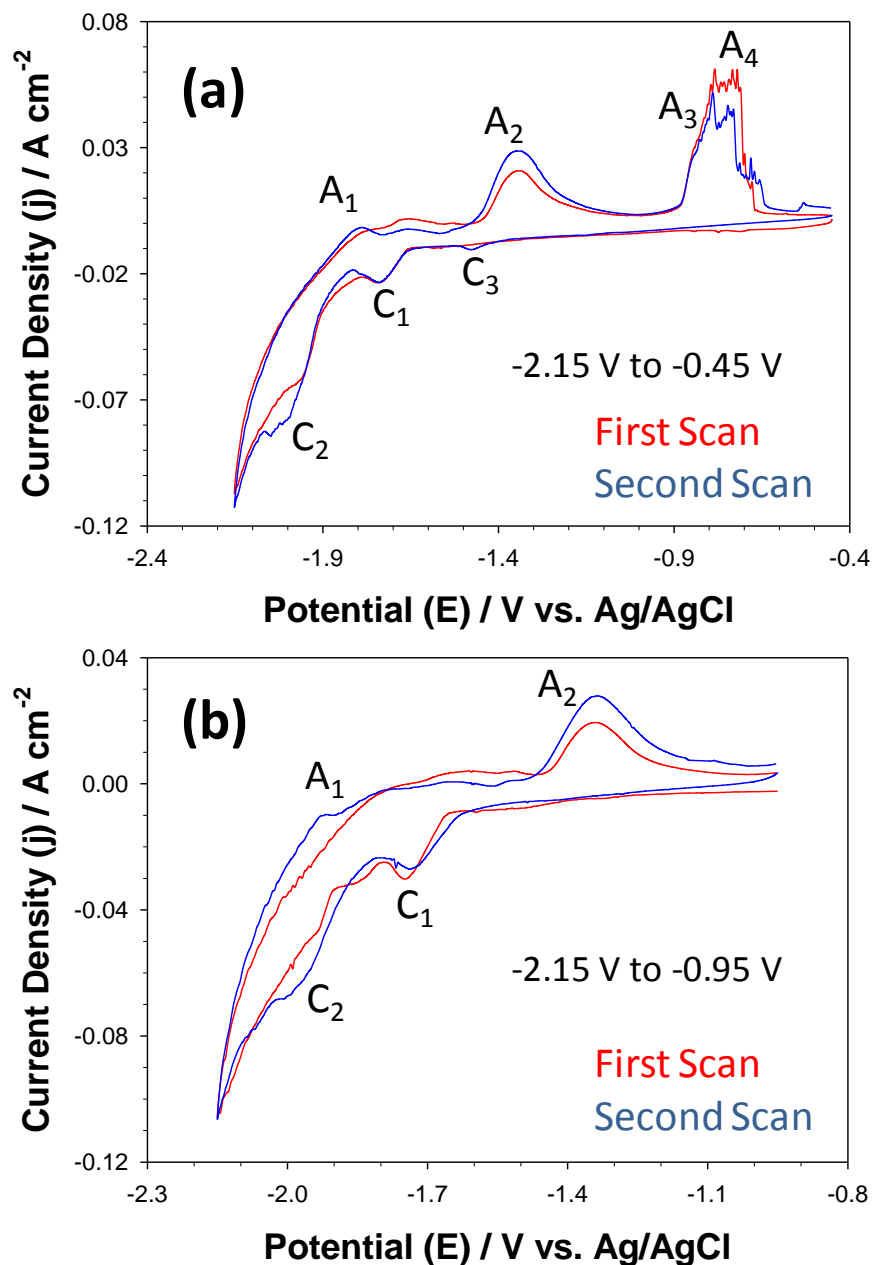
Figure 7.1 – CV curves of ZrO_2 in $CaCl_2$ at 810°C using a potential range of (a) -2.15 V to -0.45 V and (b) -2.15 V to -0.95 V.

In this CV plot, the C_3 current peak is notably absent in both first and second scans (as well as subsequent cycles), confirming the relationship between peaks C_3 and A_3/A_4 and the probable causality based on the thermodynamic predictions for Zr chlorination.

Investigating the independent redox chemistry of ZrO_2 and CeO_2 is vital to appraise the potential for a partial separation and acts as an effective baseline for any potential co-oxide interspecies reactions which may occur from scanning the pre-mixed ZrO_2-CeO_2 binary. **Figure 7.2** displays the overlain first cycle CV curves of each constituent oxide. Here it's possible to observe the much narrower cathodic reduction potential between the $Ce(III)$ to Ce^0 reaction, as discussed in the previous chapter, and the Zr_xO to Zr^0 reduction (-2.10 V vs. -1.88 V respectively). Despite the several hundred mV discrepancy, the region of cathodic activity for both species do overlap and hence it's possible for co-species to form. Additionally the understanding of the pO^{2-} solubility dependant CeOCl phases is a crucial point of inquiry which will be looked at in the context of an unavoidable CeO_2 reduction.
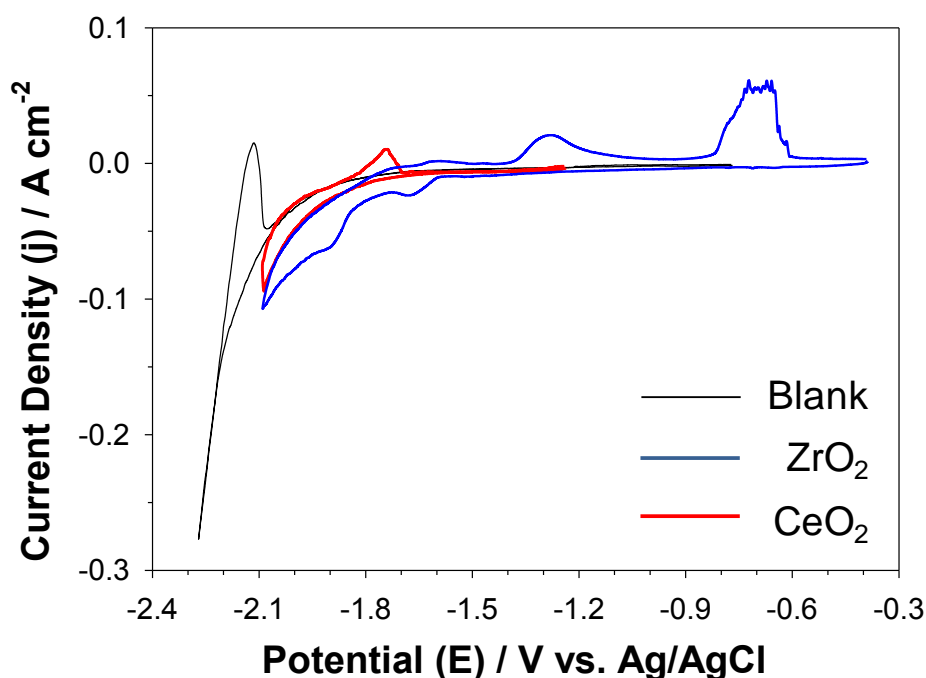
Figure 7.2 – First cycle CV plots of ZrO_2 (red) and CeO_2 (blue) in $CaCl_2$ at 810°C.

The next stage is therefore to analyse by voltammetry the electrochemical reactions of the binary metal oxide, ZrO_2-CeO_2, followed by potentiostatic

reductions at a range of potentials related to the partial reduction products and assumed complete co-reduction.

7.2.1.2. Electrochemical Characteristics of ZrO_2-CeO_2

ZrO_2-CeO_2 powders prepared by ball milling were loaded into the MCE cavity electrodes as per the usual method and scanned to a near full potential window with a cathodic end point of -2.13 V (Purple curve, **Figure 7.3**). The resultant plot retained nearly all of the former current response detail from the individual oxides, which is an indicator of the immiscibility of final reduction products and essentially a chemical inertness of materials to one another, unlike the $2NiO$-CeO_2 binary. Comparing **Figures 7.3** with **Figure 7.2**, combined with the understanding of reactions from thermodynamic and empirical work in previous chapters, it is possible to identify specific reactions at a given current response.
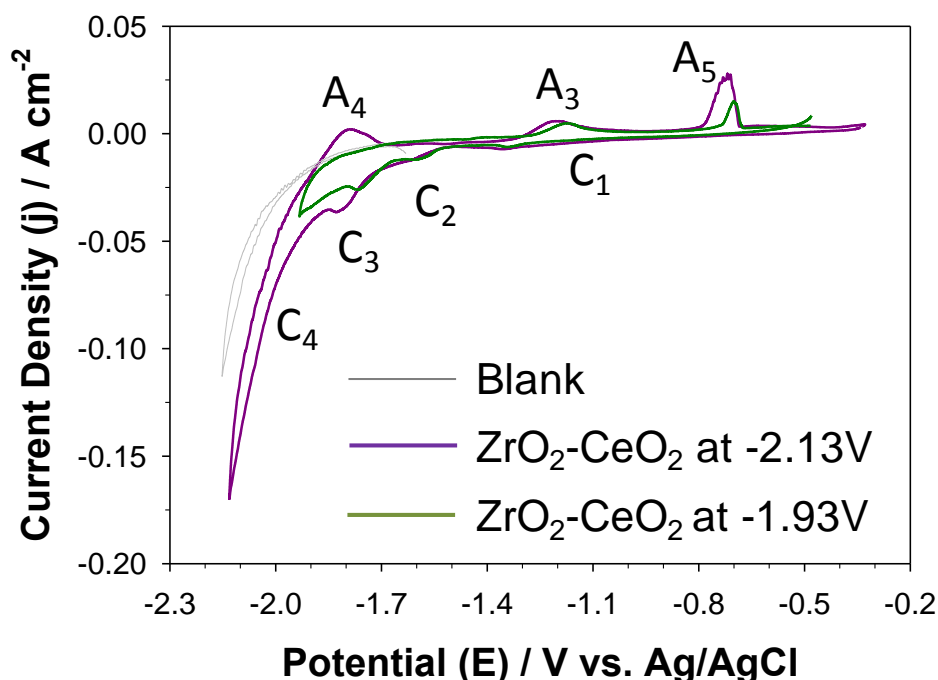
Figure 7.3 – CVs of ZrO_2-CeO_2 loaded Mo MCEs in molten $CaCl_2$ at 810°C, scanned to -2.13 V vs. Ag/AgCl (purple) and to -1.93 V vs. Ag/AgCl (green).

Current peaks C_1 and C_4 for example are judged to be the Ce(IV)-Ce(III)-Ce(0) reaction cascade whereas C_2 and C_3 represent the two stage

reduction of ZrO_2. The first anodic peak at -1.85 V (A_4) is attributed to the stripping of produced Ce metal, which of course when attempting partitioning is an undesirable process both in terms of achieving selectivity and reducing current efficiency. When the cathodic potential limit of the ZrO_2-CeO_2 CV was limited to the region for a full ZrO_2 reduction (-1.93 V; incorporating a slight overpotential) shown by the green curve in **Figure 7.3**, the anodic stripping peak for Ce (A_4) is notably absent. Indicatively, this means no full reduction of the cerium intermediate phase occurred at the same potential range for producing metallic Zr. However as previously demonstrated the loss of Ce containing species at negative cathodic potentials for extended durations is a key concern.

Performing multiple CV cycles on the ZrO_2-CeO_2 loaded MCE at a scan rate of 50 mV s^{-1} (**Figure 7.4**) revealed the anodic peak current for the A_4 reaction (I_p^A) did not fully manifest until scans two and three. This suggests a high energy barrier for the respective reduction reaction requiring a second cycle to reach peak reaction rate. All other current peaks began subsiding following the first cycle and continuing until the eighth, which may coincide with a gradual loss of material, not unexpected due to the liquid nature of metallic Ce and the volatility of the various zirconium chlorides. Of particular interest is the apparent lack of alloying phases between the metallic Ce and Zr products which is a contradiction to the known complete mutual solubility of Pu and U (to a maximum of 0.7% ɤPu in U [251]). Therefore it is of additional academic relevance to consider the direct co-reduction and potential solid-liquid phase separation brought about by a complete reduction of the ZrO_2-CeO_2 binary.
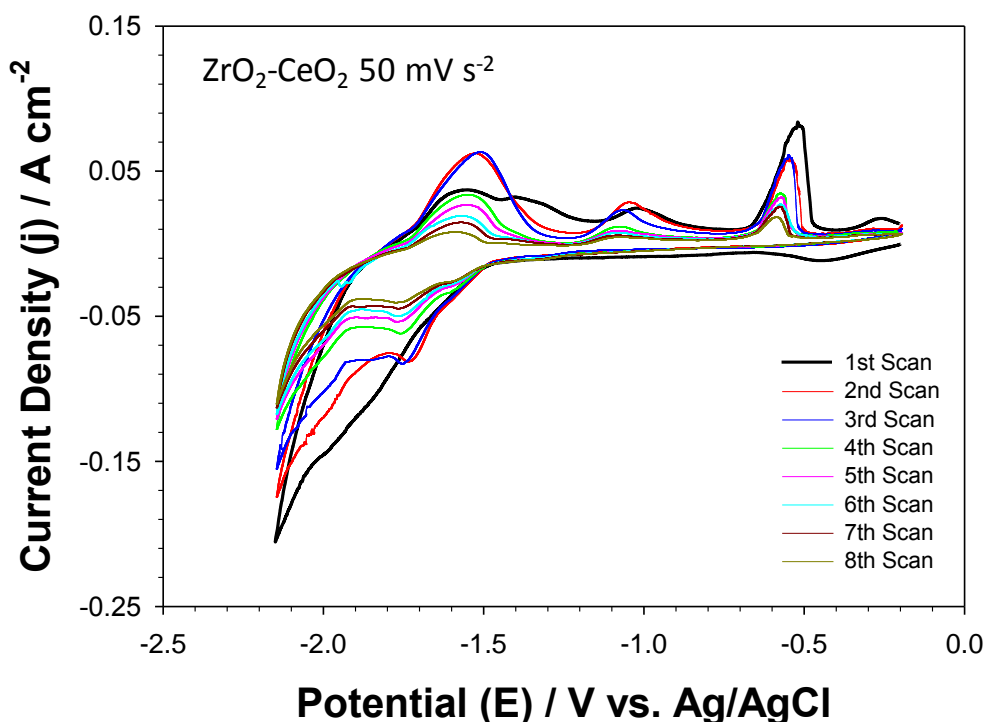
Figure 7.4 – Multi-cycle CV of ZrO_2-CeO_2 in $CaCl_2$ at 810°C. Scan rate: 50 mV s^{-1}, potential window: -2.15 V to -0.2 V.

Although a direct correlation to partitioning isn't applicable for the active spent fuel components due to the unique formation of solid solutions, the prospect of an electrochemical reduction is of vital consideration when aiming to circumvent the use of chemical reductants as in the ANL process.

7.2.2. Direct Reduction of ZrO_2-CeO_2

7.2.2.1. Implementing a Basket Electrode for Ce Recovery

The molten nature of Ce and Pu (MP of 795°C and 639°C respectively) within the $CaCl_2$ electrolyte makes their containment and maintaining a strict process flow sheet more challenging. While lower melting point molten salt electrolytes exist which can facilitate operation in solid phase, the benefits of using higher temperatures and pure $CaCl_2$ for the direct electrodeoxidation is considerable. Furthermore the validation of bulk electrolysis of lanthanide oxides is notoriously difficult, with controversy regarding the capacity for an FFC based reduction i.e. without involving electrolyte decomposition. Therefore in confirming the electrochemical

242

route for Ce production as a foundation for the direct electrochemical co-reduction of spent fuel oxides to metallic states may be possible.

Pelletised electrodes were used in two separate experiments, one composed of 1.0 g of pure untreated CeO_2 and the other of 1.1 g of the ball milled stoichiometric ZrO_2-CeO_2, both formed by pressing and sintering. The oxide pellets were then suspended above a Ti basket cathode with Mo binding wire and mesh and attached onto a threaded section of a SS rod using 5 mm nuts (CeO_2 shown in **Figure 7.5a**). **Figures 7.5b-d** are of the post-electrolysed CeO_2 cathode following constant cell voltage electrolysis at 3.2 V for 15 hours.
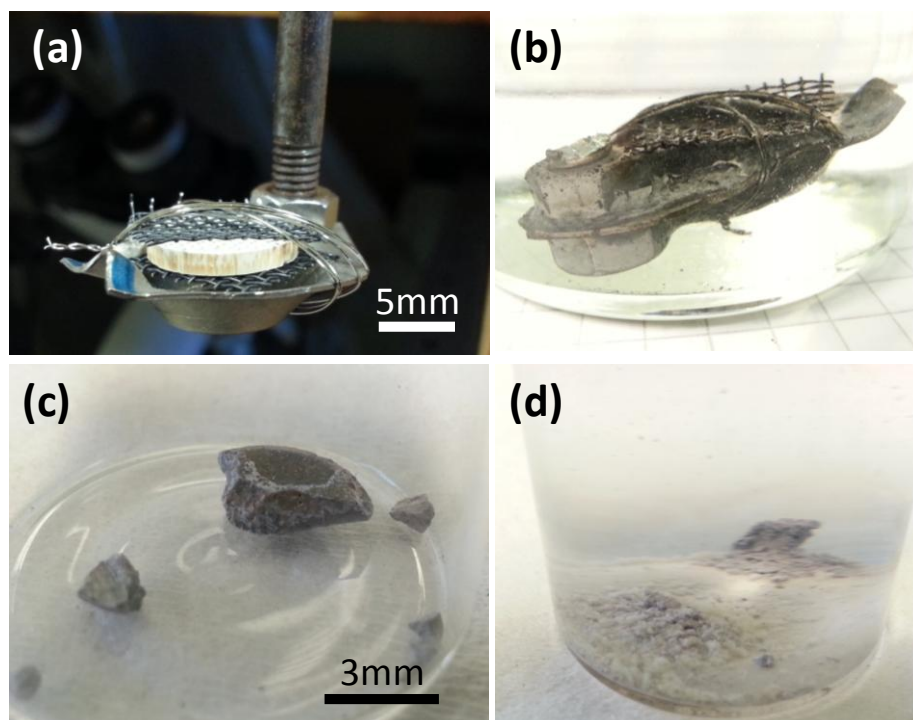
Figure 7.5 – Photographs of (a) a bespoke Ti basket cathode with CeO_2 pellet, (b) the electrode after electrolysis washed in DMSO, (c) the recovered product stored in argon, and (d) after mixing the product with water for 5 minutes.

Visual inspection of the recovered electrolysed pellet in **Figure 7.5b** shows a collapse of the top Mo mesh which had covered the initial oxide pellet. This was an indicator that either a loss of the pellet had occurred, a phenomenon seen previously due to the chemical shift in oxoacidity, or as

predicted the oxide had been completely reduced to the liquid metallic phase and condensed into the basket below. After washing it was apparent the latter was true, as a small ingot of metal with physical properties similar to Ce was recovered. Notably the recovered ingot was in the exact shape of the basket itself suggesting a process of solidification from liquid phase had occurred. The total weight of the recovered ingot pieces was 0.75 g giving a mass loss of 0.25 g, whereas the calculated mass loss from the removal of oxygen atoms alone should theoretically be 0.23 g. The minor divergence may be explained by the dissolution of both Ce metal (all metals possessing at least fractional solubility in molten chloride salts) and CeO^+ in the relatively large quantity of supporting electrolyte required to accommodate the basket cathode (400 g). Metallic Ce reacts relatively vigorously in water to produce the hydroxide and evolve hydrogen gas. Although no spectroscopic or chromatography analysis was conducted, anecdotally the metal ingot pieces when mixed with water did immediately release a considerable amount of off-gas (**Figure 7.5d**).

In order to establish that the recovered product was indeed Ce and that reduction occurred via an electrochemical route characterisation of the electrolysis product was required, particularly as Ca has several physical features in common with Ce. Direct elemental analysis of the ingot proved to be too difficult owing to the highly reactive nature to atmospheric moisture and oxygen, inducing oxidative spallation and contaminating the analysis results. Instead indirect measurements to confirm the presence of Ce and lack of Ca were performed, consisting of a simple dissolution of the sample in concentrated 70% HNO_3 and TGA-DSC analysis to confirm phase transition temperature between solid and liquid. **Figure 7.6a** and **7.6b** shows the results of both experiments for the electrolysis product of pure CeO_2.

110mg sample in 70% conc. HNO$_3$

(a)

10 minutes

(b) **10mg sample TGA-DSC – N$_2$ atmosphere**

24 % mass loss
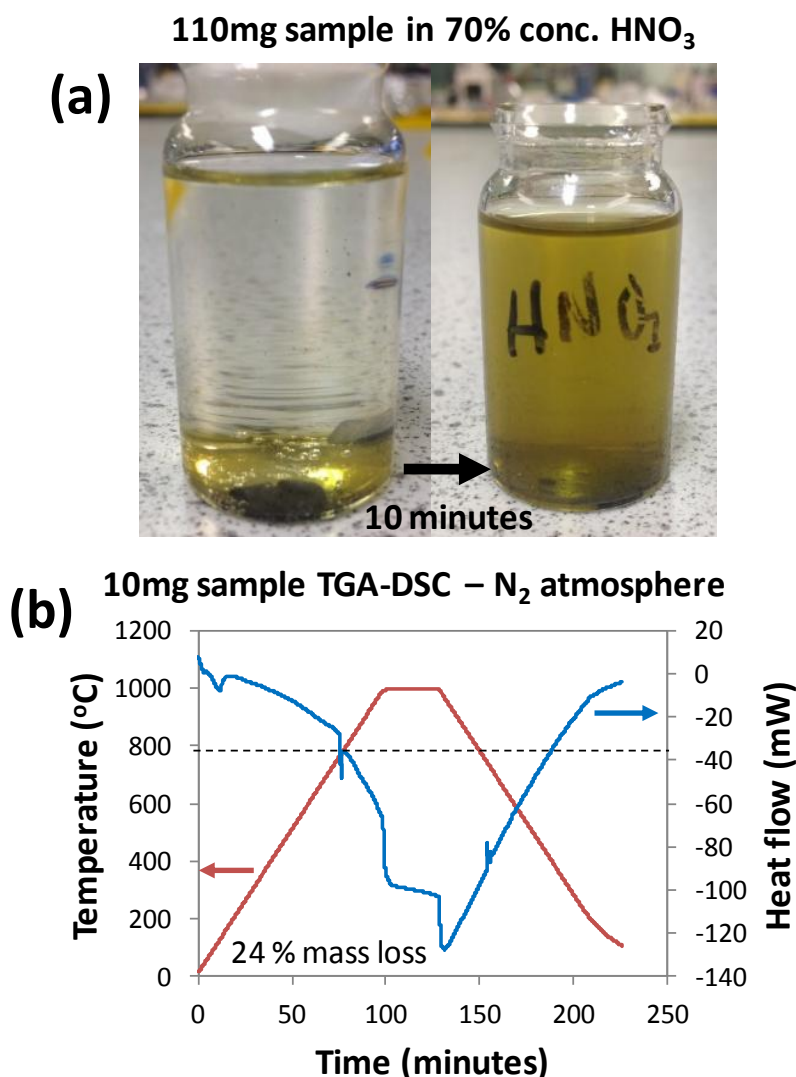
Figure 7.6 – Indirect analysis of the product form constant cell voltage electrolysis of CeO$_2$ at 3.2V for 17h. (a) Images of the product dissolution in 70% nitric acid, displaying a yellow colouration, and (b) a TGA-DSC curve in N$_2$ atmosphere for a sweep between ambient temperature and 1000°C, held for 30 minutes.

The prominence of a yellow colour in the nitric acid solution strongly suggests the presence of metallic Ce through the generation of cerium complexes (2Ce(NO$_3$)$_3$·H$_2$O), for example in **Equation 7.1**.

$$2Ce + 6HNO_3 + 12H_2O = 2Ce(NO_3)_3·H_2O + 3H_2 \qquad \textbf{7.1}$$

However the presence of metallic cerium doesn't necessarily omit the possibility of Ca presence and by association a Ca based reduction of the CeO$_2$, particularly as the same reaction as **Equation 7.1** but for Ca creates colourless complexes. Hence TGA-DSC was used to differentiate the

presence of Ce/Ca based upon their known melting points. In the plot given in **Figure 7.6b**, the exothermic reaction on the ramping stage and endothermic reaction on the cooling stage both correlate precisely with the melting point of Ce at 795°C. At 842°C (melting point of Ca), no such heat flux could be observed confirming an absence of Ca and consequently supporting the direct electrochemical deoxidation of Ce in molten CaCl$_2$ at 810°C. Further evidence is drawn from the applied voltage itself, which at 3.2V is theoretically insufficient to cause electrolyte decomposition, especially when accounting for the effects of iR drop. Interestingly, elsewhere in the literature a phase transition of Ce from ɤ to δ under standard pressure has been described directly prior to its melting point at approximately 740°C[252], however no clear deviation from the rate of entropy change (heat flux) was recorded in the TGA-DSC experiment at this range. It's possible the rate of temperature increase was too rapid (20°C/min) for the transition to occur or perhaps the ordering shift produces no or little effect on the energy of the system.

After 130 minutes when the isostatic phase of the temperature gradient had concluded, a relatively large exergonic reaction is observed. Behaviour like this has been attributed to liquid-liquid transitions, however they usually occur at elevated temperatures (>1200°C for Ce) and only when considerable pressures are applied (13GPa)[253]. Alternatively oxidation of the Ce may have occurred where the flow of N$_2$ could not prevent oxygen ingress, but as there was a recorded mass loss from the initial sample weight, this too is unlikely. The recorded mass loss may be representative of a reaction involving gas release or sublimation, a possible consequence of a quasi-stable cerium hydroxide or oxalate produced via the very short exposure to atmosphere during transit to the TGA. In any case the

presence of Ce and absence of Ca was confirmed and significantly was shown to be recoverable using a carefully engineered basket cathode.

In the second experiment involving the direct reduction of 1.1 g of CeO_2-ZrO_2 under near identical conditions (3.2 V for 17h, **Figure 7.7** top), a similar reduction product was produced (**Figure 7.7** bottom). However in this case while the metallic Ce melted and coalesced into the shape of the Ti basket, the porous Zr frame (coloured black in the photograph) remained in position at the rim of the basket.
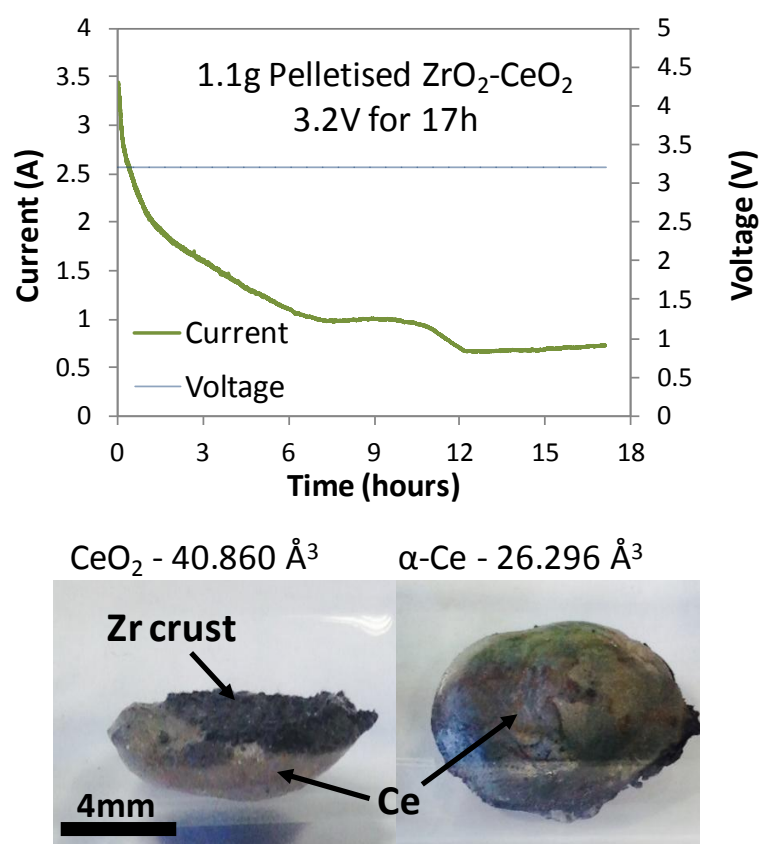
Figure 7.7 – Current-time curve for the constant cell voltage electrolysis of a ball milled ZrO_2-CeO_2 pellet using a basket cathode (top) with photographs of the resultant product after washing in DMSO and stored in argon (bottom).

An interesting prospect of elemental partitioning between the metallic phases of Ce and Zr could exist whereby the molten Ce (Pu) could drain away leaving only the solidified and desired Zr (U). However this assumes a similar electrochemistry and reduction hierarchy between active materials

and surrogates and additionally in the context of safety, producing a pure stream of metallic Pu is both a criticality risk and is the opposite to the sought after proliferation resistance. Should the system temperature be below the melting point of Pu however, the ability to co-reduce various actinide oxides to their metallic states without the decomposition of the electrolyte or addition of excess reductant is of great importance. Consequently, later in this chapter work using the lower melting point LCE electrolyte with a TiO_2-CeO_2 binary will be considered.

The reduction potentials required to produce Ce from CeO_2 or its intermediates is predicted to be slightly more negative than that for ZrO_2. As such it was deemed insightful to address whether metallic Zr could be produced from ZrO_2 at more modest voltages and what the eventual fate of Ce would be during a direct reduction of the ZrO_2-CeO_2 binary at a less cathodic applied potential.

7.2.2.2. At Potentials for a Full Reduction of ZrO_2

Constant voltage electrolysis has been performed on CeO_2 and ZrO_2-CeO_2 at voltages of 3.2 V, which is near the point of electrolyte decomposition and considerably more that theoretically required for the direct reduction of ZrO_2. A similar experiment was therefore designed using a pure pellitsed ZrO_2 electrode, wrapped in Mo mesh and secured with Mo wire. The fabricated electrode was subject to electrolysis at 3.0 V for 18 h, accounting for the calculated reduction potential of -2.13 V vs. S.Cl.E. **Figure 7.8** gives the produced current-time plot along with photographs, SEM micrographs and EDS elemental analysis of the pellet before and after reduction.
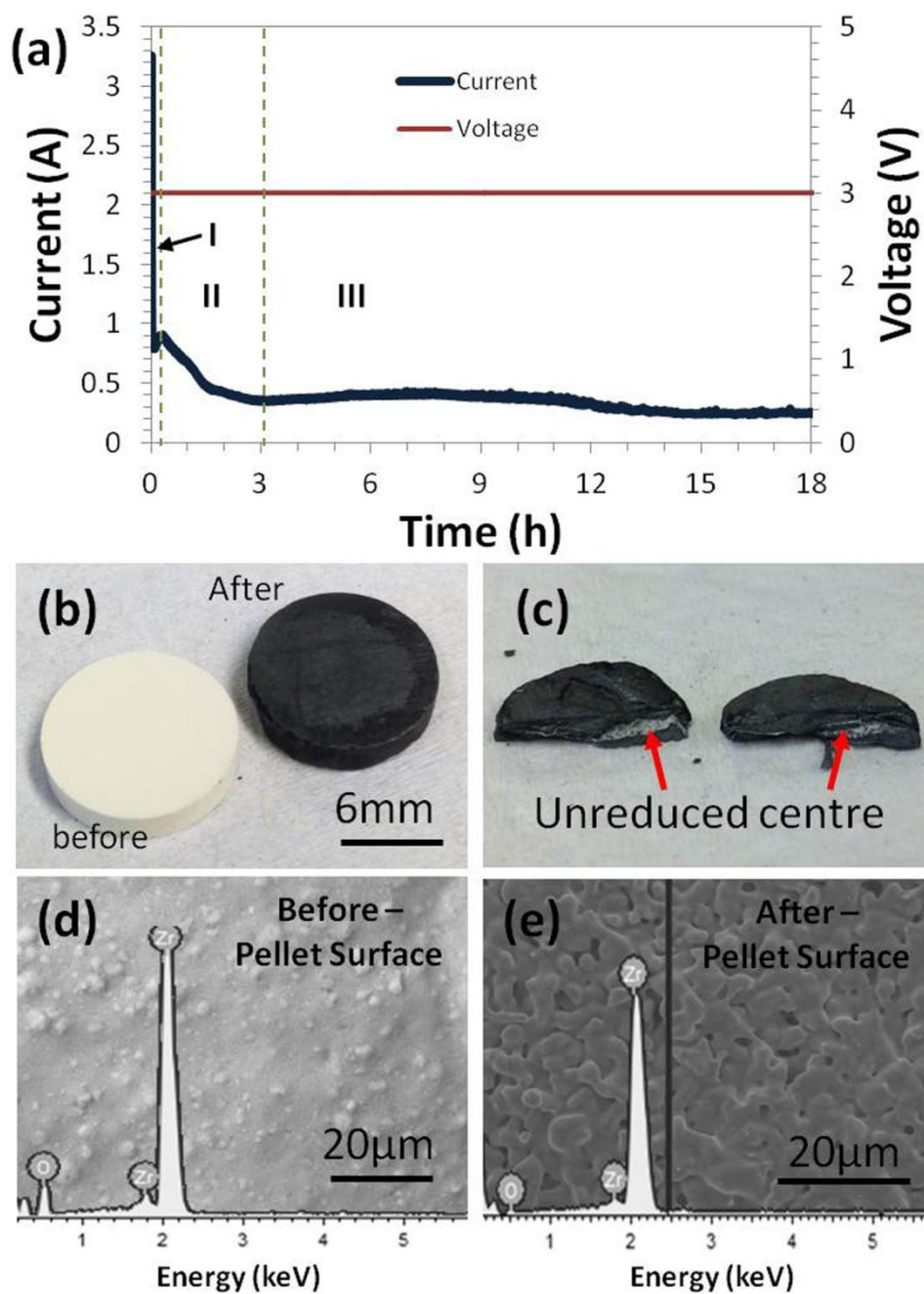
Figure 7.8 – (a) Current-time curve for the constant cell voltage electrolysis of a 1.0g ZrO$_2$ pelletised electrode at 3.0V in molten CaCl$_2$ at 810°C. (b) Photograph of ZrO2 pellet before and after electrolysis, with (c) showing the interior of the reduced pellet. (d) and (e) SEM and EDS analysis of the pellets surface before and after reduction respectively.

The current response curve in **Figure 7.8a** reveals a very typical profile for direct reduction of oxides by the FFC Cambridge Process, involving an initial current spike, relatively rapid metallisation, and a much slower 3PI propagation inwards resulting in a shallow current drop to background

levels (labelled I, II and III respectively). Once removed the initial white colour of pure ZrO_2 had been replaced by a dark grey, near black one which was mechanically resistant to bending or snapping by hand (**Figure 7.8b**). Using pliers the pellet was cleaved lengthways and revealed that despite a very clear physical change in the properties of the pellet surface, the interior remained un- or partially- reduced (**Figure 7.8c**). Examining the microstructure of each pellet before and after reduction (**Figures 7.8d** and **7.8e**) proved to be insightful in understanding why much of the interior of the pellet remained in the original ZrO_2 stoichiometry. Clearly even prior to electrolysis the pellet surface possessed a featureless microstructure void of any porosity. This is in contrast to where ZrO_2-CeO_2 was used in both powdered MCE and pelletised form suggesting that ZrO_2 powders more readily undergo densification when in direct contact to each other under the conditions used here for pressing and sintering.

After reduction to metallic Zr, as confirmed by EDS of the pellet surface, the microstructure appears to have changed slightly, but still hold a non-porous and featureless morphology. Standard metallic reduction products by FFC based processes have highly porous and nodular structures as evidenced by the work on NiO and Cr_2O_3 earlier in this thesis. It would seem the reduction of ZrO_2 must have progressed slowly due to the tightly packed oxide powders although even then it would be expected the removal of oxygen ions through ionisation would develop into an open porosity. The extent of this void space development may actually be rather marginal as derived by calculated the PBR value for ZrO_2 and Zr_3O in Chapter 6. Additionally Zr readily undergoes a surface densification at temperatures far below its melting point, in a similar manner to uranium metal. Hence it's likely there may have been early porosity development on the surface of the Zr|ZrO_2 pellet during reduction that subsequently

became marginalised due to the temperature of the molten salt causing continued sintering over the 18 h experimental duration. This would adequately explain why the interior of the pellet remained unreduced, as the exclusion of electrolyte impregnation to assist with oxygen ion diffusion led to a cessation of reduction.

In a similar experiment using a smaller pelletised ZrO_2-CeO_2 electrode (5mm dia., 150mg) in a three-electrode cell, the consequence of CeO_2 addition was assessed in both the capacity to fully reduce ZrO_2 and to examine which Ce containing species were produced. An applied reduction potential of -1.95 V vs. Ag/AgCl (+300 mV vs. Ca/Ca^{2+}) was selected based on the earlier CV work on ZrO_2, i.e. beyond the current peak associated with the Zr_3O to Zr reduction. While this potential is apparently more anodic than the voltage applied in the direct reduction of ZrO_2 explored above (+300 mV vs. Ca/Ca^{2+} compared to approximately +270 mV vs. Ca/Ca^{2+}), the three electrode cell includes iR corrections via feedback by the reference electrode whereas the two electrode cell does not. As such the applied potential should be more accurately maintained and be able to mitigate aspects of iR drop not adequately addressed during constant cell voltage electrolysis. **Figure 7.9** shows the current plot from the potentiostatic electrolysis on the small ZrO_2-CeO_2 pellet, and associated SEM and EDS results after minor grinding the final product.

From visual observations the retrieved pellet, although possessing a similar colour to the recovered product from direct ZrO_2 only reduction, was much less uniform and had a more porous structure. This allowed for relatively easy grinding by pestle and mortal and subsequent ex-situ analysis by SEM and EDS.
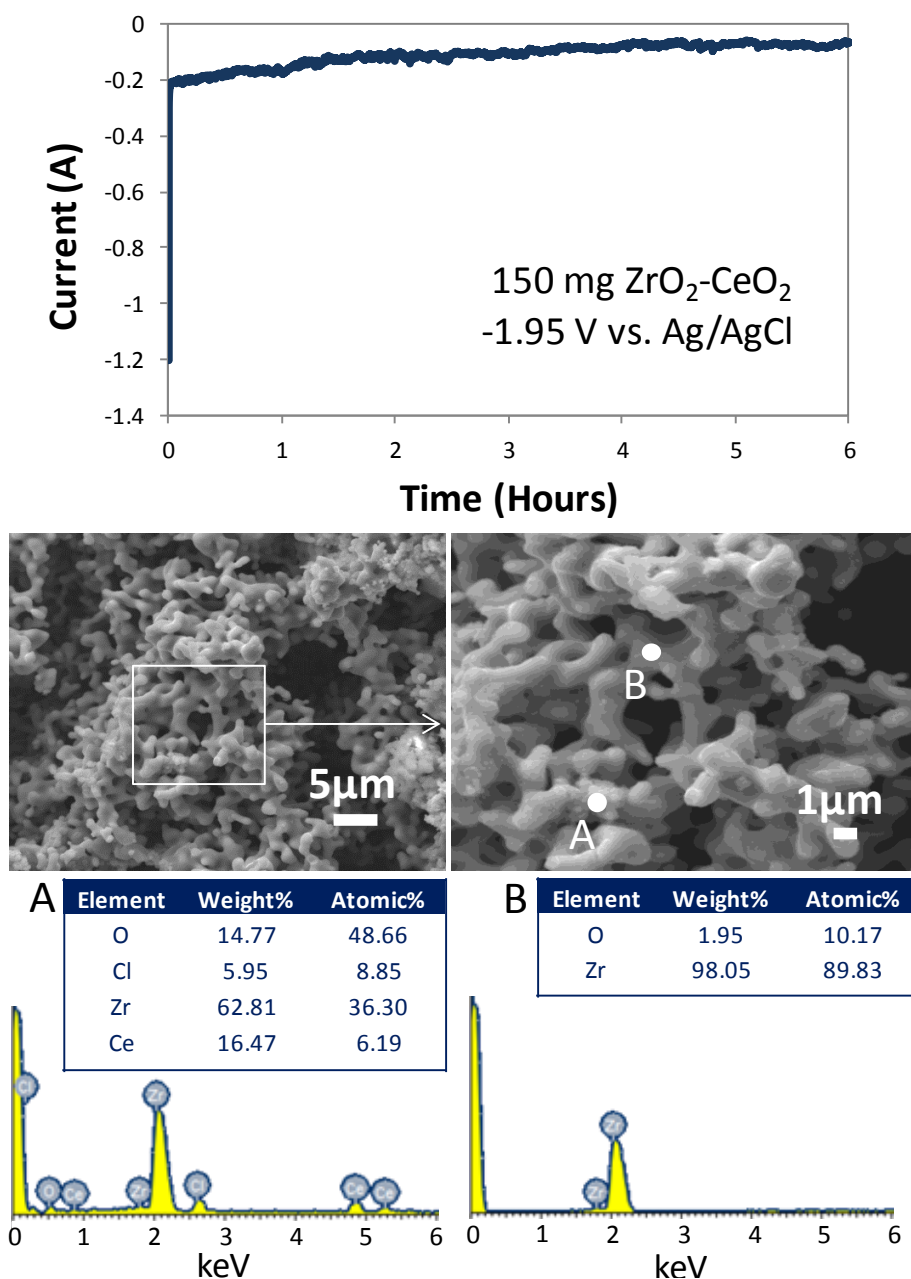
Figure 7.9 – Current response curve from an applied potential of -1.85 V vs. Ag/AgCl on a 150mg ZrO_2-CeO_2 pelletised working electrode (top) with SEM micrographs and point EDS analysis of the ground product (middle and bottom).

In clear contrast to when pure ZrO_2 was reduced, the resultant metallic Zr produced was demonstrated to have a highly porous structure which assisted a near complete deoxidation. Throughout the final product, an only fractional quantity of atomic Ce was measured stoichiometrically and morphologically indicative of CeOCl (Point A in **Figure 7.9**). The lack of Ce is conditionally identical to where the 2NiO-CeO_2 binary was electrolysed at

equally negative potentials in similar conditions, whereby it seems the solubility of partially reduced Ce(III) in the $CaCl_2$ electrolyte is sufficient to permit a near full dissolution - leaving behind the counterpart metallic species. The initial presence of CeO_2 essentially acts as porosity inducing agent through its gradual loss into the molten salt, supporting more favourable kinetics of oxygen diffusion and continued reduction of ZrO_2. Additionally the void development by Ce loss prevents grain boundary or lattice diffusion of Zr atoms that aid densification, but instead can enhance surface diffusion as a non-densifying mechanism known to develop the characteristic nodule structure of FFC produced metals. Collectively, with an applied potential which was evidently sufficient enough to reduce ZrO_2 to Zr, the associated increase in conductivity aiding electron transfer, and open porosity resulting from Ce loss, a near complete reduction was achieved after just 6 hours of the 150mg pellet.

Despite the very different chemical and electrochemical properties of NiO and ZrO_2, it appears a near identical scenario exists with both systems, when mixed with CeO_2, were subject to highly cathodic potentials. Consequently the conclusions drawn from these experiments emulate those before regarding spent fuel analogues whereby a solid, metallic U/MA reduction product could likely be recovered, but Pu would be lost to the molten salt.

7.2.3. Partial Direct Reduction of ZrO_2-CeO_2

7.2.3.1. XRD Analysis of Intermediate Products

The difference between the onset potential for CeO_2 reduction to the Ce(III) intermediate, and the reduction of said intermediate to a metallic state is relatively broad (>1.4 V). Within this potential window the extent of Ce(III) dissolution is likely influenced by electrochemical factors such as the applied potential and additionally, the lack of sufficient electrochemical

force to drive the complete reduction of either CeO_2 or ZrO_2 may permit interspecies interactions. Potentiostatic experiments were performed on the ZrO_2-CeO_2 binary in the form of small 200 mg pellets at potentials defined by the reduction peaks observed during CV of the binary/pure ZrO_2, i.e. -1.65 V (C_1) and -1.85 V (C_2) vs. Ag/AgCl. **Figure 7.10a-c** gives the current response of the two investigations, performed for 9ks and 12ks respectively, photographs of the recovered and ground products and XRD of each sample.
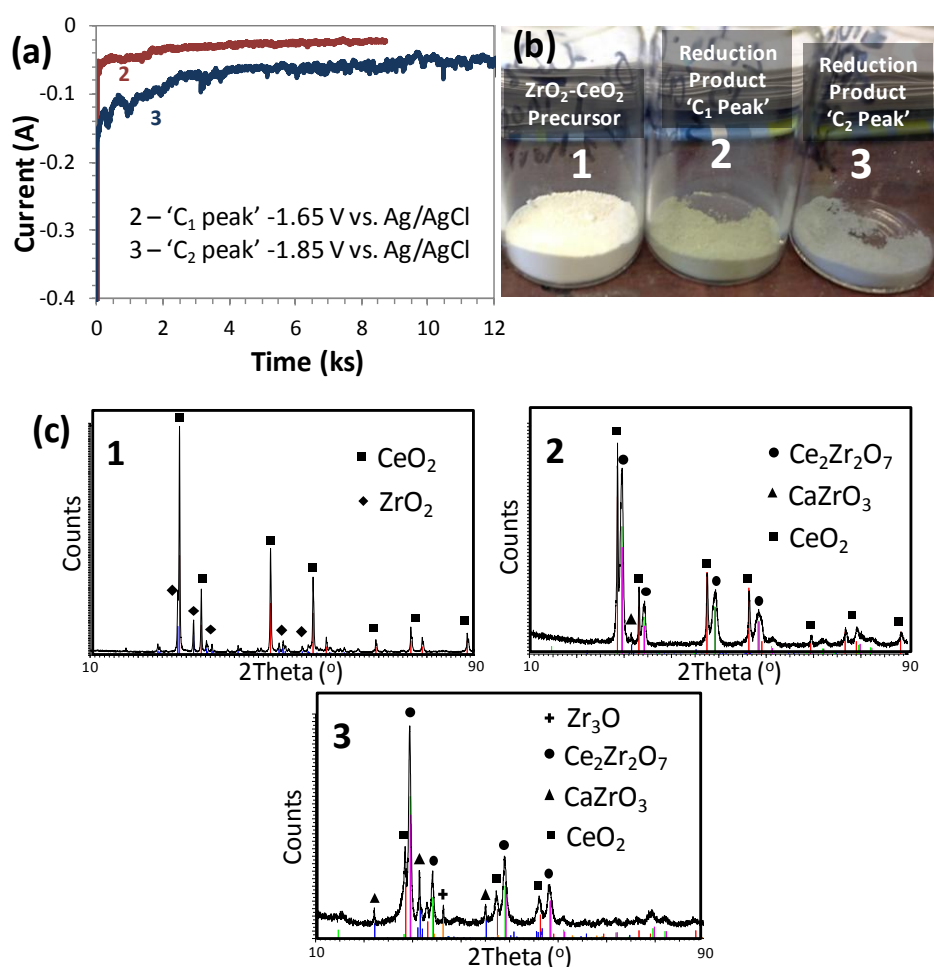
Figure 7.10 – (a) Current-time curves for two potentiostatic electrolysis experiments on 200mg ZrO_2-CeO_2 pellets (2 & 3) at -1.65V and -1.85V for 9ks and 12ks respectively. (b) Photograph of the precursor (1) and recovered products (2 & 3). (c) XRD results for the 1, 2 and 3 samples.

Analysis by XRD was able to provide qualitative information regarding the intermediate reactions occurring and reveal an increasingly complexity as

both the potential and electrolysis duration was increased. The gradual shift in phase is reflected by a stark change in colour of the ground products recovered, from an initial off-white of the ZrO_2-CeO_2 precursor to green from experiment 2 (peak C_1) and a grey-turquoise from experiment 3 (peak C_2). The product recovered after experiment 2 showed a significant drop in CeO_2 presence, and a complete absence of any ZrO_2, both of which were present in the appropriate quantity in the precursor material. Instead a partially reduced co-oxide in a pyrochlore crystal structure ($Zr_2Ce_2O_7$) was the dominant phase, coupled with the $CaZrO_3$ perovskite. As the applied potential was shifted more negatively to the region for the theorised complete reduction of ZrO_2 (peak C_2), an additional phase of Zr_3O was detected in small quantities in accordance with an increase in the quantity of $CaZrO_3$ and decrease in both $Ce_2Zr_2O_7$ and CeO_2. The transition of relative abundance suggests that $Ce_2Zr_2O_7$ was the initial partial reduction product, which either decomposes to Ce_2O_3 and $CaZrO_3$ or is directly reduced to Zr_3O at the more cathodic potentials (**Equations 7.2** and **7.3**).

$$Ce_2Zr_2O_7 + 2CaO = 2CaZrO_3 + Ce_2O_3 \hspace{2cm} \textbf{7.2}$$

$$3Ce_2Zr_2O_7 + 10e^- = 2Zr_3O + 3Ce_2O_3 + 5O^{2-} \hspace{1.5cm} \textbf{7.3}$$
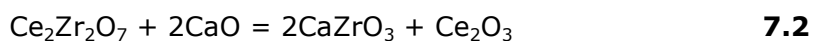
The displacement of Ce presence in the reduction product of experiment 3 compared to experiment 2 is likely a factor of the development of Ce(III) species which become solubilised in the molten salt over time as evidenced by earlier investigations at more cathodic and more anodic potentials.

Furthermore the lack of metallic Zr produced confirms the applied potential in this experiment (-1.85 V) was insufficient for a full ZrO_2 reduction despite CV curves suggesting otherwise, caused by the greater bulk oxide quantity contributing to increased cell resistance. The direct reduction of pure ZrO_2-CeO_2 at -1.95 V was able to fully reduce all ZrO_2 to the metallic

state; giving an approximate maximum of 100mV overpotential required to facilitate the complete reduction compared to CV for the ZrO_2/Zr_3O reaction. Alternatively the duration difference between experiments at -1.95 V and -1.85 V (3.5 hours) might have allowed those phases observed during the latter to become more reduced over time. Development of the various intermediate and co-oxide products facilitated by the use of modest reduction potentials may act to inhibit a full reduction due to an effective increase in electrochemical stability or physically through poorer kinetics.

Table 7.1 highlights the different phases identified by XRD and their theoretical volume change from the initial oxide precursor.

Table 7.1 – Volume and density characteristics of the species identified via XRD of potentiostatic electrolysis of ZrO_2-CeO_2 at both -1.65 V and -1.85 V vs. Ag/AgCl in molten $CaCl_2$ at 810°C[150].

Material	Volume (Å^3)	Density (g/cm^3)	Predicted Volume Change From Precursor (%)
ZrO_2-CeO_2	93.99	6.28	0
$CaZrO_3$	266.26	4.47	+ 183.29
$Ce_2Zr_2O_7$	314.62	6.07	+ 234.78
Zr_3O	291.56	6.60	+ 210.20
Zr	47.00	6.45	- 49.99

As can be seen the formation of pyrochlore and perovskite phases introduce significant volume increases, for instance $Ce_2Zr_2O_7$ (derived as the initial reduction product) contributes to a greater-than-tripling of effective volume. The $CaZrO_3$ phase is characteristic in having a blue/violet colour, similar to the Ca intercalated TiO_2 ([149], **Figure 2.23**) and has been visually identified in other experiments performed of a similar nature using larger quantities of ZrO_2-CeO_2.

The substantial increases in volume of the partially reduced intermediates identified by XRD must have been accompanied by the development of

porosity to achieve the continued reduction to other products (of Zr_3O, for example[227]) and may have been achieved through a loss of Ce to the electrolyte as described in the previous section. This would aptly explain why Ce is only present at CeO_2 and $Ce_2Zr_2O_7$, which have a relatively favourable stability as opposed to CeOCl and Ce_2O_3 which have been shown previously to be chemically unstable, as a function of melt oxoacidity.

7.2.3.2. SEM Imaging of Partially Reduced Pellets

In the previous experiments so far in this chapter, at potentials insufficient enough to permit a direct electroreduction of CeO_2 to a metallic state, there has been a consistent loss of Ce containing species observed with extent of Ce loss being an apparent function of applied potential and duration. This was investigated further here in two ways using SEM imaging to identify the characteristic morphology of Ce intermediates. Firstly at a relatively less cathodic potential (-1.6 V vs. Ag/AgCl) for 10ks, potentiostatic electrolysis was performed on small (5mm dia. 150mg) pellets of ZrO_2-CeO_2. Secondly, in accordance with the both the Ce-O-Cl and Pu-O-Cl predominance diagrams, potentiostatic electrolysis was performed on the same ZrO_2-CeO_2 pellets but at approximately +1V vs. Ca/Ca^{2+} (-1.25 V vs. Ag/AgCl) and for only 5ks. At this second potential there is theorised to be a large region of CeOCl stability and even some Ce_2O_3 stability given the oxoacidity has a pO^{2-} value below ~3[75] in molten $CaCl_2$.

In the first experiment it was noticed there was an unintended cleave approximately midway across the horizontal plane of the pellet after reduction, which became fortuitous in ex-situ analysis by SEM as it allowed for a full morphological and elemental assessment of the interior of the pellet. **Figure 7.11** shows a section of the circumference and bulk phase of the pellet revealing a clear banding structure of variable species concentration and morphology. These distinct regions are labelled 1, 2 and

3 respectively as progress towards the centre of the pellet is made. EDS elemental analysis of indiscriminate spots in each region to give the suggested stoichiometry, coupled with the known physical characteristics of each phase from the feed materials or from previous experiments, were combined to conclude which phases were dominant.

1

Element	Weight %	Atomic %
O	29.75	73.31
Cl	0.78	0.87
Ca	1.64	1.61
Zr	33.93	14.67
Ce	33.90	9.54

2

Element	Weight %	Atomic %
O	13.20	48.58
Cl	11.49	19.09
Ca	0.40	0.59
Zr	1.17	0.76
Ce	73.73	30.98

3

Element	Weight %	Atomic %
O	18.43	61.28
Cl	6.04	9.06
Ca	0.39	0.52
Zr	3.05	1.78
Ce	72.09	27.36
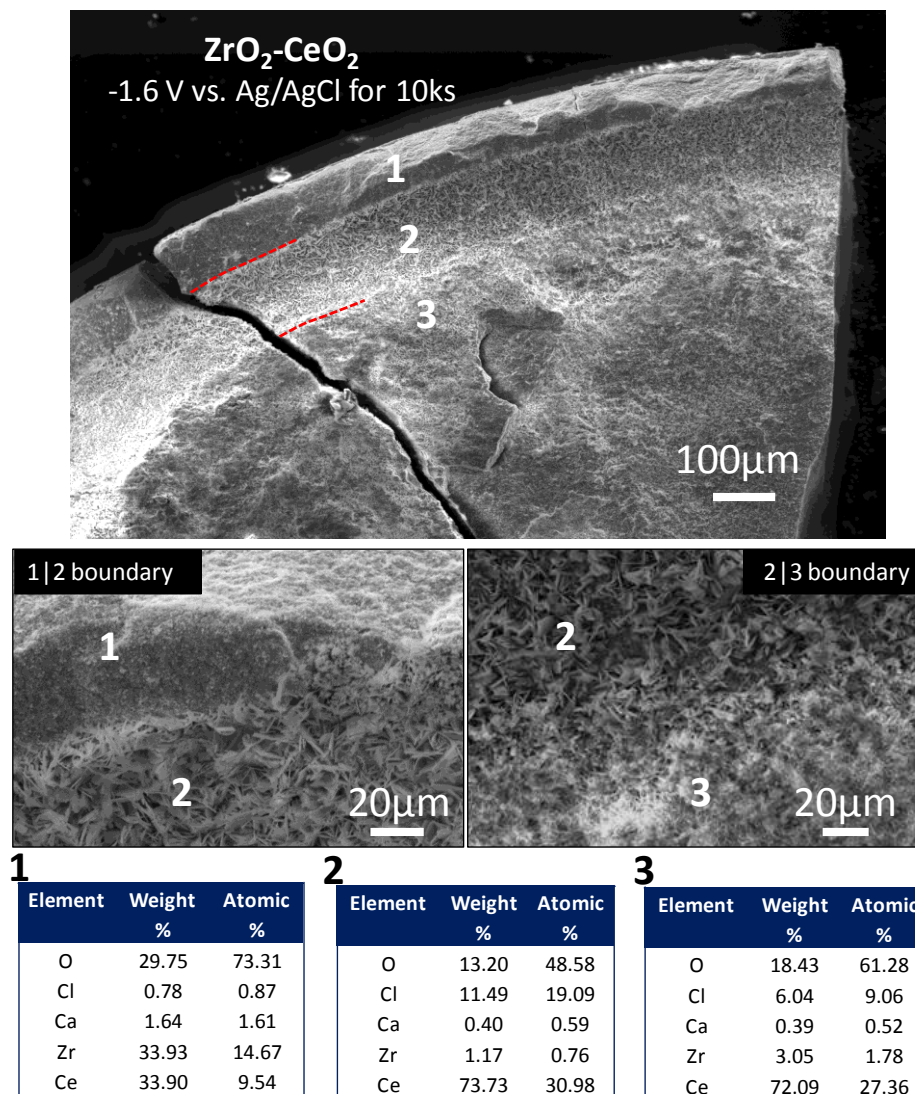
Figure 7.11 – SEM and EDS analysis of a 5mm diameter ZrO_2-CeO_2 pellet interior (150mg) following potentiostatic electrolysis at -1.6 V vs. Ag/AgCl for 10ks.

The outermost band (1) at approximately 100µm wide appears to remain in the pure ZrO_2-CeO_2 phase based upon the high content of oxygen present; however the content of Ce relative to Zr had dropped by approximately 34%. Further inwards the region marked as (2) has a vastly different morphology, one which is recognised from previous experiments

in this thesis as CeOCl, and which is supported by the large proportion of Cl presence (and low Ca, voiding the possibility of solidified $CaCl_2$ salt). Interestingly in contrast to band (1), the Zr content of (2) is near zero, with the most likely explanation that the CeOCl is a deposited layer on the surface of the bulk oxide below. The final region at the centre of the pellet (3) (spot analysis taken just beyond the 2|3 phase transition) appears to show a similar atomic composition as (2), however a limited quantity of CeOCl and more pure CeO_2, or possibly Ce_2O_3. It was believed the mechanism for this unusual structure was established owing to the potential applied being insufficient to induce any reduction of the ZrO_2 precursor and the dense packing prevented significant $CaZrO_3$ formation at this electrolysis duration. A diagrammatic description of the probable cause of the unpredicted behaviour is given in **Figure 7.12**, and assists in confirming the so far theorised solubility of the Ce(III) phase and the conditions required to permit CeOCl formation.
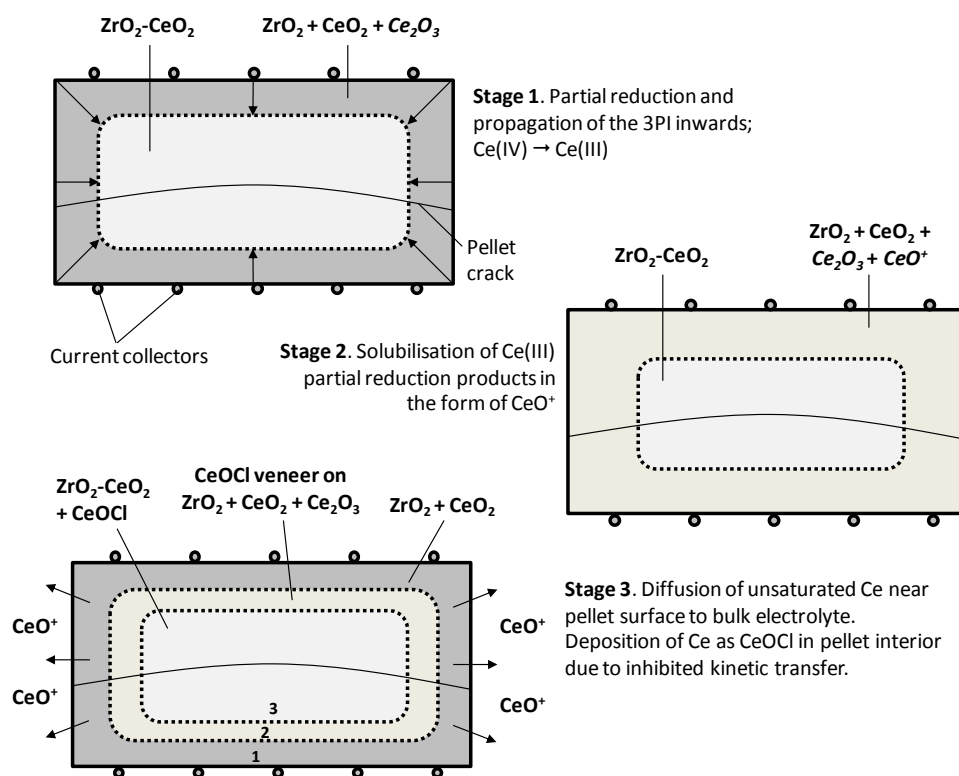
Figure 7.12 – Illustration of the observed formation of CeOCl banding in a 150mg ZrO_2-CeO_2 pellet after potentiostatic electrolysis at -1.6 V vs. Ag/AgCl for 10ks.

In the first stage, reduction progresses inwards as dictated by the 3PI from the point of contact between current collector, oxide and electrolyte. Due to the effect of increasing oxide quantity from MCE investigations, the -1.6 V potential supplied was apparently insufficient to induce any partial reduction of ZrO_2, however could provide the necessary energy to reduce CeO_2 to the Ce_2O_3 oxide. According to the literature and empirical evidence explored so far in this thesis, the Ce(III) species are at least partially soluble in molten $CaCl_2$, and manifests as the CeO^+ cation. Solubilisation of CeO^+ as reduction continues inwards represents the second stage of the process. In the final aspect, the CeO^+ content near the surface of the pellet can more readily undergo mass transport into the bulk electrolyte owing to better diffusive kinetics, whereas the ions further within the pellet are more likely to saturate.

The relative size of the CeO^+ as opposed to the produced O^{2-} from partial reduction could have left a bias towards the diffusion of O^{2-} and consequently permitted the coalescence of CeOCl onto the surface of the pellet interior where conditions were ideal. Within the core the dense structure of the pellet would have prevented both CeO^+ and O^{2-} ion migration, hence halting further CeO_2 reduction and facilitating a deposition of the Ce_2O_3 phase over CeOCl due to the higher oxygen activity. The cumulative effect is a depletion of Ce at the pellet fringe due to dissolution, a highly ordered veneer of CeOCl crystals in a narrow band in the pellet and a cessation of any reduction in the centre of the pellet due to: 1) a lack of metallisation maintaining a high charge transfer resistance, 2) limited porosity development from lack of reduction and 3) subsequent poor diffusion of O^{2-} ions.

The presence of deposited CeOCl crystallites was also observed in the second experiment where the small ZrO_2-CeO_2 pellet was subject to an

applied potential of just -1.25 V vs. Ag/AgCl for 5ks. In this case however, due in part to the relatively modest applied potential and likely also because of the short experiment duration, the first apparent Ce_2O_3 crystals were also detected by SEM and EDS (**Figure 7.13**).
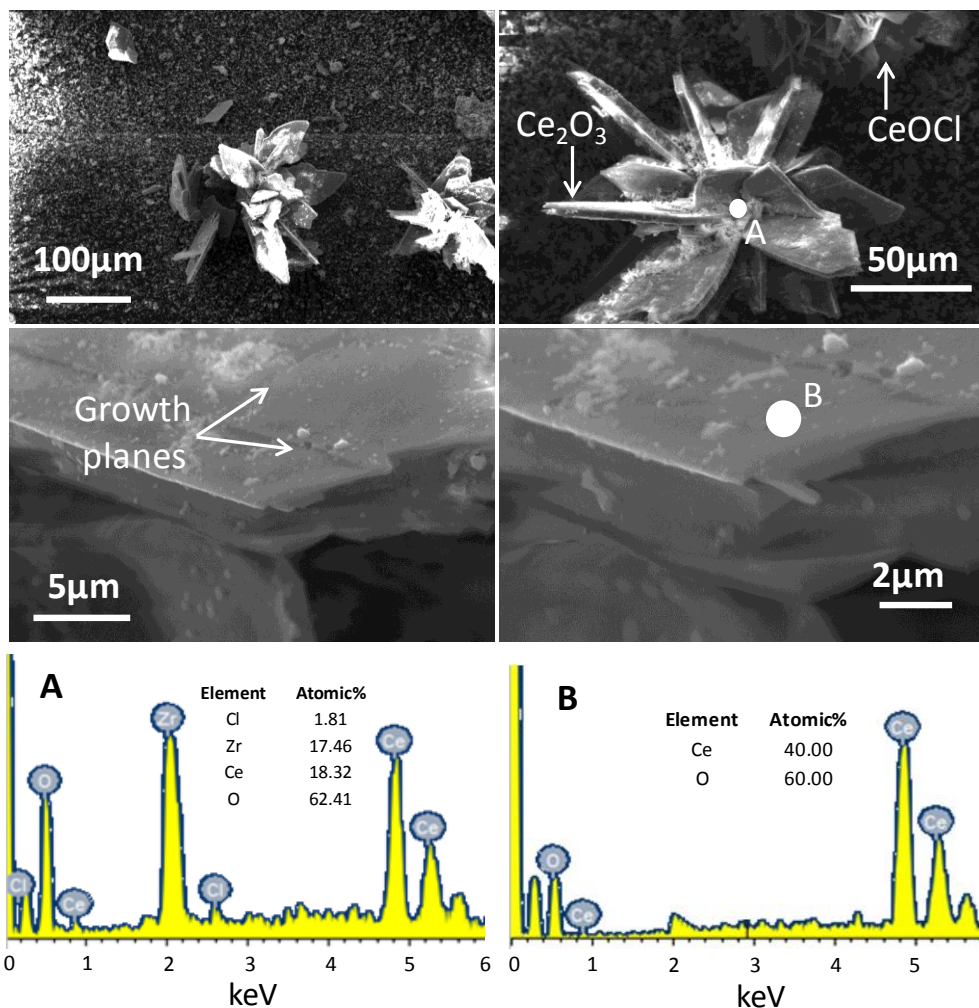
Figure 7.13 – SEM micrographs of the lightly ground reduction product from potentiostatic electrolysis of a ZrO_2-CeO_2 pellet at -1V vs. Ag/AgCl for 5ks. Included are EDS spot analyses of areas marked A and B respectively.

The less cathodic applied potential in this experiment allowed for the development of proportionally large crystals of Ce_2O_3 in a rosette arrangement (some crystals >100 μm in length) supported by the spot EDS analysis at point B. Simultaneously large CeOCl crystals could be seen (top right SEM image in **Figure 7.13**), in agreement with the earlier CV work of 2NiO-CeO_2 presented in **Figure 6.10** which displayed well formed

and vast CeOCl structures when scanned to only -1.2 V. The SEM images in **Figure 7.13** also clearly show the development of growth planes on the Ce_2O_3 crystal surface, prognostic of a deposition of the ionic form of Ce meaning dissolution had already occurred and the lack of an ample electrochemical driving force permitted an oxoacidity within the pellet supporting a stable crystallisation of Ce_2O_3. It remains unclear however whether this process occurs in-situ, during electrolysis, or is a consequence of the washing or drying procedure following removal of the sample from the retort.

These findings imply that either at the broad ranges of intermediate potentials there is an insufficient chemical potential to permit the full dissolution/migration of the Ce(III) species and/or the anodic aspect of the CV investigations provided a passivation or oxidising environment to maintain stability of the species. The latter point will be investigated further within the next sub-section using a TiO_2-CeO_2 binary and in the LCE electrolyte.

7.3. Towards a Viable LiCl-CaCl$_2$ Eutectic (LCE) Electrolyte for Processing

7.3.1. Characterisation of the LCE Electrolyte

7.3.1.1 Influence of Temperature Variation on LCE Resistance

The compositional eutectic point of the $CaCl_2$-LiCl solution remains somewhat unclear within the broader literature, with freely available DSC derived phase diagrams reporting a slightly different molar concentration ratio to other earlier researchers[77,79]. Although not intrinsically significant owing to the operational temperature of the eutectic implemented here being well above the melting point across nearly all concentrations, it is of academic interest to confirm the eutectic point of salts. In this work, the 65

mol% LiCl LCE had the lowest melting point as according to heat flux analysis by TGA-DSA of 10 mg salt samples, after analysis of 62, 65 and 68 mol %. Hence batch salt preparation for individual experiments (typically in the range of 100-350g depending on the type of experiment performed) was prepared using this ratio.

While the melting point of Pu metal effectively determines the ceiling temperature of the cell, the energy consumption and longevity of equipment benefits in maintaining a low operating temperature. This comes at the expense of limiting the kinetic transfer/ionic movement within the electrolyte which, as a function of the system thermal energy, is already compromised when compared to the use of pure $CaCl_2$ at 810^oC through reduced diffusion coefficients (D) of the transported O^{2-} anions. It's probable that an optimal temperature point or transitional period exists which adequately considers both aspects of economics and electrolysis performance, though detailed investigation of this point is beyond the scope of this thesis. Foundation studies employing EIS in pure, electrolysed LCE at three temperatures (570^oC, 600^oC and 630^oC) were however carried out to assess the electrolyte resistance of the melt and act as a comparative to the previous works in the higher temperature $CaCl_2$.

Figure 7.14 gives the EIS spectra for the LCE melt using averages from three consecutive measurements at 570^oC, 600^oC and 630^oC over a frequency range of 10 Hz to 100 kHz. The information was gathered using the Mo conductivity probe described in Chapter 5. As to be expected due to the lack of impurities and electrode design, a near identical spectra to those produced from $CaCl_2$ was obtained. Predictably owing to the lower operating temperature, the extent of solution resistance was shown to be higher at all temperatures in the LCE; 1.11 Ω at 570^oC, 1.03 Ω at 600^oC and 0.91 Ω at 630^oC, compared to 0.80 Ω in $CaCl_2$ at 810^oC.
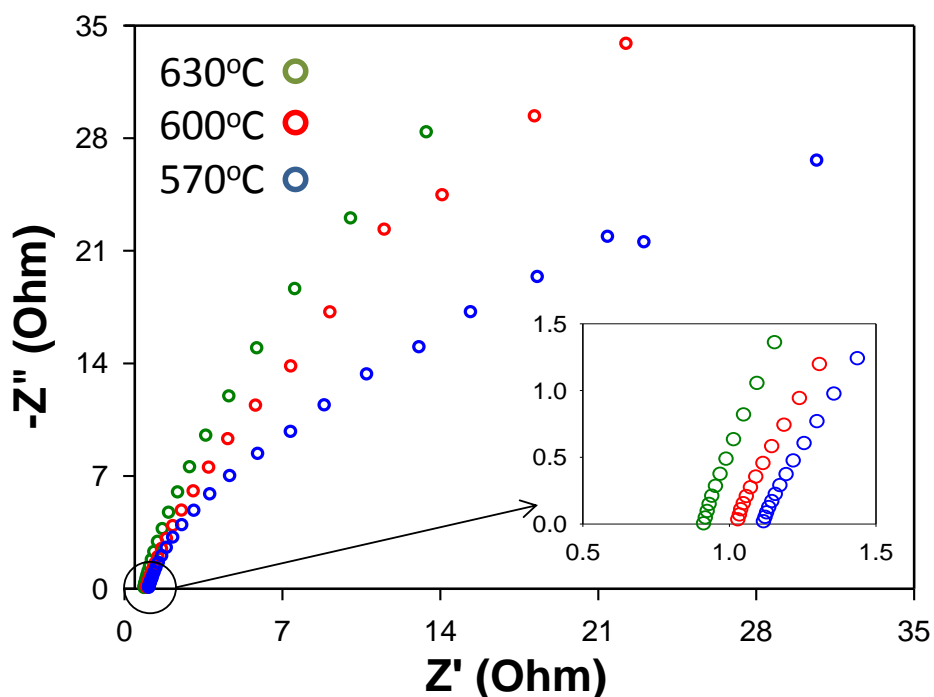
Figure 7.14 – Nyquist plot of EIS results from blank Mo electrodes in molten LCE electrolyte at 570°C, 600°C and 630°C with a frequency range of 10 Hz to 100 kHz. Inset is a higher resolution plot for R_s identification of each study (at $-Z'' = 0$).

When plotting the apparent trend of temperature versus solutions resistance for the LCE recorded variants, there appears to be a linear relationship (displayed in **Figure 7.15**). Concerning a purely thermodynamically derived relationship between electrolyte media and temperature dependant solution resistance, it would be expected a continuation of this trend for the $CaCl_2$ electrolyte be ascertained, but this was not the case. Only a single averaged measurement for the $CaCl_2$ solution resistance at 810°C was taken, however the R_s data point as plotted in **Figure 7.16** is clearly much higher than the predicted trend from the LCE data would estimate. The reason for this is perhaps twofold, firstly the LCE temperature ranges are considerably higher than the actual melting point of the eutectic (>70°C at the lowest temperature recording), whereas the $CaCl_2$ at 810°C is only 38°C above its melting point. Hence the viscosity of the $CaCl_2$ may be relatively higher than the LCE at these temperatures and act as a physical barrier to free ion movements.
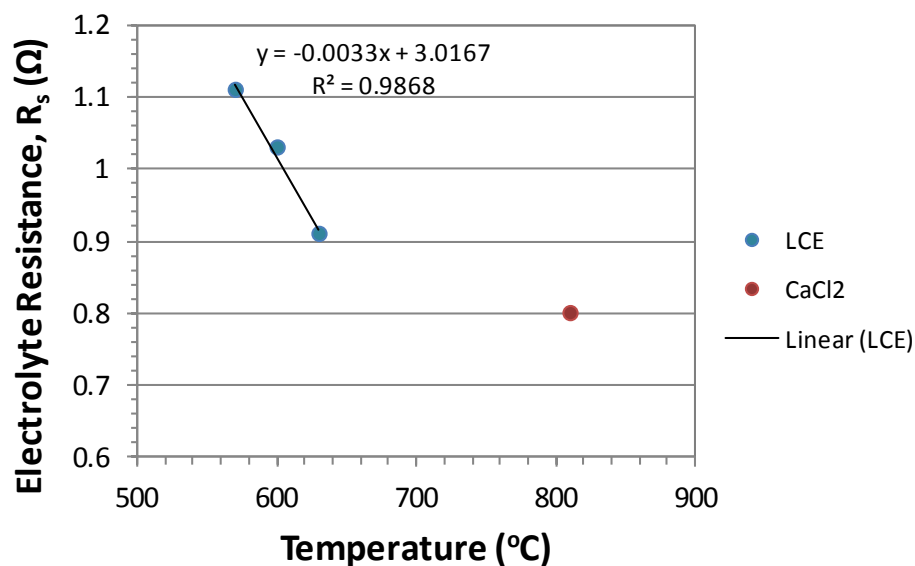
Figure 7.15 – Plot of electrolyte resistance versus temperature for both $CaCl_2$ and LCE melts derived by triplicate averaged EIS measurements.

Secondly the compositional effects of having a secondary salt in the system, particularly the monovalent Li^+ cation, may aid the ability of electronic conduction to propagate based upon intervalent charge transfer between Li^+ and Ca^{2+} ions provided the energy states are favourable enough, as governed by the Franck-Condon principle. In terms of the absolute values however, it is apparent that both salt systems perform quite similarly with regards to solution resistance, which is beneficial in promoting LCE as a suitable replacement for $CaCl_2$ in the electroreduction of oxides to metals at the examined temperatures.

Beyond the derived solution resistance from the Nyquist plot in **Figure 7.14**, the absolute peak –Z″ values of the initial hyperbolic spectra is shown to decrease as temperature decreases. This observation is usually indicative of a reduction in interfacial charge accumulation on the electrode surface (reduced C_{dl}), a relationship that is understandable given the higher resistance measured at 570°C as opposed to 630°C for example. Having established the LCE melt as being initially comparable to pure $CaCl_2$ at 810°C, it was important to consider how extensive the effects of lower

working temperatures are on the conductivity and qualitative data produced from the Ag/AgCl reference electrode. To achieve this aim, CV experiments were performed in the melt at 600°C, selected as a reasonable balance between the antagonistic concerns of cost and process utility.

7.3.1.2 Blank CV of the LCE eutectic at 600°C

Blank CV scans in the LCE using unloaded Mo MCEs were carried out as a diagnostic tool in determining the potential shift, potential window and salient redox features of the new electrolyte system. Early attempts to characterise these parameters were relatively successful, though a consistent current trough was produced on the cathodic sweep at -1.20 V vs. Ag/AgCl, extending to -1.95 V vs. Ag/AgCl (**Figure 7.16**).
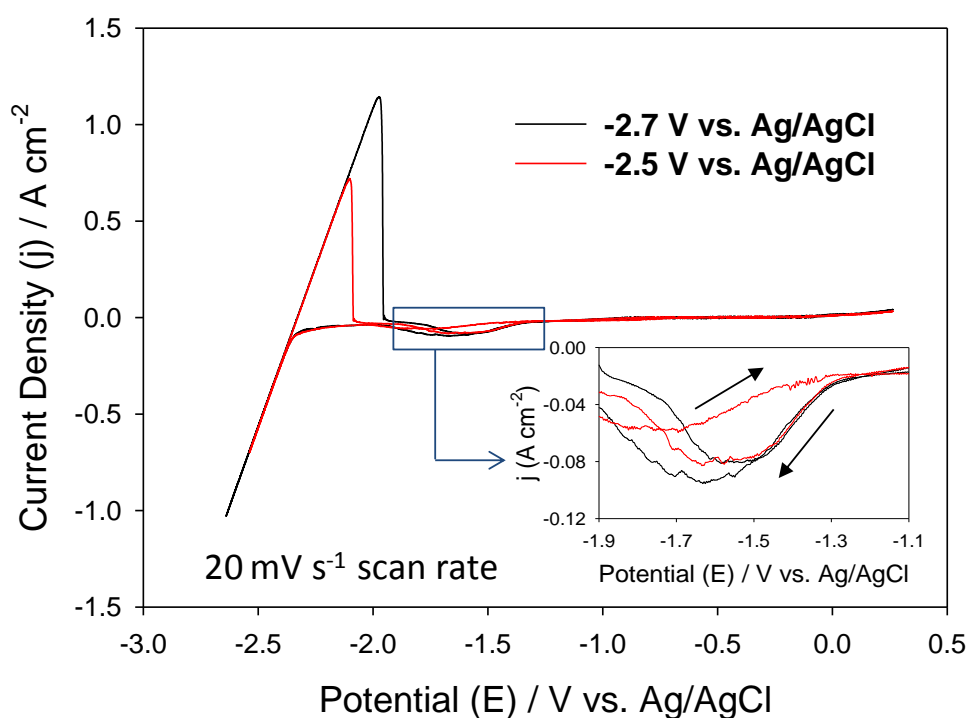
Figure 7.16 – CV curves of a blank Mo MCE in molten LCE at 600°C, scanned to cathodic potentials of -2.5 V and -2.6 V.

It was noted this current trough only appeared on experiments performed using a single batch of Mo MCE electrodes, while in others it was clearly absent (**Figure 7.17**) leading to the conclusion of surface contamination of those particular electrodes.
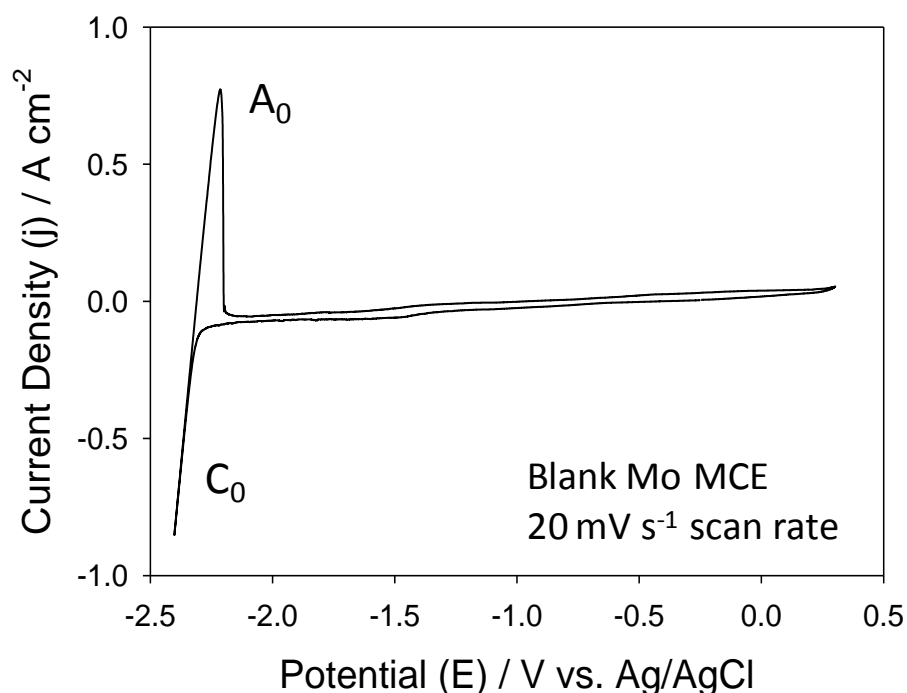
Figure 7.17 – CV of thoroughly pre-treated Mo MCEs in molten LCE at 600°C.

In both of the above figures a broad and (excluding the initial issue of contamination) electrochemically stable potential window of approximately 2.59 V was achieved. Indeed in **Figure 7.16**, when the melt was left for an hour and the cathodic limit extended from -2.5 V to -2.7 V, no potential shift was shown for the stripping peak (A_0) assigned to be for the Li^+ ion oxidation. The conclusion of a Li dominated cathodic redox tail derives from the clearly very distinguished cathodic potential increase at around -2.3 V, which compared to that for pure $CaCl_2$ displays no prominence of underpotential deposition associated with the partial reduction of Ca^{2+} ($Ca^{2+} + e^- = Ca^+$). The lack of this feature may actually prove beneficial in identifying reduction reactions occurring at very cathodic potentials which otherwise were masked in the pure $CaCl_2$ electrolyte, for example the direct reduction of Ce(III) to Ce. When considering the potential window in association with LCE at 600°C, the 2.59 V fits well with the thermodynamically predicted 2.51 V difference between LiCl decomposition and the onset of CO/CO_2 production at 600°C. Further anodic investigation

wasn't pursued here, however based on other works in molten salt using a graphite anode (with some key investigations discussed in Chapter 2), the initial oxidation current eventually transcends to a potential of working electrode dissolution and eventual Cl_2 evolution through the decomposition of the electrolyte.

CV experiments on blank Mo electrodes were able to prove a stable potential window could be established and confirm the ability of the alumina sealed Ag/AgCl reference electrode to maintain potential over semi-continuous experiments at extended durations. As the temperature of the molten salt is decreased, the ability to electro-deoxidise the oxide surrogates becomes diminished. Electrochemical investigations were therefore continued in the LCE electrolyte, again using CeO_2 as a surrogate of PuO_2 but replacing ZrO_2 with an oxide that better represents a conductivity analogue of UO_2; namely TiO_2.

7.3.2. CV of TiO_2 and CeO_2

The difficulties of using ZrO_2 as a surrogate material were often quite significant in that intermediate products ($CaZrO_3$ and Zr_3O) exhibited considerable volume expansions, preventing molten salt ingress into pellets and halting reduction progression. While TiO_2 suffers the same issues to some extent with the formation of Ca intercalated perovskites ($CaTiO_3$ and $Ca_2Ti_2O_4$) the many Magnélli phases do provide a gradual volume decrease and are more conductive than the intermediates of ZrO_2. In extension, there exists substantial industrial and commercial interest in developing an alternative to the Kroll Process for Ti (and indeed Zr) metal production that many believe the FFC Cambridge Process can provide an inexpensive and viable alternative. Consequently examining the ability to deoxidise TiO_2 to its metallic phase in the more benign conditions of the LCE electrolyte is advantageous to several fields beyond nuclear reprocessing. With some

oxides (TiO_2 in this instance) the final stages of FFC reduction becomes kinetically limited due to the difficulties of removing residual oxygen atoms diffused into the metallic structure. This type of oxygen diffusion follows a typical Arrhenius rate dependence (**Equation 7.4**);

$$D = D_o e^{(\frac{-E_a}{RT})}$$

7.4

Where D is the diffusion coefficient ($cm^2\,s^{-1}$), D_o is a prefactor ($cm^2\,s^{-1}$), E_a is the activation energy for diffusion ($J\,mol^{-1}$), T is the absolute temperature (K), and R is the universal gas constant ($J\,mol^{-1}\,K^{-1}$). Oxygen diffusion coefficients at 810°C and 600°C for α-Ti (based on $D_o = 8.9\;cm^2\,s^{-1}$ and $E_a = 220\;kJ\,mol^{-1}$ [254]) were calculated to be $2.2 \times 10^{-10}\;cm^2\,s^{-1}$ and $6.1 \times 10^{-13}\;cm^2\,s^{-1}$ respectively. These highlight the considerable kinetic difficulties which arise from lowering of the electrolyte temperature in terms of effective de-oxidation. However Ti is an example of a metal with superior oxygen affinity, creating multiple interstitials within the crystal lattice and a subsequent route for oxygen diffusion. U on the other hand is known to have exceedingly poor oxygen solubility (0.05% at its melting point [255]), effectively making the electrochemical conditions investigated here more challenging with respect to oxygen removal than could be expected for group actinide reduction.

CV was performed as per standard practice, using the oxide loaded Mo MCEs, graphite counter electrode and Ag/AgCl reference. First and second scan plots for CeO_2 are presented in **Figure 7.18** and clearly show a somewhat distinct aesthetic to the same scan in $CaCl_2$ at 810°C.

A prominent feature is the apparent current separation between forward cathodic and reverse anodic scans. While this behaviour isn't necessarily unique to the CeO_2 voltammogram, having been observed during some experiments in $CaCl_2$, it was noted in an exceptionally large number of the

LCE containing CV scans. Usually this type of current separation results from electrical charge storage by electrical double layer capacitance (EDLC) within the Helmholtz plane between the electrode interface and electrolyte.
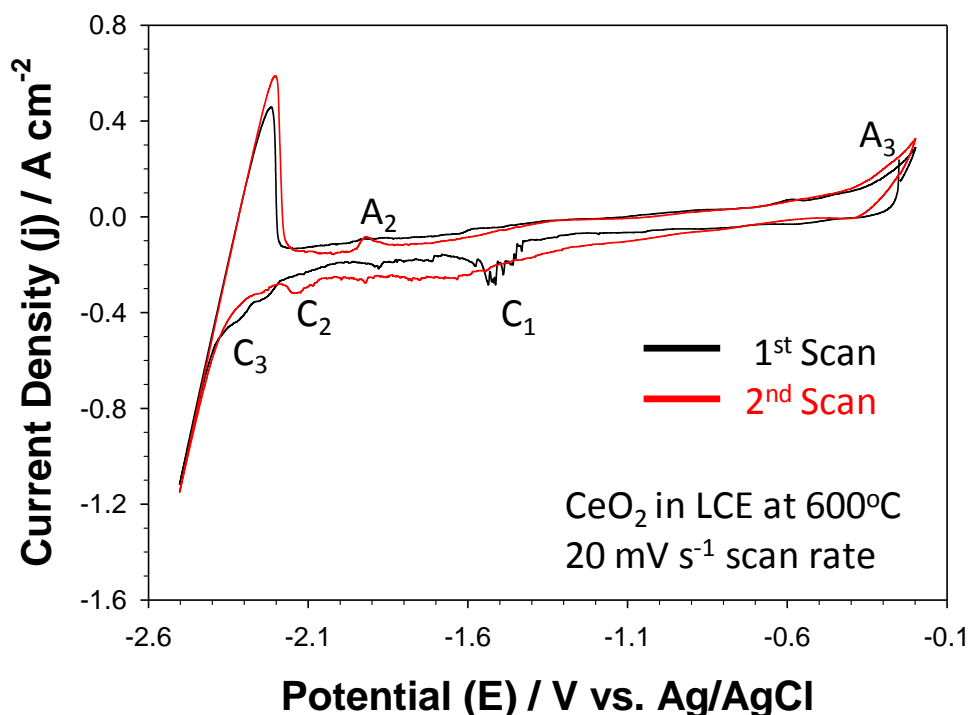
Figure 7.18 – First and second cycle CV scans for CeO_2 performed in molten LCE at 600^oC. Counter electrode: graphite, reference electrode: alumina sealed Ag/AgCl, scan rate: 20 mV s^{-1}.

It could be argued therefore that the charge transfer resistance within the LCE electrolyte is higher than that in $CaCl_2$ owing to the ability to establish and maintain a charge separation at the electrode interface. The key drawback however in terms of characterising redox activity is in clearly identifying which currents are related to the reduction or oxidation of target species and which are intrinsic background features associated with capacitance. The explicit cause of the EDLC experienced here is unknown, although as both blank scans in **Figures 7.16** and **7.17** displayed no significant aspects of capacitance, it likely results from electrolyte deterioration or from the presence of the oxides. While unlikely to cause such significant capacitance, the displacement of carbon particulates from the counter electrode introduced during reduction can store charge if in

contact with the working electrode. Both physical and electrochemical attempts were made to try and remove contaminants and potential causes of the EDLC; however none proved to be successful as a permanent solution. Fortunately the extent of capacitive currents is relatively small, and the ambient redox features for CeO_2 could still be identified.

Peak C_1 (at -1.40 V) from **Figure 7.18**, in theory should coincide with the transition of Ce(IV) to Ce(III), however the onset potential is far more negative than recorded in the $CaCl_2$ melt (ca. 500 mV). Even accounting for the decrease in temperature between electrolytes this shift is far beyond what would be reasonably expected. There are very shallow current increases on the near side of C_1, which may be the early stage reduction of CeO_2 and in which case would align more favourably with predictions. What is of particularly interest is the introduction of cathodic redox behaviour at approximately -2.2 V not previously observed in the pure $CaCl_2$ scans of CeO_2 due to the masking effect of underpotential deposition. It's very likely that this current increase (peak C_3) is the final stage reduction of either Ce_2O_3, CeOCl or CeO^+ to Ce metal, However as the current response is very marginal compared to the C_2 and C_1 peaks, it suggests this reaction is kinetically still rather difficult or that a fairly rapid dissolution procedure had been established.

On the second scan (red curve), the first cathodic peak C_1 subsides and the development of a redox couple, peaks C_2 and A_2, appears. Peak A_2 reflects the dissolution via anodic stripping of Ce metal (confirmed in $CaCl_2$), with the onset potential matching relatively well the potential from earlier works. As such peak C_2 is ascribed to the plating of Ce which may have been present in the CeO_2 CV scanned in molten $CaCl_2$, however could not be readily identified due to the Ca cathodic current tail obscuring redox reactions not associated with the partial Ca^{2+} reduction.

Fortunately there exists numerous investigations on FFC based TiO_2 electrochemistry owing to its high commercial potential and being the origin material for the process discovery. Comparing the initial CV works here with those from the literature therefore is relatively simple, albeit very few works have considered the LCE as a media for electroreduction owing to the difficulties of deoxidising TiO_2, normally necessitating elevated temperatures ($850^{o}C$-$1000^{o}C$). **Figure 7.19a** and **7.19b** Highlights a TiO_2 CV experiment in $CaCl_2$ at $850^{o}C$ taken from the literature[256] and compares it with one performed in the LCE electrolyte at $600^{o}C$. Both CVs exhibit a highly convoluted current response, representative of the relatively complex redox chemistry covered in Chapter 2.

The CV performed in the LCE melt (**Figure 7.19b**) shows two separate cycles, representing TiO_2 scanned before (red curve) and after (blue curve) a short physical and electrolytic cleaning of the electrolyte. The difference in appearance of the CV is quite substantial, having the capacitive behaviour frequently noted in the LCE experiments almost completely removed. Therefore it is indeed likely that various contaminants contribute to the capacitive aspects of the CV investigations performed in the LCE melt. The physical cleaning process involved using a rudimental scoop to skim the surface of the molten salt for floating particulates, usually carbon, while the electrochemical process was a pre-electrolysis at 2.0 V. The anodic tail in both CeO_2 and TiO_2 LCE investigations suggest the presence of iron contamination which has a theoretical redox couple (Fe^{3+} to Fe) at very positive potentials (+2.49 V vs. Li^+/Li). If true, some of the current peaks observed on the 'before cleaning' CV scan may represent the various contaminants from SS spallation of the inside retort wall falling into the melt.
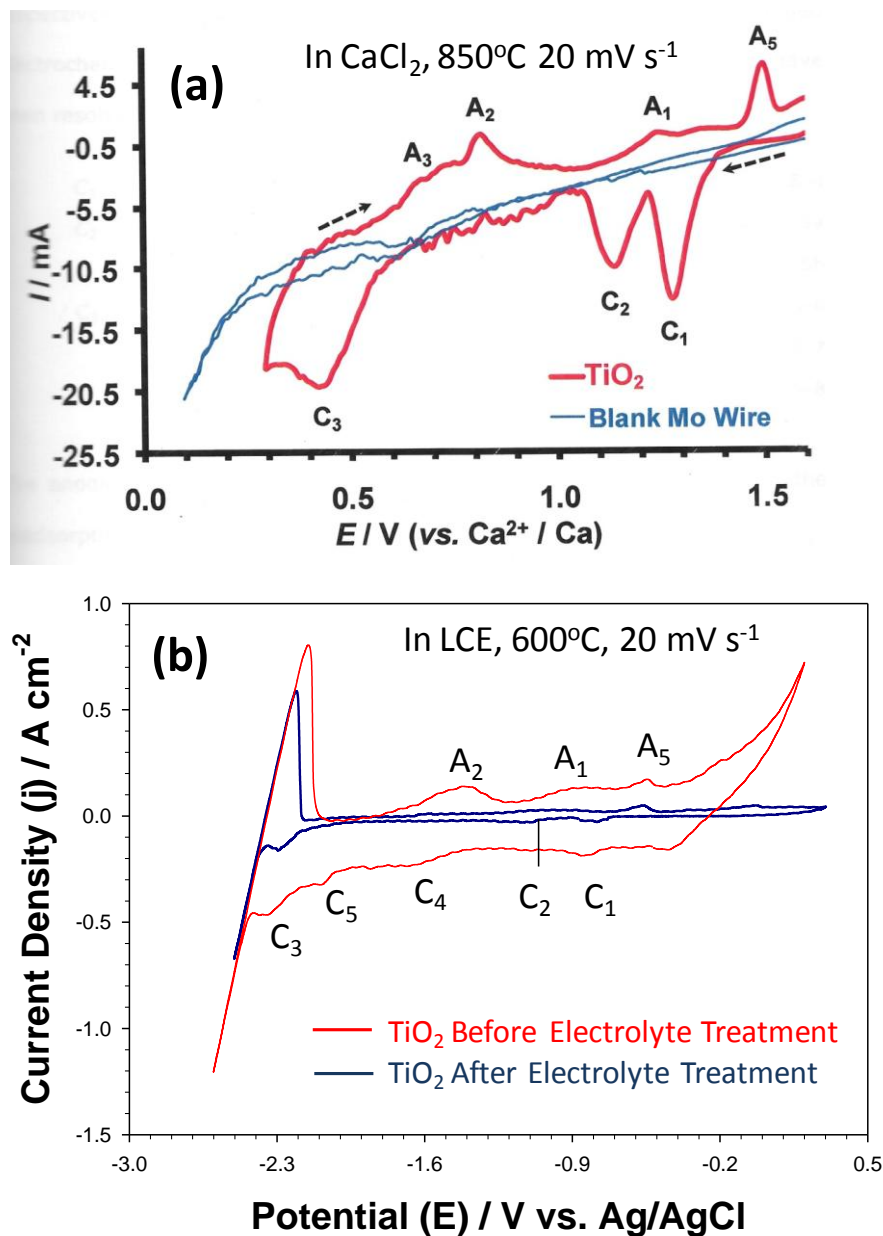
Figure 7.19 – CVs at 20 mV s^{-1} of TiO$_2$ (a) in CaCl$_2$ at 850°C [256] and (b) in LCE at 600°C before and after a physical and electrochemical cleaning process.

As aspects of unwanted contaminants were apparently removed, the 'after cleaning' CV curve helped resolve some of the ambiguity related to the cause of this current separation. These CVs recorded in the LCE were successive (following a gap of a few hours for treatments) meaning the clear potential alignment for current peaks is again a great indicator of the performance and stability of the reference electrode.

Comparing the TiO_2 scans from $CaCl_2$ and LCE reveal a very similar redox chemistry, which although expected is still a testament to the ability of LCE to provide a suitable reductive environment for relatively stable oxides. In the $CaCl_2$ electrolyte, there were only three reduction peaks, labelled C_1, C_2 and C_3 and which are outlined in **Equations 7.5-7.7** below.

$$C_1: \quad 3TiO_2 + 2e^- = Ti_3O_5 + O^{2-} \qquad \textbf{7.5}$$

$$C_2: \quad 2Ti_2O_5 + 2e^- = 3Ti_2O_3 + O^{2-} \qquad \textbf{7.6}$$

$$C_3: \quad Ti_2O_3 + 2e^- = 2TiO + O^{2-} \qquad \textbf{7.7a}$$

$$TiO + 2e^- \ Ti + O^{2-} \qquad \textbf{7.7b}$$

$$Ti\text{-}O + 2e^- = Ti + O^{2-} \qquad \textbf{7.7c}$$
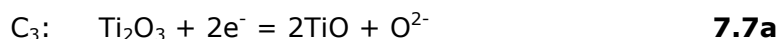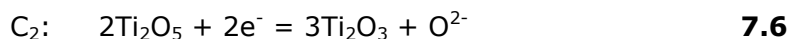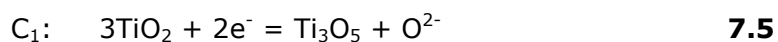
Whereas the LCE TiO_2 scan revealed two extra current peaks; C_4 and C_5. Accounting for the very marginal current response and the mentioned issues with contamination, it remains too difficult to confidently assign these peaks to given redox reactions. Furthermore, when scaling the 'after cleaning' CV curve from the LCE melt, these C_4 and C_5 peaks no longer appear and instead a remarkably similar CV curve to that in $CaCl_2$ is revealed. A primary difference however is that the onset potential for the final reduction peak (C_3) is closer to the decomposition point of the molten salt by approximately 260 mV, reflecting the lower operating temperature of the system. The less favourable kinetic factors, for instance solubility of O^{2-} ions in LiCl as opposed to $CaCl_2$, would play a diminished role at this scale of oxides although undoubtedly becomes a more important parameter for pellet or bench scale operations. The initiation of peak C_3 in LCE is at around -2.03 V, which is still over 300 mV positive of the decomposition point, suggesting in theory a direct electrochemical conversion of the oxide to metal is possible.

The anodic reactions are mostly irrelevant for this work and so will not be covered in detail; however they represent the effective reversal cathodic reactions including the expulsion of Ca intercalated Ti-O species.

Overall it would appear that although there are increased energy barriers associated with lowering the molten salt temperature, the improved electrolyte stability from LiCl coupled with kinetic benefits during reduction by maintaining $CaCl_2$ presence (higher O^{2-} diffusion) offers great potential for CV investigations. It follows that the same desirable traits would be evident during bulk electrolysis in the LCE electrolyte.

7.3.3. Selective Reduction and Recovery of Ti metal

7.3.3.1 Showcasing Reduction Studies of TiO_2-CeO_2

This section outlines some of the key reduction only experiments and analysis performed on slip cast pellets of TiO_2-CeO_2, with the intension of better understanding exhibited electrochemical and physical behaviours. The influence of electrolysis duration was examined experimentally at a single potential of -1.5 V vs. Ag/AgCl, where according to CV results the initial TiO_2 reduction proceeds, along with the proven formation of the Ce intermediate. Attempts in previous works have frequently investigated the influence of electrolysis duration at very cathodic potentials, with the aim of measuring the overall oxide content in relation to charge consumed. Here, the development of intermediate species as a function of time was deemed important where some materials, e.g. CeOCl, inflict paradigm shifting properties to the desired partitioning process. Should a lag in the formation of intermediates exist during bulk electrolysis, there may be a means of exploiting this feature in achieving a selective reduction with a procedure of controlled potential stepping. A series of ca. 800 mg TiO_2-CeO_2 sintered slip cast pellets were prepared as by the described means in Chapter 3 and independently reduced at -1.5 V for durations of 0.5, 1, 2,

4, 6 and 18 hours. **Figure 7.20** provides analysis via XRD and SEM of the recovered electrodes following washing in water for 24 h and manual grinding by pestle and mortar.
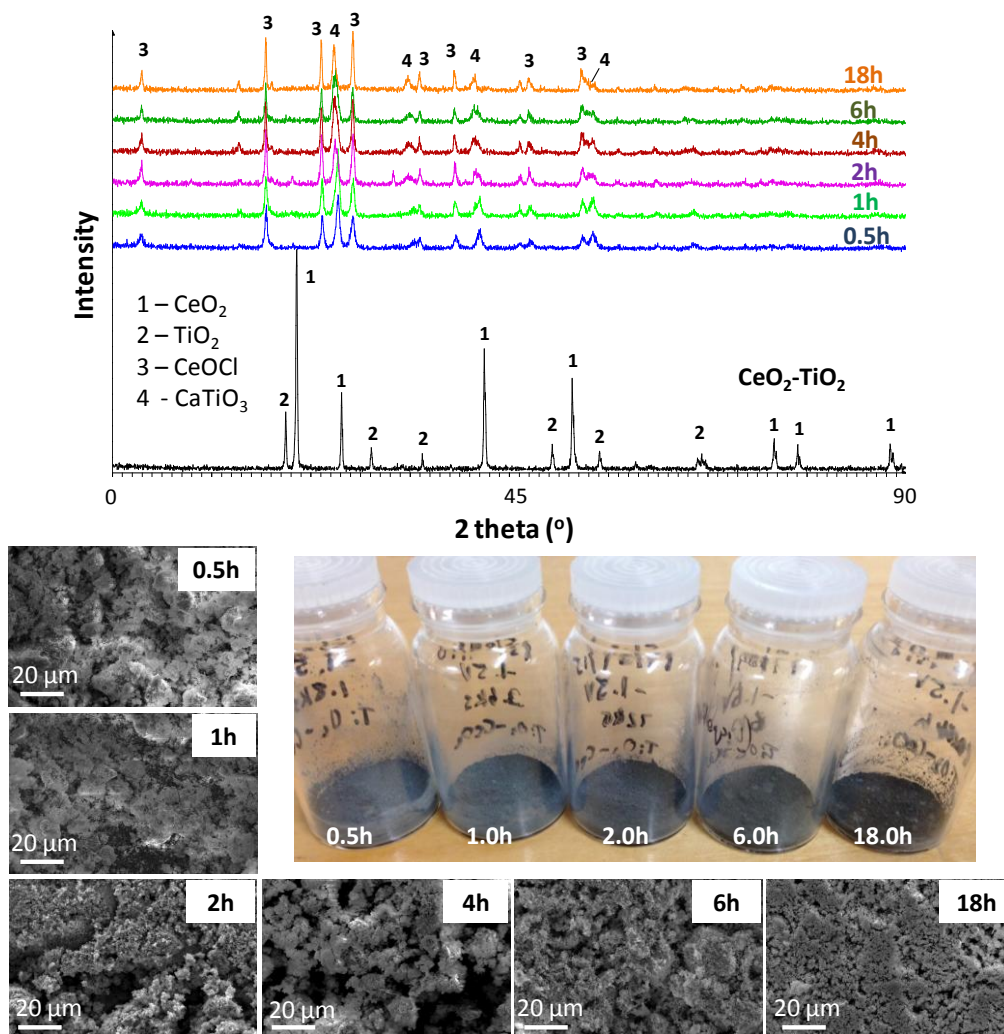
Figure 7.20 – XRD patterns of the TiO_2-CeO_2 feed material (black spectra) and of electrolysed products at -1.5 V for different durations (top). Also given are SEM micrographs of products after washing, grinding and carbon coating (bottom).

The XRD results reveal an unexpectedly simple amalgamation of species present following the reduction procedure; exclusively in the form of CeOCl and $CaTiO_3$. Despite Li being the dominant cation in the LCE electrolyte, in terms of absolute atomic quantity, no Li intercalated species of TiO_2 were detected, which is interesting owing the relatively smaller crystal ionic radius of Li^+ compared to Ca^{2+} (90pm vs. 114pm). The presence of $CaTiO_3$

is perhaps reflected by the more favourable ΔG^{o} formation value of -85.7kJ versus -106kJ for the stable $Li_2Ti_3O_7$ non-stoichiometric perovskite[120].

In all durations of electrolysis, both precursor materials of CeO_2 and TiO_2 were noticeably absent, suggesting either after even 30 minutes a complete conversion (electrochemical in the case of CeOCl and chemical for $CaTiO_3$) had occurred, or some form of selective leaching on the remaining oxides took place. The only significant changes that were recorded in the 17.5h total difference was a slight increase in the intensity and a narrowing of CeOCl peaks accompanied by a marginal decrease in $CaTiO_3$ intensity, suggesting a gradual development of more ordered CeOCl crystallites. These weren't visually observed during SEM in the same morphology as exposed in earlier studies due to the post-electrolysis manual grinding procedure; however a nominal increase in uniformity and ordering could be detected at incremental electrolysis durations. The data here highlights that (a) the initial reduction stage for CeOCl and intercalation of Ca into TiO_2 occurs very rapidly (however justifying a complete conversion is erroneous owing to the probable loss of other oxide materials) and (b) the influence of electrolysis duration at intermediate potentials has little effect on final product composition, but is rather more aggressively potential dependant (as highlighted in the ZrO_2-CeO_2 case studies).

A second investigation considered a more holistic approach to pyroprocessing by attempting to perform direct electroreduction on a simplified TiO_2-CeO_2 fuel pin analogue. With aqueous methods, the spent fuel rods as recovered from storage silos and following a cooling period are mechanically sheared into short 'pins' which undergo dissolution in nitric acid. Here, solid phase separation is the targeted methodology and so it may be possible to bypass de-cladding and voloxidation by performing

direct reduction on the clad fuel pins due to the metallic nature of the cladding and its contact with oxide spent fuel acting as a current collector.

Specifically, the process proposed here would see most utility applied to legacy oxide fuels from GENII LWRs. These spent fuel rods can undergo a significant change during their fission lifetime within the reactor, with some of these relevant features highlighted in **Figure 7.21a**. The 'bambooing' effect isn't particularly concerning with respect to pyroprocessing, as the formation of thermal stress cracks in the oxide fuels may even permit void space for electrolyte penetration. The cladding used for reactor fuel is a zirconium alloy which has some neutron transparency, vital in avoiding conflict in sub-critical fission operation. Due to the expense of this material, Ti was instead employed as the cladding to produce a dimensionally similar, binary oxide fuel pin as shown in **Figure 7.21b**.
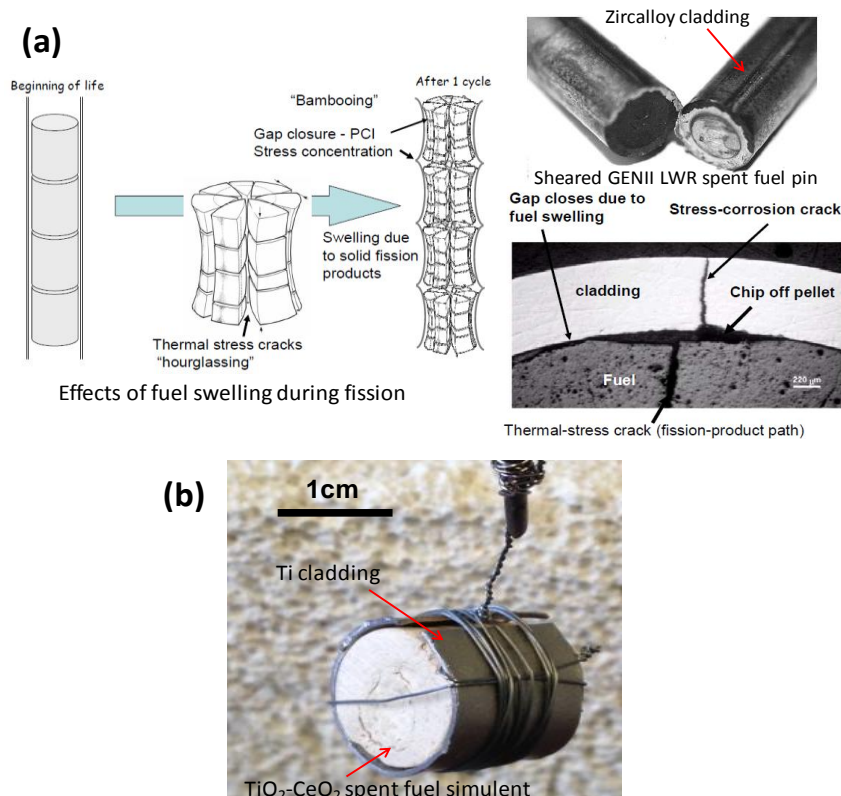
Figure 7.21 – (a) Illustrations of some key physical effects fission can have on the Zircalloy clad, GENII LWR uranium oxide fuel pins (modified from[257]). (b) Photograph of the fabricated Ti clad, TiO_2-CeO_2 binary surrogate fuel pin prior to electroreduction.

In this design a small section of the TiO_2-CeO_2 pellet circumference is exposed and not covered directly by the Ti cladding. This may not necessarily deviate from a realistic fuel pin however as the volatile release of some FP and volume expansion of spent fuel daughter nuclei can cause swelling and stress-corrosion cracks of the cladding material (illustrated in **Figure 7.21a**)[257].

The electrolysis for the ~4.5g TiO_2-CeO_2 pellet was performed using a three electrode cell to try and maintain the effective applied potential throughout the 24h duration. The chosen potential for this experiment was -2.3 V, which according to the CV results above and other works within the literature should be adequate to induce a full reduction of TiO_2 to its metallic phase. **Figure 7.22** shows the recorded current response curve for the Ti clad oxide pellet under the described conditions.
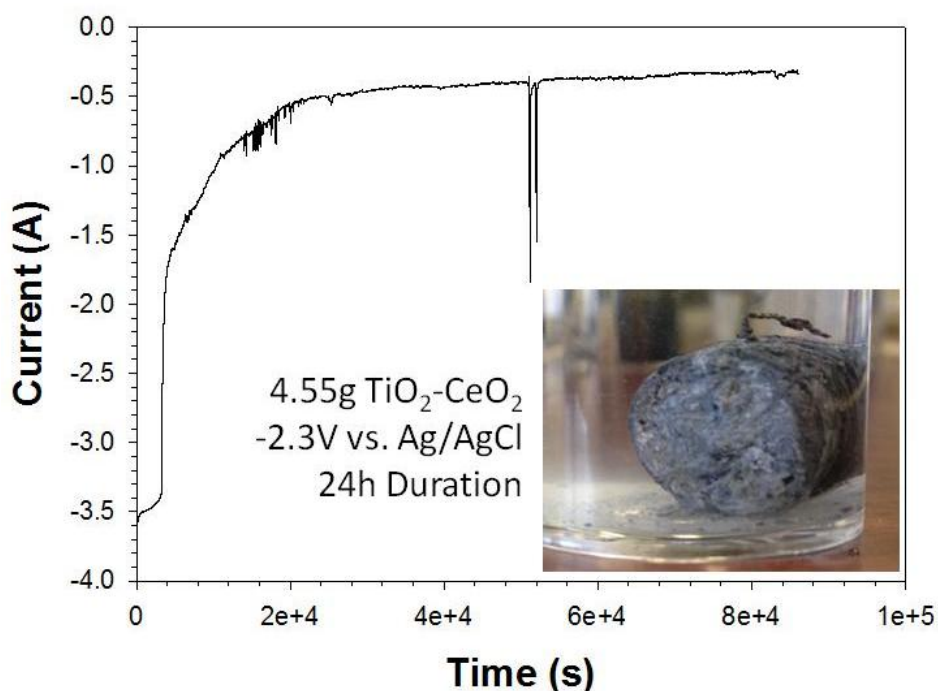
Figure 7.22 – Current-time plot from the potentiostatic electrolysis of a 4.5 g TiO_2-CeO_2 slip cast pellet with Ti cladding. Inset shows electrolysed pellet.

The current response appears very typical of the FFC based electrochemical reductions, albeit the initial current value of 3.5 A is relatively small given

the total quantity of oxide present, which may reflect a limited contact area between pellet and metal cladding and/or slow rates of reduction. Of the two regions of current instability at around 12ks and 50ks, the first may be caused by a significant internal restructuring occurring through crystal structure changes or by sudden fluctuations in the apparent surface area of the 3PI. The second disturbance is likely a case of instrumentation sensitivity picking up on external vibrations, given the extremely large spike and single data point entries. In total a considerable -55 kC charge was passed in the 24h period and when assuming a 100% current efficiency, the required theoretical charge is -18.85 kC (calculated using the average molecular weight from a 1:1 Atomic ratio of Ce:Ti) hence a supplied 398% charge was provided throughout the experiment. SEM and EDS analysis were performed on the electrolysed pellet after mounting in a conducting carbon-black epoxy resin, which permitted gentle sanding of the product 1 mm from the end surface, shown in **Figure 7.23a-d**.

Various areas of the exposed surface were examined visually and characterised by elemental presence. **Figure 7.23a** highlights the lack of void space between the original pellet surface and Ti cladding, yet clearly has a homogenous composition which is prognostic of a uniform volume expansion, evidently caused from a transition in bulk species presence. At higher magnification of the same boundary between cladding and electrolysed product, in some areas it was noted that shrinkage had occurred leading to a continuous gap between pellet and cladding. The lack of significant void space shown via SEM profiling provides an initial indication that the full extent of reduction may have been limited, driven by the exclusion of the 3PI boundary to the surface of the oxide pellet.
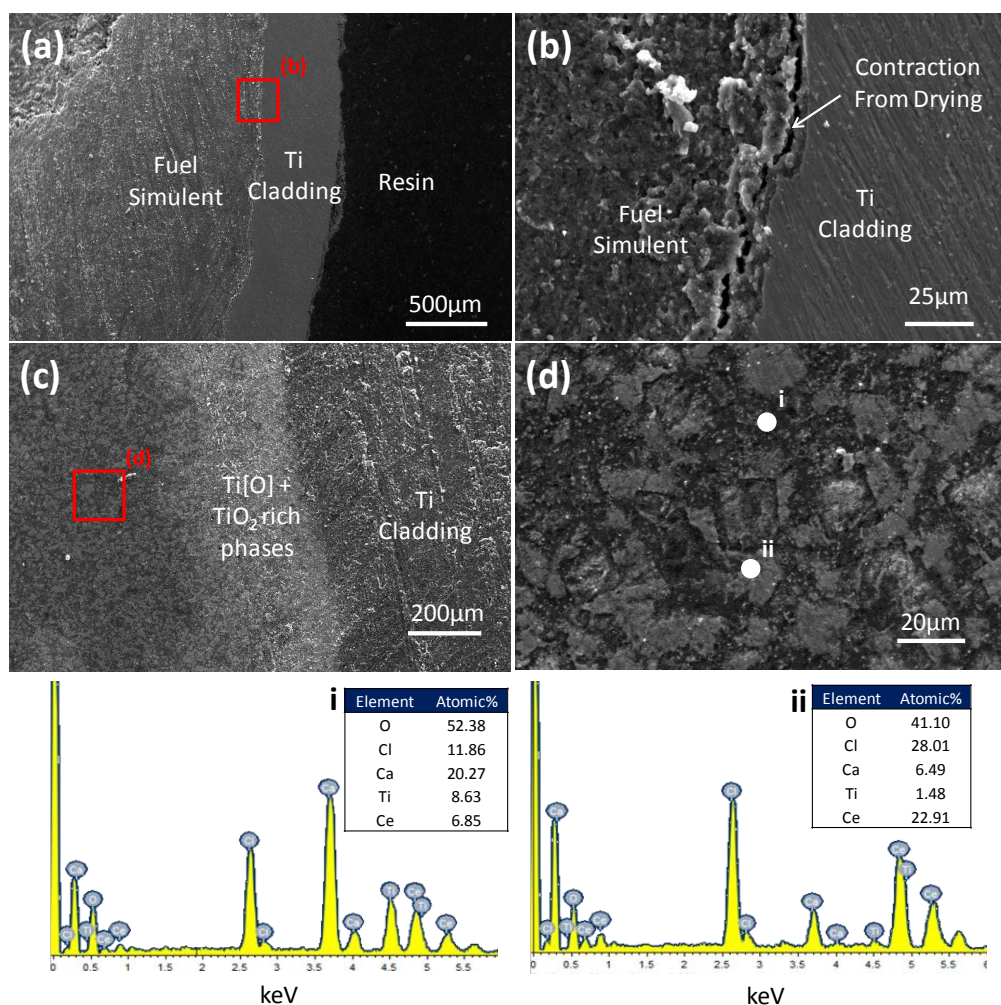
Figure 7.23 – (a)-(d) SEM images of the recovered Ti clad TiO_2-CeO_2 clip cast pellet, after gentle washing, mounting in conductive resin and grinding. Spot analysis EDS are shown for two regions in (d), denoted by i and ii.

Figure 7.23c shows the cladding|pellet interface in a region further along the pellet circumference and reveals a complete absence of void spaces. Instead an apparent banding had developed similar to those observed in the ZrO_2-CeO_2 studies, although in this instance the stoichiometry of the band closest to the Ti cladding suggests TiO_2 and $TiO_{2-\delta}$ (where δ is between 0.5 and 1) dominant phase and a subsided presence of Ce. It's probable given the knowledge accrued in previous investigations that the cause of this lack of Ce is from dissolution of the partially reduced Ce(III).

A closer examination of the interior of the pellet as given in **Figure 7.23d** shows a more sporadic morphology with lighter and darker regions. Each of

these areas were spot analysed by EDS, revealing the lighter coloured areas, marked i, are CeOCl and the darker phases, ii, is $CaTiO_3$. These finding do consolidate the XRD results from the previous experiment, however as the applied potential was 800mV more negative it was to be expected that sufficient driving force for the full reduction had been provided. Given the unique construction of the working electrode in this investigation, the absence of metallic Ti phases (or even a bulk TiO presence) suggests the design permits conditions prohibitive for the favourable electroreduction of the selected oxides. In the case of the active legacy spent fuels, it appears a significant drawback with pyroprocessing by electroreduction would be an absence of head-end processing. Consequently, the recommendations yielded by this work for a potential industrial process are to mechanically remove cladding, homogenise the oxide matrix by voloxidation and to recast the spent fuel pellets into smaller, more porous forms that can be appropriately mounted to permit favourable electrolyte contact.

7.3.3.2 Purification of FFC produced Ti by Electrorefining

Experiments from the previous sections have demonstrated two key aspects of electrochemically reducing the TiO_2-CeO_2 analogue spent fuel material. These are: (1) the extent of reduction possible at a given applied potential occurs relatively rapidly for the intermediates of each individual species and remains moderately time independent, and (2) the bulk electrolysis of large clad pellets, even given a significant theoretical overpotential, renders a full reduction unattainable due to the expansion phase volume from Ca intercalation and the impermeability of cladding material to electrolyte. These factors were considered in this section, where a series of experiments were performed in an attempt to fully reduce and

isolate the TiO_2 presence, akin to a solid phase selective recovery of U metal in an active hot cell electrorefiner.

In an early attempt to achieve selective removal of Ti presence, cyclic potentiostatic electrolysis was initiated on small (5mm dia.) TiO_2-CeO_2 pellets, with potentials based on the current responses gauged from CV of the same binary material. By reverting to small pelletised oxide working electrodes with intelligently engineered 3PI propagation pathways, the necessary overpotentials should be far less than using bulk oxide powders and hence it is envisioned that the potential for Ti production would more accurately reflect those given by CV. **Figure 7.24** shows the current response for the cycling potentiostatic electrolysis, at potentials of -2.1 V and 0.2 V vs. Ag/AgCl, as well as images of the before and after pellets.
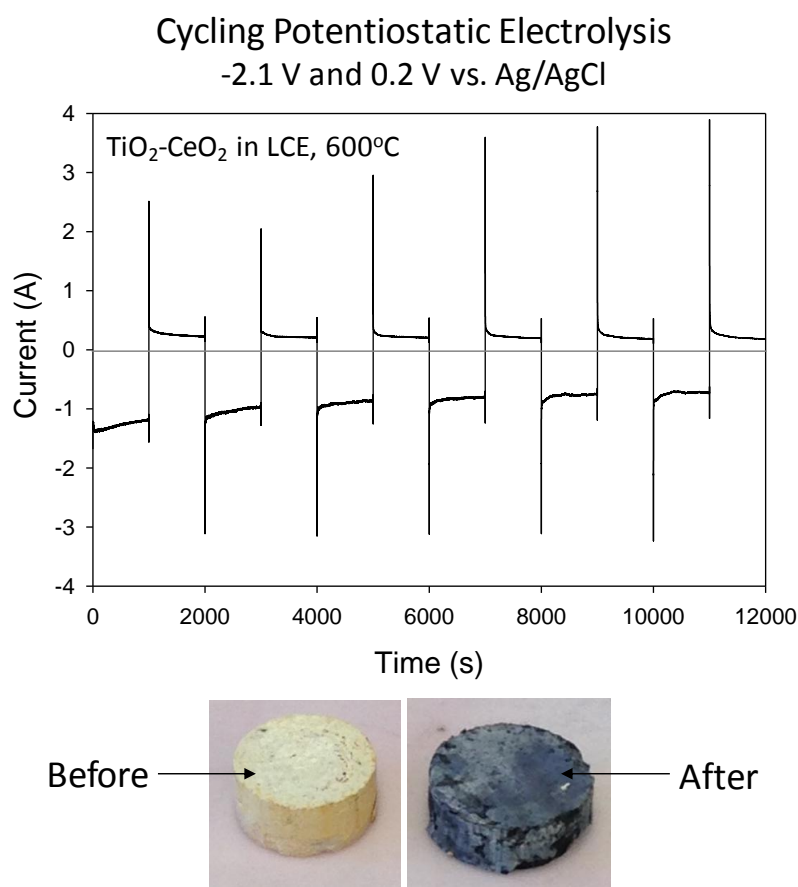
Figure 7.24 – Current response during a cyclic potentiostatic electrolysis experiment on a 120mg TiO_2-CeO_2 pelletised electrode between -2.1 V and +0.2 V with each full cycle lasting 2ks.

Clearly some degree of species transition had occurred, judged by the shift in colouration from white to greyish-blue, however no obvious shrinkage or pellet destabilisation was noted (by mass loss of O^{2-} and Ti). The peak reductive currents from **Figure 7.24** are shown to be relatively constant during each potential cycle at around -3.2 A, whereas the peak oxidative current exhibit an initial decrease by the second cycle (2.5 A to 2.0 A), and then more immediate increase until a plateau is reached by the final cycle at around 3.9 A. As the absolute values of the reduction currents in the first half of the experiment are less than the oxidation currents, it's probable they represent both the Ti partial reduction or metallisation coupled with the production of Ce(III). Ideally, the oxidation which follows each initial cycle therefore passes less current as electrons are only transferred to initiate the ionisation of Ti^{4+}. Background currents for the duration of each 1ks electrolysis segment were shown to be constant for each oxidation (at ca. 0.2 A), yet gradually decrease during successive applied reduction potentials (from -1.1 A to -0.75 A). To better comprehend what reactions may have occurred, SEM imaging of various parts of the pellet surface and interior were carried out, with simultaneous EDS elemental analysis, as presented in **Figure 7.25** and **Table 7.2**.

Considering an initial 1:1 ratio of Ti to Ce, analysis on the surface of the pellet revealed a significant loss of Ti presence, giving a new ratio of 1:10 (i.e. >90% Ti removal). While it would be convenient to attribute this loss to the effects of TiO_2 metallisation and then anodic dissolution from cycling the applied potentials, an analysis of the interior of the pellet would assist in gaining a more thorough appreciation for the plausible phenomena. Cleaving the pellet wasn't required as a small portion of the surface had apparently broken and fallen away, exposing a microcosm of the interior phase composition.
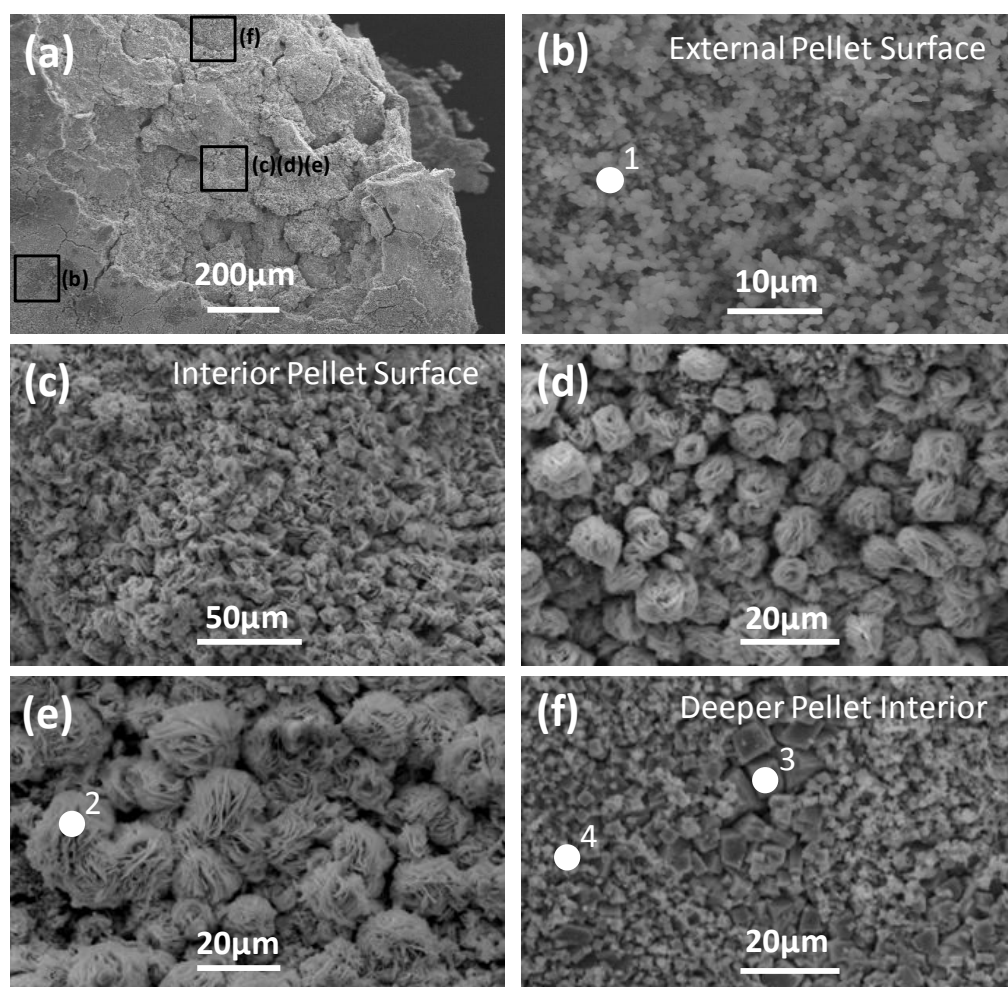
Figure 7.25 – SEM micrographs of a TiO_2-CeO_2 reduction product following cycling potentiostatic electrolysis between -2.1 V and 0.2 V for 12 ks in LCE at 600°C. (a) Pellet surface and section of exposed interior, (b) pellet surface, (c), (d) and (e) show the pellet interior and (f) a deeper exposed section of the pellet core.

Table 7.2 – EDS elemental spot analysis of various points of a TiO_2-CeO_2 electrolysis product (shown in **Figure 7.27**), with the suggested phases based on stoichiometry.

Spot Analysis	Elemental Composition (Atomic %)					Primary Stoichiometric Compositions
	O	Ti	Ce	Ca	Cl	
1	65.35	2.99	24.64	2.30	4.72	Bulk: CeO_2 Trace: $CaCl_2$, TiO_2
2	47.22	0.00	27.06	0.00	25.72	Bulk: CeOCl Trace: CeO_2
3	60.69	20.07	2.78	16.34	0.12	Bulk: $CaTiO_3$ Trace: CeO_2, Ti_2O_3
4	62.30	32.48	3.13	1.61	0.47	Bulk: TiO_2,Ti_2O_3 Trace: CeO_2, $CaTiO_3$

Morphologically, an unusual arrangement of spherical clusters appeared to cover large areas of the interior surface (Figure **7.25c-e**) which under higher magnification were constructed from a random orientation of the flat, square CeOCl crystallites. The exclusivity of this phase with a complete absence of any Ti containing species is highly diagnostic of a precipitation of the phase onto the underlying pellet bulk. Supporting evidence can be drawn from the observed shape of the crystallites, with the understanding CeOCl can form from the coalescence of Cl^- ions to the fringes of the CeO_2 lattice[245] with growth further enhanced by the diffusive transport of Ce along the fringes of the crystal planes. Similarly, large and stable CeOCl forms were produced during CV in **Figure 6.10**, where a 10 cycle experiment at modest potentials resulted in a bulk phase of CeOCl inter-dispersed within the electrode cavity. Consequently, the repeating oxidation aspect of this electrolysis is shown to permit the growth of stable forms through a passivation effect, preventing the dissolution of CeOCl (and possibly PuOCl) into the molten salt. As these forms were apparently unrestricted in growth it seems plausible the cavity in the pellet being investigated formed prior to or early in the electrolysis, as an average CeOCl diameter of 20 µm seems unlikely to develop in the closely packed bulk pellet phase. Conversely, the lack of CeOCl on the pellet surface suggests the presence of a pO^{2-} value unaccommodating for its formation, as opposed to the interior of the pellet which must have been sufficiently dense to retain enough oxygen activity for the formation of CeOCl.

As to identifying the bulk underlying phase, some exposed regions that appeared deeper within the pellet core displayed a different and less uniform morphology (**Figure 7.25f**). The cubic structures seen here are reminiscent of $CaTiO_3$ as identified in other experiments performed (see Appendix 1) and in literary works. Additionally the large presence of $CaTiO_3$

would account for the change in colour from white to blue. The other spherical powders surrounding the cubic perovskite were shown to be unreduced and partially reduced TiO_2, accompanied with only trace amounts of CeO_2, with the remaining CeO_2 lost via dissolution of the Ce(III) partial reduction product.

The constant cycling of potential in this experiment on a small TiO_2-CeO_2 pellet appears to have created a dynamic paradigm of a predictable and desirable partitioning of TiO_2 on the pellet surface, but a complicated distribution of Ce and Ti within the bulk oxide pellet. Such frequency of potential cycling plays a determining role in the established processes here, but the lack of Ti in the pellet surface does indicate that the selected potentials were sufficient in being able to target TiO_2 for removal. A next logical iteration therefore is to attempt to recover this useful partitioned material in solid phase and using a single electrolyte.

Building upon the newly understood parameters affecting the ability to partition Ti from an original TiO_2-CeO_2 binary, including the fate of soluble Ce containing phases, potentiostatic electrolysis was performed on a 800 mg slip cast TiO_2-CeO_2 pellet aiming to produce, partition and collect pure Ti. Evidence from the previous experiments suggests that a cathodic potential of -2.1 V was adequate enough to full reduce at least some TiO_2 to Ti, and the subsequent +0.2 V anodic potential enough to selectively strip formed metal atoms. There are very narrow tolerances for overpotential application with regards to the reduction due to the aim of avoiding any electrolyte decomposition, and so -2.1 V remained as the applied potential value. There was some room for a more positive anodic shift in the oxidising potential, and for the aim of encouraging the highest electromotive force for the anodic dissolution of Ti metal, the oxidisation potential applied was +0.3 V. Furthermore, whereas the frequent cycling in

the last experiment promoted a better mechanical stability from lack of significant aspects of Ce(III) chemical dissolution, the frequent oxidisation would have been counterproductive to the generation of significant quantities of Ti from TiO_2. For this reason single cathodic and anodic phases were used, with durations determined based upon the current profile achieved (i.e. time taken to reach a stable background value).

In order to successfully collect electrorefined metals, a suitable substrate is required that acts a binding site for the deposition of desired metal ions, and while graphite is an option, a more favourable choice would be a metallic base. The electrorefining performed in research institutions around the world use a variety of approaches and materials, however one promising route for the selective recovery of group actinides over lanthanides is using a reactive aluminium electrode[173]. The issue arising from the use of Al is that although a high degree of An/Ln separation can be achieved, the process takes a very long time for even small volumes of waste (>72 hours) and as the An group metals diffuse into the Al (forming $AnAl_3$ type alloys), further electrowinning is required to strip away the Al and yield fissionable actinides. In this work a non-reactive SS rod was employed instead, with the intention of being able to coat a deposit of the electroreduced metal onto its surface, without any significant interactions between host alloy and deposited species. With this solution, a physical scraping mechanism would be adequate to remove the recovered species and in theory the process should be much more rapid and far more cost efficient. Of course, using a very simple surrogate system as applied here is quite far removed from a realised active scenario, however the demonstrative principles of a non-reactive electrode and perhaps even more crucially, a single electrolyte system for both electroreduction and electrorefining, is of huge significance.

The slip cast TiO_2-CeO_2 pellet was secured to Mo wire and acted as a working electrode before being immersed in the molten LCE electrolyte (**Figure 7.26a**) and subject to potentiostatic electrolysis. Following the reduction aspect of the experiment using the standard three electrode cell, the graphite counter electrode was replaced with a clean 5 mm diameter SS rod. **Figure 7.26b** gives the current profiles from both halves of the electrolysis, with the reduction duration notably being considerably longer than the oxidation (15ks vs. 3.6ks).
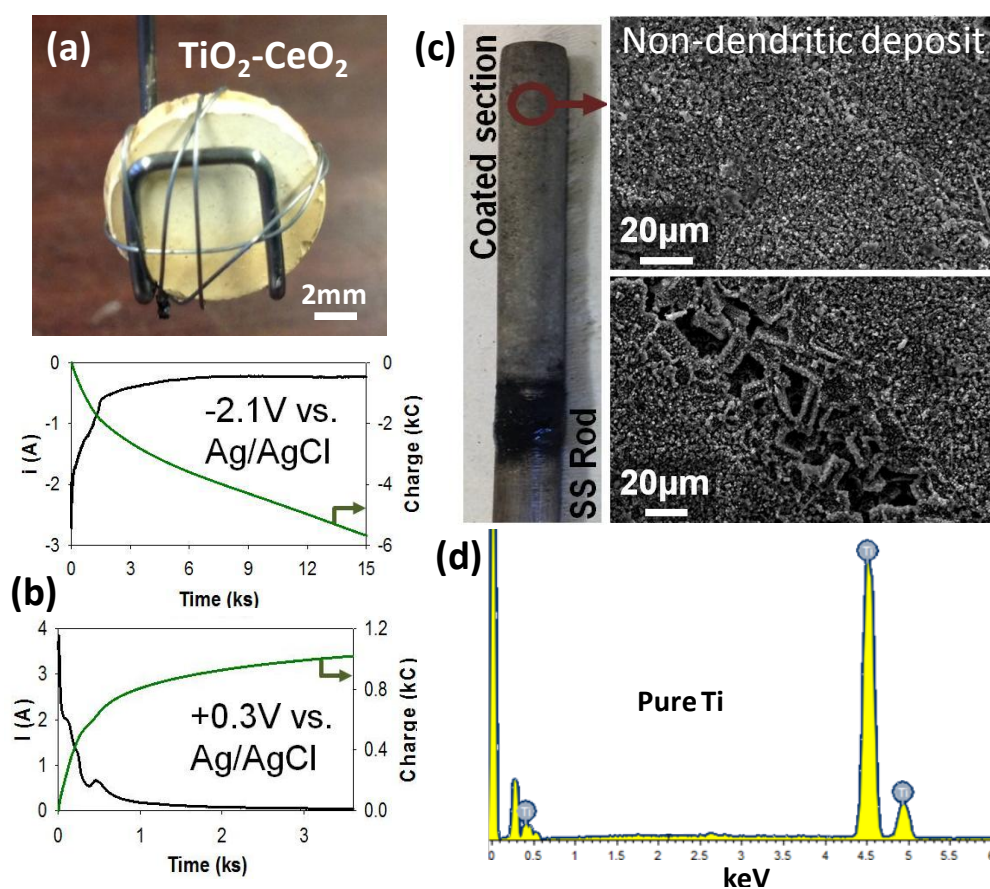
Figure 7.26 – Experimental results from the potentiostatic electrolysis in a LCE electrolyte at 600°C of, (a) TiO_2-CeO_2 slip cast pellet precursor with, (b) current-time curves for the initial reduction at -2.1V for 15ks and oxidation at 0.3V for 3.6ks. (c) SS rod used as the counter electrode during oxidation revealing the coated end section, coupled with subsequent SEM imaging and (d) EDS analysis of the surface of the coated section.

The explanation for the variation in time required to reach background current may derive from comparative difficulty in overcoming the binding

energy of the metal-oxygen bonds during reduction to the ionisation of metallic atoms during the anodic phase. As such, although the absolute charge consumed for reduction is nearly six times that for oxidation, this does not necessarily mean all of the produced Ti wouldn't have been stripped. When the working electrode was removed, no material remained making the calculation of current efficiency or extent of reduction impossible. However, following gentle washing in water the immersed 4 cm section of the SS counter electrode was shown to be a dull grey colour and when analysed by SEM for the surface of the rod, a tightly packed nodular configuration was present (**Figure 7.26c**). EDS area analysis of the approximate 200 μm x 200 μm frame supported the hypothesis that a pure Ti deposit had been layered upon the SS rod (**Figure 7.26d**).

As a rudimentary measure, but also the only available method for calculating the quantity of Ti recovered, the SS rod was weighed by mass balanced before and after electrolysis and a +90 mg difference was recorded. For an 800 mg TiO_2-CeO_2 pellet, the theoretical maximum attainable quantity of Ti is 152.3 mg, giving a yield 59 %. For a competitive process to be realised the yield of final uranium product from a pyroprocessing technology would have to be on the order of 99.8% (PUREX yields from LWR fuels), hence the recovery achieved in this experiment is far from practical. However, as an initial proof on concept and non-optimised design, with unknown variables in the washing and total Ti content, the experiment was decidedly a success. Indeed the demonstration of a single electrolyte, solid phase separation with metal recovery highlights an introductory step towards a possible simplification of pyroprocessing. The Ce presence from the original pellet likely underwent some dissolution given the time frame of the experiment, the apparent loss of any mechanical integrity of the pellet and from evidence provided by

previous experiments. The extent of Ce solubility in direct electroreduction electrolysis of pure CeO_2 is still only marginal according to an ICP-OES analysis of the $CaCl_2$ molten salt (**Figure 7.27**). Periodic sampling of the electrolyte was taken during the mass reduction of 1g and 1.5g CeO_2 at -2.1 V, and after 2 hours a 10 ppm Ce content for each run was detected.
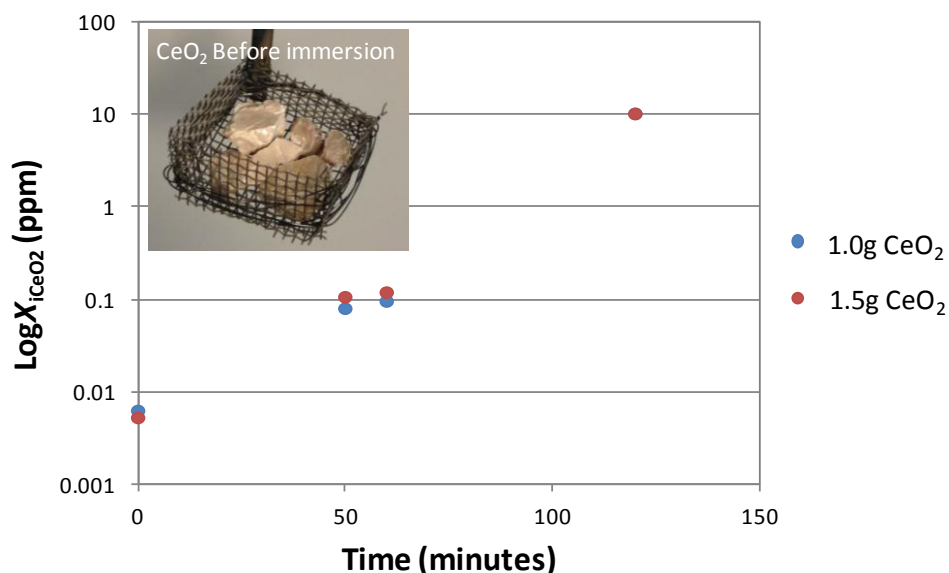
Figure 7.27 – Plot of the Log Ce concentration versus time from the electrolysis of CeO_2 at -2.1V vs. Ag/AgCl in $CaCl_2$ at 810°C, analysed by ICP-OES.

The calculated averaged dissolution rate from both runs was given to be 7.28×10^{-7} g s^{-1} in 50 g $CaCl_2$ at 810°C. Assuming the reduction proceeded as expected, the data suggests Ce(III) does indeed have some solubility in molten $CaCl_2$, although this value is notably small, particularly given the much more rapid apparent Ce loss observed in most other experiments. Given the short duration of sampling there may have been a lag in the peak rate of Ce diffusion not accurately reflected in these results and specifically to these tests, the CeO_2 precursor used were in the form of fused pieces that no doubt were much more difficult to reduce. Such small measurable Ce quantities alternatively could result from any solubilised CeO^+ precipitating within the bulk electrolyte due to oxidising contaminant species or from a direct formation of metallic Ce, of which both would leave consolidated Ce species at the base of the crucible. In any case, should

PuO_2 behave in an electrochemically and chemically similar way to Ce (as predicted), then the loss of at least some (and even all given sufficient duration) of the Pu phases from the electrode seems likely when only solid electrodes are employed during partial reduction.

A considerable portion of this thesis has dealt with the assumption that the surrogates used within have some merit as suitable analogues for spent nuclear fuel. Although the work performed certainly has broader academic and indeed commercial relevance, the specific aim of developing the foundation for an improved pyroprocessing technology requires the use active spent fuel components. Due to the difficult nature in handling and processing these materials, resources were limited and so experiments were restricted in effect to transient electroanalysis of mg quantities at the specialist NNL facility. The next section therefore covers the results from these final investigations, helping both to expand the knowledge regarding a potential electrochemical treatment of spent nuclear fuels and equally important, to assess how well the surrogates advocated here perform to the actual species considered.

7.4. Studies on PuO_2 and MOX

Descriptions of the facilities, equipment and methodology used during these experiments are provided in Chapter 2. The restrictions in place to ensure a safe operation of a high temperature rig within a high active glove box were considerable, but the result was a unique series of CV experiments on fresh PuO_2 and a 5% Pu MOX. Given below are the results and relevant discussions regarding the reactions are likely occurring during potential sweep in the limits of the potential window, how well data collected compares to those already produced using surrogates and, where appropriate, further application and work.

The uncommon nature of the experiments attempted here dictated work be performed at a licensed nuclear site, hence facilities at the National Nuclear Laboratory were utilised. **Figure 7.28** gives images of the experimental set up used to collect CV data for both PuO_2 and MOX powders. The initialisation of the experiment required careful arrangement of electrodes within the narrow quartz cell and hermetic sealing of all inlets and outlets to prevent any quantities of discharged chlorine gas escaping. Once the electrodes and salt were in place, a SS heat shield was lowered into place over the furnace, at which point no further amendments to the cell could be made and the ramping procedure for the furnace could proceed.
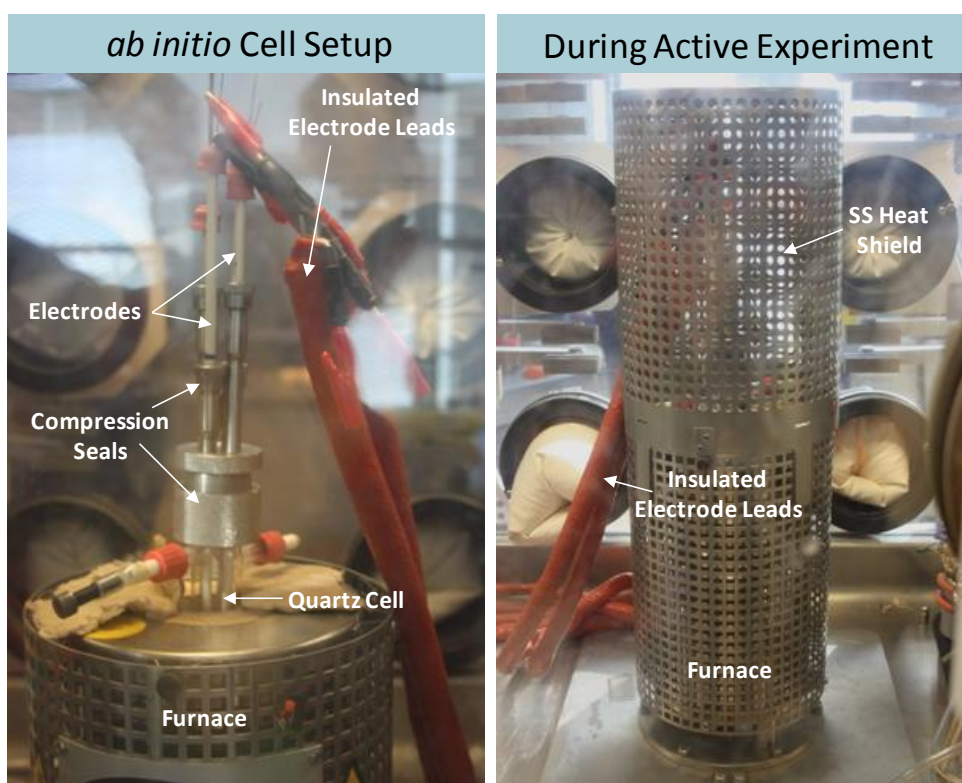
Figure 7.28 – Photographs of the active cell setup before (left) and after (right) turning on the furnace.

7.4.1. CV of PuO_2 in $CaCl_2$

Most of the investigations performed thus far have focussed in a molten $CaCl_2$ electrolyte at 810°C. Therefore the initial experiment using PuO_2 was carried out in near identical conditions to assess both the prospect for

electroreduction and the similarities between CeO_2 and PuO_2 in the benchmark FFC electrolyte. Although it was originally designed that a fully functional alumina sealed Ag/AgCl reference electrode be used for all active experiments, again to provide as identical an operational procedure as possible, this was found to be too difficult to implement. All electrodes had to be secured in place within the cell prior to the temperature ramping stage which was accomplished by first fixing the two working electrodes and counter electrode, while using the fourth port within the SS pressure sealed cap to act as a funnel to load the salt into the crucible. Following this, the funnel was removed and the reference electrode required insertion to complete the cell assembly. After several attempts to force the 5mm diameter alumina tube into the dry salt grains, it was deemed impossible to achieve the necessary displacement without either breaking the quartz cell or dislodging the loaded oxide powders within the cavity working electrodes. The only available alternative was to use a thin (1mm) loose Mo wire to act as a pseudo-reference electrode and which was subsequently employed in all experiments using the high integrity cell. Owing to the short time scales for CV experiments (<30 minutes), the possibility of potential shift was deemed generally not significant enough to influence qualitative results and was confirmed by the lack of shift over the course of, for example, a 5 cycle CV.

Given the strict safety case enforcing a lack of options in making in-situ adjustments to the experiment, recording a tangible CV gave merit to the design and execution of the cell. **Figure 7.29** gives one of the more aesthetic 1st cycle CVs for PuO_2 in ultra-pure (>99.99%, Sigma-Aldrich) untreated molten $CaCl_2$ at 810°C using a 20 mV s^{-1} scan rate.

The potential difference between the stable Ag/AgCl reference potential and the Mo/Mo^{3+} redox couple is approximately +210 mV, which becomes

important when attempting to standardise the various CV curves versus the internal reference of Ca/Ca^{2+}. Three distinct reduction peaks could be identified during the cathodic sweep of the CV, labelled C_0, C_1 and C_2, with these represented by **Equations 7.8**, **7.9** and **7.10** respectively.
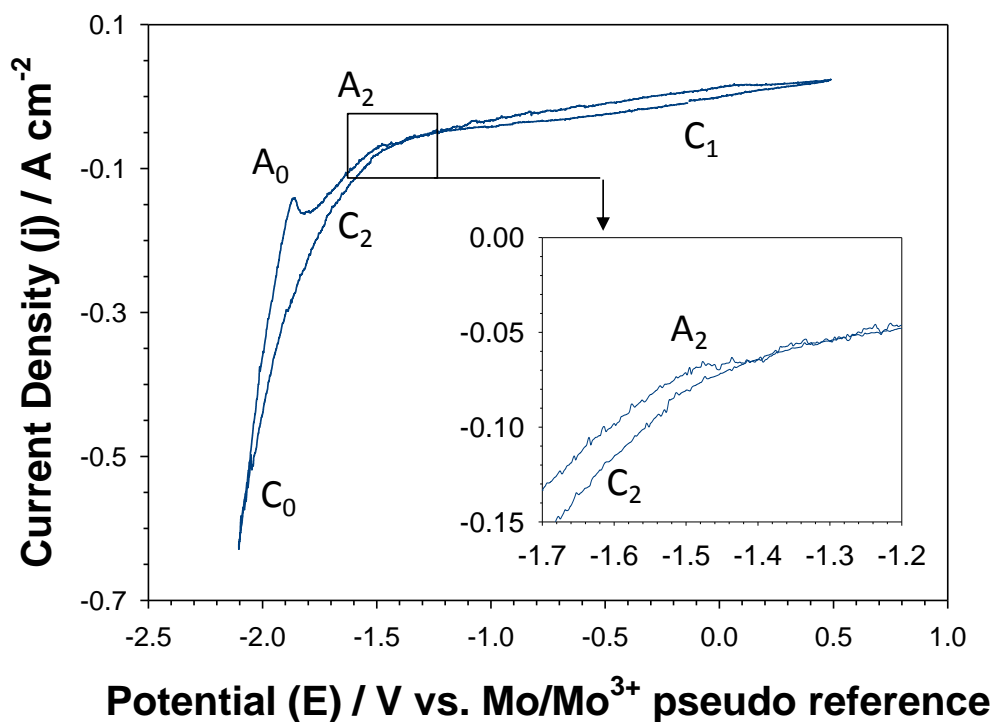
Figure 7.29 – PuO_2 CV recorded in $CaCl_2$ using a high integrity quartz cell. Inset shows the redox active region of the CV. Counter electrode: vitrious carbon, Reference electrode: Mo wire, scan rate: 20 mV s^{-1}.

$$C_0: \quad CaCl_2 + 2e^- = Ca + 2Cl^- \qquad \textbf{7.8}$$
$$(E^o_{810oC} = 0 \text{ V vs. } Ca/Ca^{2+})$$

$$C_1: \quad 2PuO_2 + 2e^- = Pu_2O_3 + O^{2-} \qquad \textbf{7.9a}$$
$$(E^o_{810oC} = +2.48 \text{ V vs. } Ca/Ca^{2+})$$

$$C_1: \quad 2PuO_2 + CaCl_2 + 2e^- = 2PuOCl + CaO + O^{2-} \qquad \textbf{7.9b}$$
$$(E^o_{810oC} = +2.56 \text{ V vs. } Ca/Ca^{2+})$$

$$C_2: \quad Pu_2O_3 + 6e^- = 2Pu + 3O^{2-} \qquad \textbf{7.10a}$$
$$(E^o_{810oC} = +0.86 \text{ V vs. } Ca/Ca^{2+})$$

$$C_2: \quad PuOCl + 3e^- = Pu + Cl^- + O^{2-} \qquad \textbf{7.10b}$$
$$(E^o_{810oC} = 0.66 \text{ V vs. } Ca/Ca^{2+})$$
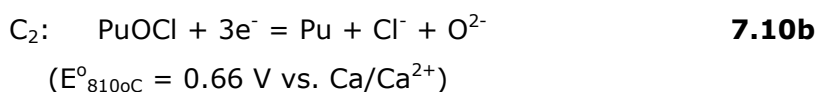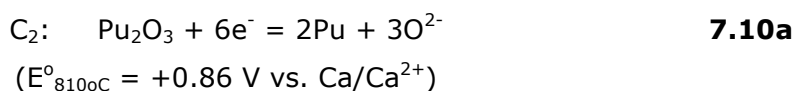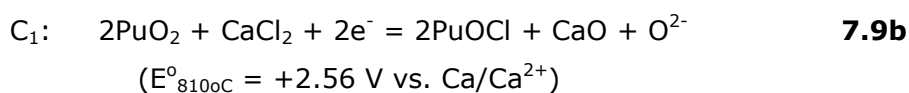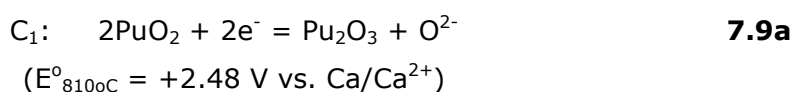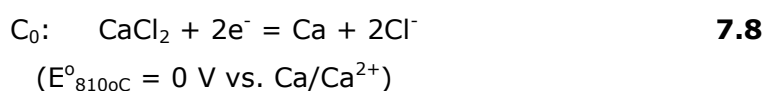
The uncertainty for reactions C_1 and C_2 derive from the variable nature of the CeO_2 analogue when investigated under the same conditions, where

the absolute oxygen activity determined the more favourable thermodynamic reduction pathway. However, given the lack of observable Ce_2O_3 in any of the CV investigations regardless of the potential applied, its likely the stable Pu(III) phase is the oxychloride (**Equation 7.9b**) and hence the C_2 reaction pertains to the oxychloride reduction (**Equation 7.10b**). The calculated standard potential for the reduction of PuOCl versus reduction of Pu_2O_3 (+657 mV vs. +861 mV) also supports a CeOCl reduction as no current peaks ~200 mV positive than C_2 in the CV exist and the +657mV vs. Ca/Ca^{2+} correlates near perfectly with the ca. -1.3 V vs. Mo/Mo^{3+} onset. Peak A_2 strongly imitates the stripping behaviour of Ce during CeO_2 in terms of positioning and appearance, and so its existence is also a key indicator that metallic Pu was produced during the short CV cathodic sweep. However, the presence of the Ca stripping peak (A_0) also means the applied cathodic limit was too negative to ascribe the formation Pu metal directly to an electrochemical process rather than a chemical one. This is considered further during the MOX investigation in the next section.

What is quite remarkable is the initial similarities between the CV curve produced for PuO_2 in this experiment, and those previously recorded for pure CeO_2 in the same media using identical parameters when corrected for current density and the internal Ca/Ca^{2+} redox pair (**Figure 7.30**).
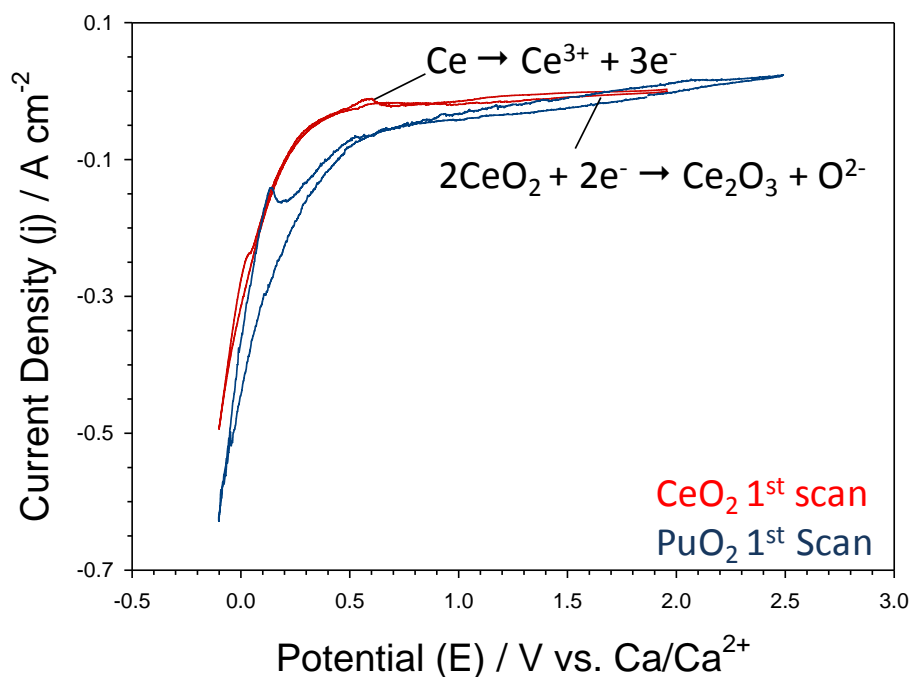
Figure 7.30 – CV curves of CeO_2 and PuO_2 recorded in $CaCl_2$ at 20 mV s^{-1} and standardised to the internal reference potential of Ca/Ca^{2+}.

The comparatively high degree of sloping exhibited by the PuO_2 CV is perhaps a direct consequence of the lack of electrochemical treatment performed on the salt (due to the restrictive working environment) and undoubtedly influences the apparent negative shift in current peak position. Indeed according to thermodynamics, PuO_2, Pu_2O_3 and $PuOCl$ are all fractionally easier to reduce than the Ce based counterparts, whereas the overlain plots show a near identical potential for each reduction and oxidation peaks.

Combining the predictive thermodynamics, the calculated reactions from predominance diagrams and the known electrochemical similarities between CeO_2 and PuO_2, it is reasonable to conclude that PuO_2 does indeed form an intermediate Pu(III) phase. Furthermore according to the transient CV analysis, aspects of material solubility are present given the redox developments in subsequent PuO_2 scans (i.e. lack of peak C_1, but maintenance of peak A_2.

Accordingly, owing the identical shapes of the current peaks, not only does PuO_2 possess the same reduction hierarchy as CeO_2, put apparently the mechanism of formation appears equally similar, which is logical given the identical phase structures and reducing environment. Maintaining plutonium in a stable form is a paramount concern of proliferation resistant and safe process. Earlier investigations on the distillation of plutonium containing alkali halide salts provided evidence that PuOCl was produced at high temperatures, but was stable enough with sufficiently low vapour pressure to be partitioned from the bulk salt[258]. Technologically this would be advantageous in implementing a salt recovery system and for process safety, particularly with the highlighted potential for PuOCl accumulation within the molten salt.

7.4.2. CV of 5% PuO_2 MOX in LCE

An attempt was made to replicate the successful CV investigations in the high integrity cell when using PuO_2 in the more complex system of a 5% PuO_2 MOX. Several advanced fast reactor designs use metallic U-Pu-Zr as a fuel source; hence the conversion of MOX generated via aqueous reprocessing potentially offers additional utility for pyroprocessing. In this instance it was deemed important to reconsider the lower melting point LCE electrolyte (at 600°C) as most viable pyro systems have criteria that mandate a modest temperature range, of which $CaCl_2$ fails to operate. An identical experimental set up was followed, using ultra-pure salts (>99.99% anhydrous LiCl, Sigma Aldrich), fixing the oxide loaded electrodes prior to filling the crucible with salt and using a Mo wire reference electrode. **Figure 7.31** gives the CV for the MOX loaded Mo working electrode, following a series of indentifying experiments to locate the potential of the cathodic limit and therefore avoid molten salt decomposition.
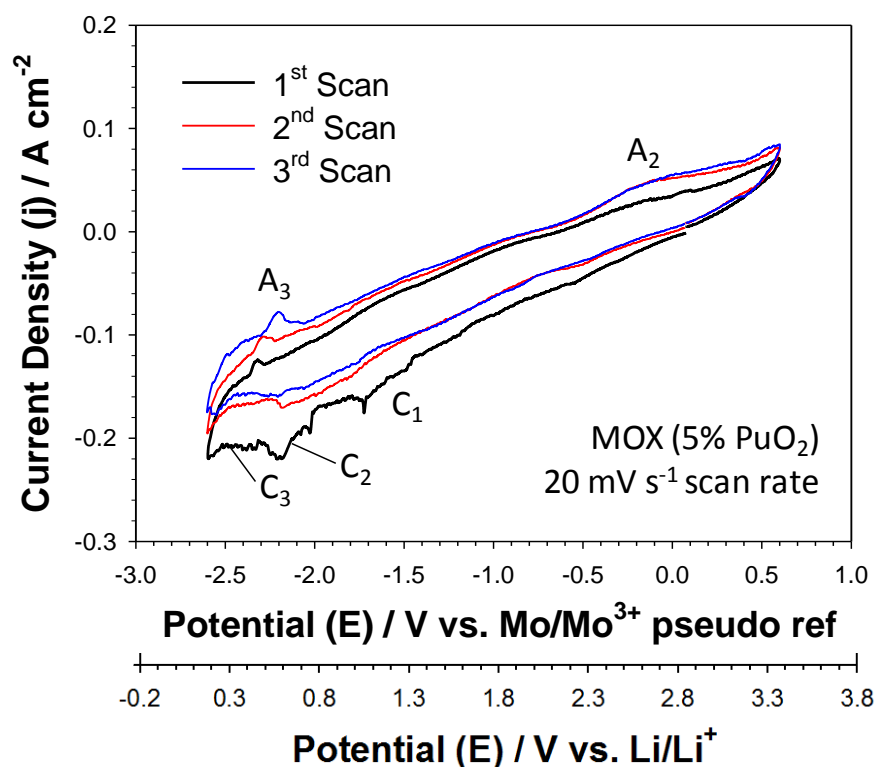
Figure 7.31 – Three-cycle CV for a 5% PuO_2 MOX fuel in LCE at 600°C. CE: vitreous carbon, RE: Mo wire, Fuel age: 2 years.

The pseudo-potential in this study had obviously shifted to a more negative standard when compared to the previous experiment using PuO_2 as caused by the drop in operational temperature. However the reference appeared stable between scans, showing only minor drift. Using the data from a CV in the same cell (taken with the blank working electrode), a second abscissa was created using the internal reference, experimentally shown to be Li/Li$^+$ dominated. It's worth noting that although the internal reference has been attributed to the Li dominated pathway, at 600°C the potential difference between the Li/Li$^+$ and Ca/Ca^{2+} redox pairs is only 53 mV, resulting in the co-reduction of both cations at anywhere from 0 to -0.53 mV vs. Li/Li^{2+}, or perhaps even more positive when accounting for aspects of underpotential deposition. The current response in the **Figure 7.31** CV is less well refined than those previously, showing some presence of interfacial capacitance, however redox peaks can be clearly identified using the calculated theoretical potentials for each peak and so be attributed to

those given reactions. From the age of the MOX fuel, (approximately 2 years) the presence of fission products generated in-situ should be only fractional and is reflected by the lack of significant current fluctuations during the CV. Consequently redox peaks can be confidently attributed to the main UO_2 and PuO_2 components. The largest peak (C_2) by absolute charge passed logically represents the bulk reaction occurring, which in this case would be for the direct reduction of UO_2 to U metal (**Equation 7.11**). According to the predominance diagrams and other works involving the reduction of UO_2, there are only very rare instances where intermediate ordered sub-oxides are created and the current response in this experiment confirms that a single four electron transfer is occurring to produce U metal[75,99].

$$C_2: \quad UO_2 + 4e^- = U + 2O^{2-}$$
$$(E^o{}_{600^oC} = +0.85 \text{ V vs. Li/Li}^+)$$

7.11
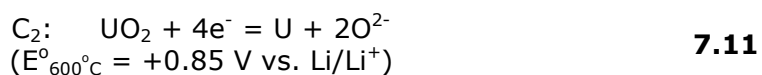
The predicted reduction potential for this reaction versus the internal Li/Li$^+$ redox pair is +0.85 V, which has excellent calibration with the onset of the C_2 peak. It would appear the electrochemical conversion of UO_2 is possible to yield metallic U in the LCE electrolyte, even at 600^oC and at the predicted thermodynamic values modest enough to avoid any electrolyte decomposition. As has been discovered however the transition from transient electroanalysis to bulk electrolysis often is not so straightforward, with the requirement for considerable overpotentials introducing poorer efficiencies, possibly lower yields and even some salt destabilisation. It is unfortunate that resources were not available to investigate these issues with the active materials tested, as great promise has been revealed with this initial proof of concept investigation. Although the current peaks appear to be the same scale on each plot, the CV scan of the MOX spent fuel has a much smaller current density than that shown in the pure PuO_2

which adequately accounts for the mass difference for the 5% PuO_2 MOX and pure PuO_2.

There is a small current increase more negative than the UO_2 reduction peak, labelled C_3 in **Figure 7.31**. Comparing this current peak to those of the PuO_2 CV scan (inclusive of the potential variations between electrolytes) the reductions are shown to be approximately identical in terms of reaction potentials. Additionally on the anodic sweep the counter reaction (A_3) is reminiscent in potential and shape for both CV investigations. These electrochemical similarities support the premise that the reactions taking place are the same, leading to the conclusion of a Pu(III) reduction to Pu^0 and its anodic dissolution into the melt. Again this is supported by the constant presence of the A_3 peak in each consecutive scan. The remaining reduction peak, C_1, possesses many of the features attributed for the initial PuO_2 reduction to its intermediate phase, including an early onset potential, broad and shallow profile and absence from the consecutive scans. The last clear redox peak, A_2, only appears on the second and third scans and was thought to be the oxidation of produced U metal, creating a reversible U/U^{3+} redox pair. Yet other CV works in various electrolytes and at a range of temperatures have described the oxidation of U metal occurring less than 500 mV positive of the initial reduction potential[35,102]. The position and scale of the current peak may be better described by the desorption of lithium ions taking place on the surface of the MOX electrode, which also accounts for some of the very slight current perturbations on the cathodic sweep not otherwise accounted for.

Compared to the implemented surrogacy systems, the reduction of UO_2 as the bulk component of the MOX powders is evidently much simpler and relatively easier to electro-deoxidise than both ZrO_2 and TiO_2. ZrO_2 and TiO_2 both exhibit various stages of intermittent suboxide and intercalated

phases which make their exact point of reduction relatively close to the CeO_2 analogue. The reduction of UO_2 however appears to be a well defined and separate reaction to the final Pu(III) reduction to Pu metal. Despite this, it follows that the outcome of applying a reduction potential to the MOX fuels at a value significant enough for UO_2 reduction but not a full reduction of PuO_2 would result in a similar empirical findings to the ZrO_2-CeO_2 experiment shown in **Figure 7.9** and $2NiO$-CeO_2 findings from **Figure 6.17**. Data gathered from these active CVs suggest Pu shares a chemical as well as electrochemical similarity to CeO_2, which is supported by the previously studied solubility of PuOCl in various molten salts, as an example[249]. As such the loss of Pu containing material will facilitate an improved kinetic approach to oxygen removal from the remaining UO_2 and, similar to the ZrO_2/TiO_2 analogue, favour the yield of a pure U product. The prospect of partitioning by selective reduction and anodic dissolution with these particular materials appears unattainable given the particular behaviour of $(Ce/Pu)O_2$, however more favourable counter oxides (shown with NiO) or probably other more predictable oxides could benefit from such a solid state partitioning process.

7.5. Conclusion

This chapter has explored in greater detail the prospect of spent fuel electrochemical treatment using the FFC Cambridge Process through a variety of analysis techniques, surrogates, operating conditions and even and initial assessment of active oxide materials. Advancement of the underlying feasibility outlined in Chapter 6 for the partial reduction and dissolution of a single component from a binary oxide matrix was attempted here, but with the more similar ZrO_2-CeO_2 spent fuel surrogates and then subsequently with TiO_2-CeO_2. In both of these examples an alternative partitioning method was inadvertently discovered, centred on

the instability of the CeO_2 intermediate reduction products formed as an unavoidable consequence of attempting to deoxidise the counterpart oxide.

The first section continued directly the work on $2NiO-CeO_2$ by applying the same principles replicated in molten $CaCl_2$ at 810^oC to ZrO_2-CeO_2. Here, ZrO_2 was characterised first by CV to establish potentials for redox activity, followed by analysis of the ZrO_2-CeO_2 binary where it was shown that no apparent alloying occurred. Despite this, the redox activity of ZrO_2 was noted as being far more complex than NiO, with the final reduction peak occurring approximately only 200mV more positive than that for CeO_2. Individual oxides were successfully bulk reduced in pellet form without the chemical assistance of electro-generated calcium metal.

Using a basket cathode, CeO_2 underwent direct electrolysis at 3.2 V for 15h, resulting in the recovery of a dense consolidated ingot of pure Ce, as identified by TGA-DSC and an indicator dissolution test in concentrated nitric acid. Reducing pure ZrO_2 proved much more difficult owing to a densification process on the pellet surface which prevented a full reduction throughout the pellet core. However the ZrO_2-CeO_2 binary, reduced at a voltage of 3.2 V provided amicable conditions to produce metallic phases of both species, including a phase separation based on the solid-liquid state of the metals at 810^oC. When the applied potential for the ZrO_2-CeO_2 binary was more precisely controlled using a three electrode cell, to a value directly for ZrO_2 (-1.85 V vs. Ag/AgCl), a near complete loss of Ce occurred thought to be due to the chemical dissolution of intermediate Ce(III) species into the molten salt. XRD results from potentiostatic electrolysis at less cathodic potentials showed Ca intercalation, pyrochlore co-oxide formation and $α-Zr_3O$, accompanying a colour shift from off-white to green to grey-blue. Each of these phases contribute to volume expansion which

was subsequently shown to inhibit further reduction inwards due to electrolyte exclusion.

SEM imaging also confirmed the loss of Ce from ZrO_2-CeO_2 pellets via the dissolution of Ce(III) phases and accompanied with CeOCl precipitation at higher oxygen activities (i.e. within the centre of the pellets tested).

The second section dealt with progressing the developed knowledge in what is effectively a very amenable electrolyte of $CaCl_2$ (owing to higher temperature and oxygen solubility) to a more feasible lower melting point eutectic of LiCl and $CaCl_2$. EIS at 570, 600 and $630^{o}C$ was performed with the produced Nyquist plot showing spectra similar to pure $CaCl_2$ at $810^{o}C$. Reconfirming the reference electrode stability and robustness came from blank CVs and highlighted both the performance of the alumina sealed Ag/AgCl reference and excellent potential window of the LCE electrolyte.

 TiO_2 was used in place of ZrO_2 in TiO_2-CeO_2 to better emulate conductivity characteristics of UO_2. Both oxides were scanned by CV, with features identical to those in $CaCl_2$ after accounting for the temperature derived potential shifts. Similarly TiO_2 could be compared very well to previous examples from the literature and suggested that despite the sacrifices in kinetic favourability, electrochemical reduction could still be accomplished in the lower temperature system. Confirmation of reduction characteristics and feasibility came from potentiostatic electrolysis experiments coupled with XRD, SEM and EDS, including an attempt at reducing a geometrically replicated clad fuel pin. The results suggest that head-end processing to create intelligently engineering preforms with small yet stable dimensions is necessary to encourage reduction. Recovery of reduced Ti (59% yield) was also accomplished in a unique experiment which encapsulated a partial reduction of TiO_2 and electrorefining to a solid electrode.

The final section helped to cement the validity of the various surrogate systems employed throughout this thesis by directly analysing pure PuO_2 and the binary MOX fuels. Given the difficulties of operation, CVs were produced which confirmed the excellent similarity between CeO_2 and PuO_2 in terms of both electrochemistry and apparently also in chemical behaviour within the molten $CaCl_2$ electrolyte. The MOX investigation also provided significant insight into the ability for an FFC based reduction of actinide oxides in a binary state, further implying a competency for the conversion of UO_2 to U and at relatively modest potentials at 600^oC. The lower melting point electrolyte may also benefit the production of metallic phases by preventing significant surface sintering and densification, a known precursor to reduction cessation. Overall the transient analysis strongly supports the capacity to at the very least provide an alternative pyrochemical scenario whereby a lower melting point electrolyte (compared to pure LiCl at 650^oC as per the ANL process) can achieve an electrochemical rather than metallothermic conversion of oxides to metals. Prospects for a considerable simplification by the use of a single electrolyte for both reduction and refining and omitting the use of a liquid electrode for speciation are also highlighted.

Chapter 8

Conclusions and Future Work

The concept of a novel FFC Cambridge Process based pyroprocessing technology for the conversion of oxide LWR fuels to metallic phases suitable for advanced reactors has been explored in this thesis.

Various factors pertaining to the ability to electro-deoxidise spent fuel surrogates were experimentally tested, including the fabrication processes, electrode designs, molten salt systems and electrolysis conditioning. The employed methodology followed a more holistic approach to experimentation, considering broader aspects of the desired pyroprocessing paradigm as much of the central work presented here was both unique and fundamentally necessary. A solid-state single-phase electrolytic partitioning of metal oxides was established on thermodynamically favourable materials, as analysed by ex-situ methods of SEM, EDS and XRD. Furthermore advancements of the current understanding of FFC based reduction were attempted by the measurements of electrolyte ionicity with implication for the wider electrochemistry field. Co-reduction of different binary oxide phases were shown possible both in the traditional FFC electrolyte; $CaCl_2$, and in the lower melting point LCE. The work overall provides a tangible contribution to spent nuclear fuel management as well as a broader service to electrochemical processing of oxides by molten salt electrolysis.

Some of the most important conclusions to be drawn from this work can be summarised as follows:

i.   The combination of a physical and an optimised electrochemical treatment for $CaCl_2$ resulted in stable potential windows for observing redox activity. Options to periodically recover salt from a semi- or fully continuous electrolytic cell were hypothesised in the context of actinide accumulation.

ii.   Feed oxides were individually analysed to gauge particle distribution and homogenisation by hand or by ball milling applied to binary oxides where large differences in morphology was identified. In head-end preparation, a route of careful processing is absolutely paramount in delivering suitable forms for successful electrolysis. Porosities in the range of 28-67% were delivered depending on the material(s) utilised, pressing method (cold pressing or slip cast) and sintering profile (temperature and duration).

iii. Sintering caused no chemical shift for any precursors besides the physical changes observed in TiO_2-CeO_2 as analysed by XPS, possibly due to a CeO_2 assisted formation of TiO_{2+x}. Laminations of thick (>3mm) pellets were almost always observed regardless of diameter by the explored methods here and while it may be possible to produce thicker forms, the effects on electroreduction are undesirable.

iv.   Manipulation of electronic field lines within the molten $CaCl_2$ electrolyte by decreasing electrolyte mass and reducing crucible geometry was shown effective in improving ionicity, demonstrably more favourable for CV analysis. The mechanism behind current efficiency issues in molten salt electrolysis was also further elucidated and refined from the literature using EIS to calculate electronic conductivity and CV on pure ZrO_2 and Cr_2O_3. Practical

solutions theoretically derived were experimentally shown to be successful in improving favoured charge appropriation.

v. A successful attempt was made at the selective partitioning of Ni from $2NiO\text{-}CeO_2$ in a three electrode cell at potentials carefully defined by CV work, coinciding with the fabrication of a stable high temperature Ag/AgCl reference electrode. The lanthanide CeO_2 was thoroughly examined as a direct analogue to PuO_2, where discrete chemical and electrochemical behaviours were observed under specific conditions (applied potential, sample purity, temperature). CeOCl was a frequent observation at intermediate potentials, with implication towards the ability to maintain a constant flow sheet of PuO_2 within the system. 85% Ni removal from a 100mg pellet was achieved following just 60 minutes of electrolysis.

vi. Partitioning was investigated on more appropriate spent fuel surrogates of $ZrO_2\text{-}CeO_2$ and $TiO_2\text{-}CeO_2$, with the former species of each binary emulating the electrochemical and conductive characteristics respectively of UO_2. The previous electrochemical route could was not possible due to the partial reduction of CeO_2 destabilising the binary oxide, however separation was still possible through either co-reduction, where liquid Ce coalesced below the metallic Zr, or a solubilisation of Ce intermediates at modest potentials and durations. LCE used for $TiO_2\text{-}CeO_2$ work proved to be an excellent medium for electroreduction and indeed electrorefining, being capable of a 59% recovery of pure Ti from the binary oxide in a single cell and simple procedure.

vii. Active works with both PuO_2 and a 5% PuO_2 MOX fuel were accomplished by the use of a bespoke high integrity quartz cell in a

negative pressure glove box. CV revealed superb coordination with thermodynamic predictions, given the accurate surrogate system of CeO_2 and PuO_2. UO_2 was apparently much easier to reduce than either ZrO_2 or TiO_2 given the single step reduction mechanism.

Although initially successful, the first iteration of the partial direct reduction and selective anodic dissolution procedure could not be successfully applied to the ZrO_2-CeO_2 or the TiO_2-CeO_2 systems owing to the unavoidable formation of Ce(III) species. Subsequent work however showed that metallisation of ZrO_2 or TiO_2 could be achieved with simultaneous Ce loss. From the apparent similarities between surrogates tested here and active materials, three key recommendations are provided for future work:

1) Perform the specific reduction methodology employed for the bulk ZrO_2-CeO_2 pellets to larger scale MOX forms, where it may be possible to either produce a consolidated metallic form (if attempted in the lower temperature LCE melt) or a pure U product by the dissolution of Pu partial reduction products into the melt.

2) Extend further the reach of the pyroprocessing approach considered here, by assessing the specific behaviour of other TRU's, FPs and MAs from the reduction of spent fuel. This could be coupled with an application of the head-end processing knowledge accrued via research on the pelletisation behaviour as a means of optimisation.

3) Apply the concept of molten salt assisted selective recovery of various metallic species from composite oxides to fields outside of nuclear waste management. As highlighted, the prospect of an intrinsically simple, economic, safe and solid state based partitioning of contaminated oxides could be incredibly useful as a means of purification.

References

1. *United Nations, Department of Economic and Social Affairs, Population Division*. *World Population Prospects: The 2015 Revision, Key Findings and Advance Tables.* **Working Pa,** (2015).

2. IEA. World Energy Outlook 2013. *Paris Int. Energy Agency* 1–7 (2013).

3. Kharecha, P. A. & Hansen, J. E. Prevented mortality and greenhouse gas emissions from historical and projected nuclear power. *Environ. Sci. Technol.* **47,** 4889–4895 (2013).

4. IPCC. Climate Change 2014 Synthesis Report. *Contrib. Work. Groups I, II III to Fifth Assess. Rep. Intergov. Panel Clim. Chang.* 1–151 (2014).

5. Brook, B. W. & Bradshaw, C. J. A. Key role for nuclear energy in global biodiversity conservation. *Conserv. Biol.* **29,** 1–11 (2015).

6. Hong, S., Bradshaw, C. J. A. & Brook, B. W. Global zero-carbon energy pathways using viable mixes of nuclear and renewables. *Appl. Energy* **143,** 451–459 (2015).

7. Poinssot, C. *et al.* Assessment of the environmental footprint of nuclear energy systems. Comparison between closed and open fuel cycles. *Energy* **69,** 199–211 (2014).

8. Gauthier-Lafaye, F., Holliger, P. & Blanc, P. L. Natural fission reactors in the Franceville basin, Gabon: A review of the conditions and results of a 'critical event' in a geologic system. *Geochim. Cosmochim. Acta* **60,** 4831–4852 (1996).

9. Fujii, Y. *et al.* The nuclear interaction at Oklo 2 billion years ago. *Nucl. Phys. B* **573,** 377–401 (2000).

10. Hu, Z. & Gao, S. Upper crustal abundances of trace elements: A revision and update. *Chem. Geol.* **253,** 205–221 (2008).

11. Uranium Mining Overview. *World Nuclear Association* (2016).

12. Glaser, A. Characteristics of the Gas Centrifuge for Uranium Enrichment and Their Relevance for Nuclear Weapon Proliferation. *Sci. Glob. Secur.* **16,** 1–25 (2008).

13. Higashi, K. & Miyamoto, Y. Taperization of Step Cascade for Uranium Enrichment by Gaseous Diffussion Process. *J. Nucl. Sci. Technol.* **13,** 30–34 (1976).

14. Nuclear Power Economics | Nuclear Energy Costs. *World Nuclear Assocaition* (2016).

15. Poinssot, C., Boullis, B. & Bourg, S. in *Reprocessing and Recycling of Spent Nuclear Fuel* 27–48 (2015).

16. Reference data Series No. 2, 2015 Edition: Nuclear Power Reactors in the World. *Int. At. Energy Agency* 1–86 (2015).

17. Nuclear Fuel Fabrication. *World Nuclear Assocaition* (2015).

18. Eloirdi, R., Ho Mer Lin, D., Mayer, K., Caciuffo, R. & Fanghänel, T. Investigation of ammonium diuranate calcination with high-temperature X-ray diffraction. *J. Mater. Sci.* **49,** 8436–8443 (2014).

19. Mellah, A., Chegrouche, S. & Barkat, M. The precipitation of ammonium uranyl carbonate (AUC): Thermodynamic and kinetic investigations. *Hydrometallurgy* **85,** 163–171 (2007).

20. Nuclear Fuel Cycle Information System - A Directory of Nuclear Fuel Cycle Facilities 2009 Edition. *IAEA, VIENNA, 2009* (2009).

21. Degueldre, C., Bertsch, J., Kuri, G. & Martin, M. Nuclear fuel in generation II and III reactors: research issues related to high burn-up. *Energy Environ. Sci.* **4,** 1651 (2011).

22. Rusov, V. D. *et al.* Ultraslow Wave Nuclear Burning of Uranium-Plutonium Fissile Medium on Epithermal Neutrons. *Prog. Nucl. Energy* **83,** 105–122 (2015).

23. Bohr, N. & Wheeler, J. A. The Mechanism of Nuclear Fission. *Phys. Rev.* **56,** 426–450 (1939).

24. Xu, Z., Kazimi, M. S. & Driscoll, M. J. Impact of High Burnup on PWR Spent Fuel Characteristics. *Nucl. Sci. Eng.* **151,** 261–273 (2005).

25. Radioactive Waste Management. *World Nuclear Association* (2015).

26. Feiveson, H., Mian, Z., Ramana, M. & Hippel, F. Von. *Managing spent fuel from nuclear power reactors: Experience and lessons from around the world*. *Report of the International Panel on Fissile Material* (2011).

27. Stages of the Nuclear Fuel Cycle. *United States Nuclear Regulatory Commission* (2014).

28. Burrows, C., Phillips, C. & Milliken, A. The Thermal Oxide Reprocessing Plant at Sellafield – Lessons Learned from 10 Years of Hot Operations and their Applicability to the DOE Environmental Management Program. *WM'06 Conf. Febr. 26-March 2, 2006, Tuscan, Arizona* (2006).

29. Yu-xing, Y. *et al.* Extraction of actinides from simulated HLLW by DHDECMP-TBP/OK. *J. Radioanal. Nucl. Chem.* **261,** 365–374 (2004).

30. Laidler, J. J., Battles, J. E., Miller, W. E., Ackerman, J. P. & Carls, E. L. Development of pyroprocessing technology. *Prog. Nucl. Energy* **31,** 131–140 (1997).

31. Hannum, W. H., Wade, D. C., McFarlane, H. F. & Hill, R. N. Nonproliferation and safeguards aspects of the IFR. *Prog. Nucl. Energy* **31,** 203–217 (1997).

32. Kolarik, Z., Müllich, U. & Gassner, F. Selective Extraction of Am(III) Over Eu(III) by 2,6-Ditriazoly- and 2,6-Ditriazinlypyridines1. *Solvent Extr. Ion Exch.* **17,** 23–32 (1999).

33. Narbutt, J. & Oziminski, W. P. Selectivity of bis-triazinyl bipyridine ligands for americium(III) in Am/Eu separation by solvent extraction. Part 1. Quantum mechanical study on the structures of BTBP complexes and on the energy of the separation. *Dalton Trans.* **41,**

14416–24 (2012).

34. Chang, Y. I. The Integral Fast Reactor. *Nucl. Technol.* **88,** 129–138 (1989).

35. Sakamura, Y., Kurata, M. & Inoue, T. Electrochemical Reduction of UO_2 in Molten $CaCl_2$ or LiCl. *J. Electrochem. Soc.* **153,** D31 (2006).

36. Nawada, H. P. & Fukuda, K. Role of pyro-chemical processes in advanced fuel cycles. *J. Phys. Chem. Solids* **66,** 647–651 (2005).

37. Koch, L. Minor actinide transmutation—a waste management option. *J. Less Common Met.* **122,** 371–382 (1986).

38. Asou, M. *et al.* A modular recycling plant concept, flexible to future fuel cycle demands. *Int. Conf. Futur. Nucl. Syst. Chall. Towar. Second Nucl. era with Adv. fuel cycles. Proceedings.* (1997).

39. Kormilitzyn, M. V. *et al.* Pyro-electrochemical reprocessing of irradiated MOX fast reactor fuel, testing of the reprocessing process with direct MOX fuel production. *Proc. Int. Conf. Atalante* 6–12 (2000).

40. Vavilov, S., Kobayashi, T. & Myochin, M. Principle and Test Experience of the RIAR ' s Oxide Pyro-Process. *J. Nucl. Sci. Technol.* **41,** 1018–1025 (2004).

41. Bychkov, A. V., Skiba, O. V., Vavilov, S. K., Kormilitzyn, M. V. & Osipenco, A. G. Overview of R.I.A.R. activity on pyro process development and application to oxide fuel and plans in the coming decade. *Proc. Work. Pyrochemical Sep. Avignon, Fr. 14-16 March 2000* 37 (2001).

42. Montuir, M. *et al.* Sensitivity of Americium and Curium Splitting Flowsheet and Running Procedure. *Procedia Chem.* **7,** 275–281 (2012).

43. Inoue, T. Actinide recycling by pyro-process with metal fuel FBR for future nuclear fuel cycle system. *Prog. Nucl. Energy* **40,** 547–554

(2002).

44. Usami, T. *et al.* Pyrochemical reduction of uranium dioxide and plutonium dioxide by lithium metal. *J. Nucl. Mater.* **300,** 15–26 (2002).

45. Koyama, T. *Nuclear engineering for pyrochemical treatment of spent nuclear fuels*. *Advanced Separation Techniques for Nuclear Fuel Reprocessing and Radioactive Waste Treatment* (Elsevier, 2011).

46. Kinoshita, K., Koyama, T., Inoue, T., Ougier, M. & Glatz, J.-P. Separation of actinides from rare earth elements by means of molten salt electrorefining with anodic dissolution of U–Pu–Zr alloy fuel. *J. Phys. Chem. Solids* **66,** 619–624 (2005).

47. Kato, T., Iizuka, M., Inoue, T., Iwai, T. & Arai, Y. Distillation of cadmium from uranium–plutonium–cadmium alloy. *J. Nucl. Mater.* **340,** 259–265 (2005).

48. Murty, K. L. L. & Charit, I. Structural materials for Gen-IV nuclear reactors: Challenges and opportunities. *J. Nucl. Mater.* **383,** 189–195 (2008).

49. Corwin, W. R. U.S. Generation IV Reactor Integrated Materials Technology Program. *Nucl. Eng. Technol.* **38,** 591–618 (2006).

50. Allen, T. R., Busby, J. T., Klueh, R. L., Maloy, S. A. & Toloczko, M. B. Cladding and duct materials for advanced nuclear recycle reactors. *JOM* **60,** 15–23 (2008).

51. McKetta, J. J. & Cunningham, W. A. *Encyclopedia of chemical processing and design, Volume 39*. (M. Dekker, 1992).

52. Takeuchi, M., Kato, T., Hanada, K., Koizumi, T. & Aose, S. Corrosion resistance of ceramic materials in pyrochemical reprocessing condition by using molten salt for spent nuclear oxide fuel. *J. Phys. Chem. Solids* **66,** 521–525 (2005).

53. Richerson, D. W., Richerson, D. W. & Lee, W. E. *Modern Ceramic*

Engineering: Properties, Processing, and Use in Design, Third Edition. **4,** (CRC Press, 2005).

54. Davis, J. *ASM Specialty Handbook: Nickel, Cobalt, and Their Alloys*. *ASM International* (2000).

55. Odette, G. R., Alinger, M. J. & Wirth, B. D. Recent Developments in Irradiation-Resistant Steels. *Annu. Rev. Mater. Res.* **38,** 471–503 (2008).

56. Mansur, L. K. Kinetic theory of radiation effects. *No. CONF-870178-1. Oak Ridge Natl. Lab., TN* (1987).

57. Volkert, C. A. Stress and plastic flow in silicon during amorphization by ion bombardment. *J. Appl. Phys.* **70,** 3521 (1991).

58. Wirth, B. D. Materials science. How does radiation damage materials? *Science* **318,** 923–4 (2007).

59. Odette, G. R., Maziasz, P. J. & Spitznagel, J. A. Fission-fusion correlations for swelling and microstructure in stainless steels: Effect of the helium to displacement per atom ratio. *J. Nucl. Mater.* **104,** 1289–1303 (1981).

60. Stoller, R. & Odette, G. *Radiation-Induced Changes in Microstructure: 13th International Symposium (Part I)*. (ASTM International, 1987).

61. Sun, C. *et al.* Superior radiation-resistant nanoengineered austenitic 304L stainless steel for applications in extreme radiation environments. *Sci. Rep.* **5,** 7801 (2015).

62. Wang, L. M., Dodd, R. A. & Kulcinski, G. L. Gas effects on void formation in 14 MeV nickel ion irradiated pure nickel. *J. Nucl. Mater.* **141-143,** 713–717 (1986).

63. Mitchell, M. A. & Garner, F. A. Neutron-induced swelling of binary Ni-Al alloys. *J. Nucl. Mater.* **187,** 103–108 (1992).

64. Kolotushkin, V. P. & Votinov, S. N. Structural factor and effects of

low-temperature radiation damage in structural materials. *Met. Sci. Heat Treat.* **48,** 452–458 (2006).

65.   Carter, G. & Nobes, M. J. A phenomenological model of ion-induced crystallization and amorphization. *J. Mater. Res.* **6,** 2103–2108 (2011).

66.   Krefft, G. B. & EerNisse, E. P. Volume expansion and annealing compaction of ion-bombarded single-crystal and polycrystalline α-Al_2O_3. *J. Appl. Phys.* **49,** 2725 (1978).

67.   Zinkle, S. J. Effect of irradiation spectrum on the microstructural evolution in ceramic insulators. *J. Nucl. Mater.* **219,** 113–127 (1995).

68.   Nakamura, R., Ishimaru, M., Yasuda, H. & Nakajima, H. Atomic rearrangements in amorphous Al_2O_3 under electron-beam irradiation. *J. Appl. Phys.* **113,** 064312 (2013).

69.   Forsberg, C. W. *Molten Salt Reactors (MSRs): Coupling Spent Fuel Processing and Actinide Burning*. (Advances in Nuclear Fuel Management III, American Nuclear Society, Hilton Head, South Carolina, 2003).

70.   Ha, S. H., Menchavez, R. N. & Koo, Y.-M. Reprocessing of spent nuclear waste using ionic liquids. *Korean J. Chem. Eng.* **27,** 1360–1365 (2010).

71.   Salanne, M., Simon, C., Turq, P. & Madden, P. A. Calculation of Activities of Ions in Molten Salts with Potential Application to the Pyroprocessing of Nuclear Waste. *J. Phys. Chem.* **2008,** 1177–1183 (2008).

72.   Mohandas, K. S. Direct electrochemical conversion of metal oxides to metal by molten salt electrolysis: a review. *Miner. Process. Extr. Metall.* **122,** 195–212 (2013).

73.   Venkatesh, A. *et al.* Modeling the Anodic Behavior of U, Zr, and U-Zr

Alloy in Molten LiCl-KCl Eutectic. *Nucl. Technol.* **182,** 98–110 (2013).

74. Williams, A. N., Phongikaroon, S. & Simpson, M. F. Separation of CsCl from a ternary CsCl–LiCl–KCl salt via a melt crystallization technique for pyroprocessing waste minimization. *Chem. Eng. Sci.* **89,** 258–263 (2013).

75. Brown, L. D. *et al.* Predominance diagrams of uranium and plutonum species in both lithium chloride–potassium chloride eutectic and calcium chloride. *J. Appl. Electrochem.* **43,** 1235–1241 (2013).

76. Hur, J.-M., Hong, S.-S. & Lee, H. Electrochemical reduction of UO_2 to U in a LiCl–KCl-Li_2O molten salt. *J. Radioanal. Nucl. Chem.* **295,** 851–854 (2012).

77. Mahendran, K. H., Nagaraj, S., Sridharan, R. & Gnanasekaran, T. Differential scanning calorimetric studies on the phase diagram of the binary LiCl–$CaCl_2$ system. *J. Alloys Compd.* **325,** 78–83 (2001).

78. Grube, G. & Rudel, W. Double Salt Formation in the Solid State in the System LiCl-$CaCl_2$. *z. Anorg. u. Allgem. Chern.* **133,** 375–388 (1924).

79. Janz, G. J. *Molten Salts Handbook*. (Elsevier, 2013).

80. Choi, E.-Y. *et al.* Effect of the UO_2 form on the electrochemical reduction rate in a LiCl–Li_2O molten salt. *J. Nucl. Mater.* **437,** 178–187 (2013).

81. Schwandt, C. & Fray, D. Determination of the kinetic pathway in the electrochemical reduction of titanium dioxide in molten calcium chloride. *Electrochim. Acta* **51,** 66–76 (2005).

82. Schwandt, C. & Fray, D. The electrochemical reduction of chromium sesquioxide in molten calcium chloride under cathodic potential control. *Zeitschrift für Naturforsch. A* **62,** 655–670 (2007).

83. Mohandas, K. S. & Fray, D. J. Electrochemical Deoxidation of Solid Zirconium Dioxide in Molten Calcium Chloride. *Metall. Mater. Trans.*

B **40,** 685–699 (2009).

84. Herrmann, S. & Li, S. Electrolytic reduction of spent nuclear oxide fuel as part of an integral process to separate and recover actinides from fission products. *Sep. Sci. Technol.* **41,** 1965–1983 (2006).

85. Sakamura, Y. & Omori, T. Electrolytic reduction and electrorefining of uranium to develop pyrochemical reprocessing of oxide fuels. *Nucl. Technol.* **171,** 266–275 (2010).

86. Barnes, L. & Williamson, M. Developments in Electrolytic Reduction: Effect of Rare Earth Oxides. *2nd Int. Pyroprocessing Res. Conf.* (2008).

87. Schwandt, C., Doughty, G. & Fray, D. The FFC-Cambridge process for titanium metal winning. *Key Eng. Mater.* **436,** 13–25 (2010).

88. Park, S., Park, B. & Jeong, S. Characteristics of an integrated cathode assembly for the electrolytic reduction of uranium oxide in a LiCl-Li$_2$O molten salt. *J. Radioanal. Nucl. Chem.* **268,** 489–495 (2006).

89. Park, B., Lee, H., Choung, W., Hur, J. & Seo, C. Development of an electrochemical reduction process in ACPF. *2008 Int. Pyroprocessing Res. Conf.* (2008).

90. Park, W. *et al.* An experimental study for Li recycling in an electrolytic reduction process for UO$_2$ with a Li$_2$O–LiCl molten salt. *J. Nucl. Mater.* **441,** 232–239 (2013).

91. Benedict, R. W. W. *et al.* Pyroprocessing progress at Idaho National Laboratory. *Adv. Nucl. Fuel Cycles Syst. Glob. 2007* INL/CON–07–12983 (2007).

92. Chen, G. & Fray, D. Cathodic refining in molten salts: Removal of oxygen, sulfur and selenium from static and flowing molten copper. *J. Appl. Electrochem.* **31,** 155–164 (2001).

93. Li, Z., Guo, J., Hu, R., Ru, L. & Wang, H. Carbon Anode for the

Formation of Carbon Monoxide and its Impact on the Molten-salt Electrolysis. *Asian J. Chem.* **26,** 2565–2570 (2014).

94. Li, W., Jin, X., Huang, F. & Chen, G. Z. Metal-to-Oxide Molar Volume Ratio: The Overlooked Barrier to Solid-State Electroreduction and a 'Green' Bypass through Recyclable NH_4HCO_3. *Angew. Chemie Int. Ed.* **49,** 3203–3206 (2010).

95. Chen, G. Z., Fray, D. J. & Farthing, T. W. Cathodic deoxygenation of the alpha case on titanium and alloys in molten calcium chloride. *Metall. Mater. Trans. B* **32,** 1041–1052 (2001).

96. Chen, H., Jin, X., Yu, L. & Chen, G. Z. Influences of graphite anode area on electrolysis of solid metal oxides in molten salts. *J. Solid State Electrochem.* **18,** 3317–3325 (2014).

97. Kilby, K. T., Jiao, S. & Fray, D. J. Current efficiency studies for graphite and SnO_2-based anodes for the electro-deoxidation of metal oxides. *Electrochim. Acta* **55,** 7126–7133 (2010).

98. Mohandas, K. & Fray, D. Novel electrochemical measurements on direct electro-deoxidation of solid TiO_2 and ZrO_2 in molten calcium chloride medium. *J. Appl. Electrochem.* **41,** 321–336 (2011).

99. Vishnu, D. S. M. *et al.* Mechanism of Direct Electrochemical Reduction of Solid UO_2 to Uranium Metal in $CaCl_2$-48mol% NaCl Melt. *J. Electrochem. Soc.* **160,** 394–402 (2013).

100. Sri Maha Vishnu, D. *et al.* Factors Influencing the Direct Electrochemical Reduction of UO_2 Pellets to Uranium Metal in $CaCl_2$-48 mol% NaCl Melt. *J. Electrochem. Soc.* **160,** 583–592 (2013).

101. Sri Maha Vishnu, D., Sure, J. & Mohandas, K. S. Corrosion of high density graphite anodes during direct electrochemical de-oxidation of solid oxides in molten $CaCl_2$ medium. *Carbon N. Y.* **93,** 782–792 (2015).

102. Joseph, T. B., Sanil, N., Mohandas, K. S. & Nagarajan, K. A Study of

Graphite as Anode in the Electro-Deoxidation of Solid UO_2 in LiCl-Li_2O Melt. *J. Electrochem. Soc.* **162,** 51–58 (2015).

103. Jeong, S. M. *et al.* Electrochemical reduction behavior of U_3O_8 powder in a LiCl molten salt. *Electrochim. Acta* **55,** 1749–1755 (2010).

104. Sakamura, Y., Omori, T. & Inoue, T. Application of Electrochemical Reduction to Produce Metal Fuel Material from Actinide Oxides. *Nucl. Technol.* **162,** 169–178 (2008).

105. Jeong, S. M., Shin, H.-S., Cho, S.-H., Hur, J.-M. & Lee, H. S. Electrochemical behavior of a platinum anode for reduction of uranium oxide in a LiCl molten salt. *Electrochim. Acta* **54,** 6335–6340 (2009).

106. Choi, E.-Y. *et al.* Electrochemical reduction of UO_2 in LiCl–Li_2O molten salt using porous and nonporous anode shrouds. *J. Nucl. Mater.* **444,** 261–269 (2014).

107. Yin, H. *et al.* On the development of metallic inert anode for molten $CaCl_2$–CaO System. *Electrochim. Acta* **56,** 3296–3302 (2011).

108. Kim, S.-W. *et al.* Electrochemical behavior of liquid Sb anode system for electrolytic reduction of UO_2. *J. Radioanal. Nucl. Chem.* **303,** 1041–1046 (2015).

109. Burheim, O. & Haarberg, G. M. Effects of inert anodes in the FFC Cambridge reduction of hematite. *Miner. Process. Extr. Metall.* **119,** 77–81 (2010).

110. Barnett, R., Kilby, K. T. & Fray, D. J. Reduction of Tantalum Pentoxide Using Graphite and Tin-Oxide-Based Anodes via the FFC-Cambridge Process. *Metall. Mater. Trans. B* **40,** 150–157 (2009).

111. Iwahara, H., Esaka, T. & Mangahara, T. Mixed conduction and oxygen permeation in the substituted oxides for $CaTiO_3$. *J. Appl. Electrochem.* **18,** 173–177 (1988).

112. Jiao, S. & Fray, D. J. Development of an Inert Anode for Electrowinning in Calcium Chloride–Calcium Oxide Melts. *Metall. Mater. Trans. B* **41,** 74–79 (2009).

113. Kim, S.-W., Choi, E.-Y., Park, W., Im, H. S. & Hur, J.-M. A conductive oxide as an O_2 evolution anode for the electrolytic reduction of metal oxides. *Electrochem. commun.* **55,** 14–17 (2015).

114. Ward, R. G. & Hoar, T. P. The Electrolytic Removal of Oxygen, Sulphur, Selenium, and Tellurium from Molten Copper. *J. Inst. Met.* **90,** 6–12 (1961).

115. Chen, G., Fray, D. & Farthing, T. Direct electrochemical reduction of titanium dioxide to titanium in molten calcium chloride. *Nature* **407,** 361–4 (2000).

116. Fray, D., Farthing, T. & Chen, Z. Removal of substances from metal and semi-metal compounds. *US Pat. 7,790,014* (2010).

117. Chen, G., Fray, D. & Farthing, T. Metal and alloy powders and powder fabrication. *World Patent 2* (2002).

118. Fray, D. J., Copcutt, R. C. & Chen, G. Z. Treating a solid precursor material comprising three or more species, including first and second metals or metalloids (M1, Z) and a non-metal species (X), by electro-deoxidation in contact with a melt comprising a fused salt (M2Y). (2008).

119. Fray, D. J., Schwandt, C. & Doughty, G. R. Electrochemical method and apparatus. (2005).

120. Outokumpu Research & Oy. HSC Chemistry v6.1. (2015).

121. Chen, G. Z., Gordo, E. & Fray, D. J. Direct electrolytic preparation of chromium powder. *Metall. Mater. Trans. B* **35,** 223–233 (2004).

122. Okabe, T. H., Nakamura, M., Oishi, T. & Ono, K. Electrochemical deoxidation of titanium. *Metall. Trans. B* **24,** 449–455 (1993).

123. Okabe, T. H., Deura, T. N., Oishi, T., Ono, K. & Sadoway, D. R.

Electrochemical deoxidation of yttrium-oxygen solid solutions. *J. Alloys Compd.* **237,** 150–154 (1996).

124. Suzuki, R. O., Aizawa, M. & Ono, K. Calcium-deoxidation of niobium and titanium in Ca-saturated CaCl$_2$ molten salt. *J. Alloys Compd.* **288,** 173–182 (1999).

125. Ono, K. & Suzuki, R. O. A new concept for producing Ti sponge: Calciothermic reduction. *JOM* **54,** 59–61 (2002).

126. Suzuki, R. O. Calciothermic reduction of TiO$_2$ and in situ electrolysis of CaO in the molten CaCl$_2$. *J. Phys. Chem. Solids* **66,** 461–465 (2005).

127. Suzuki, R., Ono, K. & Teranuma, K. Calciothermic reduction of titanium oxide and in-situ electrolysis in molten CaCl$_2$. *Metall. Mater. Trans. B* **34,** 287–295 (2003).

128. Ono, K. Fundamental aspects of calciothermic process to produce titanium. *Mater. Trans.* **45,** 1660–1664 (2004).

129. Suzuki, R., Tatemoto, K. & Kitagawa, H. Direct synthesis of the hydrogen storage V–Ti alloy powder from the oxides by calcium co-reduction. *J. Alloys Compd.* **385,** 173–180 (2004).

130. Baba, M., Ono, Y. & Suzuki, R. Tantalum and niobium powder preparation from their oxides by calciothermic reduction in the molten CaCl$_2$. *J. Phys. Chem. Solids* **66,** 466–470 (2005).

131. Ueda, I., Baba, M., Kikuchi, T. & Suzuki, R. O. Formation of niobium powder by electrolysis in molten salt. *Electrochim. Acta* **100,** 269–274 (2013).

132. Descallar-Arriesgado, R. F., Kobayashi, N., Kikuchi, T. & Suzuki, R. O. Calciothermic reduction of NiO by molten salt electrolysis of CaO in CaCl$_2$ melt. *Electrochim. Acta* **56,** 8422–8429 (2011).

133. Kikuchi, T. *et al.* Rapid reduction of titanium dioxide nano-particles by reduction with a calcium reductant. *J. Phys. Chem. Solids* **75,**

1041–1048 (2014).

134. Suzuki, R. O. Direct reduction processes for titanium oxide in molten salt. *JOM* **59,** 68–71 (2007).

135. Wang, D., Qiu, G., Jin, X., Hu, X. & Chen, G. Electrochemical metallization of solid terbium oxide. *Angew. Chemie Int. Ed.* **45,** 2384–2388 (2006).

136. Chen, G. Z. & Fray, D. J. Voltammetric Studies of the Oxygen-Titanium Binary System in Molten Calcium Chloride. *J. Electrochem. Soc.* **149,** E455 (2002).

137. Dring, K., Dashwood, R. & Inman, D. Predominance Diagrams for Electrochemical Reduction of Titanium Oxides in Molten $CaCl_2$. *J. Electrochem. Soc.* **152,** 184 (2005).

138. Yan, X. Y. & Fray, D. J. Fused salt electrolytic reduction of solid oxides and oxide mixtures for green production of metals and alloys. *Miner. Process. Extr. Metall.* **116,** 17–24 (2007).

139. Li, G., Wang, D., Jin, X. & Chen, G. Electrolysis of solid MoS_2 in molten $CaCl_2$ for Mo extraction without CO_2 emission. *Electrochem. commun.* **9,** 1951–1957 (2007).

140. Abdelkader, A. M., Hyslop, D. J. S., Cox, A. & Fray, D. J. Electrochemical synthesis and characterization of a NdCo5 permanent magnet. *J. Mater. Chem.* **20,** 6039 (2010).

141. Stevenson, A., Hu, D. & Chen, G. Z. Molten Salt Assisted Electrochemical Separation of Spent Fuel Surrogates by Partial Direct Reduction and Selective Anodic Dissolution. *ECS Trans.* **64,** 333–350 (2014).

142. Zou, X. Y., Xie, H. W., Zhai, Y. C. & Lang, X. C. Direct Deoxidation of $ZrOCl_2$ Powder to Zirconium With Non-Sintering. *Adv. Mater. Res.* **146-147,** 775–779 (2010).

143. Zhu, Y. *et al.* Electrolytic reduction of mixed solid oxides in molten

salts for energy efficient production of the TiNi alloy. *Chinese Sci. Bull.* **51,** 2535–2540 (2006).

144. Abdelkader, A. M. & Fray, D. J. Direct electrochemical preparation of Nb–10Hf–1Ti alloy. *Electrochim. Acta* **55,** 2924–2931 (2010).

145. Bhagat, R., Jackson, M., Inman, D. & Dashwood, R. Production of Ti–W Alloys from Mixed Oxide Precursors via the FFC Cambridge Process. *J. Electrochem. Soc.* **156,** E1 (2009).

146. Littlewood, R. Diagrammatic Representation of the Thermodynamics of Metal-Fused Chloride Systems. *J. Electrochem. Soc.* **109,** 525 (1962).

147. Dring, K., Dashwood, R. & Inman, D. Voltammetry of Titanium Dioxide in Molten Calcium Chloride at 900°C. *J. Electrochem. …* **152,** 104 (2005).

148. Bhagat, R. *et al.* In situ synchrotron diffraction of the electrochemical reduction pathway of TiO_2. *Acta Mater.* **58,** 5057–5062 (2010).

149. Alexander, D. T. L., Schwandt, C. & Fray, D. J. The electro-deoxidation of dense titanium dioxide precursors in molten calcium chloride giving a new reaction pathway. *Electrochim. Acta* **56,** 3286–3295 (2011).

150. Jain, A. *et al.* Commentary: The Materials Project: A materials genome approach to accelerating materials innovation. *APL Mater.* **1,** 011002 (2013).

151. Jiang, K. *et al.* 'Perovskitization'-Assisted Electrochemical Reduction of Solid TiO_2 in Molten $CaCl_2$. *Angew. Chemie Int. Ed.* **45,** 428–432 (2006).

152. Xiao, W., Jin, X., Deng, Y., Wang, D. & Chen, G. Z. Rationalisation and optimisation of solid state electro-reduction of SiO_2 to Si in molten $CaCl_2$ in accordance with dynamic three-phase interlines based voltammetry. *J. Electroanal. Chem.* **639,** 130–140 (2010).

153. Centeno-Sánchez, R. L., Fray, D. J. & Chen, G. Z. Study on the reduction of highly porous TiO_2 precursors and thin TiO_2 layers by the FFC-Cambridge process. *J. Mater. Sci.* **42,** 7494–7501 (2007).

154. Gordo, E., Chen, G. Z. & Fray, D. J. Toward optimisation of electrolytic reduction of solid chromium oxide to chromium powder in molten chloride salts. *Electrochim. Acta* **49,** 2195–2208 (2004).

155. Chen, G. Z. & Fray, D. J. A morphological study of the FFC chromium and titanium powders. *Miner. Process. Extr. Metall.* **115,** 49–54 (2006).

156. Shannon, R. D. Revised effective ionic radii and systematic studies of interatomic distances in halides and chalcogenides. *Acta Crystallogr. Sect. A* **32,** 751–767 (1976).

157. Nohira, T., Yasuda, K. & Ito, Y. Pinpoint and bulk electrochemical reduction of insulating silicon dioxide to silicon. *Nat. Mater.* **2,** 397–401 (2003).

158. Xiao, W. & Wang, D. The electrochemical reduction processes of solid compounds in high temperature molten salts. *Chem. Soc. Rev.* **43,** 3215–28 (2014).

159. Xiao, W. *et al.* Electrochemically Driven Three-Phase Interlines into Insulator Compounds: Electroreduction of Solid SiO_2 in Molten $CaCl_2$. *ChemPhysChem* **7,** 1750–8 (2006).

160. Qiu, G. *et al.* Metallic Cavity Electrodes for Investigation of Powders. *J. Electrochem. Soc.* **152,** E328 (2005).

161. Xiao, W., Jin, X., Deng, Y., Wang, D. & Chen, G. Z. Three-phase interlines electrochemically driven into insulator compounds: a penetration model and its verification by electroreduction of solid AgCl. *Chemistry* **13,** 604–12 (2007).

162. Basin, A. S., Kaplun, A. B., Meshalkin, A. B. & Uvarov, N. F. The LiCl-KCl binary system. *Russ. J. Inorg. Chem.* **53,** 1509–1511 (2008).

163. Brown, L. D. *et al.* Following the electroreduction of uranium dioxide to uranium in LiCl–KCl eutectic in situ using synchrotron radiation. *J. Nucl. Mater.* **464,** 256–262 (2015).

164. Vishnu, D., Sanil, N. & Murugesan, N. Determination of the extent of reduction of dense UO_2 cathodes from direct electrochemical reduction studies in molten chloride medium. *J. Nucl. Mater.* **427,** 200–208 (2012).

165. Kurata, M., Inoue, T., Serp, J., Ougier, M. & Glatz, J.-P. Electro-chemical reduction of MOX in LiCl. *J. Nucl. Mater.* **328,** 97–102 (2004).

166. Choi, E.-Y. *et al.* Electrochemical reduction behavior of a highly porous SIMFUEL particle in a LiCl molten salt. *Chem. Eng. J.* **207-208,** 514–520 (2012).

167. Choi, E.-Y. *et al.* Electrochemical reduction of porous 17kg uranium oxide pellets by selection of an optimal cathode/anode surface area ratio. *J. Nucl. Mater.* **418,** 87–92 (2011).

168. Park, G. & Lee, J. Effect of impurities on the microstructure of DUPIC fuel pellets using the SIMFUEL technique. *Nucl. Eng. Technol.* **40,** 191–198 (2008).

169. Iizuka, M., Akagi, M. & Koyama, T. High-temperature distillation and consolidation of U–Zr cathode product from molten salt electrorefining of simulated metallic fuel. *J. Nucl. Mater.* **448,** 259–269 (2014).

170. Kim, G.-Y. *et al.* A study on the electrochemical deposition behavior of uranium ion in a LiCl–KCl molten salt on solid and liquid electrode. *J. Electroanal. Chem.* **682,** 128–135 (2012).

171. Jafarian, M., Gobal, F., Danaee, I. & Mahjani, M. Impedance spectroscopy study of aluminum electrocrystallization from basic molten salt ($AlCl_3$–NaCl–KCl). *Electrochim. Acta* **52,** 5437–5443

(2007).

172. Wang, C. S. *et al.* Electrochemical separation of uranium and cerium in molten LiCl–KCl. *J. Radioanal. Nucl. Chem.* **298,** 581–586 (2013).

173. Souček, P. *et al.* Separation of actinides from irradiated An–Zr based fuel by electrorefining on solid aluminium cathodes in molten LiCl–KCl. *J. Nucl. Mater.* **459,** 114–121 (2015).

174. Glatz, J.-P. *et al. Development of Pyrochemical Separation Processes for Recovery of Actinides from Spent Nuclear Fuel in Molten LiCl-KCl, Molten Salt Chemistry from lab to applications*. *Molten Salts Chemistry* (Elsevier, 2013).

175. Shaplygin, I. S. & Lazarev, V. B. Calcium-platinum oxide Ca_4PtO_6 - growth problems and polymorphism. *Mater. Res. Bull.* **10,** 903–908 (1975).

176. Turrillas, X., Laviron, C., Vincent, H., Pannetier, J. & Joubert, J. C. Synthesis and characterization of a new calcium platinum oxide: $Ca_2Pt_3O_8$. *J. Solid State Chem.* **67,** 297–307 (1987).

177. Wang, H., Siambun, N., Yu, L. & Chen, G. A robust alumina membrane reference electrode for high temperature molten salts. *J. Electrochem. …* **159,** 740–746 (2012).

178. Menge, O. Die binären Systeme von MgCl2 und $CaCl_2$ mit den Chloriden der Metalle K, Na, Ag, Pb, Cu', Zn, Sn "und Cd. *Zeitschrift für Anorg. Chemie* **72,** 162–218 (1911).

179. Kolman, D., Park, Y. & Stan, M. An assessment of the validity of cerium oxide as a surrogate for plutonium oxide gallium removal studies. *LANL* **US1999,** (1999).

180. Bard, A., Faulkner, L., Leddy, J. & Zoski, C. *Electrochemical methods: fundamentals and applications*. (Wiley, 1980).

181. Albery, W., Chen, Z. & Horrocks, B. Spectroscopic and electrochemical studies of charge transfer in modified electrodes.

Faraday Discuss. Chem. Soc. **88,** 247–259 (1989).

182. Brockie, N. Applications of Liquid Cathode Electrochemistry Towards the Nuclear Industry. (University of Edinburgh, 2011).

183. Orazem, M. E. & Tribollet, B. *Electrochemical Impedance Spectroscopy*. (John Wiley & Sons, 2011).

184. Norman, J. Van & Tivers, R. A Study of HCl in the LiCl-KCl Eutectic. *J. Electrochem. Soc.* **118,** 258–259 (1971).

185. Ault, B. & Andrews, L. Salt-molecule matrix reactions. Infrared spectra of the $M^+ HCl^{2-}$ and $M^+ Cl^{3-}$ ion pairs in solid argon. *J. Am. Chem. Soc.* **97,** 3824–3826 (1975).

186. Evans, J. & Lo, G. Vibrational Spectra of the Cl^{3-} Ion and Evidence for the Existence of Cl^{5-}. *J. Chem. Phys.* **44,** 3638–3639 (1966).

187. Chen, G. & Fray, D. Understanding the electro-reduction of metal oxides in molten salts. *Light Met.* **TMS 2004,** 881–886 (2004).

188. Seidell, A. *Solubilities of inorganic and metal organic compounds*. (Norstrand, 1940).

189. Al-Najjar, H. & Al-Sammerrai, D. Thermogravimetric determination of the heat of vaporization of some highly polar solvents. *J. Chem. Technol. Biotechnol.* **37,** 145–152 (1987).

190. Jackson, B., Jackson, M. & Dye, D. Production of NiTi via the FFC Cambridge process. *J. Electrochem. Soc.* **155,** 171–177 (2008).

191. Dring, K., Bhagat, R., Jackson, M., Dashwood, R. & Inman, D. Direct electrochemical production of Ti–10W alloys from mixed oxide preform precursors. *J. Alloys Compd.* **419,** 103–109 (2006).

192. Bhagat, R., Jackson, M., Inman, D. & Dashwood, R. The Production of Ti–Mo Alloys from Mixed Oxide Precursors via the FFC Cambridge Process. *J. Electrochem. Soc.* **155,** E1 (2008).

193. Peng, J., Jiang, K., Xiao, W. & Wang, D. Electrochemical Conversion of Oxide Precursors to Consolidated Zr and Zr–2.5Nb Tubes. *Chem.*

Mater. **20,** 7274–7280 (2008).

194. Hyslop, D., Abdelkader, A., Cox, A. & Fray, D. Electrochemical
      synthesis of a biomedically important Co–Cr alloy. *Acta Mater.* **58,**
      3124–3130 (2010).

195. Orr, R., Sims, H. & Taylor, R. A review of plutonium oxalate
      decomposition reactions and effects of decomposition temperature
      on the surface area of the plutonium dioxide product. *J. Nucl. Mater.*
      465, 756–773 (2015).

196. Jubin, R. Spent Fuel Reprocessing. *Introduction to Nuclear Chemistry
      and Fuel Cycle Separations Course, Consortium for Risk Evaluation
      With Stakeholder Participation* (2008).

197. Guérard, D. Ball milling in the presence of a fluid: results and
      perspectives. *Rev. Adv. Mater. Sci* **18,** 225–230 (2008).

198. Gauthier, M. *Engineered materials handbook*. (ASM International,
      1995).

199. Czanderna, A., Rao, C. & Honig, J. The anatase-rutile transition. Part
      1.—Kinetics of the transformation of pure anatase. *Trans. Faraday
      Soc.* **54,** 1069–1073 (1958).

200. Balachandran, U. & Eror, N. G. Electrical conductivity in non-
      stoichiometric titanium dioxide at elevated temperatures. *J. Mater.
      Sci.* **23,** 2676–2682 (1988).

201. Lu, Y., Hirohashi, M. & Sato, K. Thermoelectric Properties of Non-
      Stoichiometric Titanium Dioxide TiO_{2-x} Fabricated by Reduction
      Treatment Using Carbon Powder. *Mater. Trans.* **47,** 1449–1452
      (2006).

202. Guo, J., Janik, M. J. & Song, C. Density Functional Theory Study on
      the Role of Ceria Addition in $Ti_xCe_{1-x}O_2$ Adsorbents for Thiophene
      Adsorption. *J. Phys. Chem. C* **116,** 3457–3466 (2012).

203. Aronson, S., Rulli, J. & Schaner, B. Electrical properties of

nonstoichiometric uranium dioxide. *J. Chem. Phys.* **35,** 1382–1388 (1961).

204. Scanlon, D. O. *et al.* Band alignment of rutile and anatase TiO_2. *Nat. Mater.* **12,** 798–801 (2013).

205. Peabody, C. M. & Doto, P. C. Production of ceramic grade plutonium dioxide. *Am. Nucl. Soc. Meet. New Orleans, Louisiana, USA* **7,** 17 (1975).

206. Haarberg, G., Osen, K., Thonstad, J., Heus, R. & Egan, J. Electronic conduction in molten cryolite saturated with alumina. in *No. BNL-43723; CONF-9005235--3. Brookhaven National Lab., Upton, NY (USA)* (1990).

207. Haarberg, G., Osen, K. & Thonstad, J. Measurement of electronic conduction in cryolite alumina melts and estimation of its effect on current efficiency. *Metall. Trans. B* **24,** 729–735 (1993).

208. Ma, M. *et al.* Extraction of titanium from different titania precursors by the FFC Cambridge process. *J. Alloys Compd.* **420,** 37–45 (2006).

209. Lu, H., Jia, W., Xu, C., Liao, C. & Huan, H. Study on Improving the Current Efficiency of the Direct Reduction of Titanium Dioxde to Titanium. *Light Met. 2005 as held 134 th TMS Annu. Meet.* 1145–1148 (2005).

210. Stöhr, U. & Freyland, W. Electrochemical impedance investigations of redox mechanisms of refractory metal compounds in molten salts. I. Niobium chloride and oxychloride in CsCl–NaCl. *Electrochim. Acta* **44,** 2199–2207 (1999).

211. Terakado, O., Poh, P. & Freyland, W. Electron Spin Resonance Study of Electron Localization and Dynamics in Metal–Molten Salt Solutions: Comparison of $M–M_X$ and $Ln–Ln_{X3}$ Melts (M= Alkali Metal, Ln= Rare Earth Metal, X= Halogen. *J. Phys. Condens. Matter* **15,** 1553 (2003).

212. Logan, D. & Siringo, F. Disordered Madelung potentials and the electronic structure of ionic liquid alloys with application to Csy (CsAu) 1-y. *J. Phys. Condens. Matter* **4,** 3695 (1992).

213. Koslowski, T. Refractory Metals in Molten Salts: Theory and Simulation of Geometry, Electronic Structure, and Electron Transport. *J. Chem. Phys.* **113,** 10703–10711 (2000).

214. Parrinello, M. & Rahman, A. Study of an F center in molten KCl. *J. Chem. Phys.* **80,** 860 (1984).

215. Koslowski, T. & Logan, D. Electronic structure of liquid charge-transfer alloys: a numerical study. *J. Phys. Chem.* **98,** 9146–9152 (1994).

216. Bronstein, H. & Bredig, M. The Electrical Conductivity of Solutions of Alkali Metals in their Molten Halides. *J. Am. Chem. Soc.* **80,** 2077–2081 (1958).

217. Stöhr, U. & Freyland, W. Intervalence charge transfer and electronic transport in molten salts containing tantalum and niobium complexes of mixed valency. *Phys. Chem. Chem. Phys.* **1,** 4383–4387 (1999).

218. Dosaj, V., Aksaranan, C. & Morris, D. R. Thermodynamic properties of the calcium + calcium chloride system measured by an electrochemical technique. *J. Chem. Soc. Faraday Trans. 1 Phys. Chem. Condens. Phases* **71,** 1083 (1975).

219. Corrigan, D. K., Blair, E. O., Terry, J. G., Walton, A. J. & Mount, A. R. Enhanced electroanalysis in lithium potassium eutectic (LKE) using microfabricated square microelectrodes. *Anal. Chem.* **86,** 11342–8 (2014).

220. Lee, K.-R., Lee, J.-H. & Yoo, H.-I. Reassessment of conventional polarization technique to measure partial electronic conductivity of electrolytes. *Solid State Ionics* **181,** 724–729 (2010).

221. Riess, I. Review of the limitation of the Hebb-Wagner polarization

method for measuring partial conductivities in mixed ionic electronic conductors. *Solid State Ionics* **91,** 221–232 (1996).

222. Zein El Abedin, S., Terakado, O., Endres, F., Nattland, D. & Freyland, W. Intervalence charge transfer in mixed valence neodymium iodide melts: Electronic conductivity and optical absorption spectra. *Phys. Chem. Chem. Phys.* **4,** 5335–5339 (2002).

223. Selloni, A., Carnevali, P., Car, R. & Parrinello, M. Localization, hopping, and diffusion of electrons in molten salts. *Phys. Rev. Lett.* **59,** 823–826 (1987).

224. Freyland, W., Garbade, K. & Pfeiffer, E. Optical Study of Electron Localization Approaching a Polarization Catastrophe in Liquid K_x-KCl_{1-x}. *Phys. Rev. Lett.* **51,** 1304–1306 (1983).

225. Rollet, A., Salanne, M. & Groult, H. Structural effects on the electrical conductivity of molten fluorides: Comparison between $LiF-YF_3$ and $LiF-NaF-ZrF_4$. *J. Fluor. Chem.* **134,** 44–48 (2012).

226. Dworkin, A. S., Bronstein, H. R. & Bredig, M. A. Ionic melts as solvents for electronic conductors. *Discuss. Faraday Soc.* **32,** 188 (1961).

227. Peng, J. *et al.* Cyclic Voltammetry of ZrO_2 Powder in the Metallic Cavity Electrode in Molten $CaCl_2$. *J. Electrochem. Soc.* **157,** 1 (2010).

228. Qiu, G. *et al.* Roles of Cationic and Elemental Calcium in the Electro-Reduction of Solid Metal Oxides in Molten Calcium Chloride. *Zeitschrift für Naturforsch. A* **62,** 292–302 (2007).

229. Jeong, S., Jung, J., Seo, C. & Park, S. Characteristics of an electrochemical reduction of Ta_2O_5 for the preparation of metallic tantalum in a $LiCl-Li_2O$ molten salt. *J. Alloys Compd.* **440,** 210–215 (2007).

230. Wang, S., Haarberg, G. & Kvalheim, E. Electrochemical Behavior of

Dissolved Fe_2O_3 in Molten $CaCl_2$-KF. *J. Iron Steel Res. Int.* **15,** 48–51 (2008).

231. Barnett, R. & Fray, D. Electro-deoxidation of Ta_2O_5 in calcium chloride–calcium oxide melts. *J. Mater. Sci.* **49,** 4148–4160 (2014).

232. Wagner, C. The determination of small deviations from the ideal stoichiometric composition of ionic crystals and other binary compounds. *Prog. Solid State Chem.* **6,** 1–15 (1971).

233. Schwandt, C., Alexander, D. & Fray, D. The electro-deoxidation of porous titanium dioxide precursors in molten calcium chloride under cathodic potential control. *Electrochim. Acta* **15,** 3819–3829 (2009).

234. Schwandt, C. Understanding the electro-deoxidation of titanium dioxide to titanium metal via the FFC-Cambridge process. *Miner. Process. Extr. Metall.* **122,** 213–218 (2014).

235. Caravaca, C. *et al.* Solubilization studies of rare earth oxides and oxo halides, application of electrochemical techniques in pyrochemical processes. *6th Exch. Meet. Molud, Spain* 625 (2000).

236. Mohandas, K. & Fray, D. FFC Cambridge process and removal of oxygen from metal-oxygen systems by molten salt electrolysis: an overview. *Trans. Indian Inst. Met* **57,** 579–592 (2004).

237. Neumann, J. P., Zhong, T. & Chang, Y. A. The Ni−O (Nickel-Oxygen) system. *Bull. Alloy Phase Diagrams* **5,** 141–144 (1984).

238. Pilling, N. . & Bedworth, R. . The oxidation of metals at high temperatures. *J. Inst. Met.* **29,** 529–582 (1923).

239. Zhang, Y. *et al.* Preparation of $CeNi_2$ intermetallic compound by direct electroreduction of solid CeO_2-2NiO in molten LiCl. *J. Rare Earths* **30,** 923–927 (2012).

240. Claux, B., Serp, J. & Fouletier, J. Electrochemical reduction of cerium oxide into metal. *Electrochim. Acta* **56,** 2771–2780 (2011).

241. Zhao, B., Wang, L., Dai, L. & Cui, G. Direct electrolytic preparation of

cerium/nickel hydrogen storage alloy powder in molten salt. *J. Alloys Compd.* **468,** 379–385 (2009).

242. Zhao, B., Lu, X., Zhong, Q., Li, C. & Chen, S. Direct electrochemical preparation of $CeNi_5$ and $La_xCe_{1-x}Ni_5$ alloys from mixed oxides by SOM process. *Electrochim. Acta* **55,** 2996–3001 (2010).

243. Maher, R. C. *et al.* Reduction Dynamics of Doped Ceria, Nickel Oxide, and Cermet Composites Probed Using In Situ Raman Spectroscopy. *Adv. Sci.* **3,** 1–8 (2015).

244. Okamoto, H. Ce-Ni (Cerium-Nickel). *J. Phase Equilibria Diffus.* **26,** 397 (2005).

245. Kępiński, L. & Okal, J. Occurrence and Mechanism of Formation of CeOCl in Pd/CeO2 Catalysts. *J. Catal.* **192,** 48–53 (2000).

246. Castrillejo, Y., Bermejo, M. R. R., Pardo, R. & Martínez, A. M. M. Use of electrochemical techniques for the study of solubilization processes of cerium–oxide compounds and recovery of the metal from molten chlorides. *J. Electroanal. Chem.* **522,** 124–140 (2002).

247. Ogawa, T. & Minato, K. Dissolution and formation of nuclear materials in molten media. *Pure Appl. Chem.* **73,** 799–806 (2001).

248. Roth, R. S., Negas, T. & Cook, L. P. *Phase Diagrams for Ceramists*. (American Chemical Society, 1978).

249. Lambertin, D. & Ched'homme, S. Plutonium chemical properties in NaCl–KCl and $CaCl_2$ at 1073K. *J. Nucl. Mater.* **341,** 124–130 (2005).

250. Ghosh, S. & Vandarkuzhali, S. Redox behaviour of cerium oxychloride in molten $MgCl_2$–NaCl–KCl eutectic. *Electrochim. Acta* **52,** 1206–1212 (2006).

251. Peterson, D. E. & Foltyn, E. M. The Pu-U (Plutonium-Uranium) system. *Bull. Alloy Phase Diagrams* **10,** 160–164 (1989).

252. Richard, N. & Bernard, S. Phase transitions in cerium by pseudopotential methods. *J. Alloys Compd.* **323-324,** 628–631

(2001).

253. Cadien, A. *et al.* First-order liquid-liquid phase transition in cerium. *Phys. Rev. Lett.* **110,** 125503 (2013).

254. Khanna, A. *Introduction to high temperature oxidation and corrosion*. (ASM International, 2002).

255. Yemel'Yanov, V. S. & Yevstyukhin, A. I. *The Metallurgy of Nuclear Fuel: Properties and Principles of the Technology of Uranium, Thorium and Plutonium*. (Elsevier, 2013).

256. Hu, D. Near-Net-Shape Electrochemical Metallisation of Oxide Precursors into Ti-6Al-4V Products in Molten $CaCl_2$. (University of Nottingham, 2011).

257. Olander, D. R. Nuclear Fuels: Present and Future. *Eng. J.* **13,** 1–28 (2009).

258. Seitz, M. G. in *Nuclear Materials Safety Management* (eds. Peddicord, K. L., Lazarev, L. N. & Jardine, L. J.) 65–68 (Kluwer Academic Publishers, 1998).
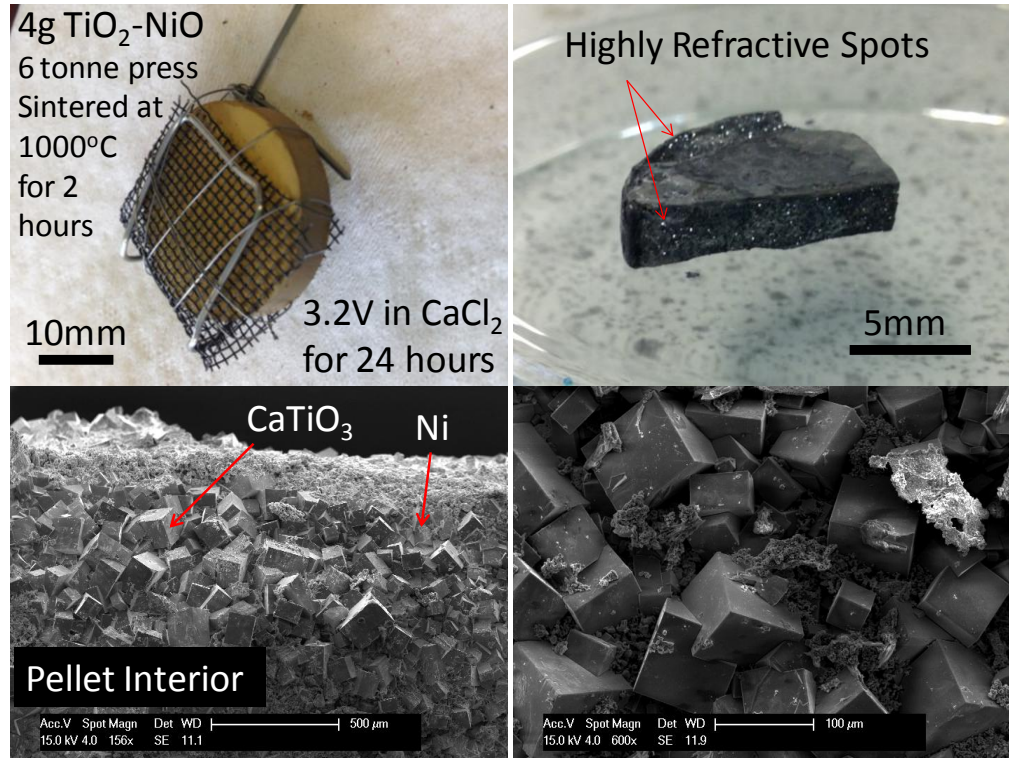
Appendix A – Miscellaneous Reduction Studies

1. TiO_2-NiO

Figure A-1 – Pelletised TiO_2-NiO electrode before and after constant voltage electrolysis in $CaCl_2$ for 24h at 3.2V (850^oC), with accompanying SEM image showing highly ordered and highly refractive cubic morphology of formed $CaTiO_3$.
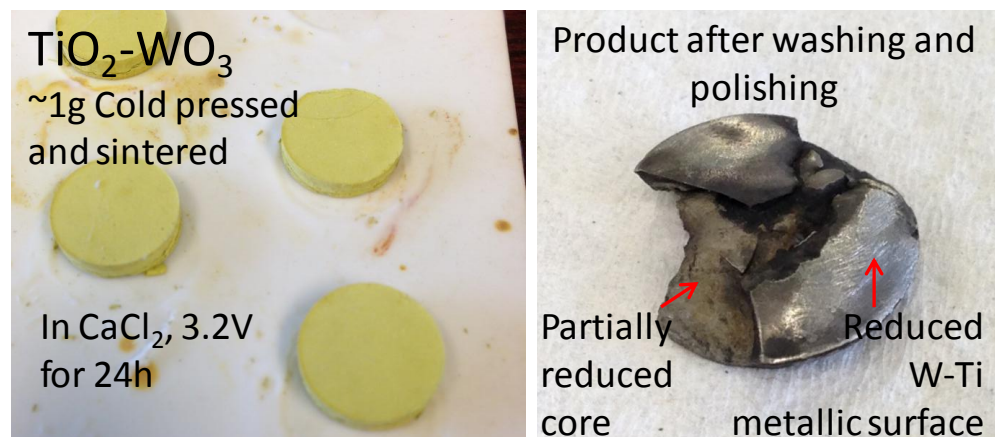
2. TiO_2-WO_3

Figure A-2 – TiO_2-WO_3 pressed and sintered pellets with a reduced Ti-W 'superalloy' product.

3. Ti-6Al-4V Alloy

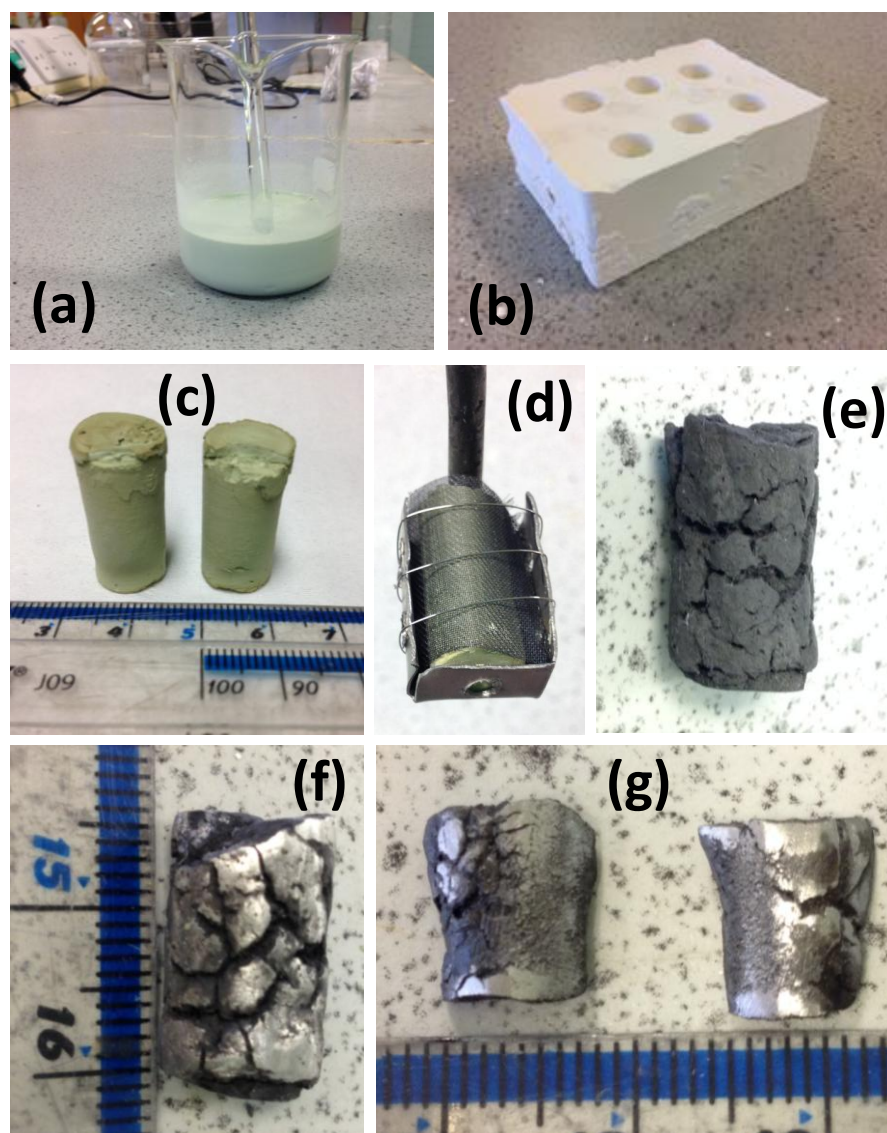**Figure A-3** – (a) TiO$_2$-Al$_2$O$_3$-V$_2$O$_3$ slurry created via mixed oxide powders with water sunder ultrasonification. (b) CaSO$_4$ mould for creating slip case rods (shown in (c)). (d) Electrode assembly using a custom Ti basket to yield (e) the reduction product and (f) and (g) after light polishing.

Appendix B –Inert Anode Test

Investigations of a viable oxygen evolving inert anode for use in molten salt electrolysis, based on the utility of doped perovskite phases.
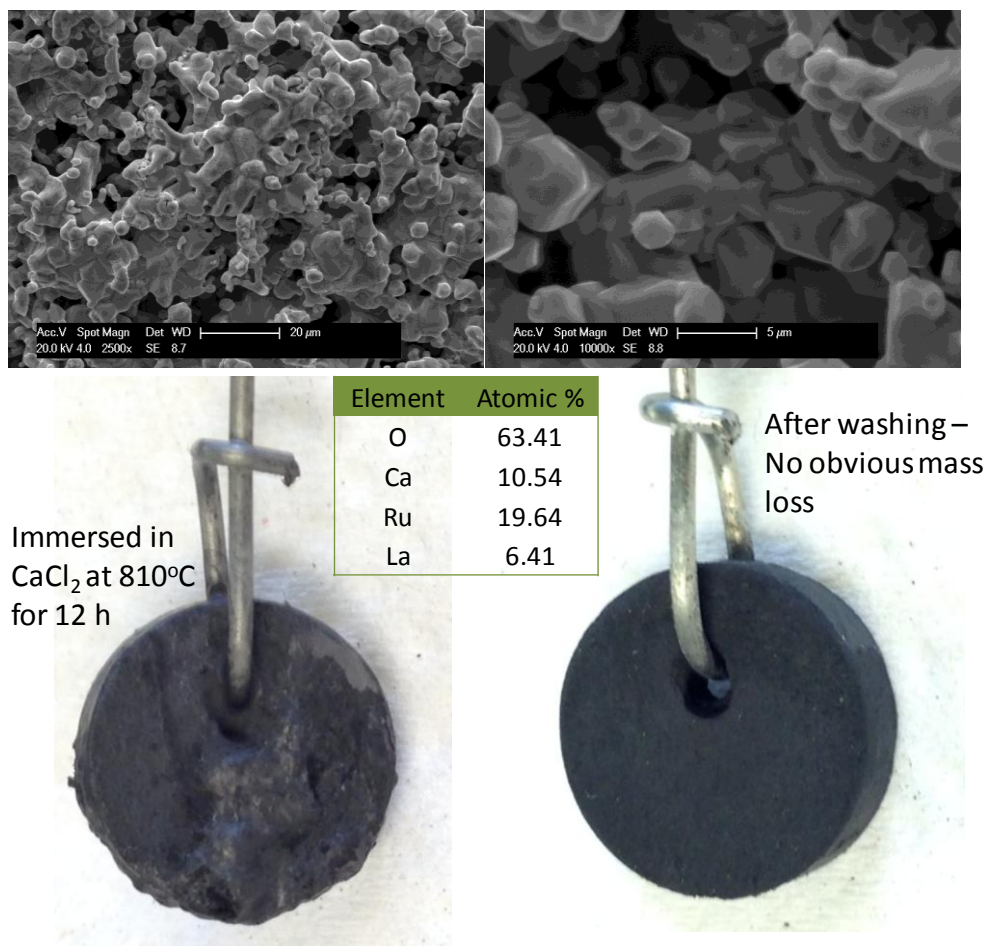
Sintered at 1400°C for 12 hours

Element	Atomic %
O	63.41
Ca	10.54
Ru	19.64
La	6.41

Immersed in CaCl$_2$ at 810°C for 12 h

After washing – No obvious mass loss

Figure B-1 – SEM images of the sintered bespoke La$_{0.33}$Ca$_{0.67}$RuO$_3$ inert anode fabricated from pressing constituent oxides at stoichiometric quantities and sintering at 1400°C for 12 hours (top, note full densification was not achieved). Photographs of the recovered electrode after exposure to molten CaCl$_2$ for 12 hours and after washing, with no discernible mass loss (bottom).